DGK Ausschuss Geodäsie (DGK)
der Bayerischen Akademie der Wissenschaften

Reihe C | Dissertationen | Heft Nr. 966

Longjiang Tang

Multi-GNSS Real-time Precise Orbit Determination

München 2025

Verlag der Bayerischen Akademie der Wissenschaften, München

ISSN 0065-5325 ISBN 978-3-7696-5378-6

DGK Ausschuss Geodäsie (DGK)
der Bayerischen Akademie der Wissenschaften

Reihe C Dissertationen Heft Nr. 966

Multi-GNSS Real-time Precise Orbit Determination

An der Fakultät VI - Planen Bauen Umwelt
der Technischen Universität Berlin
zur Erlangung des akademischen Grades
Doktor der Ingenieurwissenschaften
- Dr.-Ing. -
genehmigte Dissertation

vorgelegt von

Longjiang Tang, M. Sc.

München 2025

Verlag der Bayerischen Akademie der Wissenschaften, München

ISSN 0065-5325 ISBN 978-3-7696-5378-6

Adresse des Ausschusses Geodäsie (DGK)
der Bayerischen Akademie der Wissenschaften:

Ausschuss Geodäsie (DGK) der Bayerischen Akademie der Wissenschaften
Alfons-Goppel-Straße 11 ● D – 80 539 München
Telefon +49 – 89 – 23 031 1113 ● Telefax +49 – 89 – 23 031 - 1283 / - 1100
e-mail post@dgk.badw.de ● http://www.dgk.badw.de

Promotionsausschuss:
Vorsitzender: Prof. Dr. Frank Flechtner
Gutachter: Prof. Dr. Dr. h.c. Harald Schuh
Gutachter: Prof. Dr. Urs Hugentobler
Gutachter: Prof. Dr. Paweł Wielgosz
Gutachter: Prof. Dr. Maorong Ge

Tag der wissenschaftlichen Aussprache: 17. Januar 2025

Diese Dissertation ist auf dem Server des Ausschusses Geodäsie (DGK)
der Bayerischen Akademie der Wissenschaften, München unter <http://dgk.badw.de/>
sowie auf dem Server der TU Berlin unter < https://doi.org/10.14279/depositonce-23168>,
Berlin 2025, elektronisch publiziert

ISSN 0065-5325 ISBN 978-3-7696-5378-6

Acknowledgments

With generous support and assistance from numerous individuals, the completion of this dissertation has been made possible.

First and foremost, I would like to express my deep gratitude to my supervisors, Maorong Ge and Harald Schuh. I sincerely thank them for offering me the opportunity to conduct my research at GFZ, providing essential facilities, sharing their profound expertise in space geodesy, continuously encouraging me to strive for excellence, and offering the financial support necessary for my work. My sincere appreciation also goes to Benjamin Männel for his valuable advice and selfless support. I am equally grateful to Prof. Urs Hugentobler and Prof. Pawel Wielgosz for agreeing to co-supervise my research and for their constructive comments and insightful suggestions.

I appreciate Jungang Wang for sharing his creative insights and supporting my studies. Special acknowledgment is also given to Zhiguo Deng, my roommate Zhiwei Qin, my colleague Xiao Chang, Hanbing Pen, Xinyuan Jiang, Bobin Cui, Xiang Zuo, Wen Huang, Liangwei Nie for fruitful discussion and sharing of various academic ideas. I enjoyed a wonderful time with every colleague in the Real-Time GNSS group at GFZ.

My sincere thanks go to our IT colleagues, Thomas Nischan and Sylvia Magnussen, for promptly addressing my server-related inquiries, greatly facilitating the smooth progress of my research. Special acknowledgment is extended to Andre Brandt for his continuous and invaluable support.

Finally, I wish to express my heartfelt thanks to my family for their unconditional love, support, and understanding. Most importantly, my deepest appreciation goes to my beloved wife, Congying Shao, for her unwavering support, patience, understanding, and love throughout this journey.

My stay at GFZ has been financially supported by the DFG project, to which I am extremely grateful.

Abstract

Providing real-time precise positioning services with Global Navigation Satellite Systems (GNSSs) has a profound impact on various fields such as autonomous driving, natural hazard monitoring and early warning, and surface loading. Stable, reliable, and high-precision real-time satellite orbits and clocks are the prerequisites for real-time Precise Point Positioning (PPP) services. Serving as the essential information for real-time precise positioning, satellite orbits are usually estimated with the latest available observations and predicted for real-time applications. However, the orbit accuracy drops progressively when the orbit update interval becomes longer. This thesis focuses on investigating the provision of high-precision satellite orbits in the real-time, including dynamic orbit modeling, ambiguity fixing and data processing strategy.

Solar radiation pressure (SRP) is the most critical non-gravitational force acting on satellite orbits, especially in the eclipsing seasons. Taking GPS orbit as an example, it is demonstrated that the number of unknown parameters in the Empirical CODE Orbit Model (ECOM), which served as a parameterization model, can be reduced if there is a precise a priori box-wing model. For those eclipsing satellites, the shadow factor is recommended to apply in the D (pointing toward to the Sun) direction instead of all three directions. The active parameters in Y and B directions could absorb some unknown forces under eclipse seasons. The superiority of combining the a priori precise box-wing model with five-parameter ECOM (ECOM1) as well as adding shadow factor only in the D direction is proved by orbits and Earth rotation parameters. Compared with the solution with only the ECOM1 model as a parameterization model, the RMS values of orbit day boundary discontinuity (DBD) are improved by 17.8%, 22.7%, and 26.1% for the BLOCK IIR satellites in eclipsing seasons in the along, cross, and radial direction, respectively.

Another key role for high-precision satellite orbits is carrier phase integer ambiguity resolution (IAR). Besides double difference (DD) IAR, undifferenced (UD) IAR has also been proven to be achievable in precise orbit determination (POD). The POD solution derived from UD IAR is demonstrated to be superior to that from DD IAR. For example, the orbit accuracy of BDS MEO satellites is improved by 21.7% and 10.4% in the along and cross component, respectively. Similar results can be observed from geodetic parameters including ERPs, station coordinates and geocenter coordinates. The orbits and geodetic parameters demonstrate that the differences between DD IAR and UD IAR solutions stem from the absence of independent DD ambiguities and incorrectly fixed DD ambiguity, in which the former takes the primary leading to orbit differences. Solving the above two problems is challenging, particularly when dealing with a massive network, so UD IAR is highly recommended for daily GNSS data processing.

In the last part, a novel data processing strategy that parallels the epoch processing and significantly enhances the computation efficiency is proposed. In our proposed strategy, a 24-

hour processing job is split into several sub-sessions that are processed in parallel, and then stacked to solve and recover parameters. Together with paralleling other procedures such as orbit integration and using open multi-processing (openMP), the multi-GNSS POD of 120 satellites using 90 stations can be fulfilled within 30 min. With historical information, including fixed UD ambiguities and cleaned observations, the network solution with 100 stations and 120 satellites can be finished in 10 min, in which one iteration of parameter estimation only costs 3 min. The predicted orbits derived from epoch-parallel-based solution equal to the legacy sequential batch solution. Compared with IGS products, the average 1D RMS values of user-available predicted orbits updated per 10 min are 3.1, 5.8, 3.4, 138.8, 18.1, and 6.8 cm for GPS, GLONASS, Galileo, BDS GEO, BDS IGSO, and BDS MEO satellites, respectively. The DBDs of corresponding orbits are around 1.0 cm for MEO satellites.

This thesis demonstrates the feasibility of the proposed strategies in providing high-precision near real-time satellite orbits. The refined satellite force modeling and ambiguity fixing strategy improve the accuracy, while the proposed epoch-parallel strategy can shorten orbit update time effectively with the aid of multi-nodes and historical information. The stable and high-precision satellite orbits are beneficial for real-time clock estimation, precise point positioning, and atmospheric sounding.

Kurzfassung

Die Bereitstellung von Echtzeit-Präzisionspositionierungsdiensten mit Globalen Satellitennavigationssystemen (GNSS) hat einen tiefgreifenden Einfluss auf verschiedene Bereiche wie autonomes Fahren, Überwachung von Naturgefahren und Frühwarnungsystemen sowie Oberflächenbelastung. Stabile, zuverlässige und hochpräzise Echtzeit-Satellitenbahninformationen und Taktkorrekturen sind die Voraussetzung für Echtzeit-Präzisionspositionsbestimmungsdienste. Satellitenorbits, die als wesentliche Informationen für die Echtzeit-Präzisionspositionierung dienen, werden in der Regel mit den neuesten verfügbaren Beobachtungen geschätzt und für Echtzeitanwendungen vorhergesagt. Die Genauigkeit der Bahnen nimmt jedoch progressiv ab, wenn das Intervall für die Bahnaktualisierung länger wird. Diese Arbeit konzentriert sich auf die Untersuchung der Bereitstellung von hochpräzisen Satellitenorbits in Echtzeit, einschließlich dynamischer Bahnenmodellierung, Fixierung der GNSS-Mehrdeutigkeiten und Datenaufbereitungsstrategie.

Der Strahlungsdruck der Sonne (SRP) ist die kritischste nicht-gravitative Kraft, die auf Satellitenorbits wirkt, insbesondere in den Erdschattendurchgängen. In dieser Studie wird am Beispiel der GPS-Bahn gezeigt, dass die Anzahl der unbekannten Parameter im Empirischen CODE-Orbitmodell (ECOM), das als Parametrisierungsmodell dient, reduziert werden kann, wenn ein präzises a priori Box-Wing-Modell vorhanden ist. Für diese sich im Schatten befindlichen Satelliten wird empfohlen, den Schattenfaktor in Richtung D (zum Sonnenpunkt hin) anstatt in allen drei Richtungen anzuwenden. Die aktiven Parameter in den Richtungen Y und B könnten einige unbekannte Kräfte während der Eklipsesaisons absorbieren. Die Überlegenheit der Kombination des a priori präzisen Box-Wing-Modells mit dem fünfparameterigen ECOM (ECOM1) sowie der Hinzufügung des Schattenfaktors nur in Richtung D wird durch Bahnen und Erdrotationsparameter nachgewiesen. Im Vergleich zur Lösung mit nur dem ECOM1-Modell als Parametrisierungsmodell werden die RMS-Werte der Bahngrenzdiskontinuität (DBD) der BLOCK IIR-Satelliten in den Eklipsesaisons in der Längs-, Quer- und Radialrichtung um 17,8%, 22,7% bzw. 26,1% verbessert.

Eine weitere wichtigef Faktor für hochpräzise Satellitenorbits ist die Lösung der Trägerphasen-Mehrdeutigkeiten (IAR). Neben der Auflösung der doppelten Differenz (DD) hat sich gezeigt, dass auch die Auflösung der undifferenzierten (UD) IAR bei der präzisen Bahnbestimmung (POD) erreichbar ist. Die aus UD IAR abgeleitete POD-Lösung erweist sich als überlegen gegenüber der aus DD IAR. Beispielsweise wird die Bahngenauigkeit der BDS-MEO-Satelliten in den Längs- und Querkomponenten um 21,7% bzw. 10,4% verbessert. Ähnliche Ergebnisse sind bei geodätischen Parametern wie ERPs, Stationskoordinaten und Geozentrumkoordinaten zu beobachten. Sowohl die Bahnen als auch die geodätischen Parameter zeigen, dass die Unterschiede zwischen DD IAR und UD IAR-Lösung auf das Fehlen unabhängiger DD-Mehrdeutigkeiten und falsch fixierter DD-Mehrdeutigkeiten zurückzuführen sind, wobei die erstere die Hauptursache für Bahnunterschiede darstellt. Die Lösung der beiden oben genannten Probleme ist besonders bei der Bewältigung eines großen

Netzwerks herausfordernd, daher wird UD IAR für die tägliche GNSS-Datenverarbeitung dringend empfohlen.

Im letzten Teil wird eine neuartige Datenverarbeitungsstrategie vorgeschlagen, die die Epochenverarbeitung parallelisiert und die Recheneffizienz erheblich verbessert. In unserer vorgeschlagenen Strategie wird ein 24-Stunden-Verarbeitungsvorgang in mehrere Teilabschnitte unterteilt, die parallel verarbeitet und dann gestapelt werden, um Parameter zu lösen und wiederherzustellen. Zusammen mit der Parallelisierung anderer Verfahren wie der Bahnenintegration und der Verwendung von Open-Multi-Processing (OpenMP) kann die Multi-GNSS-POD von 120 Satelliten mit 90 Stationen innerhalb von 30 Minuten durchgeführt werden. Mit vorhandenen Informationen, einschließlich fixierter UD-Ambiguitäten und bereinigter Beobachtungen, kann die Netzwerklösung mit 100 Stationen und 120 Satelliten in 10 Minuten abgeschlossen werden, wobei eine Iteration der Parameterabschätzung nur 3 Minuten dauert. Die aus epochenparallelen Lösungen abgeleiteten vorhergesagten Bahnen entsprechen der traditionellen sequentiellen Batch-Lösung. Verglichen mit IGS-Produkten zeigen sich 1D-RMS-Werte der alle 10 Minuten aktualisierten vorhergesagten Bahnen für GPS-, GLONASS-, Galileo-, BDS-GEO-, BDS-IGSO- und BDS-MEO-Satelliten von 3,1, 5,8, 3,4, 138,8, 18,1 bzw. 6,8 cm. Die DBDs der entsprechenden Bahnen liegen bei etwa 1,0 cm für MEO-Satelliten.

Diese Arbeit zeigt die Machbarkeit der vorgeschlagenen Strategien zur Bereitstellung von hochpräzisen Satellitenbahnen in Echtzeit auf. Die verfeinerte Modellierung von Satellitenkräften und die Strategie der Mehrdeutigkeitsfixierung verbessern die Genauigkeit, während die vorgeschlagene epochenparallele Strategie die Bahnenaktualisierungszeit effektiv verkürzen kann, unterstützt durch mehrere Rechnerknoten und verfügbare Informationen. Die stabilen und hochpräzisen Satellitenorbits sind vorteilhaft für die Echtzeit-Uhrenschätzung, die präzise Punktpositionierung und die Beobachtung der Atmosphäre.

List of Figures

List of Tables

List of Abbreviations

AC	Analysis Center, e.g., COD, GFZ, BKG
ARP	Antenna Reference Point
BDS	The BeiDou Navigation Satellite System
BKG	Bundesamt für Kartographie und Geodäsie
CERES	Clouds and the Earth's Radiant Energy system
CODE	Center for Orbit Determination in Europe
CoM	Center of Mass
CPU	Central processing unit
CRF	Celestial Reference Frame
CRS	Celestial Reference System
DBD	Day-boundary-discontinuity
DCB	Differential code biases
DD	Double-difference
DOY	Day of Year
DSB	Differential signal bias
dUT1	UT1-UTC, the time difference between UT1 and UTC
ECOM	Empirical CODE Orbit Model
ECOM1	Five-parameter ECOM model
ECOM2	Nine-parameter ECOM model
ERP	Earth Rotation Parameter
FOC	Full Operational Capability
GEO	Geostationary Earth Orbit
GFZ	GFZ Helmholtz Centre for Geosciences (GFZ Helmholtz-Zentrum für Geoforschung)
GNSS	Global Navigation Satellite Systems
GLONASS	Globalnaya navigatsionnaya sputnikovaya sistema
GM	Earth's gravitational constant
GMF	Global Mapping Function
GNSS	Global Navigation Satellite System
GPS	Global Positioning System
GSPM	GPS solar radiation model
IAR	Integer ambiguity resolution
IERS	International Earth Rotation and Reference Systems Service
IF	Ionosphere-free
IFB	Inter Frequency Bias
IGS	International GNSS Service
IGSO	Inclined GeoSynchronous Orbit
IGU	IGS Ultra-rapid products
ISB	Inter-system biases
ITRF	International Terrestrial Reference Frame
ITRS	International Terrestrial Reference System
JPL	NASA Jet Propulsion Laboratory
LEO	Low earth orbit
LSQ	Least-squares
MEO	Medium Earth orbit

MGEX	Multi-GNSS Experiment
NEQ	Normal equation
NL	Narrow-lane
NNC	No-Net Conditions
NNR	No-net-rotation
NNS	No-net-scale
NNT	No-net-translation
OSB	Observable-specific Signal Biases
PANDA	Position And Navigation Data Analyst
POD	Precise orbit determination
PPP	Precise point positioning
QZSS	Quasi-Zenith Satellite System
R	Earth's equatorial radius
RMS	Root mean Square
RTS	Real-time service
SLR	Satellite laser ranging
SRF	Satellite body reference frame
SRIF	Square root information filter
SRP	Solar Radiation Pressure
SSD	Solid-state drive
STD	Standard deviation
UPD	Uncalibrated phase delay
UD	Undifferenced
WL	Wide-lane
WHU	Whuhan University
ZHD	Zenith Hydrostatic Delay
ZWD	Zenith Wet Delay

List of Contents

1 Introduction

1.1 Overview

Global Navigation Satellite System (GNSS) profoundly impacts on various fields, including navigation, surveying, geodesy and geodynamics. Owing to the continuous signal tracking from globally distributed stations, GNSS contributes to the spatial and temporal densification of the International Terrestrial Reference Frame (ITRF) (Altamimi & Collilieux, 2009; Altamimi et al., 2018; Bizouard et al., 2018). Since mid-1995, the International GNSS Service (IGS) Analysis Centers (ACs) started to deliver satellite orbits and clocks, station coordinates, and earth rotation parameters (ERPs) (Geoffrey et al., 1994; Ferland & Piraszewski, 2009; Rebischung et al., 2016; Rebischung, 2021). The operational provision of precise satellite orbit and clock products provided by IGS ACs also contribute to the study of crustal movements, slow slip events, and surface mass redistribution (El-Mowafy & Bilbas, 2016; Kobayashi & Tsuyuki, 2019; Zhang et al., 2021; White et al., 2022; Heki & Jin, 2023).

Since 2013, IGS has launched real-time service (RTS). Through RTS, the IGS extends its capability to support applications requiring real-time access to IGS products, for example, self-driving cars (Knoop et al., 2017; Elsheikh et al., 2019), unmanned aerial vehicles (Ragauskas et al., 2017), weather monitoring (Li et al., 2015). The RTS is an official GNSS service providing access to precise real-time products, including orbit and clock corrections, code and phase biases and so on[1]. Among those real-time products, precise satellite orbits and clocks are the most essential parts for RT precise point positioning (PPP) applications. The satellite clocks are usually estimated via a filter (Laurichesse et al., 2013; Zuo et al., 2021), while the orbit estimation can be carried out by the least-squares (LSQ) batch processing (TA Springer & Hugentobler, 2001; Lutz et al., 2014) or epoch-wise filtering (Laurichesse et al., 2013).

For most IGS RT ACs, the available real-time orbits are predicted from the batch least-squares solution owing to its feasibility of routine processing. IGS began providing ultra-rapid (IGU) GPS orbits in November 2000 and then reduced the update latency of ultra-rapid orbits from 12 to 6 h in April 2004 (TA Springer & Hugentobler, 2001; Jan Kouba, 2009a). As a member of the Multi-GNSS Experiment (MGEX) ACs, German Research Centre for Geosciences (GFZ) started to provide five GNSS system ultra-rapid products with a 3-hour update rate in November 2015, including GPS, GLONASS, Galileo, BDS, and QZSS (Deng et al., 2017). Whuhan University (WHU) provided hourly updated multi-GNSS orbits with an accuracy of 3 to 5 cm (Zhao et al., 2017).

The rest of the ACs also provide real-time orbits via filtering, such as the square root information filter (SRIF) at JPL (Bertiger, Bar-Sever, Dorsey, Haines, Harvey, Hemberger, Heflin, Lu, Miller, Moore, et al., 2020) and the Kalman filter at CNES (Laurichesse et al., 2013).

[1] https://igs.bkg.bund.de/ntrip/

For the filter-based method, the stochastic constraint is introduced in the orbit state elements update, which is formed as a linear blend of the previous estimate and the current measurement information.

1.2 Motivation and objective

High-precision real-time orbits are prerequisites for real-time applications. Nevertheless, generating high-precision real-time orbits from a batch solution still faces many challenges, such as imperfect solar radiation pressure (SRP) model, incorrect integer ambiguity resolution, and time-consuming processing procedure. With more satellites and stations involved, a huge number of unknown parameters must be estimated and among them the number of undifferenced (UD) ambiguity parameters is the most. In that case, the computation time is always a burden. Since the orbit accuracy drops progressively when the orbit update interval becomes longer (Dai et al., 2019; Duan et al., 2019), enhancing computation time means providing better satellite orbits. Therefore, numerous studies have been conducted to address these challenges.

1.2.1 Solar radiation pressure modeling

SRP is the dominant non-gravitational perturbation for GNSS satellites, which relies on the knowledge of satellite-related properties. The SRP models are mainly divided into two categories, the analytical and empirical models. Analytical models such as the box-wing and ray tracing approach are established based on the physical properties of the satellite components, including the area and its optical property, and the satellite attitude. Despite the analytical models having a clear physical interpretation, they can still cause large model errors due to the possible inaccurate satellite structure or optical property. There are two feasible methods refine these models. The first one is to adjust optical coefficients of reflection, diffusion, absorption with satellite tracking data (Rodriguez-Solano et al., 2012), named adjustable box-wing model. Based on the observed GNSS observations and a priori satellite metadata, a plenty of studies have been implemented to get high-precision adjustable box-wing models (Duan et al., 2019; Duan et al., 2020; Duan & Hugentobler, 2021; Duan et al., 2022). The second one is to develop an expression of Fourier series based on the analysis of accelerations caused by SRP, such as the ROCK model series (ROCK-S, ROCK-T), which was developed by the satellite manufacturer Rockwell International (H. Fliegel et al., 1985; H. Fliegel, 1989; H. F. Fliegel et al., 1992; H. F. Fliegel & Gallini, 1996), and the GPS solar radiation model (GSPM) developed by Jet Propulsion Laboratory (JPL) (Y. Bar-Sever & Kuang, 2005).

In addition to the models derived from physical-based methods, the empirical SRP models are developed by fitting the long-term orbit estimates regardless of the satellite metadata—for instance, the Empirical CODE Orbit Model (ECOM) developed by the Center for Orbit Determination in Europe (CODE) (Beutler et al., 1994). The ECOM was then further refined

by reducing the periodic terms in the satellite–Sun direction, that is, the ECOM1 model with five coefficients (T. A. Springer et al., 1999). The ECOM2 was developed in 2015 to consider the SRP variation caused by different satellite shapes, for instance, the Galileo satellites (Arnold et al., 2015). Both ECOM1 and ECOM2 are widely used as parameterization models by several ACs (Guo et al., 2016; Deng et al., 2017; Prange, Beutler, et al., 2020). However, estimating more parameters in ECOM2 can cause an overparameterization and destabilize orbit solutions, and the pure parameterization models may also introduce draconitic errors in GNSS-based geodetic products (Meindl et al., 2013; Rodriguez-Solano et al., 2014). To minimize the number of SRP parameters and consider the SRP force components that cannot be described by the parameterization model, an a priori SRP model is recommended (Oliver Montenbruck, Steigenberger, & Hugentobler, 2014). Hence, a hybrid strategy of combining the a priori box-wing model and the parameterization model, that is, ECOM1 or ECOM2, is beneficial for the orbit quality (P. Steigenberger et al., 2015; Li et al., 2019).

The orbit differences among different ACs have been proven to be largely caused by using different approaches to SRP modeling (Sibthorpe et al., 2011). Many studies also reported that the performances of different SRP models are related to specific satellite types (Chang et al., 2021). For instance, ECOM1 has better performance than ECOM2 in terms of predicated orbit precision (Y. Liu et al., 2019). In addition, an analysis of Chinese BDS Inclined Geosynchronous Orbit (IGSO) and medium Earth orbit (MEO) orbits indicated that the box-wing model can remove the β- and μ-dependent systematic orbit errors (Guo et al., 2017). All the analyses mentioned above have summarized the discrepancy of satellite orbit precision between ECOM1 and ECOM2 and the importance of the a priori box-wing model. Despite the above studies, a comprehensive investigation of different SRP models especially when satellites are in eclipse seasons is still lacking.

1.2.2 Integer ambiguity resolution

For network solutions, integer ambiguity resolution (IAR) approaches are mainly divided into two categories: Double-difference (DD) IAR and UD IAR. DD IAR achieves IAR by forming ambiguity difference between station pairs and satellite pairs, in which common hardware delays originating in satellite transmitters and receivers are eliminated and the resulted DD ambiguity has natural integer feature (Blewitt, 1989; Dong & Bock, 1989). Over the past three decades, DD IAR is widely adopted in GNSS network processing by most IGS ACs for routine GNSS data processing, such as JPL, CODE and GFZ. For DD IAR of a massive network, the step of picking independent DD ambiguities from the entire network can be very time-consuming. Currently, two alternative strategies are proposed to reduce computation burden. One is selecting the most-easy-to-fix independent DD ambiguities on each baseline firstly and then across the entire network (M. Ge et al., 2005b). The other one is firstly determining a subset with optimal independent baselines and then independent DD ambiguities are picked on each baseline (Blewitt, 2008).

On the other hand, the hardware delay at satellite and receiver sides, that is, uncalibrated phase delay (UPD), can be estimated and applied as corrections to recover the integer feature of UD ambiguities, and thus, the UD IAR can be performed. UD IAR was primarily developed for PPP and aimed to realize IAR station by station (M. Ge et al., 2007; Laurichesse et al., 2009; Collins et al., 2010) and was also applied for network solution for better computation efficiency (Chen et al., 2014). Recently, UD IAR is adopted by several IGS ACs for network solutions (Strasser et al., 2018; Katsigianni et al., 2019; Deng et al., 2022; Calero-Rodríguez et al., 2023). Compared with DD IAR, UD IAR is more efficient for the network solutions since the fixed carrier-phases ambiguities can be converted into carrier-ranges so that a huge number of ambiguity parameters are not involved (H. Chen et al., 2014; Ruan & Wei, 2019; Xie et al., 2023). Beyond computation efficiency, H. Chen et al. (2014) also show that the orbit quality of UD IAR is better than that of DD IAR by 10% in terms of orbit overlaps, which is further confirmed by Deng et al. (2022). Furthermore, station coordinates derived from UD IAR are demonstrated to be superior to solutions from DD IAR (Geng & Mao, 2021).

Although many studies have highlighted computation efficiency and improved quality of satellite orbits and station positions as advantages of UD IAR, the reason of the differences are not yet investigated comprehensively. Geng and Mao (2021) show that the improved coordinate accuracy of UD IAR is possibly caused by the incorrectly resolved DD ambiguities in DD IAR. However, their study concentrates on the PPP solution, the impact on a global network solution for precise orbit determination should be more important as there are more parameters involved. They also showed the dependency of the solutions on the specific implementation of the DD IAR strategies, but without further investigation on the reasons.

1.2.3 Data processing efficiency

The straightforward way to reduce the computing time is parallel processing, including the parallel processing of sub-networks, individual satellites or constellations, and sub-sessions. The results of parallel processed tasks will be combined later to generate final orbit products. In the network parallel processing, the network is divided into several sub-networks to be processed in parallel, and NEQs of sub-networks are combined by utilizing a certain number of common stations to derive a final solution (Beutler et al., 1996; Bruni et al., 2018; Zurutuza et al., 2019; Pintori et al., 2021). As the satellite and receiver clocks are eliminated during parallel processing, they cannot be combined by stacking the NEQs and thus it is not equivalent to the integrated solution. In a satellite or constellation parallel processing, each group of satellites is processed separately in parallel and delivered to users (Q. Chen et al., 2021). The constellation solutions can be combined via common parameters, such as ERP and station coordinates, which would potentially improve the consistency and precision of orbits. However, it is still not possible to combine other processing parameters such as tropospheric parameters and receiver clocks, as they are pre-eliminated once inactive. Another method is to split an undivided processing into several sub-sessions and each sub-session is processed separately but in parallel to generate the sub-session NEQs. In this study, a session refers to

the time length of observations involved in a processing job, for example, a 24-hour session in the daily POD jobs. All the sub-session NEQs are stacked, with all necessary parameters combined, including both global parameters such as ERP, orbits, and station coordinates, and the processing parameters such as ambiguities covering different sub-sessions. This method is much more efficient as the computation burden can be shared by several computing nodes. Jiang et al. (2021) applied the epoch-parallel into multi-GNSS precise orbit determination (POD) with double-differenced observations. However, they keep all parameters in the NEQ, including the tropospheric delays, clocks, and ambiguities, which consumes a huge amount of time in the multi-GNSS POD with un-differenced observations. In addition, keeping the ambiguities in the NEQ leads to an enormous NEQ, slowing the speed of inversion.

In addition, special algorithms are also developed for solving a GNSS network with a huge number of stations. By keeping only active parameters in the NEQ, M. Ge et al. (2006) reduces the requirement of computer memory and computation burden. The optimized algorithms based on newly developed processors, i.e., block-partitioned algorithms (Quintana-Orti et al., 2008; Gong et al., 2017) and Open Multi-Processing (openMP) (Chandra et al., 2001) continue improving the computation efficiency. Since most active parameters in GNSS POD are ambiguities, a carrier-range method is brought up and successfully implemented in the huge network processing with the UD ambiguity resolution (Blewitt; et al., 2010; H. Chen et al., 2014). However, because precise orbits and clocks are the prerequisite for PPP IAR, it therefore cannot be applied to ultra-rapid POD of a network solution with around 100 stations. Y. Cui, Chen, et al. (2021) also designed a parallel computing of large GNSS network, which is suitable for multi-core and multi-node environments, by decomposing the GNSS modelling tasks of each epoch to different nodes and cores. However, the efficiency was demonstrated with PPP and baseline processing of large GNSS networks instead of network solution itself which is essential for ultra-rapid GNSS POD. Of course, with the improvement of modern computer power like modern central processing unit (CPU) and solid-state drive (SSD), the efficiency in GNSS POD can be further improved (Li et al., 2018).

Facing with sharply increased number of GNSS observations, a huge number of parameters must be handled in the least-squares batch processing. Parameter estimation takes the majority of the computation time of a GNSS data processing task. Beside from the refinement of parameter-elimination strategy proposed by X. Chen et al. (2022), multiple parallel-processing strategies are proposed to improve data processing efficiency, for example sub-networks, individual satellite constellations and sub-sessions. Among all the ultra-rapid orbits provided by IGS ACs, the shortest orbit update interval is still one hour. As the update interval increases, the users can only access the predicted orbits of a longer arc which are of worse quality.

1.2.4 Objective

Based on the previous studies, the primary objective of this thesis is to provide high-precision real-time satellite orbits. The performance of different SRP models, especially during eclipse seasons, is discussed first, which is a prerequisite for high-precision orbits. Different from the

DD IAR commonly applied in network solutions, the characteristics of UD IAR in POD are further investigated to reveal the possible cause of its superiority. After achieving these objectives, strategies for improving data processing efficiency are proposed and validated. Specifically, the following questions will be discussed.

- How to choose the appropriate SRP model and handle the shadow factor?
    - What is the performance of box-wing models and empirical models on eclipsing satellites.
    - How the shadow factor should be applied in the SRP modeling for eclipsing satellites?
- What are the benefits of applying UD IAR in POD?
    - How is the agreement between UD IAR and DD IAR?
    - If not well, how to explain the potential discrepancy?
    - what are the advantages of UD IAR on satellite orbits, as well as other geodetic parameters?
- How to improve data processing efficiency for real-time POD processing?
    - How to utilize the advantages of multiple computer resources?
    - How to integrate historical information to speed up data processing?
    - How is the impact of predicted orbits and clocks on real-time PPP after improved data processing efficiency?

The performance of different SRP models, including the box-wing and adjustable box-wing as the a priori model, and the ECOM1 and ECOM2 as the parameterization model, is analyzed and the handling of the shadow factor in the SRP modeling for eclipsing satellites is also investigated. The performance of UD IAR is discussed with an emphasize on satellite orbits and geodetic parameters and the consistency between UD IAR and DD IAR is investigated to find out where the potential discrepancy originates from. Based on the refined SRP model and UD IAR, the strategies for shortening orbit update interval are proposed by applying multiple computer resources and introducing historical information. Finally, an example of RT PPP with predicted orbits and clocks is performed to show the superiority of shortening orbit update interval.

When the data processing efficiency is improved and the orbit update interval is shortened, this thesis also performs an example of RT PPP to show the advantage of shortening orbit update interval. Owing to the high-stability hydrogen clocks onboard, the accuracy of one-hour clock estimates for Galileo is better than 0.1 ns (X. Wang, Chai, et al., 2020; H. Ge et al., 2021). The corresponding kinematic PPP accuracy in each component is better than 0.2 m, without significant accuracy degradation (Yang et al., 2017; Peng et al., 2019). Therefore, investigating the feasibility of RT PPP with both predicted orbits and clocks derived from

batch processing products provides an additional option for users in some cases, for example interruption in data communicating.

1.3 Outline

This section describes the background, motivation and objectives of this study and the structure of the thesis. The outline of this thesis is given below:

Chapter 2 briefly describes the basic theoretical backgrounds of precise orbit determination and the data processing methods. The modeling of satellite orbits is introduced, together with the signal delay models. The least-squares adjustment is then presented briefly. Two integer ambiguity resolution strategies are also described. The POD processing strategy is summarized based on Position And Navigation Data Analyst (PANDA) software at the end of this chapter.

In Chapter 3, the main focus lies on evaluating of the applicability of different SRP models and the shadow factor on eclipsing satellites. This chapter begins by analyzing the relationship between the ECOM model and box-wing models. Apart from the introduction of SRP models, how to handle the shadow factor and its impact on eclipsing satellites are also discussed. The data processing procedure is summarized secondly. Thirdly, the performance of different SRP models and the shadow factor assessed based on unknown ECOM parameters, satellite orbits and ERPs.

Chapter 4 investigates the characteristics of UD IAR on POD. The theoretical relationship between UD IAR and DD IAR is discussed first. Based on the characteristics of UPDs, a flowchart of UD IAR in POD is presented. Then the performance of UD IAR is evaluated in terms of estimated UPDs, satellite orbits, ERPs, station coordinates and geocenter coordinates. By setting different POD scenarios, in which the only difference is the strategy of ambiguity fixing, the possible reasons causing the orbit discrepancy between UD IAR and DD IAR are analyzed. The impact of the discrepancy on geodetic parameters is also investigated.

With the refined SRP model achieved in Chapter 3 and UD IAR realized in Chapter 4, the strategies for improving data processing efficiency (i.e., shortening orbit update interval) are proposed in Chapter 5. Before introducing the detailed epoch-parallel processing strategy, the consistency of the legacy batch processing and the proposed strategy is demonstrated theoretically. Then, the epoch-parallel processing strategy is realized in PANDA software is realized and its processing efficiency on multi nodes (i.e., servers) is presented. Except the newly introduced data, all the others is clean, i.e. without either outliers or cycle slips. Using the historical information of data cleaning will reduce the computation time significantly. The fixed UD ambiguities are removed in the parameter estimation. The orbit accuracy of user-available parts with different orbit update intervals is validated. The advantage of shortening orbit update interval is also demonstrated by an example of RT PPP with predicted orbits and clocks at the end of this chapter.

Finally, the major findings from this study are summarized in Chapter 6, together with a concise outlook for the research work in the foreseeable future.

2 Theory of precise orbit determination

In this Chapter, the theoretical background of GNSS POD is introduced. The data processing method including satellite orbits, signal delay models, least-squares adjustment, and integer ambiguity resolution are then introduced concisely, which serves as the fundamental role of the following study. The detailed data processing strategies are also discussed in Section 2.5.

2.1 Satellite Orbits

Currently, there are two methods to determine satellite orbits, including kinematic and dynamic orbit determination (Ashkenazi et al., 1990). Kinematic orbit determination is sensitive to measurement quality and observational geometry, often applied for Low earth orbiters (LEO). In contrast, dynamic orbit determination, applied to determine GNSS satellite orbits, is less sensitive to observation gaps and outlier. Beside from measurement quality, the quality of satellite orbits could be poor due to limited force model accuracy. In the determination of satellite orbits with GNSS observations, the knowledge of a GNSS satellite's attitude or orientation in space is vital for accounting for horizontal satellite antenna offset with respect to mass center, representing SRP and describing variations of the phase measurement caused by the circularly polarized nature of GNSS signals. In this section, the satellite force models are first summarized. Then, the variational equations are described in Section 2.1.2. Finally, the details of the GNSS satellite attitude are described in Section 2.1.3.

2.1.1 Force models

According Newton's second law of motion, for the motion of a satellite around a central body (i.e., Earth), various forces acting on a satellite result in an acceleration

$$\ddot{\mathbf{r}}(t) = \boldsymbol{a}(t, \boldsymbol{r}, \dot{\mathbf{r}}, \boldsymbol{\beta}), \tag{2.1}$$

where $\boldsymbol{t}$ is time, $\boldsymbol{r}$ the satellite's position, $\dot{\mathbf{r}}$ the satellite's velocity $\dot{\mathbf{r}}$, and $\boldsymbol{\beta}$ is a number of additional force model parameters. The force model parameters $\boldsymbol{\beta}$ are required for forces which are not exactly known and must be represented precisely with unknown parameters. Equation (2.1) is called equation of motion. Integrating Equation (2.1) leads to the velocity of the center-of-mass and again to the position. The satellite state vector $\mathbf{X}^{\mathbf{s}}(t) = [\mathbf{r}(t), \dot{\mathbf{r}}(t)]^{\mathbf{T}}$ at each epoch depends on the unknown initial state vector $\mathbf{X}_0^{\mathbf{s}} = [\mathbf{r_0}, \dot{\mathbf{r}}_\mathbf{0}]^{\mathbf{T}}$ and force model parameters $\boldsymbol{\beta}$.

The acceleration $\boldsymbol{a}$ can be represented as follows

$$\boldsymbol{a} = \boldsymbol{a}_g + \boldsymbol{a}_{ng} + \boldsymbol{a}_{emp}, \tag{2.2}$$

where $\boldsymbol{a}_g$ is the sum of accelerations caused by conservative forces, including Earth's gravity field, astronomical tides, solid Earth tides, ocean tides, atmospheric tides, pole tides, and ocean pole tides. Those conservative forces can be modeled with sufficient accuracy and

corresponding in-depth descriptions are provided in the IERS conventions (Petit & Luzum, 2010). $\boldsymbol{a}_{ng}$ is the sum of accelerations caused by non-gravitational forces, including solar radiation pressure, Earth radiation pressure, antenna thrust and atmospheric drag force (mainly for LEOs). Some non-gravitational forces, such as solar radiation pressure, often cannot be modeled with sufficient accuracy. This is because the precise physical properties of the satellite, such as its shape and materials, are prerequisites for accurate modeling and may not be precisely known. In most cases, satellite operators have not officially disclosed this information, or some disclosed values from ground calibration may need be adjusted again due to the space environment. Therefore, empirical model parameters have to be estimated to compensate for unmodeled forces, e.g., radiation of thermal blankets, thermal radiation from the satellite radiators, solar panels thermal radiation, thermal radiation of excess solar array power (shunt). $\boldsymbol{a}_{emp}$ are empirical accelerations, consisting of constant and periodic terms.

Solar radiation pressure

Currently, direct SRP acting on the GNSS satellites can be handled using parametrization models, such as the Empirical CODE Orbit Model (Arnold et al., 2015), a priori models like adjustable box-wing model (Rodriguez-Solano et al., 2012), or hybrid models that combine the two.

Box-wing model

As the name suggests, the Box-Wing model uses a small number of surfaces to describe momentum transfer of photons according to the Lambert law (Milani et al., 1987; H. F. Fliegel et al., 1992; Rodriguez-Solano et al., 2012). The physical interaction between the SRP and satellite solar panel is formulated as

$$\boldsymbol{a}_{SRP,sp} = -d\frac{AS_0}{mc}\cos\theta\left[(\alpha+\delta)\cdot\boldsymbol{e}_D + 2\left(\frac{\alpha}{3}+\rho\cos\theta\right)\cdot\boldsymbol{e}_N\right], \quad (2.3)$$

where d denotes the squared ratio between Earth–Sun and satellite–Sun distance; A denotes the area of solar panel, m denotes the mass of the satellite, S_0 denotes the solar flux at 1 AU ($\approx 1376\ W/m^2$), c denotes the velocity of light in vacuum, α, ρ, and δ denote the fractions of absorbed, specularly reflected, and diffusely scattered photons, respectively. $\boldsymbol{e}_D$ denotes the unit vector from satellite to Sun. $\boldsymbol{e}_N$ denotes the unit normal vector of surface. θ denotes the angle between $\boldsymbol{e}_D$ and $\boldsymbol{e}_N$ ($cos\theta \geq 0$).

For the satellite body, surfaces are usually covered by multi-layer insulation (MLI) blankets, which will reradiate the absorbed energy back into space instantly. The acceleration of a surface can be represented as follows

$$\boldsymbol{a}_{SRP,i} = -d\frac{AS_0}{mc}\cos\theta[(\alpha+\delta)\cdot\boldsymbol{e}_D + k_1(\alpha+\delta)\cdot\boldsymbol{e}_N + k_2\rho\cos\theta\cdot\boldsymbol{e}_N]. \quad (2.4)$$

The coefficients k_1 and k_2 depend on the shape of satellite body, with $k_1 = \frac{2}{3}$ and $k_2 = 2$ in case of a flat surface or $k_1 = \frac{\pi}{6}$ and $k_2 = \frac{4}{3}$ in case of a cylindrical surface (H. F. Fliegel et al., 1992).

The total acceleration induced by solar radiation can then be obtained as the sum of the accelerations from all surfaces.

$$\boldsymbol{a}_{SRP,i} = f \cdot \left(\sum_i^n \boldsymbol{a}_{SRP,i} + \boldsymbol{a}_{SRP,sp}\right) \tag{2.5}$$

where n is the number of illuminated surfaces and f is the shadow factor, representing the percentage of the Sun that is visible from the satellite's point of view based on a conical shadow model (Oliver Montenbruck et al., 2002). The in-depth introduction of shadow factor can be found in Chapter 3.

As mentioned at the beginning of this section, modeling solar radiation pressure analytically based on Equations (2.3) and (2.4) requires detailed information of all satellite surfaces. However, in most cases, satellite manufactures only provide this information in a simplified form (GSA, 2017; CSNO, 2019a, 2019b), The detailed structures on the surfaces, e.g., signal transmitting antenna units, communication antenna, radiators and thrusters, is missing. Therefore, the accuracy of such an analytical model is limited even if the area and material properties are available. Moreover, current box-wing model do no account for self-shadowing, e.g., antennas (C. Wang et al., 2018a) and solar panels casting shadows on the bus. When a detailed 3D models of the satellites are available, ray tracing has been demonstrated to be a useful way to model solar radiation pressure analytically (Ziebart, 2004).

Facing the situation with limited information on satellite surfaces, an adjustable box-wing model is proposed by Rodriguez-Solano et al. (2012) to estimate the coefficients of optical properties of the satellite surfaces as well as other additional parameters (e.g., solar sensor bias and solar panel rotation lag) using tracking data. Then the coefficients of the box-wing model for several satellite types, including GPS, GLONASS, Galileo, and BDS, have been updated with a similar approach (Duan et al., 2019; Duan et al., 2020; Duan & Hugentobler, 2021, 2022; Duan et al., 2022). The orbit results and SLR residuals confirms the advantages of the application of box-wing model, even though these adjusted optical properties do not strictly fulfill the constraint $\alpha + \delta + \rho = 1$.

ECOM model

Due to the restriction of attitude accuracy, the complex components in illuminated surfaces, and the existence of thermal radiations, the adjustable box-wing model cannot fully describe all the solar radiation on the satellite surface. In absence of sufficiently accurate analytical solar radiation pressure models, empirical models are commonly applied in GNSS satellite orbit determination. These models aim to describe the effect of solar radiation pressure on satellite orbits by means of a set of empirical coefficients, which can be set up as parameters in the orbit determination process.

The most widely used empirical models are the ECOM presented by Beutler et al. (1994) and its extensions (Arnold et al., 2015; X. Chen et al., 2023). The acceleration of solar radiation pressure with ECOM model can be represented by

$$\boldsymbol{a}_{SRP} = f \cdot (D(\mu)\mathbf{e}_D + Y(\mu)\mathbf{e}_Y + B(\mu)\mathbf{e}_B) \tag{2.6}$$

where μ denotes the satellite's argument of latitude, which is replaced by the angular argument $\Delta\mu = \mu - \mu_s$ and μ_s is the Sun's argument of latitude in satellite orbital plane for straightforward interpretation (Arnold et al., 2015). $\mathbf{e}_D$ denotes the unit vector in the satellite-sun direction (i.e., D direction), $\mathbf{e}_Y$ denotes the unit vector along the satellite's solar panel axis (i.e., Y direction), and $\mathbf{e}_B$ completes the right-handed frame (i.e., B direction). In different ECOM models, the functions D(μ), Y(μ), and B(μ) are represented as a truncated Fourier series

$$\begin{aligned} D(\mu) &= D_0 + \sum_i \left(D_{Ci}cos(i\mu) + D_{Si}sin(i\mu)\right) \\ Y(\mu) &= Y_0 + \sum_i \left(Y_{Ci}cos(i\mu) + Y_{Si}sin(i\mu)\right) \\ B(\mu) &= B_0 + \sum_i \left(B_{Ci}cos(i\mu) + B_{Si}sin(i\mu)\right) \end{aligned} . \quad (2.7)$$

The acceleration along each axis consists of constant $\boxdot_0$ and i-per-revolution sine and cosine terms ($\boxdot_{Ci}$,$\boxdot_{Si}$). Within the analysis centers of the IGS, the two most common ECOM models are ECOM1 with five parameters ($D_0, Y_0, B_0, B_{C1}, B_{S1}$), as proposed in T. A. Springer et al. (1999) and ECOM2 with nine parameters ($D_0, D_{C2}, D_{S2}, D_{C4}, D_{S4}, Y_0, B_0, B_{C1}, B_{S1}$), as proposed in (Arnold et al., 2015). The major difference between ECOM1 and ECOM2 is the addition of the twice-per-revolution terms in D direction, which aims to mitigate the systematic effects caused by the elongated shape of GLONASS and Galileo satellite buses (Arnold et al., 2015). With multi-year orbit observations, some modified ECOM model are proposed to improve the ability of the model, for example ECOM3 with seven parameters ($D_0, D_{C2}, D_{S2}, Y_0, B_0, B_{C1}, B_{S1}$) (Prange, Villiger, et al., 2020), and ECOME model, with seven parameters ($D_0, D_{S4}, D_{S6}, Y_0, B_0, B_{C1}, B_{S1}$) for BDS IGSO and MEO (X. Chen et al., 2023). Besides on the solar radiation pressure, the estimated unknown empirical parameters can take the role of absorbing some unmodeled forces on satellite, such as thermal forces. Sidorov et al. (2020) found that the ECOM2 model with additional D_{S1} and activation of the constant term in the Y direction leads to a substantial reduction of orbit misclosures, especially the radial orbital component during eclipse seasons.

Earth radiation

In addition to the direct solar radiation pressure, the satellite also suffers pressures from the Earth-reflected shortwave optical radiation and emitted longwave infrared radiation, the second largest non-gravitational forces. The optical albedo radiation is produced by scattering and reflecting the incident solar radiation on the Earth's surface. The infrared radiation is a near-isotropic re-emission of the direct solar radiation absorbed by the Earth. Inclusion of Earth radiation and antenna thrust reduces the GPS orbit radius by 2 cm, resulting in a corresponding reduction of the observed bias of satellite laser ranging (SLR) residuals (Rodriguez-Solano et al., 2011). Therefore, it is essential to consider this force in GNSS data processing.

The acceleration caused by by one element of Earth's surface can be computed as

$$\mathbf{a}_{ERP} = \frac{AS_0}{\pi r^2}\cos\theta_E \sum_i^N \left(R\cos\theta_S \boldsymbol{a}_{SRP,i}(\alpha_O, \delta_O, \rho_O) + \frac{E}{4}\boldsymbol{a}_{SRP,i}(\alpha_I, \delta_I, \rho_I)\right), \quad (2.8)$$

where A is the area of the element on Earth's surface, N the number of illuminated satellite's surfaces, r the distance between the satellite and the element's center, k the shadow function of Earth's surface. θ_E is the angle between the vector from the element's center (instead of the Sun) to the satellite $\mathbf{e}_D$ and the normal vector of the Earth's surface element $\boldsymbol{n}$. θ_S is the angle between the vector from the element's center to the Sun $\mathbf{e}_{Sun}$ and the normal vector of the Earth's surface element $\boldsymbol{n}$. α_O, δ_O and ρ_O are the respective optical properties of satellite's surface materials. α_I, δ_I and ρ_I are the respective infrared properties of satellite's surface materials. R is the reflectivity of the element, that is albedo. E is the emissivity of the element. The albedo and emissivity can be expressed analytically using a twice-order zonal spherical harmonic model (Knocke et al., 1988), or using data from a finite element model, e.g., the Clouds and the Earth's Radiant Energy System (CERES).

Although the CERES data is available from March 2000 until today (with a delay of few months), this is not enough for reprocessing or operational data processing within the IGS. For computation efficiency, an analytical model, independent of the CERES data is proposed and represented as

$$\mathbf{a}_{ERP} = \frac{T^2 S_0}{r^2}\cos\theta_E \sum_{i=1}^{N}\left(\frac{2R}{3\pi}C_1\boldsymbol{a}_{SRP,i}(\alpha_O,\delta_O,\rho_O) + \frac{1-R}{4}\boldsymbol{a}_{SRP,i}(\alpha_I,\delta_I,\rho_I)\right), \quad (2.9)$$

where T is top of atmosphere fluxes, around 6401000 m. the $C_1 = (\pi - \theta_S)\cos(\theta_S) + \sin(\theta_S)$ is a function of angle θ_S. The albedo R is set as a constant value, such as 0.34. Rodriguez-Solano et al. (2011) found that the most important model components are the solar panels of the satellites while different Earth radiation models have a minor impact on orbits at GPS altitudes.

Antenna thrust

Antenna thrust is a small acceleration acting on GNSS satellites caused by the transmission of radio navigation signals. The acceleration due to antenna thrust can be expressed as (Milani et al., 1987)

$$\mathbf{a}_{AT} = \frac{P}{c \cdot m}\frac{\mathbf{r}}{|\mathbf{r}|} \quad (2.10)$$

where P is the satellite's transmit power in Watt, m is satellite's mass in kg, $\mathbf{r}$ is satellite's geocentric position. The above expression assumes a narrow-beam, rotationally symmetric gain pattern and an antenna boresight directed toward the Earth's center. The transmit power of GPS, GLONASS, Galileo, and BeiDou satellites with a high-gain antenna are measured by Peter Steigenberger et al. (2017) and new related data can be found on the IGS website[2].

2.1.2 Variational equations

Through variational equations, satellite state vector, as well as some unknown force model parameters, such as SRP parameters can be solved. The equations of satellite motion can be expressed as a first-order differential equation system

[2] https://igs.org/mgex/metadata/

$$\dot{\boldsymbol{X}}(t) = \vec{f}(t, \boldsymbol{X}, \boldsymbol{\beta}), \tag{2.11}$$

based on the state vector

$$\dot{\boldsymbol{X}}(t) = \begin{bmatrix} \dot{\boldsymbol{r}}(t) \\ \boldsymbol{a}(t, \boldsymbol{r}, \dot{\mathbf{r}}, \boldsymbol{\beta}) \end{bmatrix}. \tag{2.12}$$

and the vector of force model parameters $\boldsymbol{\beta} = [\beta_1 \quad \cdots \quad \beta_n]^T$. In Equation **Error! R eference source not found.**, $\boldsymbol{r}$ and $\dot{\boldsymbol{r}}$ are vectors of satellite position and velocity, respectively.

Deriving Equation (2.11) with respect to the initial state vector $\boldsymbol{X_0}$ leads to

$$\frac{\partial \dot{\boldsymbol{X}}(t)}{\partial \boldsymbol{X_0}} = \frac{\partial f(t, \boldsymbol{X}, \boldsymbol{\beta}, \cdots)}{\partial \boldsymbol{X}} \cdot \frac{\partial \boldsymbol{X}(t)}{\partial \boldsymbol{X_0}}. \tag{2.13}$$

by introducing the state transition matrix

$$\boldsymbol{\Phi}(t) = \frac{\partial \boldsymbol{X}(t)}{\partial \boldsymbol{X_0}} = \begin{bmatrix} \frac{\partial \boldsymbol{r}(t)}{\partial \boldsymbol{r_0}} & \frac{\partial \boldsymbol{r}(t)}{\partial \dot{\boldsymbol{r}}_0} \\ \frac{\partial \dot{\boldsymbol{r}}(t)}{\partial \boldsymbol{r_0}} & \frac{\partial \dot{\boldsymbol{r}}(t)}{\partial \dot{\boldsymbol{r}}_0} \end{bmatrix}, \tag{2.14}$$

which contains the partial derivatives of the satellite position and velocity with respect to the initial position and velocity. Substituting $\frac{\partial f(t, \boldsymbol{X}, \boldsymbol{\beta}, \cdots)}{\partial \boldsymbol{X}}$ and $\frac{\partial \boldsymbol{X}(t)}{\partial \boldsymbol{X_0}}$, Equation (2.13) can be written as

$$\dot{\boldsymbol{\Phi}}(t) = \begin{bmatrix} \mathbf{0}_{3\times3} & \mathbf{I}_{3\times3} \\ \frac{\partial \boldsymbol{a}(t, \boldsymbol{r}, \dot{\boldsymbol{r}}, \boldsymbol{\beta})}{\partial \boldsymbol{r}(t)} & \frac{\partial \boldsymbol{a}(t, \boldsymbol{r}, \dot{\boldsymbol{r}}, \boldsymbol{\beta})}{\partial \dot{\boldsymbol{r}}(t)} \end{bmatrix} \boldsymbol{\Phi}(t). \tag{2.15}$$

Starting from the initial value $\boldsymbol{\Phi_0} = \mathrm{I}$, the state transition matrix for each epoch t can be determined by numerical integration using Equation (2.15) .

Derivating Equation (2.11) with respect to the unknown force model parameters $\boldsymbol{\beta}$ gives

$$\frac{\partial \dot{\boldsymbol{X}}(t)}{\partial \boldsymbol{\beta}} = \frac{\partial \boldsymbol{f}(t, \boldsymbol{X}, \boldsymbol{\beta}, \cdots)}{\partial \boldsymbol{\beta}} + \frac{\partial \boldsymbol{f}(t, \boldsymbol{X}, \boldsymbol{\beta}, \cdots)}{\partial X} \cdot \frac{\partial \boldsymbol{X}(t)}{\partial \boldsymbol{\beta}}. \tag{2.16}$$

by introducing the parameter sensitivity matrix

$$\mathbf{S}(t) = \frac{\partial \boldsymbol{X}(t)}{\partial \boldsymbol{\beta}} = \begin{bmatrix} \frac{\partial \boldsymbol{r}(t)}{\partial \boldsymbol{\beta}} \\ \frac{\partial \dot{\boldsymbol{r}}(t)}{\partial \boldsymbol{\beta}} \end{bmatrix}, \tag{2.17}$$

which the partial derivatives of the satellite state with respect to the unknown force model parameters $\boldsymbol{\beta}$, Equation (2.16) can be written as

$$\dot{\mathbf{S}}(t) = \begin{bmatrix} \mathbf{0}_{3\times3} & \mathbf{I}_{3\times3} \\ \frac{\partial \boldsymbol{a}(t, \boldsymbol{r}, \dot{\boldsymbol{r}}, \boldsymbol{\beta})}{\partial \boldsymbol{r}(t)} & \frac{\partial \boldsymbol{a}(t, \boldsymbol{r}, \dot{\boldsymbol{r}}, \boldsymbol{\beta})}{\partial \dot{\boldsymbol{r}}(t)} \end{bmatrix} \mathbf{S}(t) + \begin{bmatrix} \mathbf{0}_{3\times3} \\ \frac{\partial \boldsymbol{a}(t, \boldsymbol{r}, \dot{\boldsymbol{r}}, \boldsymbol{\beta})}{\partial \boldsymbol{\beta}} \end{bmatrix}. \tag{2.18}$$

Starting from the initial value $\mathbf{S_0} = 0$ (Milbert & Jekeli, 2023), the state transition matrix for each epoch t can be determined by numerical integration using Equation (2.18). The state transition and parameter sensitivity matrices are then used to connect the GNSS observation equations to the orbit parameters $(\mathbf{X_0}, \boldsymbol{\beta})$.

Additional empirical parameters are often set up to further mitigate imperfections in the applied force models. Various parametrizations are implemented (see Jäggi et al. (2006), for

examples) and in use among the IGS analysis centers. One of them is so-called pseudostochastic pulses (Beutler et al., 1996), which are small, instantaneous velocity changes at specific epochs, for example at the center of a 24-hour orbit arc. Such empirical parameters are usually constrained in order to limit their negative impact due to overparameterization. The main reason is that they usually do not have a physical interpretation and the dynamic nature of an orbit should be maintained as much as possible. Ideally, future improvements in force modeling would render this type of parameter unnecessary.

2.1.3 Satellite attitude

The knowledge of a GNSS satellite's attitude or orientation in space is vital for high precision applications. As mentioned by O. Montenbruck et al. (2015), satellite attitude model in POD mainly affects the following three aspects:

- Phase center correction. It is necessary to correctly account for satellite antenna offsets with respect to the center of mass and potential direction-dependent variations.
- phase wind-up correction. The circularly-polarized nature of GNSS signals leads to variations of the phase measurement depending on the relative orientation between the transmitting and receiving antennas.
- Non-gravitational force modeling. Knowing the orientation of a satellite's body and solar panels is important for modeling accelerations induced by solar and Earth radiation pressure and atmosphere drags for LEOs during orbit integration.

Satellite attitude is defined as the orientation of a satellite body-fixed reference frame (SRF) with respect to a specified reference frame, such as terrestrial reference frame (TRF) or celestial reference frame (CRF). However, the origins and axes of SRF depend on the definition for example by satellite manufactures. Attitude control is the manner of maintaining the attitude in space, for example the transmitting antenna of most of the GNSS satellite always toward the earth and its solar panels perpendicular to the Sun direction. Adopting the IGS-specific body frame orientation leads to a common formulation of the nominal attitude of all GNSS satellites in yaw-steering mode irrespective of their specific orbit and constellation (O. Montenbruck et al., 2015). It is defined as follows:

Origin: located in the satellite's center of mass.

$\boldsymbol{e}_x$ **axis**: pointing towards the permanently sunlit panel of the satellite bus.

$\boldsymbol{e}_y$ **axis**: pointing along the solar panel rotation axis in the direction defined by ($\boldsymbol{e}_y = \boldsymbol{e}_z \times \boldsymbol{e}_x$).

$\boldsymbol{e}_z$ **axis**: pointing along the antenna boresight direction.

The rotation matrix from this SRF to the CRF is represented as

$$\mathbf{R}_{SRF}^{CRF} = [\boldsymbol{e}_x \quad \boldsymbol{e}_y \quad \boldsymbol{e}_z], \tag{2.19}$$

which describes the satellite's attitude or orientation in space. Note that all vectors in this section are given in the CRF. Satellite attitude should obey the following two rules to achieve better service. One is that the satellite antenna needs to point to the Earth's center to ensure enough signal strength around the Earth. The other one is that solar panel needs to be

perpendicular to the satellite-Sun direction for maximum energy input. Most satellites follow a nominal yaw-steering behavior outside of so-called eclipse seasons.

Nominal Attitude Model

Following the IGS conventions, the two kinds of commonly applied nominal modes for GNSS satellites are yaw-steering mode and orbit normal mode (O. Montenbruck et al., 2015). The yaw-steering mode, rotating around the Z axis (defined in SRF), is predominantly applied by GNSS satellites in medium Earth orbit (Y. E. Bar-Sever, 1996; J. Kouba, 2009b). On the other hand, orbit normal mode, keeping a constant alignment in the local orbit frame without rotation, is usually used by GNSS satellites in geostationary or geosynchronous orbits (O. Montenbruck et al., 2015).

For the yaw-steering mode, the unit vectors of three SRF axes are defined as

$$\boldsymbol{e}_x^{YS} = \boldsymbol{e}_y^{YS} \times \boldsymbol{e}_z^{YS} \tag{2.20}$$

$$\boldsymbol{e}_y^{YS} = \frac{\boldsymbol{e}_\odot \times \boldsymbol{e}_r}{\|\boldsymbol{e}_\odot \times \boldsymbol{e}_r\|} \tag{2.21}$$

$$\boldsymbol{e}_z^{YS} = -\boldsymbol{e}_r. \tag{2.22}$$

Here, $\boldsymbol{e}_r = \frac{r}{\|r\|}$ is the normalized satellite position vector, $\boldsymbol{e}_\odot = \frac{r_{sun}-r}{\|r_{sun}-r\|}$ the unit vector pointing from the satellite towards the Sun. r_{sun} and r are the position vectors of the Sun and satellite, respectively.

For the orbit normal mode, the unit vectors of three SRF axes are aligned with the orbital frame and are defined as

$$\boldsymbol{e}_x^{ON} = -\boldsymbol{e}_a \tag{2.23}$$

$$\boldsymbol{e}_y^{ON} = -\boldsymbol{e}_c \tag{2.24}$$

$$\boldsymbol{e}_z^{ON} = -\boldsymbol{e}_r. \tag{2.25}$$

Here, the unit vectors $\boldsymbol{e}_a$, $\boldsymbol{e}_c$, and $\boldsymbol{e}_r$ represent the along, cross, and radial axes of a local orbit frame. Rotating the orbit normal frame around the $\boldsymbol{e}_z$ axis by the nominal yaw angle (Y. E. Bar-Sever, 1996)

$$\psi_{nom} = atan2(-tan\beta, sin\mu) \tag{2.26}$$

is so called the yaw-steering model. Here, $\beta = \text{acos}\left(-\boldsymbol{e}_c \cdot \frac{r_{Sun}}{\|r_{Sun}\|}\right) - \frac{\pi}{2}$ is an angle between the Earth-Sun vector r_{Sun} and the satellite's orbital plan (J. Kouba, 2009b). $\mu = \mu(r) - \mu(r_{Sun}) + \pi$ is an orbit angle describing the position of the satellite along the orbit counting from orbit midnight, which is the point farthest from the Sun (Beutler et al., 1994). When the angle between the (satellite–Earth) and (satellite–Sun) vectors is close to 0, the yaw rate will exceed the maximum hardware yaw rates near noon and midnight, as shown in Figure 2.1. In that case, special attitude models are established to describe the orientation variation of satellites.

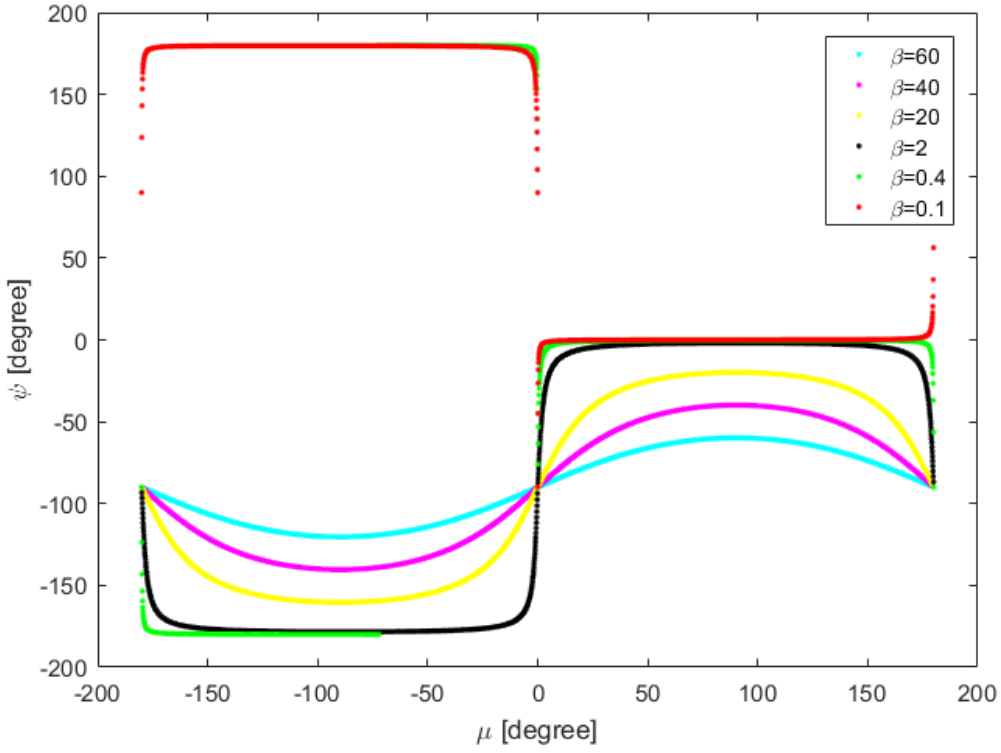

Figure 2.1 Nominal yaw around orbit midnight for various angles β.

Special attitude behavior around orbit noon and midnight

A major problem of the yaw-steering attitude mode is that a satellite would have to yaw at a very high rate around the orbit noon and midnight points when the Sun is close to the orbital plane (Y. E. Bar-Sever, 1996). At very low angles, for example $|\beta| < 1°$, the yaw rate required to maintain the nominal attitude usually exceeds the maximum yaw rate a satellite can physically achieve. Another problem is that when a satellite crosses Earth's shadow, which happen once per revolution at orbit midnight when the μ angle is below a certain threshold (e.g., 14° for GPS), the Sun is invisible and solar sensors mounted on the satellite cannot provide information to the attitude control system (Y. E. Bar-Sever, 1996). For these reasons, satellite manufacturers developed special attitude behavior around orbit noon and midnight. This behavior can differ between manufacturers and different satellite types from the same manufacturer (J. Kouba, 2009b). For example, GPS-IIR satellites manufactured by Lockheed Martin behave differently during shadow crossings than GPS-IIA and GPS-IIF satellites, which were manufactured by Rockwell International/Boeing. GPS-IIA and GPS-IIF satellites also do not share the same behavior. In addition, satellites might not necessarily behave the same way around orbit noon and midnight. The general implemented attitude modes used by GNSS are shown in Figure 2.1, including GPS, Galileo, GLONASS and BDS. Note that most BDS-2I/2M satellites have transitioned to BDS-3I/3M modes.

Table 2.1 GNSS Satellite Attitude modes.

Satellite type	Default	Midnight	Noon	References
GPS-II/IIA	N	Y0	Y1	Y. E. Bar-Sever (1996), J. Kouba (2009b)
GPS-IIR/IIR-M	N	Y0	Y0	J. Kouba (2009b)

GPS-IIF	N	Y0	Y3	Dilssner (2010), Dilssner, Springer, and Enderle (2011), Kuang et al. (2017)
GPS-IIIA	N	Y0	Y0	Peter Steigenberger et al. (2020)
GLO	N	Y2	Y4	Dilssner, Springer, Gienger, et al. (2011)
GAL-1	N	S0	S0	GSA (2017)
GAL-2	N	S1	S1	GSA (2017)
BDS-2G/3G	O	O	O	C. Wang et al. (2018b), Dilssner (2017)
BDS-2I/2M	N	ON	ON	Dai et al. (2015) ,C. Wang et al. (2018b)
BDS-3I/3M	N	S1	S1	C. Wang et al. (2018b), CSNC (2019)

- N: The nominal yaw-steering mode
- O: The orbit normal mode which is a quite a simple yaw attitude control mode compared to the other models
- yaw models adopted by other GNSS satellites
- ON: The orbit normal mode with switches between yaw-steering (N) and orbit normal attitude (O) under certain conditions
- S0/S1: The "smoothed" yaw-steering modes which happen during a lower β angle and near noon or midnight.
- Y0/Y1/Y2/Y3/Y4: the model with linear yaw changes and its details can be found in the list references. All modes only require an approximate orbit and some satellite- or type-specific metadata, for example the maximum yaw rate, as input.

Figure 2.1 reveals that GPS features yaw maneuvers with a constant yaw rate. During midnight, BLOCK IIF satellites start maneuver when entering the eclipse, while BLOCK IIR and IIF satellites start when the yaw speed reaches their maximum values. Taking the yaw angle computed by PANDA as a reference, the difference is less than 2.6° with respect to CODE and 9.3° with respect to WHU. The attitudes generated by GFZ show apparent differences from others, especially for BLOCK IIIA satellites. During noon, three satellite types show the same yaw behavior. They only differ in their maximum yaw rates, which are approximately 0.12°/s, 0.20°/s, and 0.11°/s for GPS-IIA, GPS-IIR, and GPS-IIF, respectively (J. Kouba, 2009b; Dilssner, 2010).

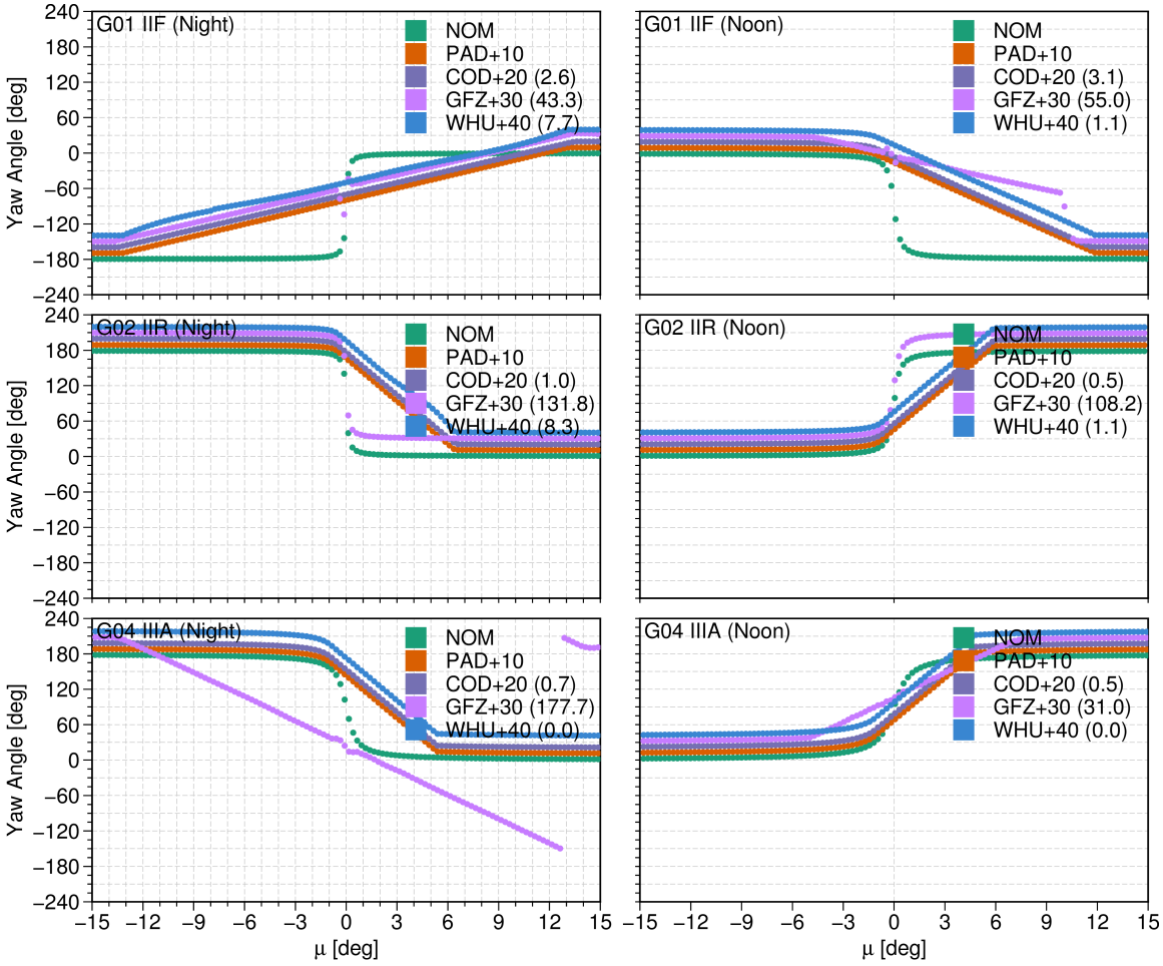

Figure 2.2 Attitude behavior of some GPS satellites around orbit midnight (left panel) and noon (right panel) in 2023. NOM stands for the nominal attitude, PAD the attitude used in PANDA software, COD the attitude applied in CODE, GFZ the attitude applied in GFZ MGEX products and WHU the attitude applied in Wuhan University. The values in each label stand for the maximum attitude difference with respect to corresponding PAD results. For a clear show, the yaw angles derived from PAD, COD, GFZ, and WHU are shifted 10°, 20°, 30°, and 40°, respectively.

Figure 2.3 shows the attitudes of GLONASS satellites, including GLONASS-M and GLONASS-K generations. Similar to the GPS results, significant differences are observed in the yaw attitudes derived from GFZ products, especially for night maneuvers. For the night maneuver, it seems that GFZ products keep a constant value during the eclipse and then recover rapidly at the end. This attitude mode does not fit the reality, as the yaw rates at the end of the eclipse are possibly larger than the maximum yaw rates. For the noon maneuver, GFZ also performs a different attitude mode. The yaw differences between our calculations and WHU and CODE products are less than 5°, except for the yaw variation of GLONASS-K1B in CODE products. A nominal attitude is applied in GLONASS-K1B in CODE products. Among three AC products, the yaw angles calculated in our software are close to that derived from WHU products, which indicates that the attitude modes of GLONASS satellites are identical in the two products.

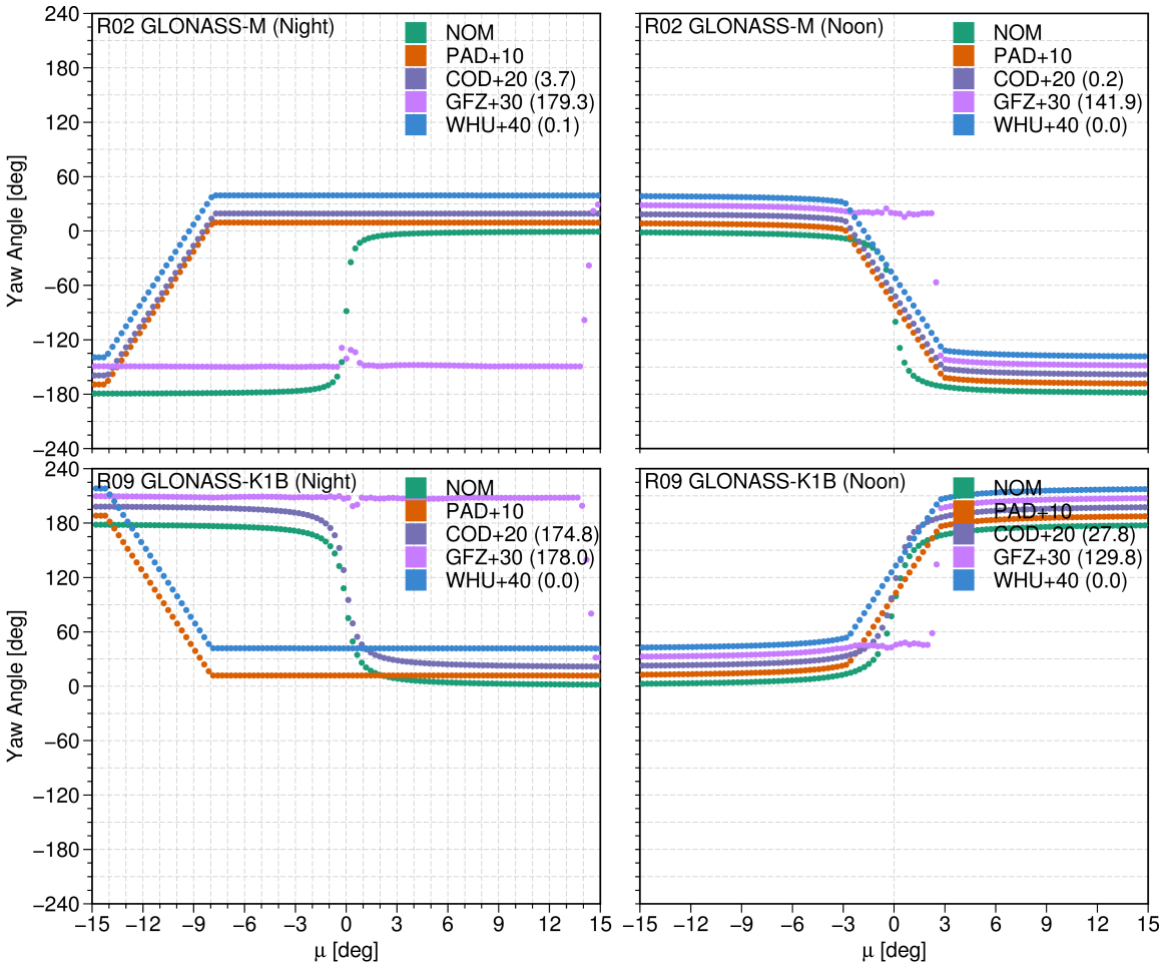

Figure 2.3 Attitude behavior of some GLONASS satellites around orbit midnight (left panel) and noon (right panel) in 2023. NOM stands for the nominal attitude, PAD the attitude used in PANDA software, COD the attitude applied in CODE, GFZ the attitude applied in GFZ MGEX products and WHU the attitude applied in Wuhan University. The values in each label stand for the maximum attitude difference with respect to corresponding PAD results. For a clear show, the yaw angles derived from PAD, COD, GFZ, and WHU are shifted 10°, 20°, 30°, and 40°, respectively.

Figure 2.4 shows the attitudes of Galileo satellites, including PRN E02 and E14, in a highly eccentric orbit. Compared with other systems, the yaw angles of Galileo satellites between different AC products are consistent owing to the published satellite metadata[3]. The maximum difference of satellite yaw angle is less than 0.1°, except for the noon maneuver calculated by GFZ. However, the two satellites (E14, E18) show different performances when applying the identical attitude mode of other FOC satellites. A discontinuity, larger than 30°, is observed in while the satellite is running out of the eclipse, which also exists in the noon maneuver. Interestingly, the yaw angles derived from the CODE product are continuous during the night and noon maneuvers. The attitude modes of E14 and E18 need further investigation in the future.

[3] https://www.gsc-europa.eu/support-to-developers/galileo-satellite-metadata

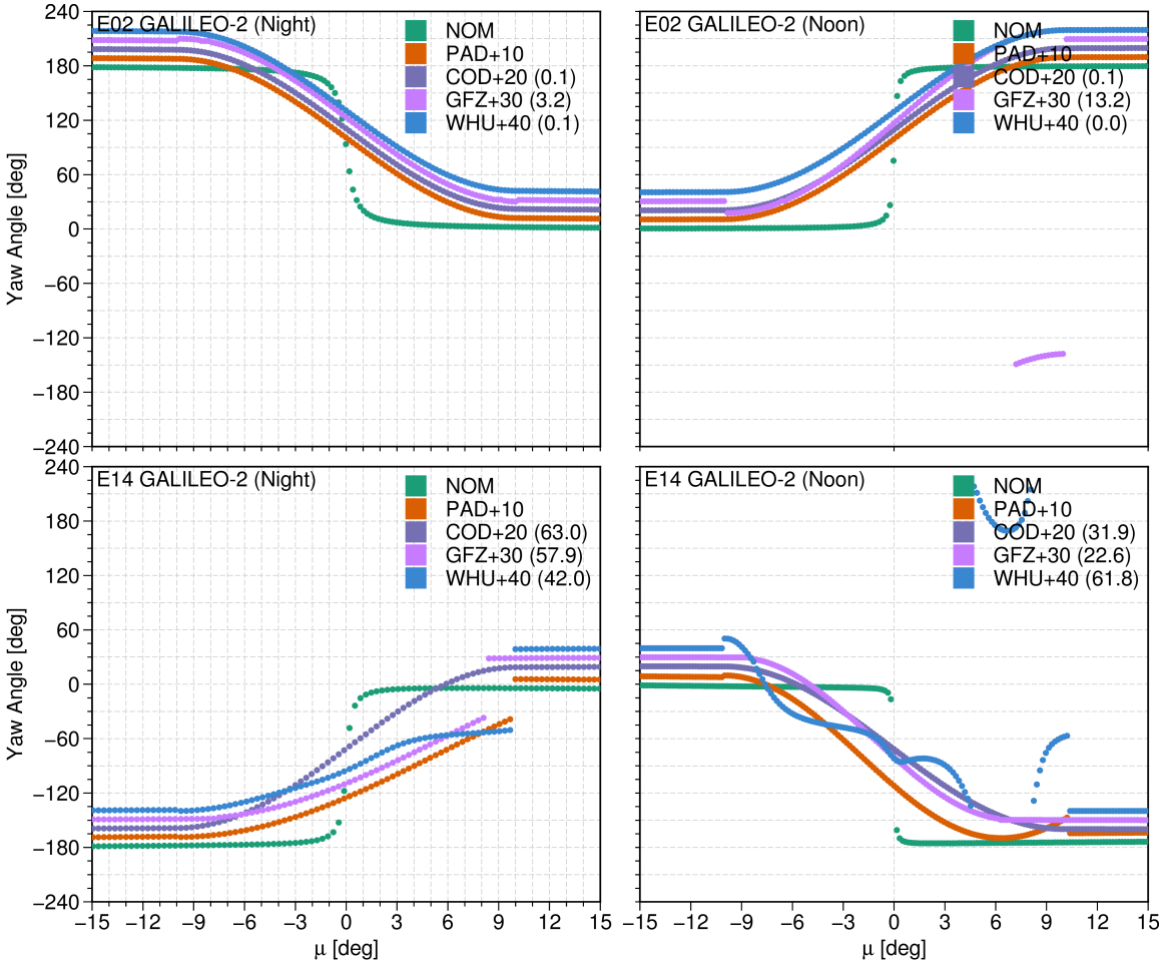

Figure 2.4 Attitude behavior of some Galileo satellites around orbit midnight (left panel) and noon (right panel) in 2023. NOM stands for the nominal attitude, PAD the attitude used in PANDA software, COD the attitude applied in CODE, GFZ the attitude applied in GFZ MGEX products and WHU the attitude applied in Wuhan University. The values in each label stand for the maximum attitude difference with respect to corresponding PAD results. For a clear show, the yaw angles derived from PAD, COD, GFZ, and WHU are shifted 10°, 20°, 30°, and 40°, respectively.

Figure 2.5 shows the attitudes of BDS satellites, including BDS-2 IGSO/MEO and BDS-3 IGSO/MEO satellites. For BDS-2 IGSO and some BDS-2 MEO satellites, satellite attitude mode has transitioned from nominal yaw-steering attitude to orbit normal attitude. For BDS-3 and some BDS-2 MEO (e.g., SVN C015 and C017) satellites, the "smoothed" yaw-steering modes mentioned in Table 2.1 are used. Among the three products, the GFZ products show a different performance for BDS-3 MEO CAST and IGSO satellites, in which the attitude of BDS-3 MEO CAST satellites is abnormal. Similar to the attitude of GLONASS-K1B in CODE products, a nominal attitude mode is applied for BDS-3 IGSO satellites in GFZ products.

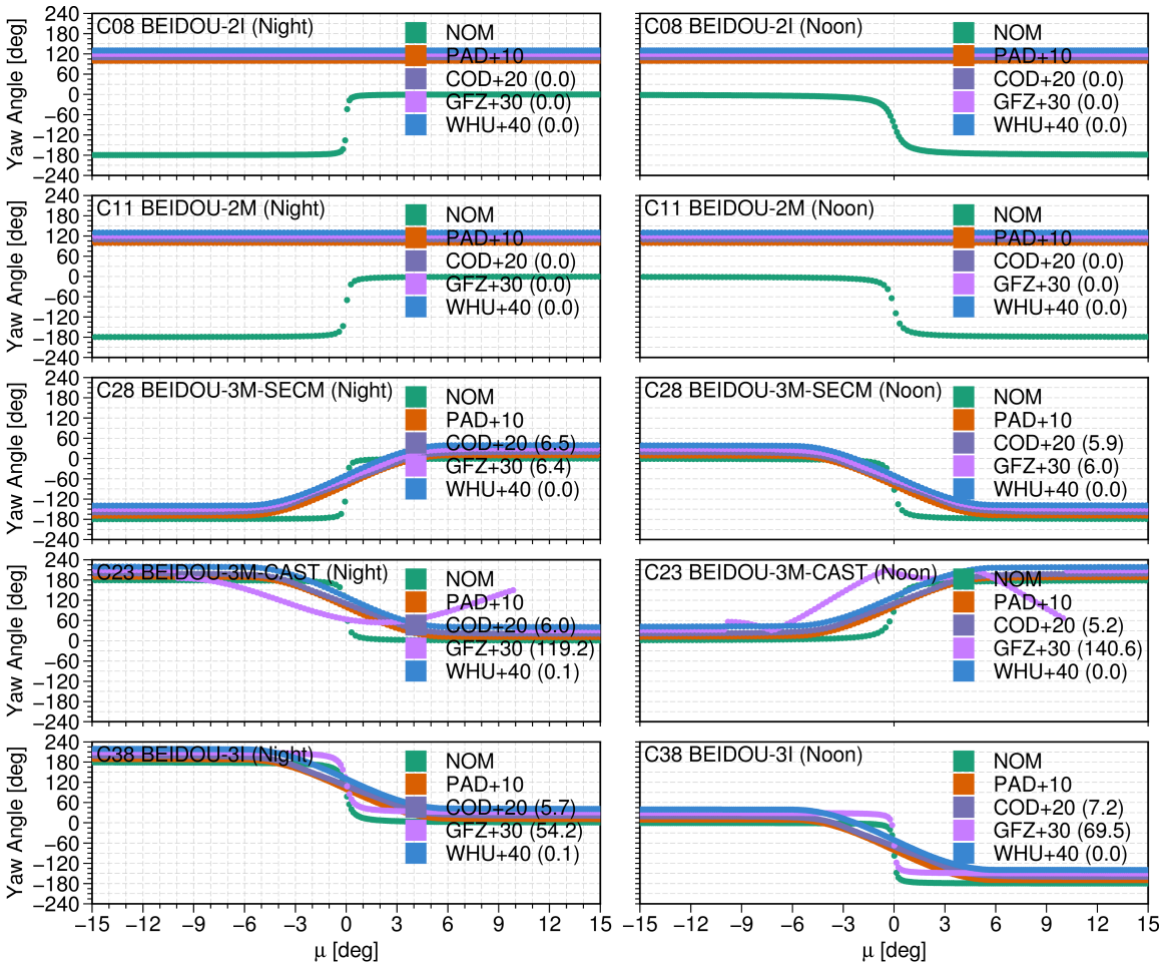

Figure 2.5 Attitude behavior of some BDS satellites around orbit midnight (left panel) and noon (right panel) in 2023. NOM stands for the nominal attitude, PAD the attitude used in PANDA software, COD the attitude applied in CODE, GFZ the attitude applied in GFZ MGEX products and WHU the attitude applied in Wuhan University. The values in each label stand for the maximum attitude difference with respect to corresponding PAD results. For a clear show, the yaw angles derived from PAD, COD, GFZ, and WHU are shifted 10°, 20°, 30°, and 40°, respectively.

2.2 Observation equations and modeling

In this section, the very basic background about GNSS algorithms is described. As the GNSS technique has been developed for decades and the technical details are very well documented, basic models shall not be described again but referred to the related literature given below.

2.2.1 Basic observation equations

The generic ionosphere-free (IF) observation equations for pseudo-range and carrier-phase observations from satellite to receiver are described by

$$\begin{cases} P_{IF} = \left|\mathbf{X}^{\mathrm{s}}(t_s) - \mathbf{T}_{TRS}^{CRS}(t_r)\mathbf{X}_{\mathrm{r}}(t_r)\right| + c(\bar{\tau}_r - \bar{\tau}^s) + t_{trop} + \varepsilon_{P,IF} \\ L_{IF} = \left|\mathbf{X}^{\mathrm{s}}(\mathrm{t_s}) - \mathbf{T}_{TRS}^{CRS}(t_r)\mathbf{X}_{\mathrm{r}}(t_r)\right| + c(\bar{\tau}_r - \bar{\tau}^s) + t_{trop} + \bar{N}_{r,IF}^s + \varepsilon_{L,IF} \end{cases} \quad (2.27)$$

with

$$\bar{\tau}_r = \tau_r + b_{r,IF}, \bar{\tau}^s = \tau^s + b_{IF}^s \quad (2.28)$$

$$\bar{N}_{r,IF}^s = N_{r,IF}^s + \Delta\phi_{r,IF} + \Delta\phi_{IF}^s \quad (2.29)$$

$$\Delta\phi_{r,IF} = B_{r,IF} - b_{r,IF}, \Delta\phi_{IF}^s = -B_{IF}^s + b_{IF}^s, \quad (2.30)$$

where P_{IF} and L_{IF} denote pseudo-range and phase observations in the unit of meter, respectively; $\mathbf{X}^s(t_s)$ is the satellite position at the signal transmitting time t_s in Geocentric Reference System (GCRS); $\mathbf{X}_{\mathrm{r}}(t_r)$ the station position at the signal receiving time t_r in International Terrestrial Reference System (ITRS); $\mathbf{T}_{TRS}^{CRS}(t_r)$ the transition matrix converting station positions from ITRS to GCRS. c the speed of light in vacuum; τ_{rec} the receiver clock offset; $\tau^s$the satellite clock offset; $b_{r,IF}$ and b_{IF}^s the receiver- and satellite-related code biases; $B_{r,IF}$ and B_{IF}^s the receiver- and satellite- related phase biases; t_{trop} the slant tropospheric delay; $N_{r,IF}^s$ the IF phase ambiguities; $\Delta\phi_{r,IF}$ and $\Delta\phi_{IF}^s$ the receiver and satellite UPD, respectively; $\varepsilon_{P,IF}$ and $\varepsilon_{L,IF}$ the measurement noise and other unmodelled errors for the pseudo-range and carrier phase observations, respectively. The inter-system/frequency dependent code biases relative to the GPS biases at the receiver end are considered in multi-GNSS POD. The other errors are modelled and corrected while forming IF equations, for example observable-specific bias, phase wind-up, and relativistic effects.

2.2.2 Delay modeling

Besides from estimating some of parameters mentioned in Equation (2.27), the remaining errors need to be modeled during GNSS data processing.

Tropospheric Delay

When going through troposphere (0–60 km altitude) the signals, affected by the atmospheric pressure, temperature, and humidity, is called the tropospheric delay (Böhm & Schuh, 2013). As the troposphere is a nondispersive medium with respect to GNSS signals, this delay does not depend on the frequency of the signal. The delay is commonly split into a hydrostatic part and a wet part. The hydrostatic, accounting for roughly 90% of the total delay can be modeled accurately. The wet part, on the other hand, can change rapidly in space and time and be hardly modeled. Therefore, it is essential to estimate a residual wet delay in high-precision GNSS processing. The tropospheric delay at the signal path can be represented as

$$t_{trop} = m_H(e)\mathrm{D}_{ZH} + m_W(e)(\mathrm{D}_{Zw} + \Delta\mathrm{D}_{Zw}) + m_G(e) * (\mathrm{D}_{GN}\mathrm{cos}a + \mathrm{D}_{GE}\mathrm{sin}a), \quad (2.31)$$

where D_{ZH} and D_{Zw} are the a priori hydrostatic and wet delays in zenith direction, respectively; m_H, m_W, and m_G are the hydrostatic, wet and gradient mapping functions, respectively. The residual zenith wet delay $\Delta\mathrm{D}_{Zw}$ is the remaining part to be estimated. The hydrostatic delay can be calculated accurately given the accurate pressure profile using the Saastamoinen

equation (Saastamoinen, 1972). Since tropospheric delays can also be systematically biased with respect to a horizontal direction, D_{GN} and D_{GE} are the north-south and east-west gradient delays that must be estimated. They depend on the azimuth angle a of the observation at the station. The mapping functions are usually provided as empirical functions, e.g., the Global Mapping Function (J. Boehm, Niell, et al., 2006), Vienna Mapping Functions (Johannes Boehm, Werl, et al., 2006; Landskron & Böhm, 2018).

Signal biases

Pseudo-range biases are hardware delays that occur during the transmission and reception of GNSS signals (Teunissen & Montenbruck, 2017). They are generally categorized as either satellite signal-related or receiver-type-related biases. On the satellite end, a delay exists between the signal generation and transmission at the antenna. The same is the case on the receiver end, where there is a delay between signal receiving and the actual observations of a specific signal. There are two types of signal biases corresponding to the observation types: pseudo-range biases and phase biases. The phase biases will be discussed in Section 2.4. These signal biases can be estimated and provided as corrections in advance. In terms of pseudo-rang biases, there are currently two kinds of corrections. One is by providing the differences among different pseudo-range types, including the traditional differential code biases (DCB), and and the recent differential signal bias (DSB) (Jefferson et al., 2001; Oliver Montenbruck, Hauschild, et al., 2014; N. Wang et al., 2015). The other one is Observable-specific Signal Biases (OSB) (Villiger et al., 2019; N. Wang, Li, et al., 2020). In general, signal biases differ per constellation, satellite, frequency, signal attribute (e.g., C, W, I, Q), as well as receiver hardware and firmware (related to signal processing approaches). Therefore, DSB or OSB is recommended in daily data processing.

Station displacement

When the observation equations are set up in the CRF, the receiver position is

$$\mathbf{X}_{\mathrm{r}}(t_r) = \widetilde{\mathbf{X}}_{\mathrm{r}}(t_r) + \Delta\boldsymbol{X}_{r,tides}(t_r) + \Delta\boldsymbol{X}_{r,loading}(t_r), \tag{2.32}$$

where $\widetilde{\mathbf{X}}_{\mathrm{r}}(t_r)$ is the benchmark without any corrections, $\Delta\boldsymbol{X}_{r,tides}(t_r)$ and $\Delta\boldsymbol{X}_{r,loading}(t_r)$ are the tidal and loading deformations, respectively. Time-variable tide displacements $\Delta\boldsymbol{X}_{r,loading}(t_r)$ contain Solid Earth tides, Ocean Tides, Atmospheric Tides, Pole Tides and Ocean Pole Tides. As the IERS conventions (Petit & Luzum, 2010) provide in-depth descriptions of these models and how to apply the respective corrections, no further explanations will be given here. The loading displacements $\Delta\boldsymbol{X}_{r,loading}(t_r)$ are mainly induced by atmospheric pressure, wind-induced ocean currents, and changes in terrestrial water storage (Klos et al., 2021).

Antenna phase center offsets and variations

Various antenna-related offsets and corrections have to be taken into account in GNSS processing. For the antenna reference points (ARPs), the satellite orbits refer to center-of-mass positions, while the receiver coordinates refer to the position of a marker that represents the station. Moreover, the electronic center of an antenna can vary for different frequencies. In that case, antenna center offsets and variations need to be considered as well.

Antenna offsets

At the station, the ARP is usually located at the bottom of the physical antenna. Since ground station antennas are often mounted on monuments, the connection between station marker and ARP is

$$\boldsymbol{X}_{r,ARP} = \boldsymbol{X}_{r,Marker} + \mathbf{R}_{LRF}^{TRF}\Delta\boldsymbol{X}_{r,Eccentricity}, \tag{2.33}$$

Station operators usually provide $\Delta\boldsymbol{X}_{r,Eccentricity}$ in a local topocentric reference frame (i.e., north, east, up). Therefore, this vector has to be transformed to the TRF via $\mathbf{R}_{LRF}^{TRF}$.

At the satellite, the center of mass (COM) and the ARP are related via

$$\boldsymbol{X}_{ARP}^{s} = \boldsymbol{X}_{COM}^{s} + \mathbf{R}_{SCF}^{CRF}\left(\Delta\boldsymbol{X}_{Eccentricity}^{s} - \Delta\boldsymbol{X}_{COM}^{s}\right). \tag{2.34}$$

Here, the center-of-mass offset $\Delta\boldsymbol{X}_{COM}^{s}$ and the eccentricity of the ARP $\Delta\boldsymbol{X}_{Eccentricity}^{s}$ are given in the SRF with respect to a physical origin $\mathbf{R}_{SCF}^{CRF}$. The location of this origin and the orientation of the SRF depend on the corresponding definition. For this reason, the IGS has adopted a common SRF for all GNSS satellites (O. Montenbruck et al., 2015). The constant ARP and origin make the Origin-ARP vector $\Delta\boldsymbol{X}_{Eccentricity}^{s}$ constant over time because they are tied to the physical structure of the satellite. In contrast, the position of the center of mass can change over time, mainly due to the usage of propellant to maneuver the satellite. For example, the center of mass of two Galileo satellites in highly eccentric orbit (E14 and E18) have changed by about 5 cm after a large part of their on-board propellant are consumed to correct their orbits (Navarro-Reyes et al., 2015; GSA, 2017). In Equation (2.34), both $\Delta\boldsymbol{x}_{COM}^{CRF,s}$ and $\Delta\boldsymbol{x}_{Eccentricity}^{CRF,s}$ are supposed to be known (i.e., have been published by satellite manufacturers). However, Galileo is the only one to publish these values among four GNSS constellations considered in this thesis. For other three constellations, estimated offsets between the satellite center of mass and the antenna center are available (Schmid et al., 2007). Recently, new launched satellites start to publish calibrated offset values, for example GPS-IIIA satellites.

Antenna center offsets and variations

Following the sign conventions of the IGS ANTEX file format (Markus Rothacher & Schmid, 2010), antenna center offset and variation corrections for a satellite or receiver antenna can be applied as

$$ant(f) = -k^{ARF}\Delta\boldsymbol{X}_{PCO}(f) + \Delta\boldsymbol{X}_{PV}(f,a,e). \tag{2.35}$$

Here, $\Delta \boldsymbol{X}_{PCO}(f)$ is the offset from the antenna reference point to the electronic antenna center for a signal f and k^{ARF} is line-of-sight vector, which is defined from the local antenna center to the remote antenna center. Due to the large distance between GNSS transmitters and receivers, this vector is equivalent to the line-of-sight vector between the receiver and satellite antenna reference points. The vector $\Delta \boldsymbol{X}_{PV}(f, a, e)$ in Equation (2.35) is phase correction (PV), which describes direction-dependent variations for a signal. a and e are the azimuth and elevation angles, respectively.

Carrier-phase wind-up

From the perspective of an inertial frame, a ground-based receiver antenna rotates with Earth. At the same time, a GNSS satellite orbiting Earth constantly adjusts its attitude and, thus, its antenna orientation. The relative orientation between the two antennas continuously changes over time and, therefore, leads to variations in the phase measurements. This phase variations caused by the change in relative orientation of transmitter and receiver antennas is called phase wind-up (J.-T. Wu et al., 1992). The phase wind-up in terms of cycles can be modeled as

$$\mathrm{pwu}_{\mathrm{r}}^{s} = sign(\eta) \cos^{-1}\left(\frac{\boldsymbol{D}^s \cdot \boldsymbol{D}_r}{\|\boldsymbol{D}^s\| \|\boldsymbol{D}_r\|}\right), \tag{2.36}$$

where η, $\boldsymbol{D}^s$ and $\boldsymbol{D}_r$ are defined respectively as

$$\eta = \boldsymbol{k} \cdot (\boldsymbol{D}^s \times \boldsymbol{D}_r) \tag{2.37}$$

$$\boldsymbol{D}^s = \boldsymbol{x}^s - \boldsymbol{k} \cdot (\boldsymbol{k} \cdot \boldsymbol{x}^s) - \boldsymbol{k} \times \boldsymbol{y}^s \tag{2.38}$$

$$\boldsymbol{D}_r = \boldsymbol{x}_r - \boldsymbol{k} \cdot (\boldsymbol{k} \cdot \boldsymbol{x}_r) + \boldsymbol{k} \times \boldsymbol{y}_r, \tag{2.39}$$

Respectively. Here $\boldsymbol{k}$ is the unit vector from transmitter to receiver, $\boldsymbol{x}^s$ and $\boldsymbol{y}^s$ are the corresponding dipole unit vectors of the transmitting antenna in local reference system, $\boldsymbol{x}_r$ and $\boldsymbol{y}_r$ are the corresponding dipole unit vectors of the receiver antenna in local reference system. In a local reference system, $\boldsymbol{e}_{\boldsymbol{x}_r}$ points towards a vendor-defined reference marker in the plane normal to the antenna boresight direction and $\boldsymbol{e}_{\boldsymbol{z}_r}$ points along the antenna boresight direction, while $\boldsymbol{e}_{\boldsymbol{y}_r}$ completes the left-handed frame. Note that continuity of the phase correction in Equation (2.36) has to be maintained if the relative rotation exceeds 360°.

Relativistic effects

Various relativistic effects have to be considered in GNSS processing (Ashby, 2003; Formichella et al., 2021). Relativity not only affects dynamic satellite orbits, but also satellite clocks and signal propagation. For the effects on signal propagation, these effects can be directly applied as range corrections to the observations.

First of all, time dilation and gravitational redshift cause a constant frequency offset in the satellite clocks (Ashby, 2003). The offset depends on the semimajor axis of the satellite orbit and thus differs per GNSS constellation. However, this offset is corrected for on a hardware level directly in the satellites so that for ground-based receivers the apparent satellite clock

frequency conforms to its nominal value. Therefore, no explicit correction of this constant offset is required when processing GNSS observations.

Next to this constant offset, periodic variations caused by the slight eccentricity of the satellite orbits affect satellite clock frequencies as well. According to Ashby (2003), this effect can be modeled directly as a range correction

$$\rho_{relativity}^{eccentricity}(\mathrm{t}) = \frac{2}{c^2}\mathbf{X}^s(t)\dot{\mathbf{X}}^s(t). \tag{2.40}$$

The variations in Earth's gravitational potential due to Earth's oblateness can also cause an additional periodic variation in the satellite clock frequency (Jan Kouba, 2004). This effect is represented as

$$\rho_{relativity}^{J_{2,0}}(\mathrm{t}) = \frac{3}{2}\mathrm{J}_{2,0}\frac{\mathrm{R}^2}{\mathrm{c}}\sqrt{\frac{\mathrm{GM}}{\mathrm{a}^3}}\sin^2 i\,\sin\big(2\mathrm{u}(\mathrm{t})\big), \tag{2.41}$$

where $J_{2,0} = 1.083 \times 10^{-3}$ is the potential coefficient describing Earth's oblateness, R Earth's equatorial radius, GM Earth's gravitational constant, a the semimajor axis of the satellite's orbit, and i its inclination angle. The argument of latitude $\mathrm{u}(\mathrm{t}) = \omega + v(t)$ describes the position of the satellite in the Keplerian orbit based on the argument of perigee ω and the true anomaly v. However, it is IGS convention to not apply this correction in GNSS processing according to Jan Kouba (2009a).

The curvature of spacetime is another factor delaying GNSS signals (Ashby, 2003). The range correction due to this delay, referred to as Shapiro effect can be modeled as

$$\rho_{relativity}^{spacetime}(\mathrm{t}) = \frac{2GM}{c^2}\ln\left(\frac{\|\mathbf{X}^s\|+\|\boldsymbol{x}_r\|+\rho_r^s}{\|\mathbf{X}^s\|+\|\boldsymbol{x}_r\|-\rho_r^s}\right), \tag{2.42}$$

where, ρ_r^s is the geometric range between receiver and satellite. The maximum Shapiro effect is approximately 2 cm (i.e., 60 ps) for MEO satellites of GNSS and 2.3 cm (i.e., 70 ps) for IGSO satellites. A correction for the Sagnac effect is necessary in case the computations are conducted in an Earth-fixed reference frame (Ashby, 2003). However, in the context of this thesis, the observation equations are set up in an inertial reference frame and receiver positions and velocities are rotated into this frame when needed. Therefore, this correction can be disregarded and is not further discussed here.

2.3 Parameter estimation

The least-squares adjustment is well known and widely used in geodetic data processing. In this section, the algorithm of parameter estimation and NEQ stacking is described. The comprehensive background is referred to the literature (Brockmann, 1997; Thaller, 2008; Koch, 2013).

2.3.1 Least-squares adjustment

In case of the GNSS processing, let $\boldsymbol{f}(\boldsymbol{x})$ the functional model for phase or code observations in Equation (2.27), which is generally nonlinear w.r.t. to unknown parameters $\boldsymbol{x}$ and has to be linearized by expanding it into a Taylor series at its initial value $\boldsymbol{x_0}$

$$\boldsymbol{l} = \boldsymbol{f}(\boldsymbol{x}_0) + \mathbf{A}(\boldsymbol{x} - \boldsymbol{x_0}) + \boldsymbol{e}, \tag{2.43}$$

where the design matrix

$$\mathbf{A} = \frac{f(x_0)}{\partial \boldsymbol{x}}|_{x_0} \tag{2.44}$$

is the Jacobian of f with respect to the parameters $\boldsymbol{x}$ at the initial values $\boldsymbol{x_0}$. Introducing the shorthand $\Delta\boldsymbol{l} = \boldsymbol{l} - \boldsymbol{f}(\boldsymbol{x_0})$ for observation residuals and $\Delta\boldsymbol{x} = \boldsymbol{x} - \boldsymbol{x_0}$ for parameter corrections, Equation (2.43) can also be written as

$$\Delta\boldsymbol{l} = \mathbf{A}\Delta\boldsymbol{x} + \boldsymbol{e}. \tag{2.45}$$

The observations in $\boldsymbol{l}$ can have different measurement accuracies and are possibly correlated. This information can be represented by the covariance matrix of observations $\boldsymbol{\Sigma_l}$. Inverting this matrix results in the weight matrix

$$\mathbf{P} = \sigma_0^2 \Delta \boldsymbol{\Sigma_l^{-1}}, \tag{2.46}$$

where σ_0 is an a priori unitless variance factor, for example $\sigma_0^2 = 1$.

Minimizing the weighted sum of squared residuals

$$\|\boldsymbol{e}\|^2 = \boldsymbol{e}^T\mathbf{P}\boldsymbol{e} = (\Delta\boldsymbol{l} - \mathbf{A}\Delta\boldsymbol{x})^T P(\Delta\boldsymbol{l} - \mathbf{A}\Delta\boldsymbol{x}) \rightarrow min \tag{2.47}$$

leads to the so-called normal equations

$$\mathbf{A}^T\boldsymbol{P}\mathbf{A}\Delta\boldsymbol{x} = \mathbf{A}^T\mathbf{P}\Delta\boldsymbol{l}, \tag{2.48}$$

where

$$\mathbf{N} = \mathbf{A}^T\boldsymbol{P}\mathbf{A} \tag{2.49}$$

denotes the normal equation matrix, and

$$\mathbf{W} = \mathbf{A}^T\mathbf{P}\Delta\boldsymbol{l} \tag{2.50}$$

is the vector of the right-hand side. Solving the system of equations results in the estimated parameter corrections

$$\Delta\boldsymbol{x} = \mathbf{N}^{-1}\boldsymbol{W} \tag{2.51}$$

and, in combination with the initial values x_0, the estimated parameters $\hat{\boldsymbol{x}}$ is

$$\hat{\boldsymbol{x}} = \boldsymbol{x_0} + \Delta\boldsymbol{x}. \tag{2.52}$$

In many cases, solving a nonlinear least-squares adjustment requires iteration, which means the estimated parameters $\hat{\boldsymbol{x}}$ are introduced back into Equation (2.43) as initial values $\boldsymbol{x_0}$ and the system of equation is solved repeatedly until convergence is reached. Moreover, the iteration in GNSS data processing also plays a role of data cleaning. The estimated variance factor

$$\hat{\sigma}_0^2 = \frac{\hat{\boldsymbol{e}}^T\boldsymbol{P}\hat{\boldsymbol{e}}}{n-m} \tag{2.53}$$

can then be computed based on the estimated residuals

$$\hat{\boldsymbol{e}} = \Delta\boldsymbol{l} - \mathbf{A}\Delta\hat{\boldsymbol{x}} \tag{2.54}$$

and the number of observations n and parameters m. Using the law of error propagation, the covariance matrix of estimated parameters follows as

$$\Delta\boldsymbol{\Sigma}_{\hat{\boldsymbol{x}}} = \hat{\sigma}_0^2\mathbf{N}^{-1}. \quad (2.55)$$

Starting from these basic formulas for the least squares adjustment, several manipulations of the system of normal equations can be carried out.

2.3.2 Constraints of parameters

To solve the problem of data rank-defection occurring in GNSS data processing or strengthen solutions, external information is usually introduced, i.e., either constrain some parameters to a priori value with the corresponding uncertainties or constrain a set of parameters with certain conditions. This step can be done by applying the pseudo-observation equation named 'Gauss-Markoff model with restrictions/conditions'.

Constraints based on the a priori stochastic information

To constrain parameters x to corresponding known values x_c with the corresponding uncertainty σ_x, the pseudo-observation equation reads

$$v_x = \Delta x - l_x, \mathrm{P}_x = \frac{1}{\sigma_x^2}, \quad (2.56)$$

where Δx is unknown parameters, l_x is the residual $(x_c - x_0)$. The constraint can also be applied between two parameters x_i and x_j, e.g., the two ZTD parameters at consecutive epochs in the random walk process. The relationship between two parameters reads

$$x_i - x_j = \Delta x_{ij} \quad (2.57)$$

where Δx_{ij} is a known value for the tie between them which should be realized by the solution. Then, the normal equation can be retrieved easily.

Free-network constraints

Constraining ground station coordinates or so-called "No-Net Conditions" (NNC) on the normal equation are the commonly two ways of getting rid of the rank deficiency in a datum-free network (Altamimi et al., 2002). The NNC contains no-net-translation (NNT), no-net-rotation (NNR), and no-net-scale (NNS), in which the NNS is usually not applied. One applicable scenario for NNS is to estimate the GNSS satellite antenna phase offset and variation (M. Ge et al., 2005a; Schmid et al., 2007).

2.3.3 Linear parameter transformation

When the parameter vector x in a normal equation system can be transformed to another parameter vector y by linear transformation

$$x = Cy + c_0, \tag{2.58}$$

the normal equation with the new parameter vector can be obtained after a short derivation as following:

$$N_y = C^T N_x C \tag{2.59}$$

$$W_y = C^T(W_x - N_x \cdot c_0) \tag{2.60}$$

$$l_y^T P l_y = l_x^T P l_x - 2c_0^T W_x + c_0^T N_x c_0 = l_x^T P l_x - c_0^T(W_x + W_y). \tag{2.61}$$

Where $W_x = N_x l_x$ and $W_y = N_y l_y$. The linear parameter transformation is a convenient tool on which many other operations are based, for example the transformation of a priori values which often occurred in the steps of normal equations (NEQ) stacking.

2.4 Carrier phase integer ambiguity resolution

In Equation (2.27), non-integer hardware biases or other inaccurately modeled biases in the receiver and satellite end prohibit direct access to integer ambiguities. For simplicity, we assume that non-integer hardware biases have absorbed other inaccurately modelled biases, which will be mentioned separately in the following. The IF ambiguity $N_{r,IF}^s$ is also not naturally an integer, even though the hardware delays are removed. To facilitate IAR, Equation (2.29) can be decomposed into wide-lane (WL) and narrow-lane (NL) ambiguities

$$\bar{N}_{r,IF}^s = \lambda_{NL}\left(\frac{\lambda_{WL}}{\lambda_2}\left(N_{r,WL}^s + \Delta\phi_{r,WL} + \Delta\phi_{WL}^s\right) + N_{r,NL}^s + \Delta\phi_{r,NL} + \Delta\phi_{NL}^s\right), \tag{2.62}$$

where λ_{WL} and λ_{NL} are the wavelength of WL and NL ambiguity in the unit of meter, respectively; $\Delta\phi_{r,WL}$ and $\Delta\phi_{r,NL}$ the WL and NL UPD in receiver end, respectively; $\Delta\phi_{WL}^s$ and $\Delta\phi_{NL}^s$ the WL and NL UPD in satellite end, respectively; $N_{r,WL}^s$ and $N_{r,NL}^s$ integer WL and NL ambiguity in the unit of cycle, respectively. Usually, only integer WL ambiguity is inserted in to Equation (2.62), the WL UPDs ($\Delta\phi_{r,WL} + \Delta\phi_{WL}^s$) are ignored and thus merged to NL fractional part. Resolving DD-ambiguities (DD IAR) or directly fixing UD ambiguities by correcting UPDs with the estimated values (UD IAR) are the two typical methods to obtain IAR.

Double-difference integer ambiguity resolution

In the DD IAR, the hardware delay at satellite and receiver sides (i.e., UPDs) are eliminated by double difference and then the integer nature can be easily recovered. Over the past three decades, DD IAR is widely adopted in GNSS network processing by most IGS ACs for routine GNSS data processing, such as JPL, CODE and GFZ.

By forming DD-ambiguities between two selected stations (m, n) and satellites (i, j), the hardware delays mentioned in Equation (2.62) can be eliminated directly (M. Ge et al., 2005b)

$$N_{mn,IF}^{ij} = N_{m,IF}^i - N_{m,IF}^j - N_{n,IF}^i + N_{n,IF}^j. \tag{2.63}$$

After eliminating common code and phase biases in Equation (2.62), both WL ambiguities ($N_{mn,WL}^{ij}$) and NL ambiguities ($N_{mn,NL}^{ij}$) restore integer nature and can be fixed to integers directly. Once they are fixed to integers, the estimated IF ambiguity is expressed as

$$\widetilde{N}_{mn,IF}^{ij} = \lambda_{NL}\left(\frac{\lambda_{WL}}{\lambda_2}\widetilde{N}_{mn,WL}^{ij} + \widetilde{N}_{mn,NL}^{ij}\right). \tag{2.64}$$

Then, the following tight constraint is imposed to the four related UD ambiguities in Equation (2.63) as

$$\widetilde{N}_{r,IF}^{s} - N_{mn,IF}^{ij} = 0;\ \sigma = 0.001\ mm \tag{2.65}$$

where σ is the uncertainty of DD ambiguity constraint. Note that a tight constraint is usually applied, that is," $0.001\ mm$" in this study. The ambiguity-fixed solutions are obtained after all selected constraints are applied.

To ensure the accuracy of orbits, clocks and other geodetic products, all theoretically independent DD ambiguities need to be selected from the whole network. For DD IAR of a massive network, the step of picking independent DD ambiguities from the entire network can be very time-consuming. The computation burden of DD IAR for a massive GNSS network is mainly caused by the formation and selection of independent DD ambiguities. Currently, there are two strategies to select independent DD ambiguities to accelerate DD IAR:

- **Picking independent DD ambiguity from global fixable ambiguities** (M. Ge et al., 2005b).

At first stage, fixable DD ambiguities in each baseline are sorted based on fixing probability and then the independence of fixed DD ambiguities is checked by Gram-Schmidt process (Cohen, 1993). Afterward, the selected DD ambiguities of all baselines are pooled together to pick an independent subset. This procedure has been implemented in the EPOS software of the German Research Center for Geosciences (GFZ) and the NAPEOS software of the European Space Agency (ESA) (Tim Springer, 2009; Reckeweg, 2020).

- **Obtaining independent DD ambiguities from the maximum independent baseline set** (Blewitt, 2008).

To accelerate DD-IAR, this strategy acquires independent DD ambiguities from the maximum independent baseline set only, rather than all possible baselines across the network. This baseline subset can be picked according to the baseline lengths or ambiguity fixing rates. Shorter baselines or those with higher fixing rates are prioritized. Compared to the approach by Ge et al. (2005), this strategy achieves computation efficient DD-IAR for a massive GNSS network consisting of thousands of stations. Blewitt (2008) refused to identify all independent DD ambiguities of a network, and demonstrated that this DD-IAR strategy was able to achieve daily horizontal coordinates of less than 1 mm different from those achieved by harnessing all independent DD ambiguities of the entire network. This DD-IAR strategy has been adopted

in GipsyX/RTGx (Bertiger, Bar-Sever, Dorsey, Haines, Harvey, Hemberger, Heflin, Lu, Miller, Moore, et al., 2020).

2.4.1 Undifferenced integer ambiguity resolution

Different from DD IAR, the hardware delay at satellite and receiver sides, that is, UPD, can be estimated and applied as corrections to recover the integer feature of UD ambiguities, and thus, the UD IAR can be performed. For recovering the integer nature of UD-ambiguities, only the fractional part is critical, whereas the integer part is anyway not separable from the integer ambiguities. With the DSBs or OSBs provided by IGS, the satellite-specific biases between different signals are calibrated priori to the UPD estimation. To recover the integer nature of WL and NL ambiguities, the fractional part of hardware delays can be separated and estimated in a reference network. Supposing there are m reference stations with n satellites observed on each station, the observation equation of WL or NL UPDs can be written as

$$\mathrm{U} = \lfloor \mathrm{I}_m \otimes \mathrm{e}_n \quad \mathrm{e}_n \otimes \mathrm{I}_m \rfloor \begin{bmatrix} \mathrm{x}_r \\ \mathrm{x}^s \end{bmatrix}, \tag{2.66}$$

where $\mathrm{U} = [U_1 \quad \cdots \quad U_{m+n}]^T$ are the fractional parts of WL or NL ambiguities; $\mathrm{x}_r = [\Delta\phi_{r,1} \quad \cdots \quad \Delta\phi_{r,m}]^T$ the WL or NL UPDs in receiver end; $\mathrm{x}^s = [\Delta\phi_1^s \quad \cdots \quad \Delta\phi_n^s]^T$ the WL or NL UPDs in satellite end; $\otimes$ is the operator of Kronecker product; I_m is the $m-$order identity matrix, respectively; e_n is the $n-$column vector with all one elements, respectively. Due to the linear dependence between receiver and satellite UPD, the rank deficiency of Equation (2.66) is 1, which can be solved by selecting one reference UPD, e.g., fixing one satellite UPD to zero. Usually, the fractional parts of WL ambiguities are derived from the corresponding carrier-phase and pseudo-range combinations (Melbourne, 1985; Wübbena, 1985). After achieving WL UPDs with Equation (2.66), then the fractional parts of NL UPD are derived from the real-valued solution. Finally, NL UPDs are estimated. For more details on UPD estimation, please refer to (M. Ge et al., 2007).

With estimated WL and NL UPDs, the integer property of WL and NL ambiguity are recovered and the corresponding IF ambiguity $\widetilde{N}_{r,IF}^s$ is imposed as an additional pseudo-observation to achieve the ambiguity-fixed solution

$$\widetilde{N}_{r,IF}^s - N_{r,IF}^s = 0;\ \sigma = 0.001\,mm. \tag{2.67}$$

Although many studies have demonstrated the stability of UD ambiguities in PPP solutions (M. Ge et al., 2007; Li et al., 2017; B. Cui, Li, et al., 2021), the UD ambiguities estimated from POD processing are not such accurate as that from PPP because much more parameters are estimated simultaneously in POD processing. This may result in a vulnerable UD IAR if directly using UD ambiguities from POD float solutions, which will be further explained in Chapter 4. Therefore, Deng et al. (2022) recommend a DD IAR procedure before performing UD IAR to ensure the accuracy of UD ambiguities.

2.5 POD processing strategy in PANDA software

The POD processing in this thesis is performed using PANDA software (J. Liu & Ge, 2003; Shi et al., 2008), which is capable of multi-GNSS post and real-time processing (Zuo et al., 2021; Tang, Wang, Zhu, et al., 2023), LEO data processing (H. Ge et al., 2022) and handling multiple space geodetic techniques (J. Wang et al., 2022). The performance of POD and PCE have been demonstrated by several studies (W. Huang, Männel, Sakic, et al., 2020; Tang et al., 2021; X. Chen et al., 2023). A vast range of applications using the software have been performed, including orbit maneuver detection (Qin et al., 2023), phase center estimation (W. Huang, Männel, Brack, et al., 2020), precipitable water vapor retrieve (J. Wang et al., 2019; Z. Wu et al., 2020), sea surface height measurement (Penna et al., 2018), earthquake detection (K. Chen et al., 2016). The PANDA software is also used by the IGS analysis centers at WHU[4], SHAO[5] and several other ACs of the iGMAS[6].

Table 2.2 lists the force models applied in POD processing (see Chapters 3, 4, and 5). The Earth's gravity field only comprises the static field, as the impact of the time-variable gravity field on GNSS POD is minor[7]. All other force models are utilized following the IERS conventions. For solar radiation pressure, the surface areas and optical properties of GNSS satellite box-wing models originate from various sources. Besides from the a priori box-wing models, additional empirical solar radiation pressure parameters are estimated. The ECOM1 model is selected for our processing. Combined with six initial state parameters, eleven parameters are set up per satellite orbit each day. The performance of different ECOM models and box-wing model will be discussed in Chapter 3.

Table 2.2 A priori force models used in satellite orbit integration.

Item	Model	Reference
Earth's gravity field	EIGEN-GRACE02S	Reigber et al. (2005)
Astronomical tides	JPL DE405	Standish (1996)
Solid Earth tides	IERS 2010	Petit and Luzum (2010)
Ocean tides	FES2014b	Lyard et al. (2021)
Pole tides	IERS 2010	Petit and Luzum (2010)
Atmospheric tides	IERS 2010	Petit and Luzum (2010)
General relativity	IERS 2010	Petit and Luzum (2010)
Solar radiation pressure	Box-wing	GPS: Duan and Hugentobler (2021), Peter Steigenberger et al. (2020) GLONASS: Duan et al. (2020) Galileo: (GSA, 2019) BDS: Duan et al. (2019), Duan et al. (2022)
Earth radiation pressure	Box-wing	Rodriguez-Solano et al. (2011)
Antenna thrust	Measured values	Peter Steigenberger et al. (2017)

The vast majority of the settings in the processing strategy are listed in Table 2.3. Following the rule of IERS conventions (2010) (Petit & Luzum, 2010), tidal deformations including solid

[4] http://www.igs.gnsswhu.cn/index.php/home/index.html?lang=en-us
[5] http://202.127.29.4/shao_gnss_ac/
[6] http://en.igmas.org/
[7] http://acc.igs.org/workshop2016/posters/Nikta_Amiri_Impact_Of_Time_Variable_Gravity_Field_on_GPS_Precise_Orbit_Determination_2016.pdf

Earth tides, ocean tides, pole tides, ocean pole tides and atmospheric tides, are added to station coordinates. For station parameters, constant station coordinate parameters are set up for each day. Some of global stations are selected as core stations to add No-Net-Rotation and No-Net-Translation constraints (Zajdel et al., 2019) with tight constraints. Note that loading deformations due to nontidal mass variations are not applied as corrections. For tropospheric residual zenith wet delays, it is estimated at each station using piece-wise constant method. Horizontal gradient delays in north-south and east-west directions are parameterized as constant components over the full day for each station. Therefore, 14 tropospheric parameters (12 for wet delays and one each for both gradient directions) were set up per station and day. For ERP parameters, polar motion, polar motion rate and length of day (LOD) are parameterized as constant components over the full day. For ambiguity fixing, DD IAR and UD IAR will be discussed in Chapter 4. UD IAR is applied in other Chapters. Taking into account the known satellite biases (N. Wang et al., 2015), integer rounding is used to separate the fractional biases and to determine the integer-valued wide-lane and narrow-lane ambiguities for all passes. Inter-system biases (ISBs), and geocenter coordinates are also considered in POD processing.

Table 2.3 Description of observation modeling strategies.

Item	Settings
Observation	Ionospheric-free combined GNSS pseudorange and phase observations, 5-min sampling
Observation weighting	UD pseudorange and phase: 0.5 m and 0.01 cycle, respectively; elevation-dependent downweighing
Station coordinates	Estimated as daily constant, no-net-rotation and no-net-translation constraints on the datum stations to IGS14 (Rebischung et al., 2016)
Receiver and satellite clock	Estimated as epoch-wise white noise
Surface displacement	IERS 2010 Conventions (Petit & Luzum, 2010)
Earth rotation parameters	IERS finals2000A product is taken as a priori values. Polar motion components estimated as daily offset and rate. UT1-UTC are fixed to the a priori value but its rate is estimated (LOD). Sub-daily variations modelled following to IERS 2010 Conventions (Petit & Luzum, 2010)
Tropospheric delay	GPT3 (Böhm et al., 2014) for the a priori zenith delay, residual zenith wet delay estimated as 2-hour piece wise constant, north and east gradients estimated as daily constant Mapping functions: GMF (J. Boehm, Niell, et al., 2006) for zenith delays and Chen-Herring (G. Chen & Herring, 1997) for horizontal gradients
Code bias	DSB product (N. Wang et al., 2015)
Ambiguity fixing	YES
Uncertainty of integer ambiguity constraints	Tight constraint: 0.001 mm

Based on satellite force and observation models, all the unknown parameters are estimated with LSQ. It must be pointed out that the estimation part is repeated several times, typically four iterations, for data cleaning and parameter update and a final iteration for generating the float solution for integer ambiguity resolution. For a network solution with 100 tracking stations and four satellite systems, the total number of unknown parameters is more than ninety thousand. To save computer memory and reduce the computation burden, only active

parameters in NEQ are kept. Otherwise, the inactive parameters will be removed immediately from the NEQ (M. Ge et al., 2006). In this case, the percentage of the parameter elimination in the whole-time consumption is at least 85%. Therefore, the OpenMP technology is introduced to accelerate parameter elimination (X. Chen et al., 2022). OpenMP consists of compiler directives, library routines, and environment variables. These instructions can be employed to build a portable, scalable model, providing developers with a simple, flexible interface for parallel processing based on multiple platforms. In parameter elimination, the NEQ should be defined as a shared memory that can be accessed by multiple threads in parallel. In the NEQ system, one element from each row or column vector can be removed without any intervention from other elements. This indicates that the entire NEQ-level computation can be separated into sub-blocks row by row, and the sub-blocks are distributed among the threads without data dependence. From the principal perspective, it is possible to parallelize the parameter elimination in a row-wise manner by using OpenMP tools.

2.6 Chapter summary

The major content of this chapter are summarized as follows.

Section 2.1 introduces the orbit modeling and satellite attitude applied in dynamic orbit determination. The quality of dynamic orbits is mainly limited by the applied force models, especially non-gravitational force models. Therefore, the basic theory of solar radiation pressure, Earth radiation, and antenna thrust is discussed in detail. Based on those force models, the variational equation used in POD is then summarized. During orbit integration, the satellite's attitude is essential for modeling accelerations induced by solar and Earth radiation pressure. Compared with published attitude products by CODE, GFZ, and WHU, the attitude models applied in PANDA are consistent with CODE and WHU, with a maximum difference less than 10°.

Section 2.2 presents the mathematical delay models of GNSS. Instead of giving the detailed models of each delay, here only the a priori models are summarized.

Section 2.3 describes the method of parameter estimation, including least-squares adjustment, constraints of a priori parameters and linear parameter transformation which will be applied in Chapter 5.

Section 2.4 discusses the method of integer ambiguity resolution, including DD IAR and UD IAR. For DD IAR, the strategy of double difference between two station-satellite pairs can recover the integer nature easily. Two strategies for selecting independent baselines are introduced. However, picking independent DD ambiguities could be a computation burden in a massive network as all theoretically independent DD ambiguities should be selected from the whole network. For UD IAR, the UPDs must be estimated in advance and then applied as corrections to recover the integer feature of UD ambiguities. The consistency of DD IAR and UD IAR will be discussed in Chapter 4.

Section 2.5 introduces the PANDA software briefly, with both the applied force models and observation models.

3 Investigation of Solar Radiation Pressure modeling

When a satellite enters the umbra or the penumbra area of the occulting bodies (usually the Earth and the Moon), that is, the eclipse season, a shadow factor is adopted to represent the degrees of Sun occultation. Different ACs adopt different strategies, either in D or all directions. Although several studies tried to refine its function model, few studies focus on the relationship between the shadow factor and the parameterization model and its impact on eclipsing satellites. The eclipse seasons are quite common for GNSS satellites. Therefore, it is necessary to investigate the orbit accuracy during eclipse seasons and clarify the proper method of combining shadow factor and the parameterization SRP model.

In this Chapter, the SRP model with the application of shadow factor is first introduced, including the analysis of the relationship between a priori box-wing model and parameterization model (that is, ECOM1 or ECOM2). Based on different data processing strategies in Section 3.2, the variations of estimated ECOM parameters, day boundary discontinuity (DBD), and ERPs are evaluated in the following sections.

Note：This chapter has been published in Tang et al. (2021). The italicized text represents the content from the published paper.

3.1 SRP model

In the third IGS reprocessing campaign, ECOM1 is suggested for BLOCK IIR and IIF and ECOM2 or GSPM with a priori box-wing models is for all the others[8]. For the SRP modeling analysis in this study, the box-wing model is used as the a priori model and ECOM1 or ECOM2 as the parameterization model. The acceleration of an in-orbit satellite caused by SRP perturbation can be expressed as

$$\boldsymbol{a}_{srp} = \boldsymbol{a}_{prior} + \boldsymbol{a}_{para}, \tag{3.1}$$

where $\boldsymbol{a}_{prior}$ denotes acceleration derived from the a priori model and $\boldsymbol{a}_{para}$ denotes the residual acceleration represented by the parameterization model with the force model parameters to be estimated.

[8] http://acc.igs.org/repro3/repro3.html

3.1.1 Relationship between box-wing and ECOM model

According to the operation law of satellite attitude, the nominal yaw-steering attitude of satellites is set by accomplishing two conditions at the same time: (1) the antennas should always point toward the center of the Earth to transmit the navigation signals; (2) the solar panels should always be perpendicular to the Sun to keep a maximum power supply. Normally, satellites will rotate around Z axis when the satellite is orbiting. In that case, the effects of SRP only concentrate on $\pm Z$ and $+X$ surfaces of the satellite body under nominal attitude. Therefore, the box-wing model in three surfaces can be represented as

$$\begin{cases} +Z: \left((\alpha_{+Z}+\delta_{+Z})\mathbf{e}_D + \left(\frac{2}{3}(\alpha_{+Z}+\delta_{+Z}) + 2\rho_{+Z}\cos(\varepsilon)\right)\mathbf{e}_{+Z}\right) l\, A_{+Z}\cos(\varepsilon) \\ +X: \left((\alpha_{+X}+\delta_{+X})\mathbf{e}_D + \left(\frac{2}{3}(\alpha_{+X}+\delta_{+X}) + 2\rho_{+X}\sin(\varepsilon)\right)\mathbf{e}_{+X}\right) l\, A_{+X}\sin(\varepsilon) \\ -Z: -\left((\alpha_{-Z}+\delta_{-Z})\mathbf{e}_D + \left(\frac{2}{3}(\alpha_{-Z}+\delta_{-Z}) + 2\rho_{-Z}\cos(\varepsilon)\right)\mathbf{e}_{-Z}\right) l\, A_{-Z}\cos(\varepsilon) \end{cases}, \quad (3.2)$$

where $\mathbf{e}_{+Z}$, $\mathbf{e}_{-Z}$ and $\mathbf{e}_{+X}$ are the unit normal vector of $+Z$, $-Z$ and $+X$ surfaces, respectively; A_{+Z}, A_{+X} and A_{-Z} the area of $+Z$, $-Z$ and $+X$ surfaces, respectively; $l = \frac{dS_0}{mc}$ and $cos(\varepsilon) = cos\,(\Delta\mu)cos\,(\beta)$. The meaning of the remaining characters $d, S_0, m, c, \Delta\mu$ and β can be found from Section 2.1.1. The range of ε angle is $(0, \pi)$. Considering the IGS conventional body-fixed frame (SCF) (O. Montenbruck et al., 2015), as shown in Figure 3.1, the transformation from SCF to DYB frame can be presented as

$$\begin{bmatrix} D \\ Y \\ B \end{bmatrix} = \begin{bmatrix} \sin(\varepsilon) & 0 & \cos(\varepsilon) \\ 0 & 1 & 0 \\ -\cos(\varepsilon) & 0 & sin\,(\varepsilon) \end{bmatrix} \begin{bmatrix} X \\ Y \\ Z \end{bmatrix}_{SCF}. \quad (3.3)$$

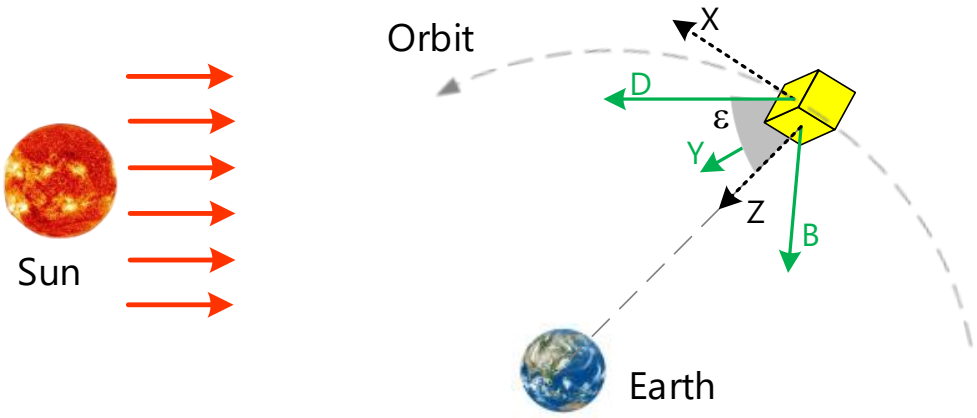

Figure 3.1 Relationship between DYB frame and SCF frame in nominal yaw-steering mode. Note that the Y-axis is identical in both DYB and SCF frames.

The accelerations of irradiated surfaces including satellite body and solar panels mainly acts on the D and B direction in DYB frame and is represented as follow

$$\begin{aligned} D &= l(D_0 + D_{1c}\cos(\varepsilon) + D_{1s}\sin(\varepsilon) + D_{2c}\cos(2\varepsilon) \\ &\quad + D_{3c}\cos(3\varepsilon) - D_{3s}\sin(3\varepsilon)) \\ B &= l(-B_{1c}\cos(\varepsilon) + B_{1s}\sin(\varepsilon) + B_{2c}\cos(2\varepsilon) \\ &\quad + B_{3c}\cos(3\varepsilon) + B_{3s}\sin(3\varepsilon)) \end{aligned} \qquad 0 < \varepsilon < \frac{\pi}{2}, \tag{3.4}$$

and

$$\begin{aligned} D &= l(D_0' - D_{1c}'\cos(\varepsilon) + D_{1s}\sin(\varepsilon) + D_{2c}'\cos(2\varepsilon) \\ &\quad - D_{3c}'\cos(3\varepsilon) - D_{3s}\sin(3\varepsilon)) \\ B &= l(-B_{1c}\cos(\varepsilon) - B_{1s}'\sin(\varepsilon) + B_{2c}'\cos(2\varepsilon) \\ &\quad + B_{3c}\cos(3\varepsilon) - B_{3s}'\sin(3\varepsilon)) \end{aligned} \qquad \frac{\pi}{2} \le \varepsilon < \pi, \tag{3.5}$$

where

$$\begin{cases} D_0 = \frac{A_{+Z}}{3}(\alpha_{+Z} + \delta_{+Z}) + \frac{A_{+X}}{3}(\alpha_{+X} + \delta_{+X}) + A_{+S}\left(1 + \alpha_{+S} + \frac{2}{3}\rho_{+S}\right) \\ D_0' = \frac{A_{-Z}}{3}(\alpha_{-Z} + \delta_{-Z}) + \frac{A_{+X}}{3}(\alpha_{+X} + \delta_{+X}) + A_{+S}\left(1 + \alpha_{+S} + \frac{2}{3}\rho_{+S}\right) \\ D_{1c} = A_{+Z}\left(1 + \frac{1}{3}\rho_{+Z}\right), D_{1s} = A_{+X}\left(1 + \frac{1}{3}\rho_{+X}\right), D_{1c}' = A_{-Z}\left(1 + \frac{1}{3}\rho_{-Z}\right) \\ D_{2c} = \frac{A_{+Z}}{3}(\alpha_{+Z} + \delta_{+Z}) - \frac{A_{+X}}{3}(\alpha_{+X} + \delta_{+X}) \\ D_{2c}' = \frac{A_{-Z}}{3}(\alpha_{-Z} + \delta_{-Z}) - \frac{A_{+X}}{3}(\alpha_{+X} + \delta_{+X}) \\ D_{3c} = \frac{A_{+Z}\rho_{+Z}}{3}\ D_{3s} = \frac{A_{+X}\rho_{+X}}{2}\ D_{3c}' = \frac{A_{-Z}\rho_{-Z}}{3} \\ B_{1c} = B_{3c} = \frac{\rho_{+X}}{2}, B_{1s} = B_{3s} = \frac{\rho_{+Z}}{2} \\ B_{2s} = \frac{A_{+Z}}{3}(\alpha_{+Z} + \delta_{+Z}) - \frac{A_{+X}}{3}(\alpha_{+X} + \delta_{+X}) \\ B_{1s}' = \frac{\rho_{-Z}}{2}\ B_{2s}' = \frac{A_{-Z}}{3}(\alpha_{-Z} + \delta_{-Z}) - \frac{A_{+X}}{3}(\alpha_{+X} + \delta_{+X})\ B_{3s}' = \frac{\rho_{-Z}}{2} \end{cases} . \tag{3.6}$$

Based on Equation(3.4) and Equation(3.5), it is obviously that accelerations of $\pm Z$, $+X$ surfaces and solar panels represented by the box-wing model can be fully allocated to coefficients in D and B directions under the nominal attitude. The amplitude of each periodic term is highly related with area and optical properties of the illuminated area, for example, determining whether a period term is significant or not (O. Montenbruck et al., 2015).

For the accelerations in D direction, it consists of constant- terms and the twice, fourth- and sixth- per-revolution terms, in which zero-per-revolution term is the biggest one. When a satellite is a cube, the fourth-per-revolution term is close to zero and can be ignored, for example, GPS IIR (Duan & Hugentobler, 2021). In contrast, the fourth-per-revolution will be significant for the cuboid-shaped satellites, for example, Galileo and BDS3 satellites. Compared with the fractions of absorbed and diffusely scattered photons, the specularly reflected scattered photons (ρ) is usually the lowest one. Hence, the sixth-per-revolution term is less significant than other periodic terms.

For the accelerations in B direction, once-, twice- and three- per-revolution terms are observed, while the once-per-revolution term is prominent. These even and odd orders the D and B direction are also found by Arnold et al. (2015).

If precise satellite metadata is available beforehand, the number of unknown parameters can be reduced to make solutions stronger. However, the official values of most satellite types are

unknown. The optical values calibrated from the ground could change in space. Some key elements (e.g., absorb, diffuse and specular reflection properties) in the box-wing model need to be estimated and updated. When a precise box-wing model is applied, the number of unknown parameters can be reduced. However, using a priori box-wing model as the satellite force model purely could also suffer from some other unmodeled forces, for example thermal radiation in Y direction (Duan & Hugentobler, 2021). Moreover, non-nominal attitude is also a possible factor influencing the accuracy of the box-wing model.

3.1.2 Shadow factor

For GNSS satellites, the main occulting body is Earth. The relative geometry between Earth, Sun, and a satellite's orbital plane leads to GNSS satellites entering eclipse seasons approximately twice per year. An eclipse season usually lasts for around one month, during which a satellite crosses Earth's shadow once per revolution, as shown in Figure 3.2*. GNSS satellites usually cross Earth's penumbra in a few minutes, while the period in full shadow can last up to an hour at the center of an eclipse season.*

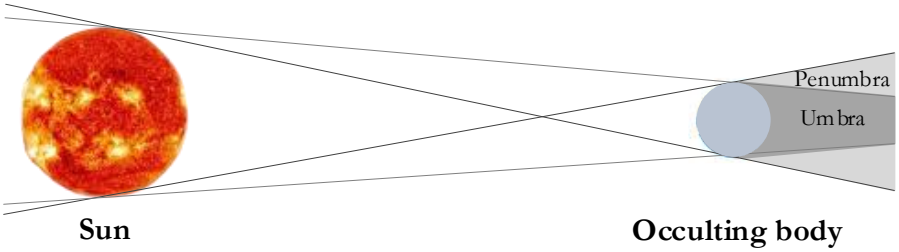

Figure 3.2 Schematic visualization of conical shadow model and partial occultation.

Figure 3.3 shows that among the 32 operational GPS satellites in 2019, the average number of eclipsing satellites is around 6 and the maximum number is 12, and a single eclipse event lasts 40 minutes on average. Moreover, some unmodeled non-SRP forces may exist and will become conspicuous for those satellites during the eclipsing season, which cannot be neglected (Sidorov et al., 2020; Duan & Hugentobler, 2021).

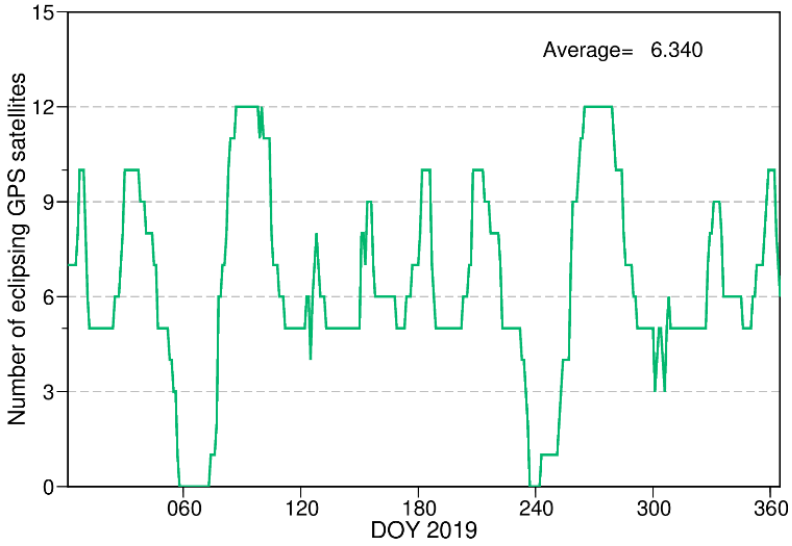

Figure 3.3 Daily number of GPS satellites in eclipse seasons in 2019.

When a satellite enters so-called eclipse seasons, a shadow factor is usually employed to describe the corresponding solar irradiance variation. Adopting the conical shadow model, the shadow factor f can be calculated in the following three cases:

- *Full phase: the Sun is fully visible to the satellite, therefore $f = 1$;*
- *Penumbra: the satellite is in the penumbra area of the Earth and the Moon and it can receive only part of the solar irradiance from the Sun, therefore*

$$f = 1 - \frac{S}{\pi r_{Sun}} \tag{3.7}$$

where S denotes the total area of the Sun occulted by the Earth and the Moon, and r_{Sun} the apparent radius of the Sun.

- *Umbra: the satellite is in the umbra of occulting bodies, therefore $f = 0$.*

When the shadow factor is applied in three directions, Equation (2.27) can be rewritten as

$$\boldsymbol{a}_{srp} = f \cdot \boldsymbol{a}_{prior} + f \cdot (D(\mu)\mathbf{e}_D + Y(\mu)\mathbf{e}_Y + B(\mu)\mathbf{e}_B) \tag{3.8}$$

The other one is that the shadow factor is applied in satellite-Sun directions and Equation (2.27) can be rewritten as

$$\boldsymbol{a}_{srp} = f \cdot \boldsymbol{a}_{prior} + f \cdot D(\mu)\mathbf{e}_D + Y(\mu)\mathbf{e}_Y + B(\mu)\mathbf{e}_B \tag{3.9}$$

The $Y(\mu)$ term usually consists of two parts. The first part is the instrument bias, namely the yaw bias, which is caused by the misalignment of solar panels or solar sensor errors and observed for BLOCK II and IIA satellites (H. F. Fliegel & Gallini, 1996). The second one is the thermal radiation, which was found on the Y surfaces (radiated from louvers) of the BLOCK IIR satellites (Oliver Montenbruck et al., 2002). The thermal radiator is designed for evacuating excessive heat from onboard payloads to space, and as a result, an

additional force is generated. However, thermal control information, not available to the public, is hardly to model. Ignoring these small forces, for example, using Equation (3.8) can degrade the orbit accuracy in the eclipse season. An inspection of Equation (3.9) shows that keeping the $Y(\mu)$ active during the Earth's shadow transitions can help to model the thermal radiation during eclipse seasons, along with other possible non-SRP nature forces in Y surfaces. Besides the $\pm Y$ surfaces, the $\pm X$ and $-Z$ surfaces may also undergo thermal radiations. Assuming there is a constant acceleration a_{-X} in the $-X$ surface and it can be represented as $a_{-X}sin(\varepsilon)$, 0, and $a_{-X}cos(\varepsilon)$ in the D, Y, and B directions, respectively. Similarly, assuming there is a constant acceleration a_{-Z} in the $-Z$ surface and it can be represented as $-a_{-Z}cos(\varepsilon)$, 0, and $a_{-Z}sin(\varepsilon)$ in the D, Y, and B directions, respectively. Therefore, these constant accelerations corresponding to the B direction can be modeled by the once-per-revolution terms in both ECOM1 and ECOM2, whereas the rest part corresponding to the D direction can only be partially modeled in ECOM1 and ECOM2, where ECOM2 has better performance due to its additional twice-per-revolution and fourth-per-revolution terms.

In addition to those potential thermal radiations mentioned above, there are other potential non-gravitational forces that need to be considered during eclipse seasons—for example, a surface undergoing heating up and cooling down periods during shadow transitions, active thermal control of shadow season, etc. If there are thermal radiation or other unmodeled non-gravitational forces in Y or other surface, keeping parameters in the Y and B directions active in the eclipse season can compensate for the forces of non-SRP nature to some extent, and this inference will be proved in the following results.

3.2 Data processing

Section 3.1 presented the relationship between box-wing and ECOM model, the ways of applying the shadow factor, and its relationship with possible unmodeled or inaccurately modeled non-SRP forces. As the ECOM2 has more periodic terms than ECOM1 in the D direction, it may have different behaviors for eclipsing satellites. Taking GPS orbits as an example, three years (2017-2019) of observation data are selected to evaluate the performance of different SRP models, with an emphasis on satellites in eclipsing seasons.

Combining the strategies of using ECOM1 or ECOM2 as the parameterization model, using no model, the box-wing, and adjustable box-wing model as a priori model, and the application of the shadow factor, i.e., in the D or DYB directions, 12 different solutions are listed, as shown in Table 1. For the box-wing model, satellite metadata and optical properties comes from the manufacturers (H. F. Fliegel & Gallini, 1996; Rodriguez-Solano et al., 2012), and for the adjustable box-wing model, adjusted metadata and optical properties are provided by (Duan & Hugentobler, 2021). Each satellite may suffer from different magnitudes of unmodeled forces, even for the same block type. Considering that the purpose of this work is to evaluate different SRP models and shadow factor, the

additional accelerations in either X or Y surface provided by Duan and Hugentobler (2021) are not considered, which are applied for remaining forces after employing the adjustable box-wing model.

Table 3.1 The 12 cases of GPS daily precise orbit determination solutions using different methods in handling the a priori model, the parameterization model, and the shadow factor. Note that the directions in which shadow factor is applied refers to the parameterization model, and in the a priori model, the shadow factor is always applied. See Equation (3.8) and (3.9) for details.

Solution	Empirical SRP Model	Shadow Factor	A Priori SRP Model
E1DYB	ECOM1	D,Y,B	None
E1DYB_BW	ECOM1	D,Y,B	Box-wing
E1DYB_ABW	ECOM1	D,Y,B	Adjustable box-wing
E1D	ECOM1	D	None
E1D_BW	ECOM1	D	Box-wing
E1D_ABW	ECOM1	D	Adjustable box-wing
E2DYB	ECOM2	D,Y,B	None
E2DYB_BW	ECOM2	D,Y,B	Box-wing
E2DYB_ABW	ECOM2	D,Y,B	Adjustable box-wing
E2D	ECOM2	D	None
E2D_BW	ECOM2	D	Box-wing
E2D_ABW	ECOM2	D	Adjustable box-wing

To minimize the possible errors caused by integration, the Adams–Bashforth–Moulton predictor–corrector integration method is switched to the Runge–Kutta–Fehlberg (RKF) integration method with small steps during the shadow transition, that is, the period from full phase to umbra or inverse.

Unlike the GLONASS, Galileo, and BeiDou satellites where the SLR tracking observations are available, the GPS BLOCK IIA, IIR, IIF, and III satellites used in this study are not equipped with retroreflector arrays, and thus using SLR as an external orbit validation is not possible (Sośnica et al., 2015). It is also not optimal to use the orbit products from the IGS ACs as a reference for comparison, as their SRP modeling and the strategies of applying the shadow factor are different and can affect the orbit product. Therefore, the following quantities are used to assess the different solutions

- *Analyses of the estimated SRP parameters: The estimated ECOM parameters should not show systematic biases if the a priori model can describe all essential characteristics of the satellite. The correlation between the satellite orbit dynamic parameters can also measure the association of these parameters;*
- *DBD of the satellite orbits: 3D distance between the orbital positions of two consecutive arcs are commonly used to assess the internal consistency of the orbit solution*
- *Agreement of the ERPs to the IERS EOP 14 C04 product. The GPS technique provides precise polar motion and LoD estimates, and thus the ERP estimates from different solutions can be compared to the IERS product. the weighted STD (WSTD) of the differences between the POD solution and the IERS 14C04 product is calculated (Bizouard et al., 2018) as*

$$WSTD = \sqrt{\frac{\sum_{i=1}^{n}(dx_i - WM)^2 \cdot P_i}{\sum_{i=1}^{n} P_i}} \tag{3.10}$$

$$WM = \frac{\sum_{i=1}^{n} dx_i \cdot P_i}{\sum_{i=1}^{n} P_i} \tag{3.11}$$

$$P_i = \frac{1}{\sigma_i^2 + \sigma_{ref,i}^2}, \tag{3.12}$$

where dx_i denotes the difference between the ERP parameters and reference values, n denotes the number of records, and σ_i and $\sigma_{ref,i}$ the formal errors of the estimates and the reference product, respectively.

We first analyze the orbital parameters in Section 3.3 and the orbit precision of the BLOCK IIR and IIF satellites in Section 3.4, and then present the ERP agreement with the IERS EOP 14C04 product in Section 3.5. For the orbit precision analyses, the BLOCK IIA satellites are not presented because precisely modeling its post-shadow recovery can be difficult (Rodriguez-Solano et al., 2013) and only one or two satellites are in operation during the time span. The newly commissioned BLOCK III satellites are also not included, as the precise adjustable box-wing model is not available until now and they may undergo outgassing phase at their initial operation period, which will influence the comparison (H. Fliegel, 1989).

3.3 Analysis of Estimated ECOM Parameters

To investigate the correlation between ECOM SRP parameters, Figure 3.4 *and Figure* 3.5 *show the correlation coefficients in the E2DYB solution among the estimated satellite dynamic parameters $(PX, PY, PZ, VX, VY, VZ, D_0, Y_0, B_0, B_{1c}, B_{1s}, D_{2c}, D_{2s}, D_{4c}, D_{4s})$ of G067, a BLOCK IIF satellite, and EPRs during non-eclipsing and eclipsing seasons, respectively. In both higher and lower β angles, the D_{2c} term is highly correlated with the D_0 and B_{1c} terms, with correlation coefficients larger than 0.9 and 0.6, respectively, and the correlation between D_{2s} and B_{1s} term is close to −1, which means that they are highly correlated. Similar correlation can also be observed for the BLOCK IIR satellites (not shown here). Comparing Figure* 3.4 *and Figure* 3.5*, the correlation coefficients become larger in eclipse seasons, i.e., the coefficients between D_{2c} and PX, B_{1c} and VX, D_0 and B_0 at lower β angle are larger than that at the higher β. Consequently, the SRP parameters in the D direction can be hardly separated from that in the Y and B directions.*

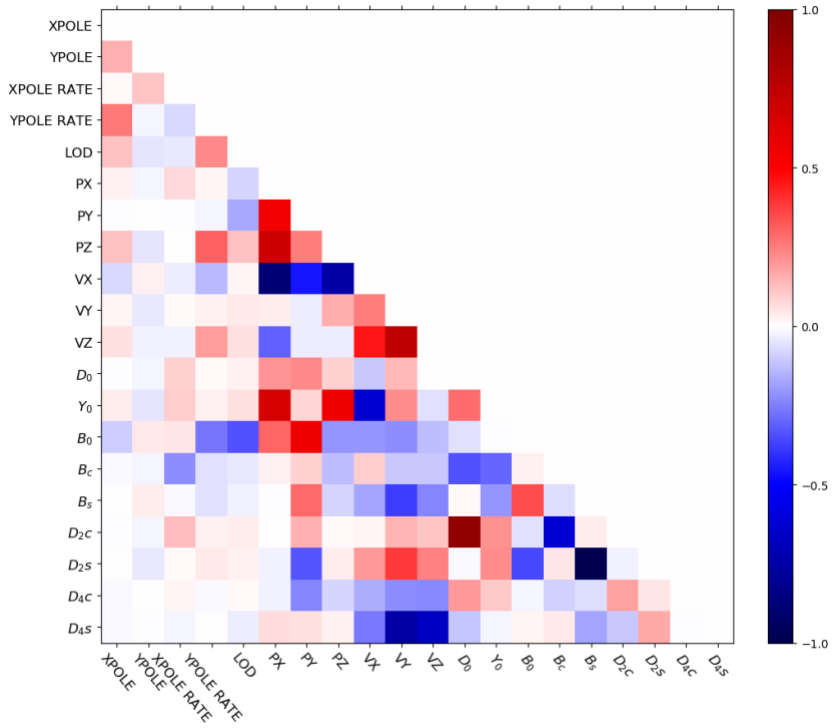

Figure 3.4 WRMS Correlation coefficients between the Earth rotation parameters and the satellite dynamic parameters using the ECOM2 as a parameterization model (E2DYB solution) for SVN G067 (BLOCK IIF) in non-eclipsing season ($\beta \approx -34.3^o$).

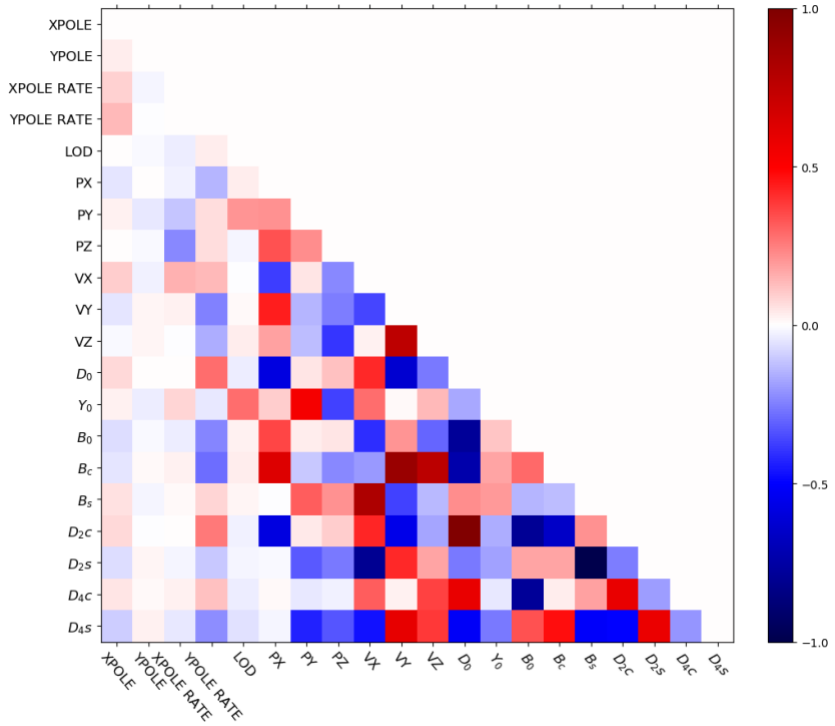

Figure 3.5 Correlation coefficients between the Earth rotation parameters and the satellite dynamic parameters using the ECOM2 as a parameterization model (E2DYB solution) for SVN G067 (BLOCK IIF) in eclipsing season ($\beta \approx -1.3^o$).

Figure 3.6 *presents the time series of estimated Y_0 for all BLOCK IIR and BLOCK IIF satellites in the E1DYB solution. The BLOCK IIR satellites show a larger Y_0 value than the BLOCK IIF satellites, which exhibits as a constant acceleration along the satellite Y-axis, that is, the Y-bias. As the accelerations caused by yaw bias are related to the Sun irradiation, the Y_0 term can be omitted as Equation (3.8) represented if it is dominated by the yaw bias. The magnitude of perturbations caused by the yaw bias for BLOCK IIR satellites is about 0.15 nm/s^2 (Duan & Hugentobler, 2021), which is consistent with the behavior of Galileo Full Operational Capability (FOC) satellites (Bertiger, Bar-Sever, Dorsey, Haines, Harvey, Hemberger, Heflin, Lu, Miller, & Moore, 2020; Sidorov et al., 2020). However, most of the estimated Y_0 coefficients for BLOCK IIR satellites are larger than 0.5 nm/s^2, indicating that there are possible thermal forces in the Y direction. Taking unmodeled non-SRP forces, Equation (3.9) is more reasonable than Equation (3.8). It is noteworthy that the highest dispersion is visible for the legacy BLOCK IIR-A and BLOCK IIR-B satellites (the upper two panels in Figure 1.6), and the largest difference is greater than 0.4 nm/s^2, whereas the variation of the Y_0 coefficient is less significant for Block IIR-M and BLOCK IIF satellites (the lower two panels in Figure 1.6). This diversity means the magnitude of thermal forces are different between the BLOCK IIR-A, BLOCK IIR-B, and BLOCK IIR-M satellites.*

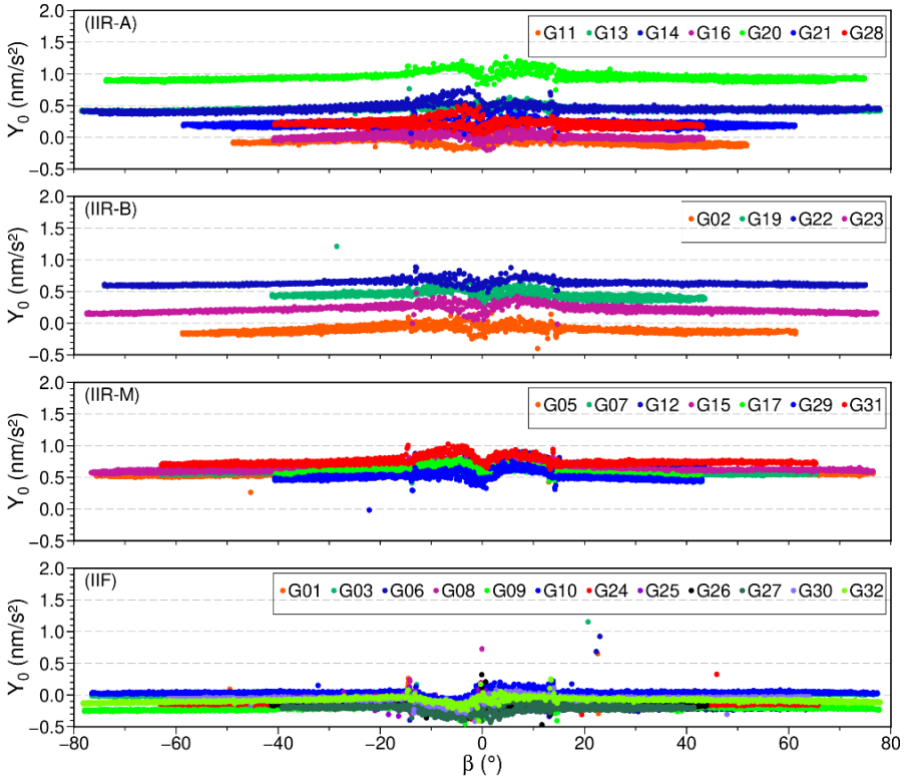

Figure 3.6 SRP coefficient Y_0 with respect to the β angle (the Sun elevation above the orbital plane) in the E1DYB solution from 2017 to 2019. From top to bottom: BLOCK IIR-A, BLOCK IIR-B, BLOCK IIR-M, and BLOCK IIF satellites, respectively. Note that there is no change of PRNs of listed satellites during this period.

For a further comparison of Equation (3.8) and Equation (3.9), taking SVN G050 (BLOCK IIR) and G073 (BLOCK IIF) as an example, the estimated coefficients in the Y and B

directions derived from the E1D and E1DYB solutions are shown in Figure 3.7*. The coefficients of SVN G050 in the B direction are shifted by 6 nm/s^2 for better view. The estimated coefficient Y_0 derived in the E1D solution shows less scatter between the phases in and out of eclipse seasons. A similar pattern was also reported when an a priori box-wing model was used (see Figure 15 in (Bury et al., 2020)). It indicates that BLOCK IIR satellites have a relatively noticeable thermal radiation in Y surfaces. In addition, the Y_0 estimates of BLOCK IIF satellite (SVN G073 in Figure* 3.7*) have a visible linear trend during eclipse seasons and are reduced after the β angle switches the sign (see Figure 4 in (Duan & Hugentobler, 2021)). This needs further investigation. In contrast to the Y_0 of BLOCK IIR satellites, the trend of B_{1c} (for instance, SVN G073) shows larger variation.*

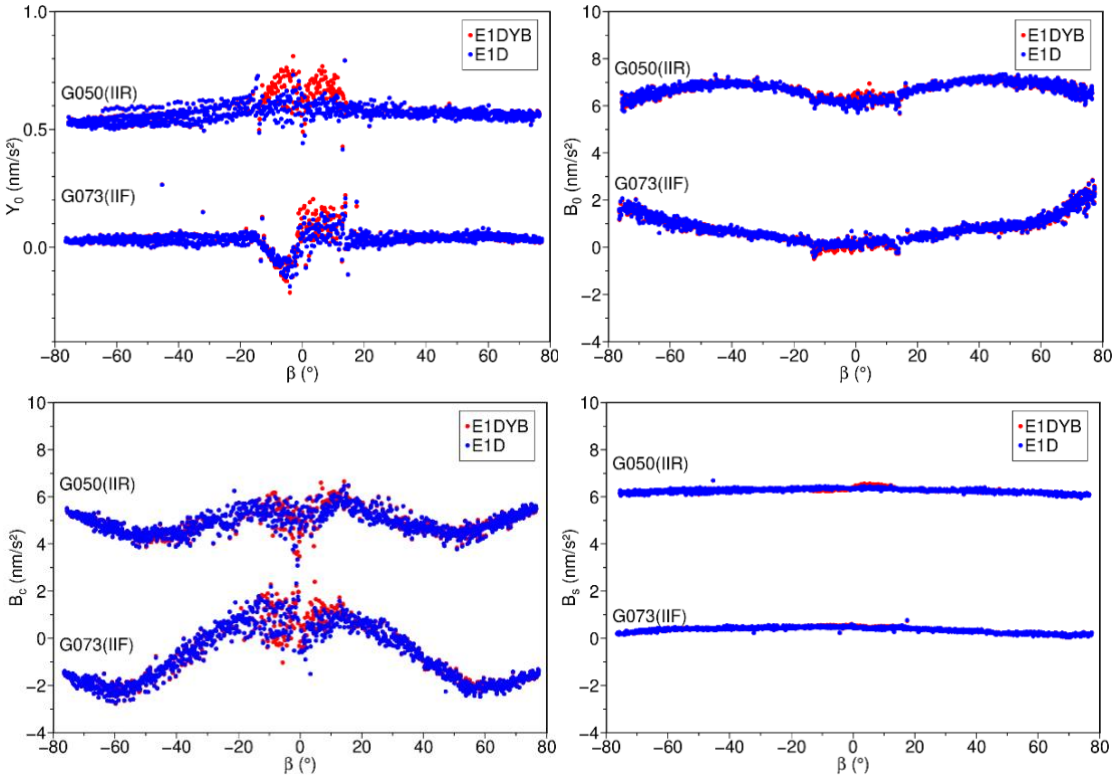

Figure 3.7 SRP coefficients Y_0 (upper left), B_0 (upper right), B_{1C} (lower left), and B_{1S} (lower right) with respect to the β angle in solution E1DYB (red dots) and solution E1D (blue dots) spanning from 2017 to 2019. The results of SVN G050 are all shifted by 6 nm/s^2 for better visualization, except for the coefficient Y_0. Note the different y-axis scales between the upper-left panel (the Y_0 panel) and the others.

Furthermore, the statistics of the estimated SRP parameters in the 12 solutions are given in Figure 3.8*. For the ECOM1 solutions (that is, using ECOM1 as the parameterization model) shown in the upper panels of Figure* 3.8*, the STD of the B_{1c} (marked with black X-cross) is improved when an a priori box-wing model is used or a shadow factor is applied only in the D direction, except for BLOCK IIF satellites, whereas other coefficients have comparable STD values between different solutions. The STD difference of B_{1c} between solution E1DYB and solution E1D_ABW is around 0.2 nm/s^2 for BLOCK IIR satellites and BLOCK IIF satellites. As for the ECOM2 solutions (that is, using ECOM2 as parameterization model) shown in the lower panels in Figure* 3.8*, the STD values of B_{1c} do not show any*

significant reductions either using box-wing models or adding the shadow factor only in the D direction, that is, between E2DYB and E2D_ABW solution. Compared with the ECOM1 solutions, all SRP coefficients in ECOM2 solutions show lower stability except for the Y_o term, and the STD values of the twice- and fourth order periodic terms are greater than 1 nm/s^2 in the ECOM2 solutions. A noticeable reduction of D_{4s} (blue star) is found when the shadow factor is applied only in the D direction and D_{2s} shows similar but smaller decline.

Summarizing the sensitivity of the GPS BLOCK IIR and IIF satellites to the accelerations in the direction of Y and B, they both suffer from the accelerations in the Y direction, which is independent on β angle, whereas the BLOCK IIF satellites show smaller accelerations. The visible changes during eclipse seasons for the BLOCK IIR satellites may be caused by the active thermal control before and after the middle of an eclipse event and can be removed mostly by considering additional accelerations in the X surfaces. The dependence of the accelerations in the B direction on β angle is caused not only by SRP but also by other non-gravitational forces, such as the thermal radiation. Applying an a priori box-wing or adjustable box-wing model will improve the stability (STD values) of periodic terms (for instance, B_c) but not for the BLOFK IIF satellites. Compared with using Equation (3.8), using Equation (3.9) has a positive effect on the stability of periodic terms, especially for the D_{4s} term of the BLOCK IIR satellites.

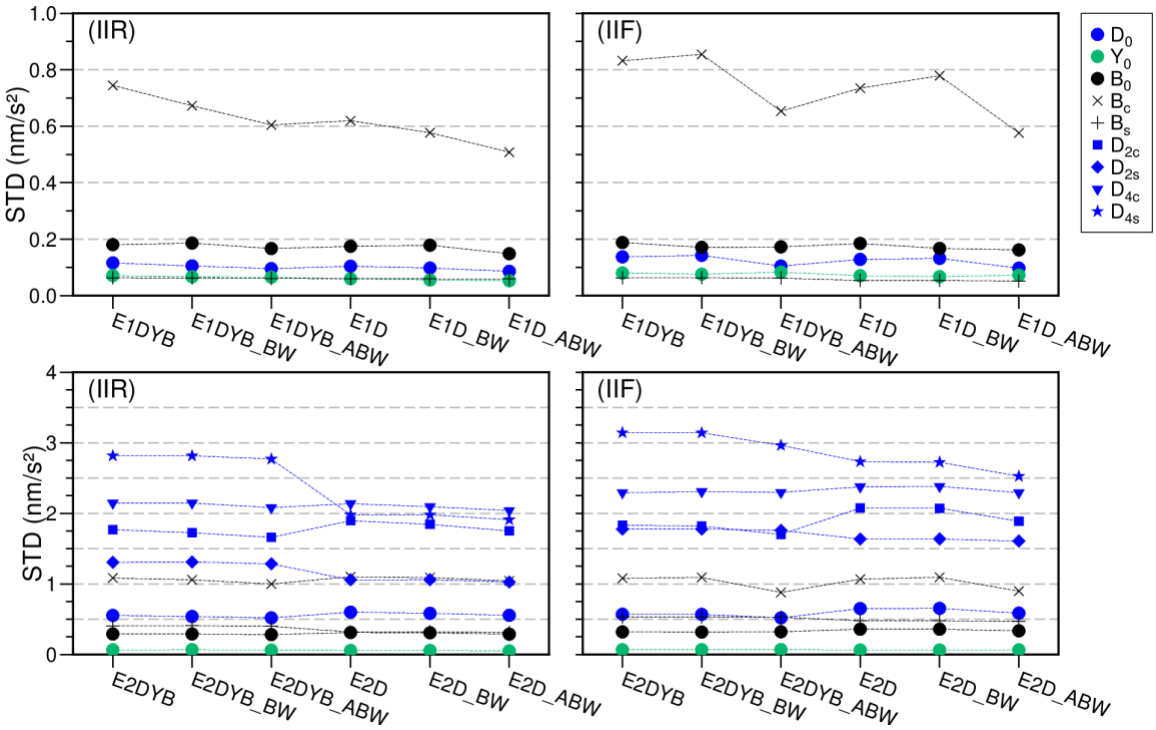

Figure 3.8 Standard deviation (STD) of SRP coefficient time series for eclipsing satellites in the 12 solutions. Upper panels: ECOM1 empirical SRP modeling; lower panels: ECOM2 empirical SRP modeling; left panels: GPS BLOCK IIR satellites; right panels: GPS BLOCK IIF satellites. Note the different y-axis scales between the upper and lower panels.

3.4 Analysis of satellite orbits

The mean 3D RMS values of orbit DBD (Griffiths & Ray, 2009) for the BLOCK IIR and IIF satellites in different solutions are shown in Figure 3.9*. The method using ECOM2 as a parameterization model (the E2DYB solution) has slightly improved orbit precision in eclipse seasons compared to that using ECOM1, especially for the BLOCK IIR satellites. Using the box-wing as an a priori model (the E1DYB_BW solution) slightly improves the orbit precision for BLOCK IIR satellites and using the adjustable box-wing as an a priori model (the E1DYB_ABW solution) further improves the orbit quality for both the BLOCK IIR and IIF satellites, in and out of eclipse seasons. By comparing each pair of solutions between the shadow factor applied in the D direction and that in the DYB directions, for instance, between the E1DYB and E1D solutions, and also between the E1DYB_ABW and E1D_ABW solutions, it is obvious that eclipsing satellites have smaller RMS values of DBD in latter solutions with the shadow factor applied only in the D direction. A slight improvement for non-eclipsing satellites can also be observed when the shadow factor is applied in the D direction of ECOM2, which can be explained by the stability improvement of higher periodic terms (D_{2s} or D_{4s}) in Figure* 3.8*.*

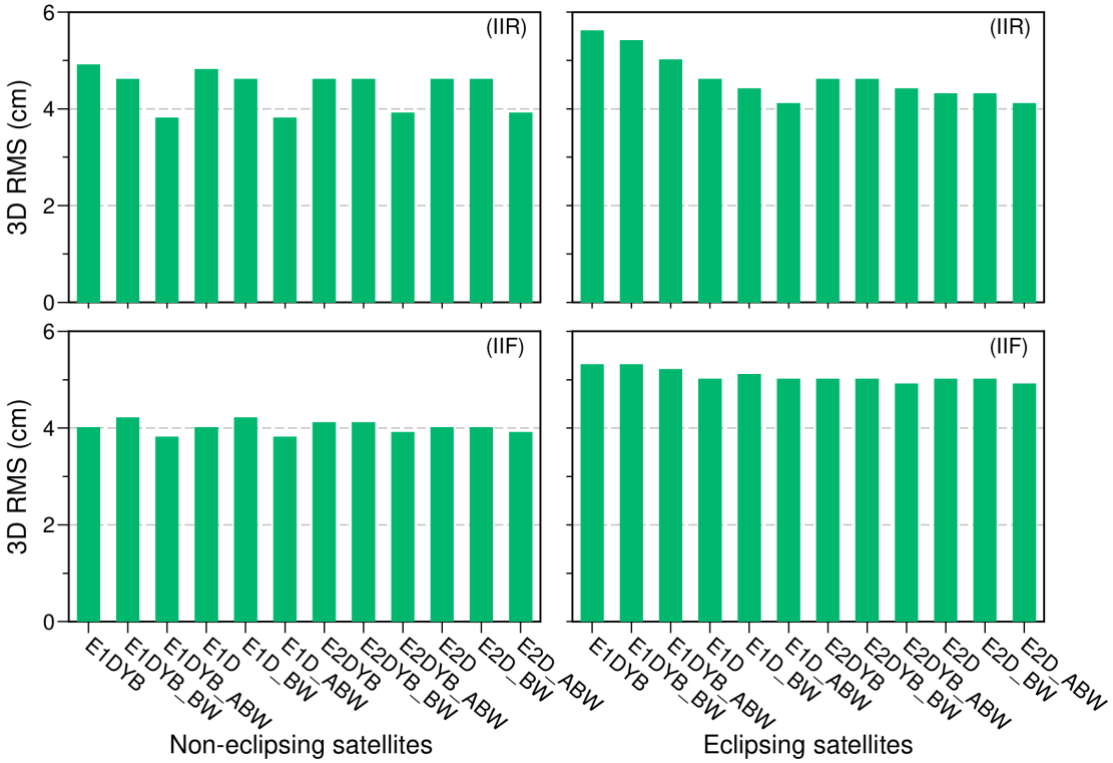

Figure 3.9 Mean 3D RMS of day boundary discontinuities in the 12 types of GPS daily precise orbit determination solutions spanning from 2017 to 2019. Upper panels: GPS BLOCK IIR satellites, and lower panels: GPS BLOCK IIF satellites. Left panels: satellites in non-eclipsing seasons; right panels: satellites in eclipsing seasons.

For the BLOCK IIR satellites, the orbit precision of E1DYB_ABW and E2DYB_ABW, in which ECOM1 or ECOM2 parameterization model is combined with the a priori

adjustable box-wing model and the shadow factor is applied in the D direction, is better than 4 cm for the non-eclipsing satellites, and close to 4 cm for eclipsing satellites. As for the BLOCK IIF satellites, using the adjustable box-wing as an a priori model slightly improves the orbit precision, whereas using the box-wing degrades the orbit precision. Therefore, the solutions using the box-wing model are not discussed in the following analysis.

Taking SVN G050 (BLOCK IIR) and SVN G073 (BLOCK IIF) as an example, Figure 3.10 *presents the radial orbit differences between solutions with the shadow factor applied in the D direction and those in the DYB directions. As shown in Figure* 3.10*, orbit differences between two methods of using the shadow factor are observed at lower β angle, in which the differences based on ECOM2 are more visible. When $\Delta\mu$ is around 0^o ($\Delta\mu + 180^o = \pm 180°$), that is, the orbit noon, the orbit differences are negative at lower negative β angle and positive at lower positive β angle. Note that BLOCK IIF satellites show a more visible pattern than BLOCK IIR satellites, which is possibly owing to instability of higher periodic terms in ECOM2 (twice-per-revolution and fourth-per-revolution term).*

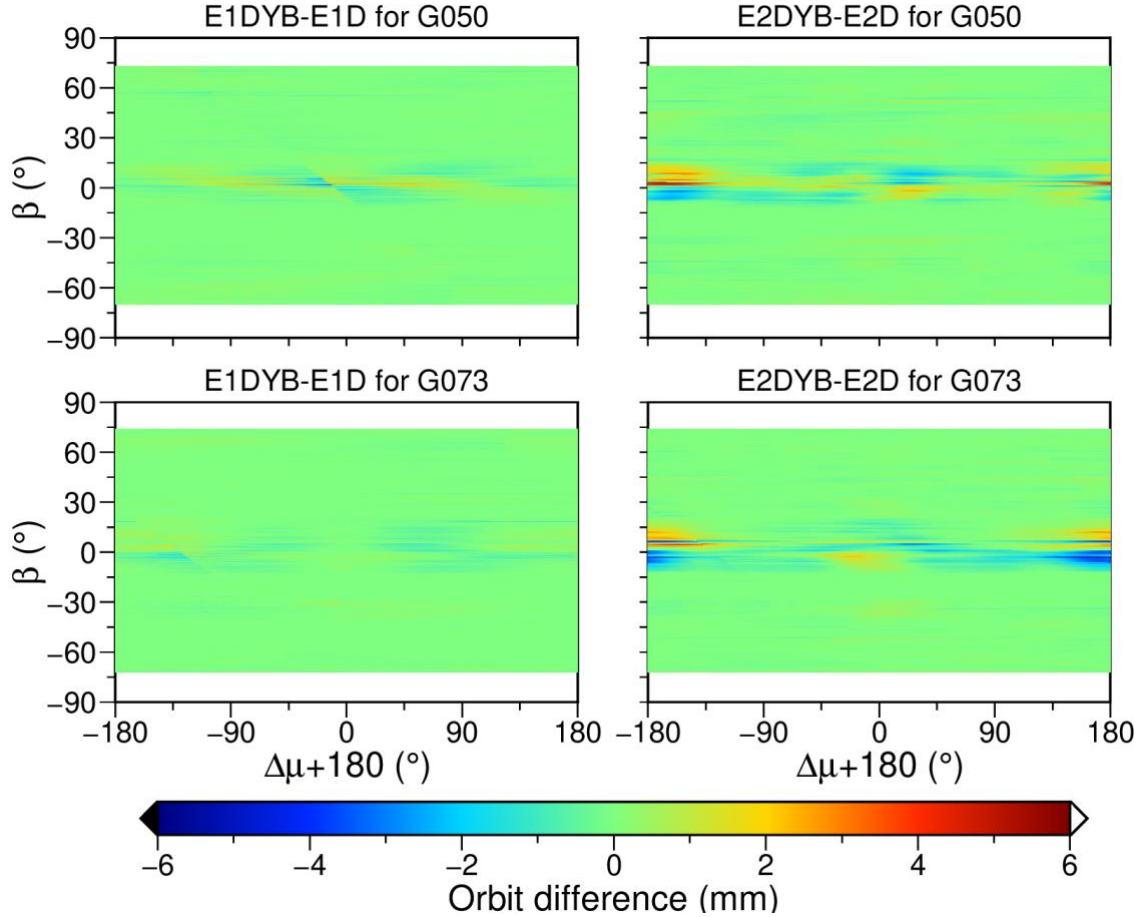

Figure 3.10 Differences of satellite orbits in the radial component caused by applying the shadow factor in the D and DYB directions for SVN G050 (BLOCK IIR, upper panels) and G073 (BLOCK IIF, lower panels) as a function of β and $\Delta\mu$ angle in 2019. $\Delta\mu$ is the angular argument. Left and right: using ECOM1 and ECOM2 as parameterization SRP models, respectively.

Moreover, the orbit differences with and without a priori box-wing models are investigated and the radial differences are shown in Figure 3.11 *and Figure* 3.12 *for the GPS SVN050 satellite (BLOCK IIR) and SVN073 (BLOCK IIF), respectively. From Figure* 3.11*, using the box-wing or adjustable box-wing as a priori model with the ECOM1 as parameterization model leads to the visible peanut-like distribution of the orbit differences, where the differences can be up to ±6 mm. This pattern is likely owing to the variation of effective illuminated area in the Z direction (pointing to Earth). Large antenna arrays, namely W-sensor, are installed in ±X surfaces of BLOCK IIR satellites, which cannot be modeled by only one constant parameter in the D direction. The differences shown in the left panel of Figure* 3.11 *are reduced when using ECOM2 as parameterization model, especially between box-wing model and no a priori model, indicating that the box-wing as a priori model does not contribute that much when ECOM2 is used as parameterization model.*

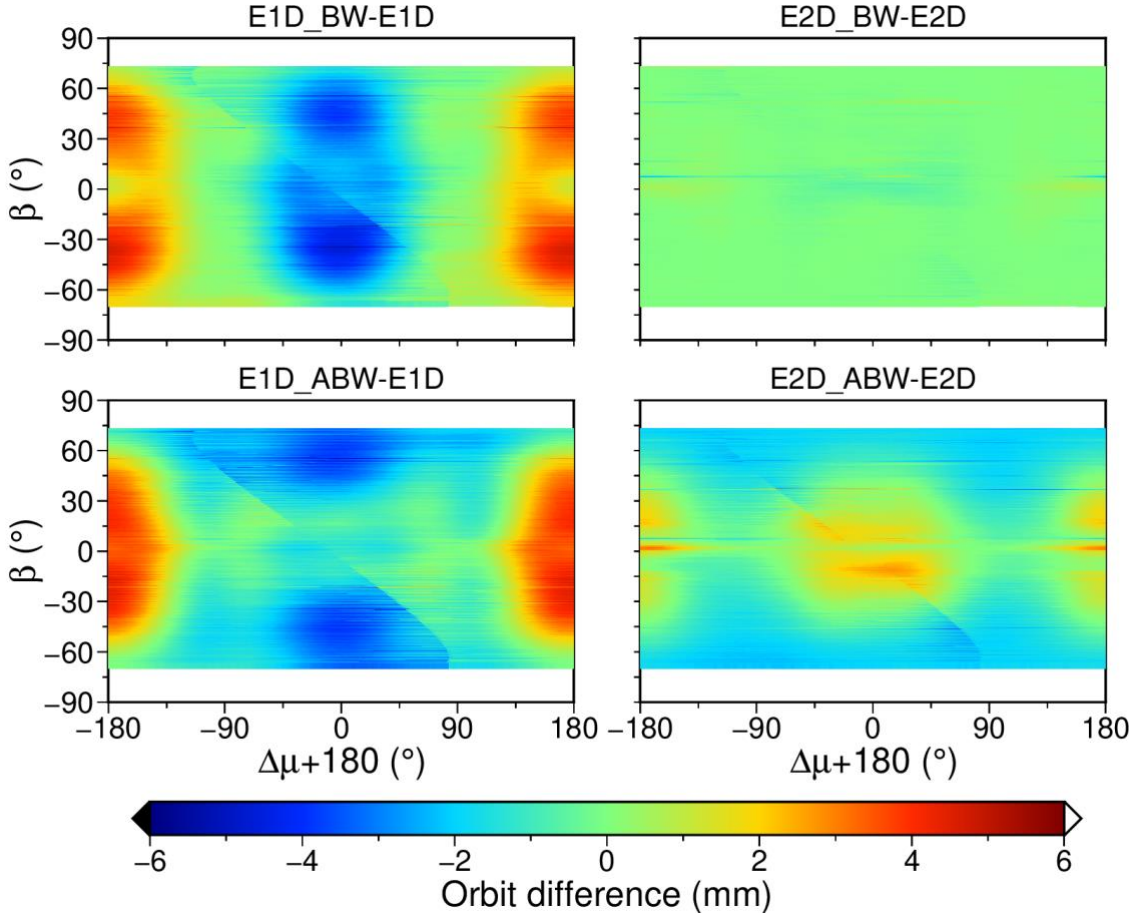

Figure 3.11 Differences of satellite orbit in the radial component between solutions using different a priori models for SVN G050 (BLOCK IIR) as a function of β and $\Delta\mu$ angle in 2019. $\Delta\mu$ is the angular argument. Upper: differences between using no a priori SRP model and using the box-wing model; lower: differences between using no a priori SRP model and using the adjustable box-wing model. Left and right panels: using the ECOM1 and ECOM2 as the parameterization model, respectively.

In addition to the BLOCK IIR satellites, the orbit radial differences of the BLOCK IIF satellites (SVN G073) shown in Figure 3.12 *are further investigated. As it is shown, the differences caused by applying a priori box-wing model are largely reduced compared with*

corresponding results of BLOCK IIR satellites shown in Figure 3.11*. Note that when using the ECOM2 as parameterization model, the visible differences at lower β angle between with and without an a priori adjustable box-wing model may be related to the adjustment of shape value in the adjustable box-wing modeling.*

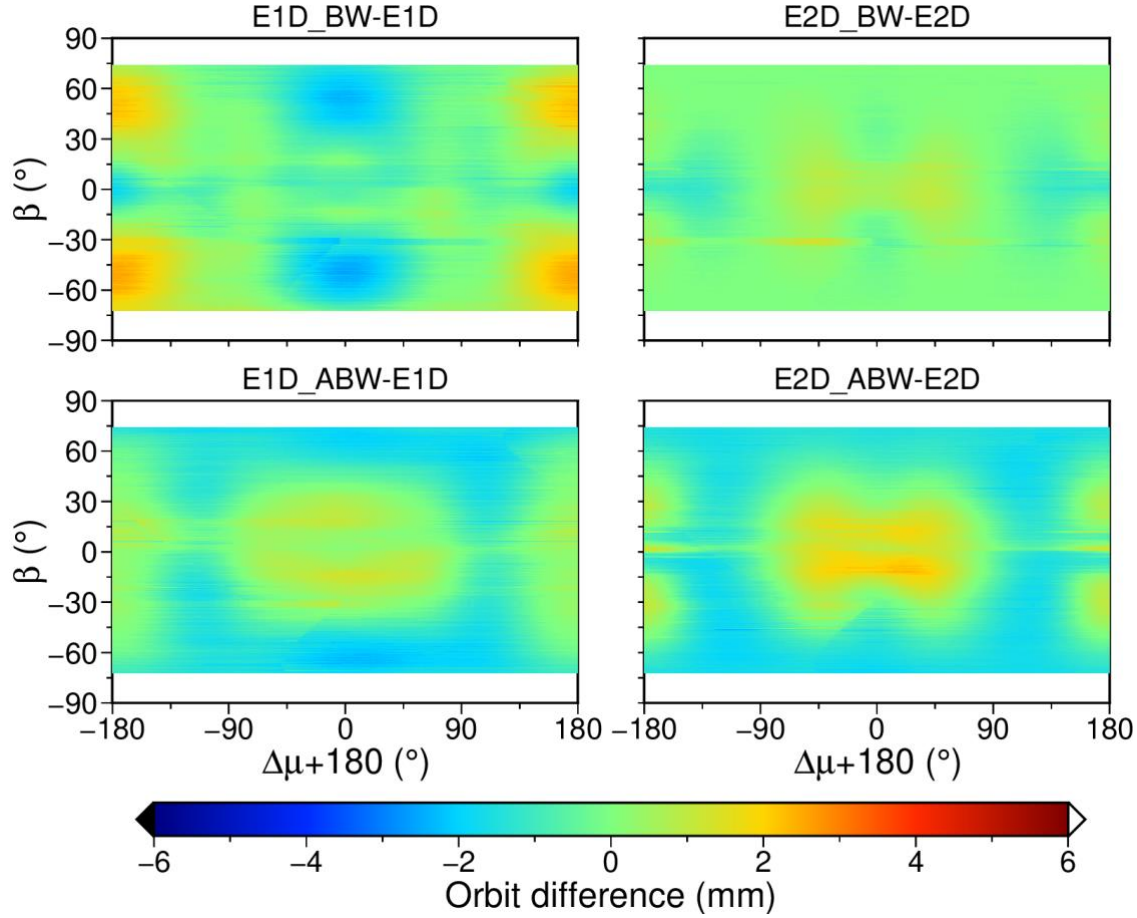

Figure 3.12 Differences of satellite orbits in the radial component between different a priori models for G073 (BLOCK IIF) as a function of β and $\Delta\mu$ angle in 2019. $\Delta\mu$ is the angular argument. Upper: differences between using no a priori SRP model and using the box-wing model; lower: differences between using no a priori SRP model and using the adjustable box-wing model. Left and right panels: using ECOM1 and ECOM2 as parameterization model, respectively.

Due to the fact that current box-wing model has a little improvement on BLOCK IIR satellite orbit precision, even a negative effect on BLOCK IIF satellites, only the adjustable box-wing model is considered for evaluation. The 3D RMS values of DBD with respect to β angle for eclipsing satellites in different solutions are shown in Figure 3.13*. For BLOCK IIR satellites shown in the upper panel, RMS values of DBD in E1DYB (red dot) and E1DYB_ABW (blue dot) solutions increase with β declining during the eclipse period. Applying the shadow factor only in the D direction removes the rising trend mostly for* $4^o < abs(\beta) < 12^o$*, that is, the E1D (black dot) and E1D_ABW (green dot) solutions. However, in the E1D solution, the RMS values still increase in the case of lower β angle, that is,* $abs(\beta) < 4^o$*. By using the ECOM2 instead of the ECOM1 and applying the shadow factor in the D direction, the RMS values are reduced to a large extent. Note the*

relatively larger RMS values of DBD are up to 6–8 cm for both BLOCK IIR and BLOCK IIF satellites at the beginning of eclipse events, that is, $13° < abs(\beta) < 14°$*. This is because the eclipsing time at the beginning or end of the eclipse seasons is less than 600 s, which may be omitted as our processing interval is 300 s.*

For the BLOCK IIF satellites shown in the lower panel of Figure 3.13*, an asymmetrical pattern is observed between negative and positive β angles, which is similar with the SRP coefficients* Y_0 *variation in Section 3.3 (see Figure* 3.6 *and Figure* 3.7*). The 3D DBD RMS of all solutions are small and close to each other with slight difference when the β angle is positive, including the E1DYB and E1DYB_ABW solutions. The large RMS values and even large difference among different solutions are also observed for BLOCK IIF satellites at transition from full phase to umbra or inverse. This phenomenon also needs further investigation.*

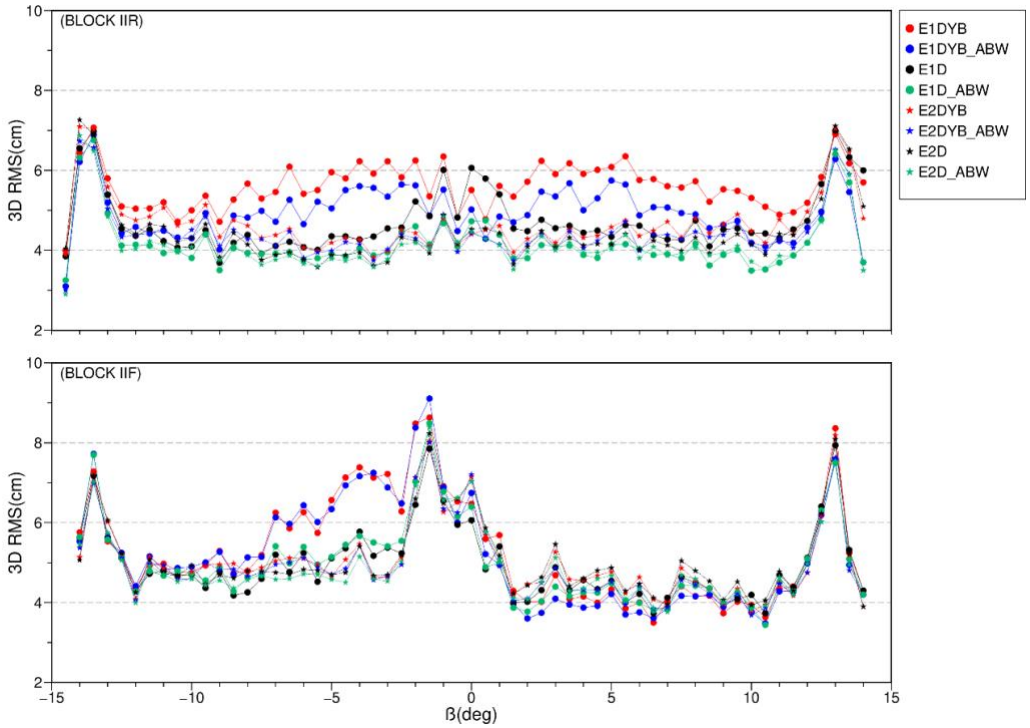

Figure 3.13 3D RMS values of DBD for BLOCK IIR (upper panel) and BLOCK IIF (lower panel) in eclipse seasons with respect to the β angle spanning from 2017 to 2019. Note that there is no difference between using no a priori SRP model and using the box-wing model; the solutions using the box-wing model are thus not presented.

Further statistics of the RMS values of DBD in the along, cross, and radial components from 2017 to 2019 are summarized in Table 3.2*. The solutions with shadow factor in the D direction are generally better than that those with shadow factor applied in the DYB directions, especially for the cross and radial components. For the BLOCK IIR satellites in eclipse seasons, the RMS values of DBD are reduced from 2.8 cm and 3.1 cm in the E1DYB solution to 2.1 cm and 2.4 cm in the E1D solution in the cross and radial directions, respectively. For the BLOCK IIF satellites in eclipse seasons, the improvement from the E1DYB to E1D solution is only 0.4 cm in the radial direction, and that in the along and*

cross directions are neglectable. When an adjustable box-wing model is used, the orbit improvement in and out of eclipse seasons and the improvement of the BLOCK IIR satellites are larger than that of BLOCK IIF satellites. The orbits are further improved when applying the shadow factor in the D direction and using the adjustable box-wing model as a priori SPR model simultaneously, that is, the E1D_ABW and E2D_ABW solutions. The values of E1D_ABW solution for BLOCK IIR satellites out of eclipse seasons are 2.3 cm, 1.7 cm, and 1.7 cm in the along, cross, and radial directions, respectively, and the corresponding values in eclipse seasons are 2.5 cm, 2.4 cm, and 2.7 cm. Moreover, the DBD of the E1D_ABW solution has a comparable accuracy with the E2D_ABW solution.

Table 3.2 RMS values of the orbit DBD in 2017–2019. The statistics in and out of eclipse seasons for both BLOCK IIR and BLOCK IIF satellites are summarized separately. A, C and R stand for the along, cross radial direction, respectively. The unit is cm. Note that there is no difference between using no a priori SRP model and using the box-wing model; the solutions using the box-wing model are thus not presented.

Solutions	BLOCK IIR					
	Eclipse			Noneclipse		
	A	C	R	A	C	R
E1DYB	2.6	2.8	3.1	2.8	2.2	2.3
E1DYB_ABW	2.5	2.4	2.7	2.3	1.7	1.7
E1D	2.5	2.1	2.4	2.8	2.2	2.3
E1D_ABW	2.4	1.9	2.0	2.3	1.7	1.7
E2DYB	2.4	2.1	2.4	2.7	2.1	2.2
E2DYB_ABW	2.3	2.0	2.3	2.4	1.8	1.7
E2D	2.4	1.8	2.3	2.7	2.0	2.2
E2D_ABW	2.3	1.7	2.2	2.3	1.7	1.7
	BLOCK IIF					
	Eclipse			Noneclipse		
	A	C	R	A	C	R
E1DYB	3.1	2.2	2.7	2.5	1.7	1.8
E1DYB_ABW	3.1	2.1	2.7	2.4	1.7	1.7
E1D	3.1	2.1	2.3	2.5	1.7	1.8
E1D_ABW	3.1	2.1	2.3	2.4	1.6	1.7
E2DYB	3.0	2.0	2.6	2.5	1.8	1.8
E2DYB_ABW	3.0	1.9	2.6	2.4	1.7	1.7
E2D	3.1	1.9	2.5	2.5	1.8	1.8
E2D_ABW	3.0	1.8	2.5	2.4	1.7	1.7

3.5 Analysis of ERPs

In addition to the performance of satellite orbit precision, the ERP components are also sensitive to the satellite orbit dynamic modeling (M. Rothacher et al., 1999). The ERP component estimates of different solutions are compared to the IERS EOP 14C04 product (Bizouard et al., 2018) and the WSTD values are given in Table 3.3*. The different methods of modeling SRP and applying the shadow factor have an insignificant impact on the ERP agreement with the IERS product, and the WSTD of each solution is around 43.6 to 44.7 μas, 23.1 to 24.8 μas, 213.2 to 216.0 μas/day, and 8.7 to 9.8 μs/day for the x-pole, y-pole, x-pole rate, and LoD components, respectively. As for the y-pole rate, however, using the*

adjustable box-wing as an a priori SRP model clearly improves the precision. For instance, the WSTD value reduces from 205.3 μas/day in solution E1DYB to 184.9 μas/day in solution E1DYB_ABW. The impact of using ECOM1 or ECOM2 models and that of applying the shadow factor in the D or DYB directions on y-pole rate precision are rather diverse. There is insignificant difference between applying the shadow factor in the D direction and in the DYB directions for the polar motion offset and rate, whereas the LoD always shows an improved precision when the shadow factor applied in the D direction. Moreover, the E1D_ABW solution has the smallest WSTD of the LoD (8.7 μs/day), which is improved by about 8% compared with the E2DYB_ABW solution (9.7 μs/day).

Table 3.3 WSTD values of the ERP differences between GPS precise orbit determination solutions and the IERS EOP 14C04 product. Note that there is no difference between using no a priori SRP model and using the box-wing model; the solutions using the box-wing model are thus not presented.

Solutions	*x*-Pole [μas]	*y*-Pole [μas]	*x*-Pole Rate [μas/day]	*y*-Pole Rate [μas/day]	LoD [μs/day]
E1DYB	44.1	24.8	214.4	205.3	9.2
E1DYB_ABW	43.7	23.4	214.4	184.9	9.3
E1D	43.6	24.4	214.6	199.5	9.1
E1D_ABW	43.9	23.3	214.7	193.2	8.7
E2DYB	44.3	23.6	215.8	190.6	9.8
E2DYB_ABW	43.8	23.3	213.3	185.6	9.7
E2D	44.7	23.5	216.0	200.3	9.2
E2D_ABW	44.0	23.1	213.2	191.4	9.1

Figure 3.14 *further presents the power spectra of the LoD in eight solutions, which demonstrates the impact of the SRP modeling. A clear reduction in the 1.04 cpy and 6.30 cpy signals is observed when applying the shadow factor in the D instead of the DYB directions. The only exception is when using the pure ECOM1 parameterization model without an a priori model, that is, between E1DYB and E1D, where the 1.04 cpy signal is larger in the E1D solution than in the E1DYB solution.*

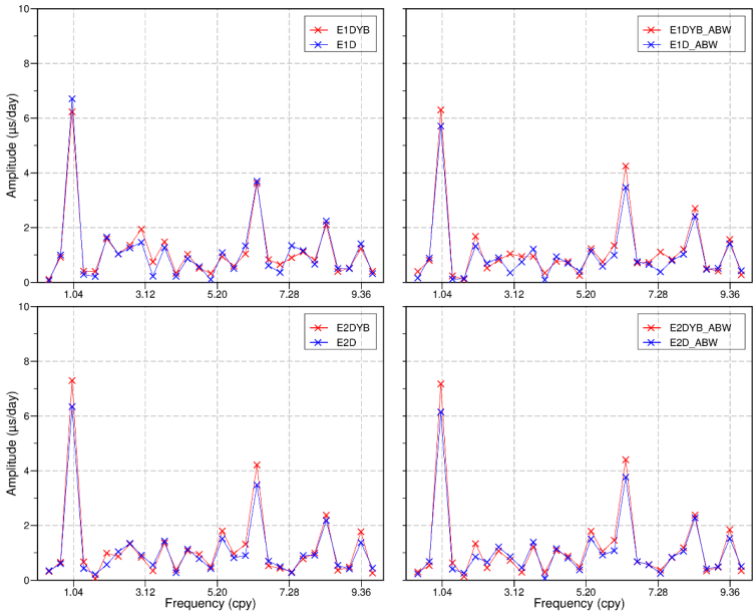

Figure 3.14 Power spectra of the LoD differences with respect to the IERS EOP 14C04 product. Upper panels: ECOM1 for the empirical SRP modeling, lower panels: ECOM2 for the empirical SRP modeling; left panels: no a priori SRP modeling, right panels: adjustable box-wing for the a priori SRP modeling.

3.6 Chapter summary

The main findings in this chapter are summarized as follows:

Section 3.1 investigates the relationship between box-wing and ECOM model and then introduces two ways of using shadow factor, which are currently used by some IGS ACs, that is to apply the factor in either the *D* only or all the *D*, *Y*, and *B* directions. For a satellite under nominal attitude model, the accelerations caused by SRP can be fully represented by the coefficients in D and B directions. The expression in D and B directions derived from box-wing model are similar to the ECOM models. Whether the periodic terms are significant depends on the shape of a satellite and optical properties. For example, the fourth-per-revolution is significant for a cuboid-shaped satellite, while it is not for a cube satellite. The number of unknown parameters in ECOM model should be reduced if there is a precise a priori box-wing model.

Taking GPS as an example, Section 3.2 introduces the setting of processing strategies and evaluated indexes, including the stability of SRP coefficients, DBD, and related ERP results.

Section 3.3 analyzes the variation of estimated ECOM parameters. For the GPS BLOCK IIR satellite, the performance of SRP coefficient Y_0 between in and out of eclipse seasons is consistent with the shadow factor that is applied in the *D* direction but rather diverse when applied in the *DYB* directions. The diversity of the coefficient Y_0 in and out of eclipse seasons is possibly stemming from non-gravitational forces in $\pm Y$ surfaces, e.g., radiator. A notable discrepancy in the behavior of Y_0 for the BLOCK IIR and BOCK IIF satellites is probably related to the difference in satellite design, thermal control model, etc., which needs further investigation in the future. For the coefficients in the *B* direction, its dependency on β angle is caused not only by SRP but also by other unmodeled non-SRP forces, which can partly be absorbed by the once-per-revolution terms in ECOM1 and ECOM2. Moreover, applying an a priori box-wing model can improve the stability of periodic terms, especially for the D_{2s} and D_{4s} terms in the *D* direction because of the parameters' correlation, except for the BLOCK IIF satellites using the a priori box-wing model. Among all solutions, the one combining a priori adjustable box-wing with ECOM1 with the shadow factor applied in the *D* direction (that is, the E1D_AWB) is recommended in future POD processing since it has the best SRP coefficient stability with the smallest STD values.

Section 3.4 shows orbit accuracy. With or without a priori adjustable box-wing model, applying the shadow factor in the *D* instead of the *DYB* directions can improve the orbit quality, especially in the cross and radial directions. Compared with the E1DYB solution using no a priori SRP and the shadow factor applied in the *DYB* directions, the RMS values of orbit DBD in the E1D_ABW solution (using a priori adjustable box-wing model with shadow factor applied in the *D* direction) are improved by 7.7%, 32.1%, and 35.5% for the BLOCK IIR satellites in non-eclipsing seasons in the along, cross, and radial direction, respectively, and the corresponding improvements in the eclipse season are 17.8%, 22.7%, and 26.1%. In the E1D_ABW or E2D_ABW solution, the BLOCK IIR satellites show similar behavior in and out of eclipse seasons.

The reason for the deteriorated performance of SRP coefficients and DBD values for the BLOCK IIF satellites when applying box-wing model can be attributed to the fact that the shape and optical properties were collected directly from some documents, which might not be accurate enough. The orbit results confirmed the advantages of applying a precise box-wing model and applying the shadow factor only in the *D* direction during eclipse seasons, which are consistent with the conclusion in Section 3.3.

Section 3.5 shows the performance of ERPs with different solutions. Applying adjustable box-wing as an a priori SRP model improves ERP precision. The WSTD value of the y-pole rated is reduced from 205.3 to 184.9 $\mu as/day$. An insignificant difference between applying the shadow factor in the D direction and in the DYB directions for the polar motion offset and rate is observed, whereas the LoD always shows an improved precision when the shadow factor is applied in the D direction, reduced from 9.7$\mu s/day$ to 8.7 $\mu s/day$.

4 Undifferenced integer ambiguity resolution

This chapter aims to investigate the performance of UD IAR on GNSS network solutions and explore the potential reasons causing discrepancies between UD IAR and DD IAR. Section 4.1 presents the insights of DD IAR and UD IAR and a realization strategy of UD IAR in GNSS data processing. Section 4.2 evaluates the performance of UPDs estimated in the network solution. Section 4.3 and Section 4.4 analyze the impacts of UD IAR on satellite orbits and other geodetic parameters, including ERP, stations coordinates and geocenter coordinates (GCC). In Section 4.5, using GPS solutions, the factors causing the difference between DD and UD IAR are investigated in terms of the quality of satellite orbits, as well as ERP, station coordinates, and GCC. Finally, conclusions are summarized in Section 4.6.

4.1 Implementation of UD IAR

Different from the high stability of float ambiguities in PPP solutions (M. Ge et al., 2007; Li et al., 2017; B. Cui, Li, et al., 2021), the float ambiguities in GNSS POD before applying ambiguity resolution are not such accurate as that from PPP because much more parameters are estimated simultaneously in POD processing. This may result in a vulnerable UD IAR if directly using ambiguities from POD float solutions, which will be further explained in Section 4.1.1. Therefore, Deng et al. (2022) recommended to perform DD IAR first to ensure the accuracy of ambiguities before applying UD IAR. Section 4.1.2 presents the implementation of UD IAR in PANDA software.

Before explaining the differences between DD IAR and UD IAR, some concepts are defined in advance as below.

- Maximum independent DD-ambiguity set

  A DD-ambiguity set containing all theoretically independent DD ambiguities which are selected from the whole network.

- Maximum independent baseline set

  A baseline set containing the maximum number of independent baselines.

- Absence of sufficient independent DD ambiguities:

  Suppose the number of selected independent DD ambiguities is typically less than that of the maximum independent DD-ambiguity set, this situation is called the absence of sufficient independent DD ambiguities.

- Outlier DD ambiguity

  The unfixable ambiguities refer to the ambiguities whose integer property cannot be recovered even after applying UPD corrections. If one or more unfixable UD ambiguities join the formation of a DD ambiguity, the DD ambiguity should not be fixed and is deemed an outlier or incorrect DD ambiguity.

4.1.1 Relationship between UD IAR and DD IAR

Suppose that there are k ambiguities in a network and all of them can be fixed to integers in UD IAR. The number of the maximum independent DD ambiguities are l, in which all UD ambiguities will be involved. The relationship between UD ambiguities and DD ambiguities can be represented as follows

$$\underbrace{\mathbf{N}_{dd}}_{l\times 1} = \underbrace{\mathbf{D}_{dd}}_{l\times k}\underbrace{\mathbf{N}_{ud}}_{k\times 1}, \tag{4.1}$$

where $\mathbf{D}_{dd}$ is the DD mapping matrix, $\mathbf{N}_{ud}$ and $\mathbf{N}_{dd}$ are the UD-ambiguity and DD-ambiguity vectors respectively. Clearly, the fixable DD-ambiguity vector $\mathbf{N}_{dd}$ cannot be transformed to UD-ambiguity vector $\mathbf{N}_{ud}$ directly since the rank of mapping matrix $\mathbf{D}_{dd}$ is l, less than k. Additional $k-l$ independent UD ambiguities, termed as reference ambiguities, have to be selected for converting DD ambiguities to UD ambiguities (Blewitt, 1989). In DD IAR, only the relative relationship between reference ambiguities and other UD ambiguities is considered. Therefore, those reference ambiguities can be deemed as "float solutions" since they are not constrained to integer values directly. In contrast, they can be fixed to integers with the aid of UPDs. This distinction underlies the limited improvements observed in real-time clock estimation within DD IAR, as reported by Zuo et al. (2023). When both independent DD ambiguities and reference ambiguities are imposed as integers, it is anticipated that the solutions obtained from DD IAR and UD IAR should be equivalent.

Although DD IAR and UD IAR are considered as equivalent theoretically, the behavior of UD IAR is highly tied to the accuracy of float ambiguities whose fractional parts are employed as UPD observations for UPD estimation. As already mentioned, the UPD is proved stable over long-term, for example, several days. However, the fractional parts of estimated UD ambiguities may vary significantly along with time because of the high correlation between ambiguities, orbit, and clock parameters in POD where both are estimated simultaneously. This is why ambiguities estimated in PPP are much more stable and accurate than those in POD. Those UD ambiguities with a lower accuracy could result in inconsistent fractional parts for the ambiguities of the same station-satellite pair but occurred at different time epochs in a session. In that case, a consistent UPD estimates for the whole session can hardly be achieved. To provide stable and accurate ambiguity estimates, which is a fundamental requirement for achieving UD IAR of high performance, the float solution must be enhanced to minimize the variation of UD ambiguities in POD processing. In contrast, the integer property of DD ambiguities can be easily recovered since the four UD ambiguities forming a DD ambiguity

are usually required to have a minimum simultaneous observation time, i.e., they are temporally close to each other. Therefore, if they are biased, they should have similar biases which consequently can be removed in the formation of DD ambiguity.

Theoretically, all independent fixed DD ambiguities need to be picked of in order to ensure a maximum fixing to achieve the best accuracy of orbits, clocks, and other geodetic products. Usually, there are two strategies of selecting independent DD ambiguities: to select the independent DD ambiguities from all fixable ambiguities of the whole network (M. Ge et al., 2005b) and to from the fixable ambiguities over a maximum set of independent baselines defined in advance (Blewitt, 2008). Both are expected to achieve comparable fixing results. However, there might be too many unfixable ambiguities over some of the pre-defined independent baselines due to poor tracking performance. This could significantly reduce the total number of total fixed ambiguities. Suppose there are three stations A, B, and C and each station tracking four satellites. If selecting the DD-ambiguities over the whole network, all independent DD ambiguity set, which contains five DD ambiguities, can be selected. If independent baselines are first determined, for example A-B and A-C, only four independent DD ambiguities can be selected since the A-4 ambiguity is excluded.

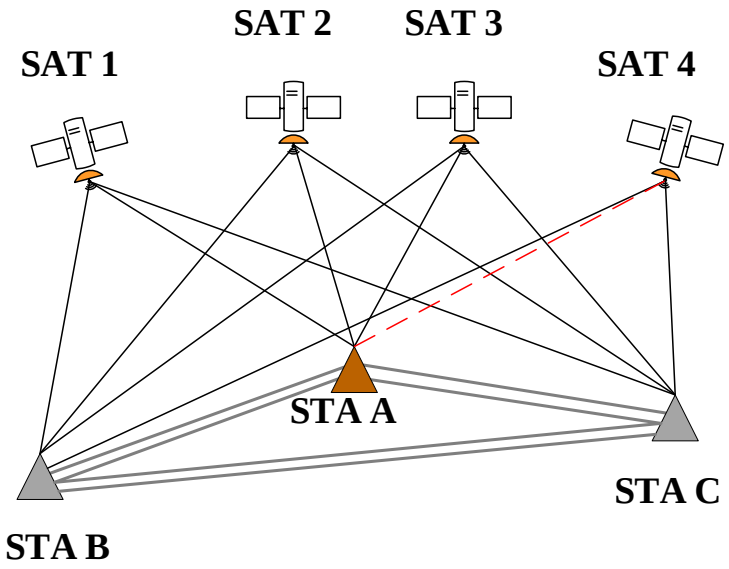

Figure 4.1 A small network with three stations and four satellites. Each satellite is observed by three tracking stations, in which the ambiguity A-4 is assumed biased.

UD IAR is much more robust than DD IAR when facing incorrectly resolved ambiguities. As opposed to UD IAR, some incorrectly resolved DD ambiguities in DD IAR can hardly be identified. The rounding method, rounding to the nearest integer, is commonly applied in a large network and only DD ambiguities close to the integer are selected for fixing, which makes it very difficult to identify wrong fixings. Usually, wrong fixings can be identified by checking the phase observation residuals after applying the fixing constraints. Some of the wrong fixings can still hardly be detected since the outlier DD ambiguities are accommodated smoothly by the cross-connected DD ambiguities in the network. However, in the UD IAR, the bad float

ambiguities have quite different fractional parts to the majority, which are easily identified while estimating UPDs. Obviously, the integer feature of the excluded outlier ambiguities cannot be recovered even after the estimated UPDs are applied and so that they will not be fixed.

When it comes to computation burden of GNSS data processing, applying UD IAR exhibits superior data processing efficiency, especially for massive networks (H. Chen et al., 2014), since upon UD ambiguities are fixed, the carrier phases can be converted to carrier ranges, which removes almost all ambiguity parameters. On the other hand, the step of selecting independent DD ambiguities is time-consuming, especially for massive network with possibly millions of DD ambiguity candidates.

4.1.2 Flowchart of UD IAR

As explained in Section 4.1.1, the performance of UD IAR is highly tied to the accuracy of float ambiguities and the float ambiguities in POD solution are not accurate enough to achieve high-precision UPDs and integer solutions. However, DD IAR can be easily conducted based on float ambiguities. After DD IAR, the ambiguities are accurate enough for UD IAR even though there could be wrong fixings and less fixings. Therefore, the POD processing with UD IAR, as shown in Figure 4.2, includes three steps:

- Ionospheric-free observations are processed to get float POD solution. Through three- or four-times iterations of parameter estimation mainly for data cleaning, the final float solution is achieved.
- Based on float solutions, DD IAR is performed to get DD ambiguity fixed solutions.
- UD IAR is then performed based on the solutions derived from DD IAR. Section 4.2 will further compare the performance of satellite UPDs in the float solution and DD-ambiguity-fixed solution, respectively. Note that the NL UPD is estimated as one value during 24 hours if there is no specific explanation.

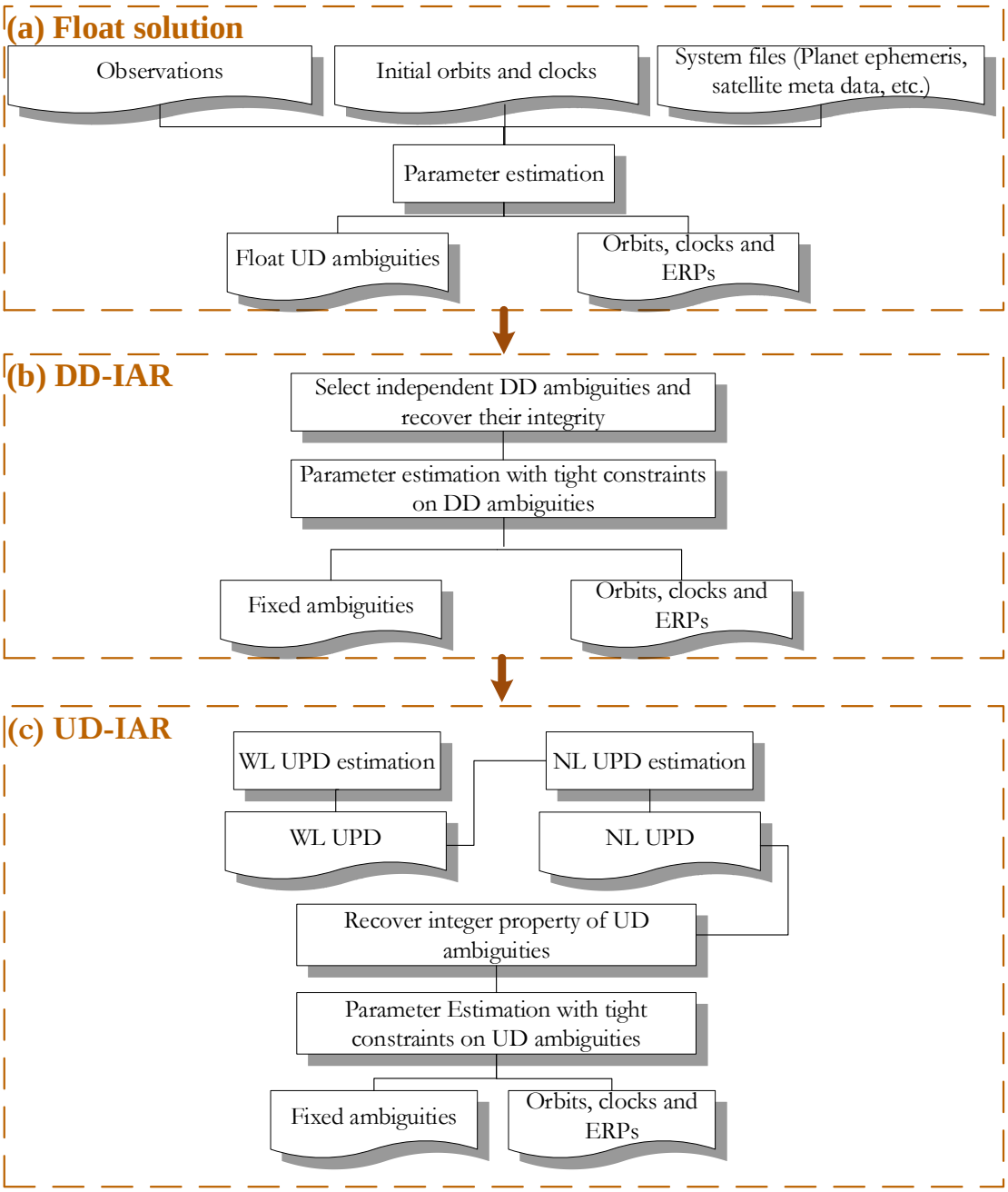

Figure 4.2 Flowchart of precise orbit determination with undifferenced ambiguity fixing.

4.2 Performance of UPD Estimation

Although a number of studies have demonstrated the stability of UD ambiguities in PPP solutions (M. Ge et al., 2007; Li et al., 2017; B. Cui, Li, et al., 2021), the performance of UD ambiguities estimated from POD processing has not been fully investigated. Since WL UPDs are only related to observations, the stability has nothing to do with the estimations, i.e. PPP or POD and will not be discussed here. The NL UPDs are estimated epoch by epoch based on the float and DD IAR solutions and the time-series are shown in Figure 4.3, respectively.

Obviously, the UDPs based on the DD-IAR solution surpass those based on the float solution in terms of stability. For the UPDs based on float solution, the STD values of NL UPD range from 0.04 to 0.2 cycles. The performance of selected UPDs in the left panel conveys that UPDs derived from float solution are not stable enough to be estimated as a constant value. In contrast, the STD values of UPDs derived from the DD IAR solution are less than 0.05 cycles, which is close to the UPD performance in PPP results (Li et al., 2017). The high stability of UPDs in the DD IAR solution demonstrates the feasibility of estimating UPD as one value for the whole session, in this case a session of 24 hours, as well as the realization of UD IAR. The different performances of NL UPDs between different satellites need further investigation in the future.

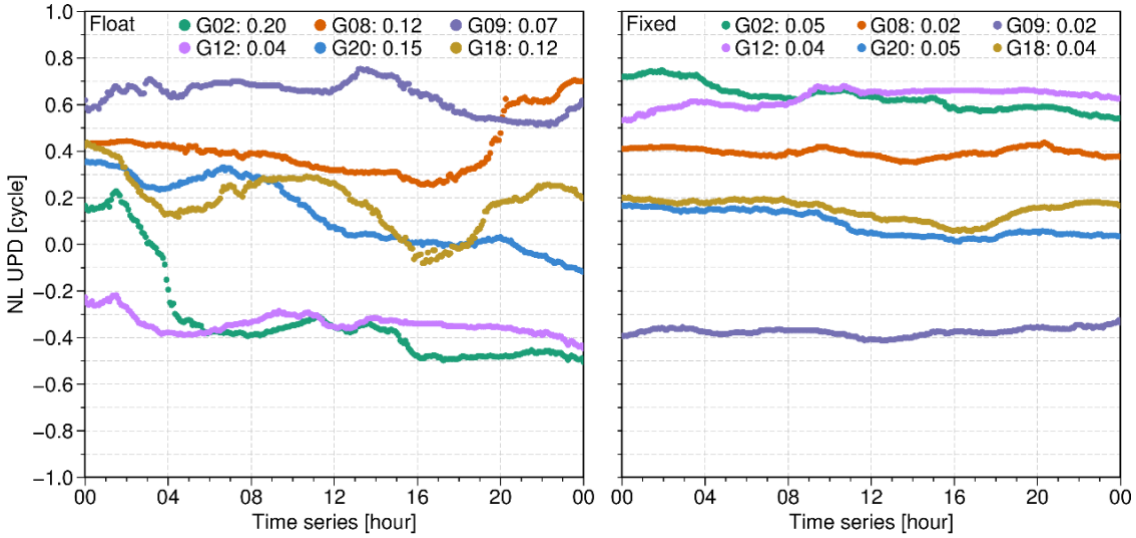

Figure 4.3 Time series of estimated GPS NL UPDs for selected satellites of DOY 001 of 2021. The UPD is estimated per 30 s. The number following each satellite PRN is its STD value. The left panel is the estimated UPDs based on the float solutions and the right panel is that based on DD IAR solution. Different colors represent different satellites.

Figure 4.4 presents the stability of all GPS, Galileo, and BDS-2/3 satellites of DOY 001, 2021. The mean STD value of GPS NL UPDs is less than 0.06 cycles. The maximum STD value is 0.08 cycles. Compared with GPS UPDs, the Galileo NL UPDs show similar performance, with mean STD value of 0.03 cycles. The BDS UPDs show the lowest stability among the three constellations, with an average value of 0.11 and 0.13 cycles for BDS-2 and BDS-3, respectively. None of GEO satellites is considered in the UPD estimation because of poor ambiguity accuracy. The STD values for newly launched BDS-3 satellites, for example, C38 - C46 are larger than 0.2 cycles because they are newly launched in 2021 and fewer observations are available, as shown in Figure 4.5. As expected, the STD values of NL UPDs decrease to 0.07 cycles after removing C38 - C46. The poorer stability of the BDS constellation with respect to GPS and Galileo constellation is possibly related to the imperfect non-conservative force models (Guo et al., 2023).

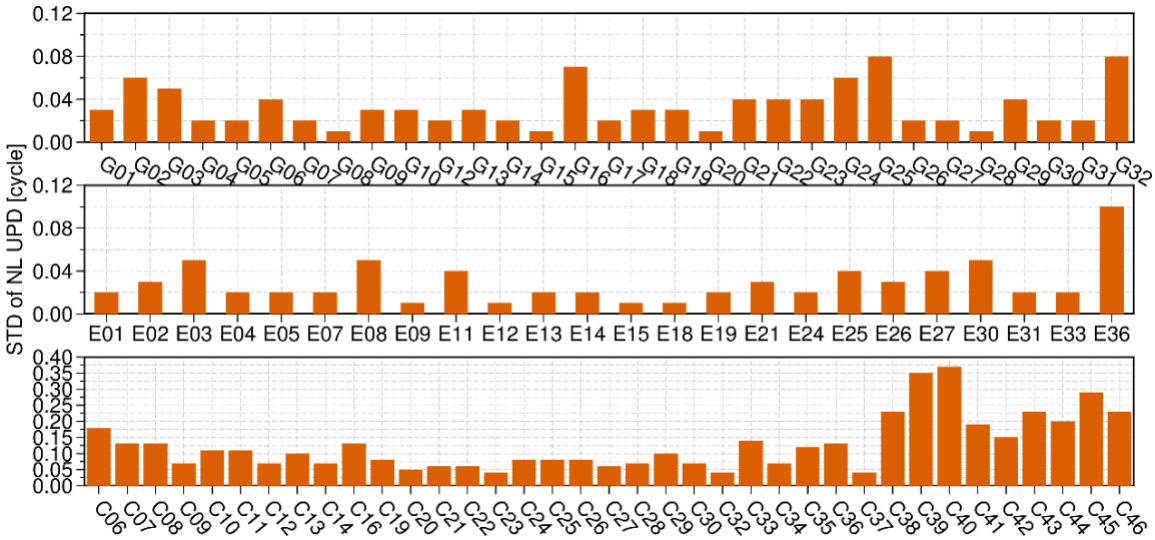

Figure 4.4 The stability of GPS (upper panel), Galileo (middle panel) and BDS (lower panel) constellations in DOY 001, 2021.

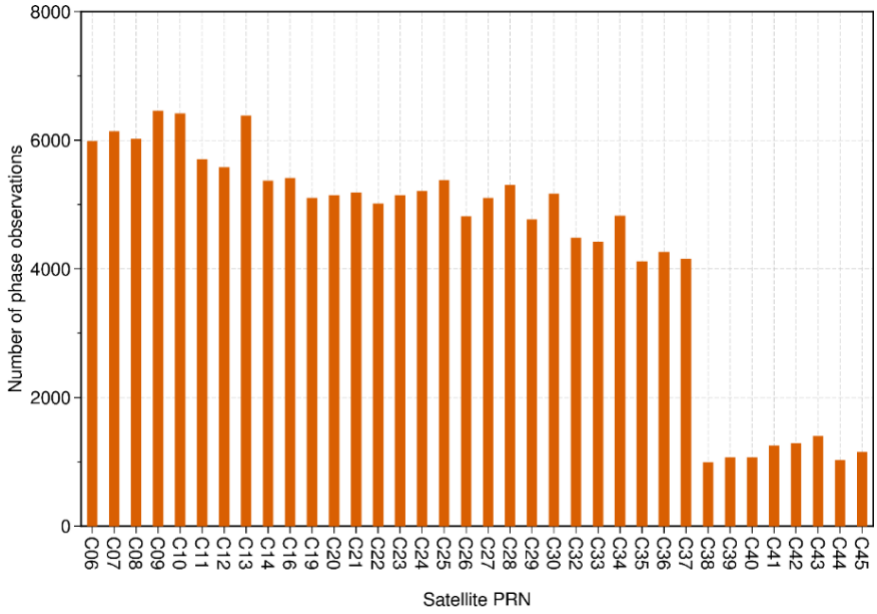

Figure 4.5 Number of total phase observations of the BDS satellites for the whole network. The newly launched satellites have much less observations because many receivers have not updated.

After the separation of both WL and NL UPDs, the ambiguities should be close to integers. The residuals can be expressed by the difference between the float ambiguities after removal of UPDs and the nearest integers, in other words, the fractional parts of the float ambiguities after removal of the estimated UPDs. The histograms of both WL residuals and NL residuals for the three constellations are presented in Figure 4.6, Figure 4.7, and Figure 4.8, respectively. The thresholds, checking whether a UD ambiguity can be fixed, of WL and NL are 0.3 cycles and 0.15 cycles, respectively. For the calculation of the ambiguity-fixing rate, the WL-fixing rate means the ratio between the number of fixed WL ambiguities and the number of all WL

ambiguities, whereas the NL-fixing rate means the ratio between the number of fixed NL ambiguities and the number of all fixable NL ambiguities.

Figure 4.6 shows the histograms of both WL and NL residuals of GPS satellites. For WL ambiguities, 91.6% of the residuals are within ±0.15 cycles, while 98.3% of residuals are within ±0.3 cycles. For NL ambiguities, the percentages of residuals within ±0.10 cycles and ±0.15 cycles are 90.5% and 94.6%, respectively. The average values of WL and NL residuals are both 0, and the STD values are 0.09 (for WL) and 0.08 (for NL) cycles, which indicates that the NL residuals have a slightly better distribution more concentrated around the zero than that of WL.

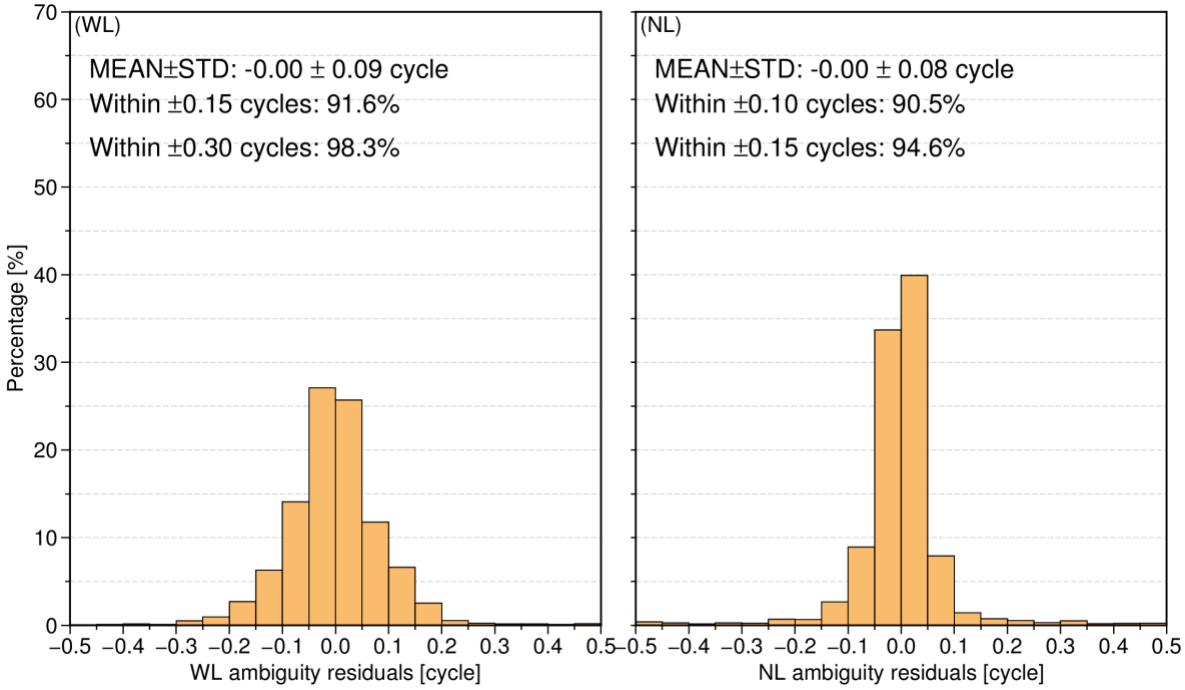

Figure 4.6 Residual distributions of the GPS WL (left panel) fractional parts (in cycles) and NL (right panel) fractional parts (in cycles) after UPD correction.

Figure 4.7 shows the histograms of both WL and NL residuals of the Galileo. The percentages of WL ambiguity residuals within ±0.15 and ±0.30 cycles are 94.7% and 98.4%, respectively. For NL ambiguities, the percentages of residuals within ±0.10 cycles and ±0.15 cycles are 97.3% and 100.0%, respectively. The STD values of WL and NL residuals are 0.08 and 0.04 cycles for WL and NL ambiguities, respectively. Both the WL and NL ambiguity residuals of Galileo perform better than those of GPS in Figure 4.6, especially for NL ambiguities. The better NL ambiguity results are possibly related to the published attitude control model and satellite metadata (GSA, 2017).

Figure 4.8 shows the histograms of both WL and NL residuals of the BDS. For WL ambiguities, 91.0% of the residuals are within ±0.15 cycles, while 97.9%, of residuals are within ±0.30 cycles. For NL ambiguities, the percentages of residuals within ±0.10 cycles and ±0.15 cycles are 84.4% and 100.0%, respectively. Compared with results derived from GPS

and Galileo, the NL ambiguity residuals within ± 0.10 cycles for BDS show the lowest percentage.

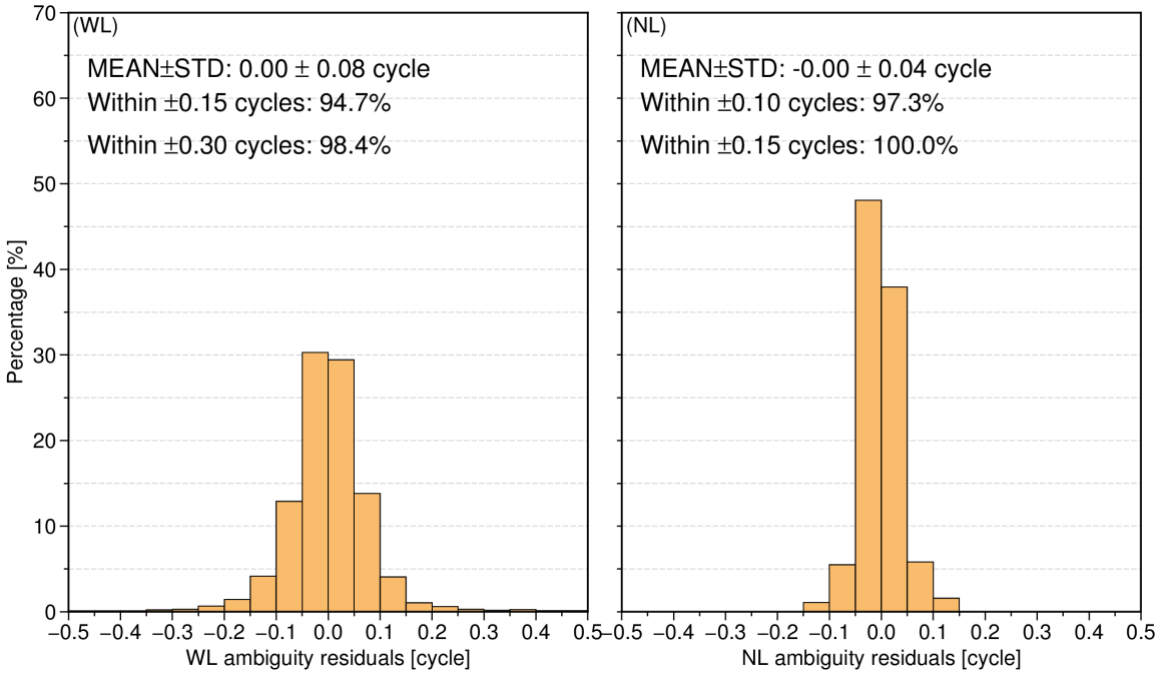

Figure 4.7 Residual distributions of the Galileo WL (left panel) fractional parts (in cycles) and NL (right panel) fractional parts (in cycles) after UPD correction.

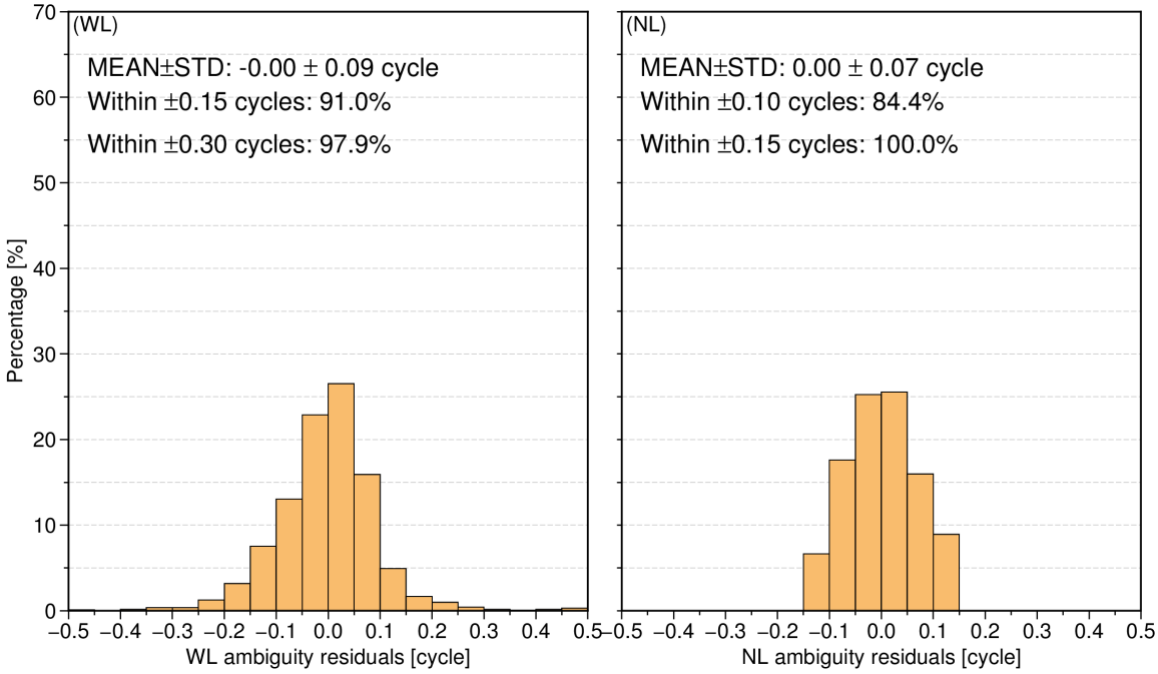

Figure 4.8 Residual distributions of the BDS WL (left panel) fractional parts (in cycles) and NL (right panel) fractional parts (in cycles) after UPD correction. Note that BDS GEO satellites are excluded and satellite-induced biases of BDS-2 are corrected before WL computation.

4.3 Impacts of UD IAR on satellite orbits

Figure 4.9 shows the average 1D RMS values of daily DBDs in along, cross, and radial components for each GPS satellite. The satellites experiencing outages according to NANU messages were not considered in the statistics, which is also suitable for the following GLONASS, Galileo, and BDS. The left panel of Figure 4.9 illustrates that the UD IAR strategy has a notable improvement in three directions, especially for the along direction. Compared with DD IAR results, the orbit derived from UD IAR is improved by 17.0%, 11.0%, and 4.0% in the along, cross, and radial components respectively. The 95th percentile of orbit precision for the DD IAR is 48.0 mm, while for UD IAR is only 40.8 mm, as shown in the right panel of Figure 4.9. In addition to the indicator of DBD, the orbit differences of average 1D RMS values between UD IAR and DD IAR with respect to IGS final products are less than 2 mm, which is not shown here. This is because the IGS final products are generated by IGS ACs are generated by DD IAR strategies.

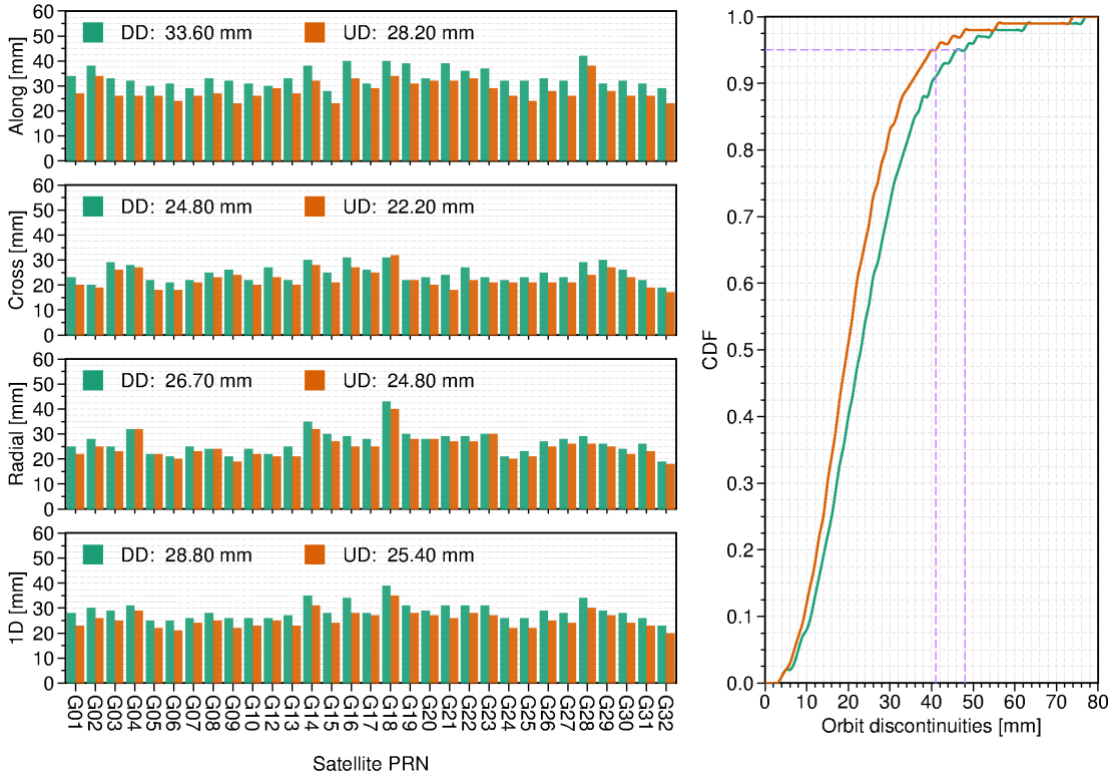

Figure 4.9 Day boundary discontinuities (DBD) for GPS orbits. Left panel is the average RMS values while right panel is the cumulative distribution function (CDF) of 1D RMS values for all GPS satellites. The pink dash-lines stand for 95th percentile.

Figure 4.10 shows the average RMS values of daily DBDs in along, cross, and radial component, and 1D for each Galileo satellite. Compared with DD IAR results, the average RMS values of UD IAR decrease from 40.4, 26.0 and 39.1 to 33.5 mm, 22.6 and 37.7 mm in the along, cross, and radial components, respectively, as shown in the left panel of Figure 4.10. The 95th percentile of orbit precision for the DD IAR is 64.0 mm, while for UD IAR is only 58.0 mm, as shown in the right panel of Figure 4.10.

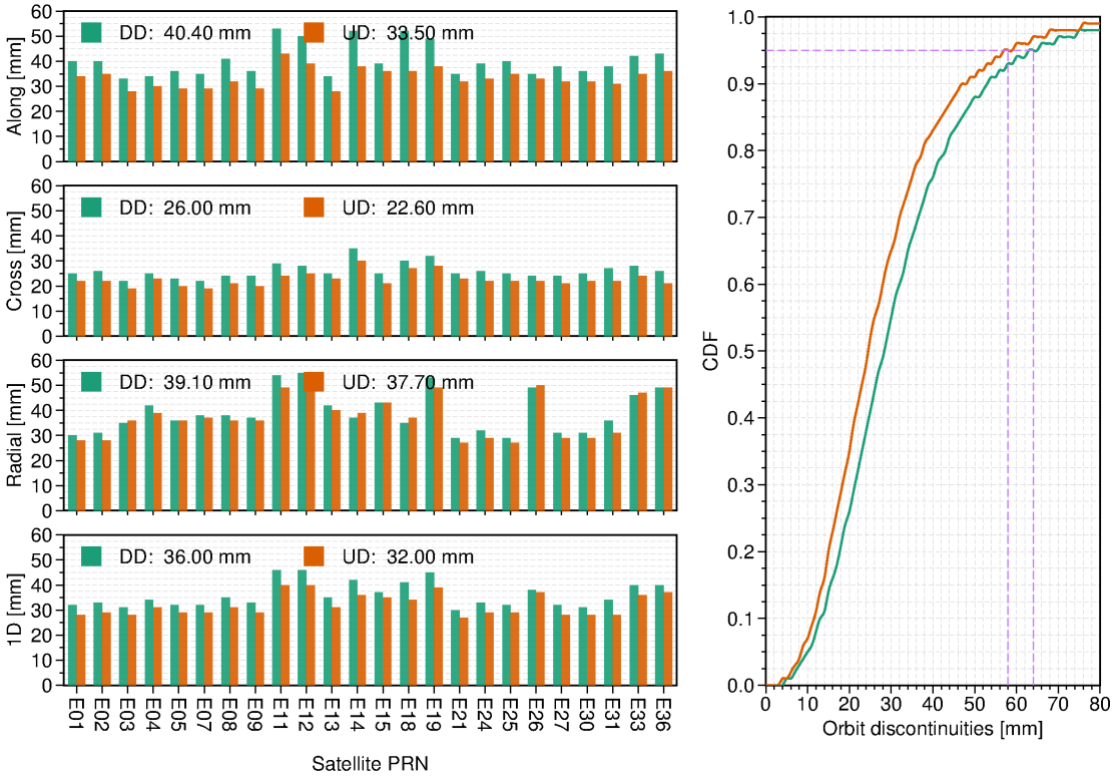

Figure 4.10 Day boundary discontinuities for Galileo orbits. Left panel is the average RMS values while right panel is the cumulative distribution function (CDF) of 1D RMS values for all Galileo satellites. The pink dash-lines stand for 95th percentile.

Figure 4.11 shows the average RMS values of daily DBDs in the along, cross, and radial components and 1D for each BDS MEO satellite. Compared with DD IAR results, the orbit derived from DD IAR is improved by 21.7% and 10.4% in the along and cross component respectively, whereas no improvement is observed in the radial component, as shown in the left panel of Figure 4.11. A noticeable correlation between DBD and the available tracking data can be identified. For satellites C19–C25 tracked by most stations, the best orbit accuracy is achieved, followed by C26–C37. The orbits of C38–C45 show the worst performance due to the fewest data available for analysis. As expected, the largest errors of up to about 172.0 mm (C43) are in along component, whereas the cross and radial orbit components show the best consistency. As shown in the right panel of Figure 4.11, the 95th percentile of orbit precision for the DD IAR and UD IAR are both larger than 120 mm.

Figure 4.12 shows the average RMS values of daily DBDs in along, cross, and radial components and 1D for each BDS GEO and IGSO satellite. For BDS GEO satellites, they show a similar performance between DD IAR and UD IAR since their difference of average 1D RMS values is only 1.6%. For BDS IGSO satellites, the UD IAR solution is slightly worse than the DD IAR solution. Due to lower orbit accuracy with an average 1D RMS value larger than 100.0 mm, poorer ambiguity parameters may be achieved and hence they may easily be fixed to wrong values resulting in a fixed solution of lower quality.

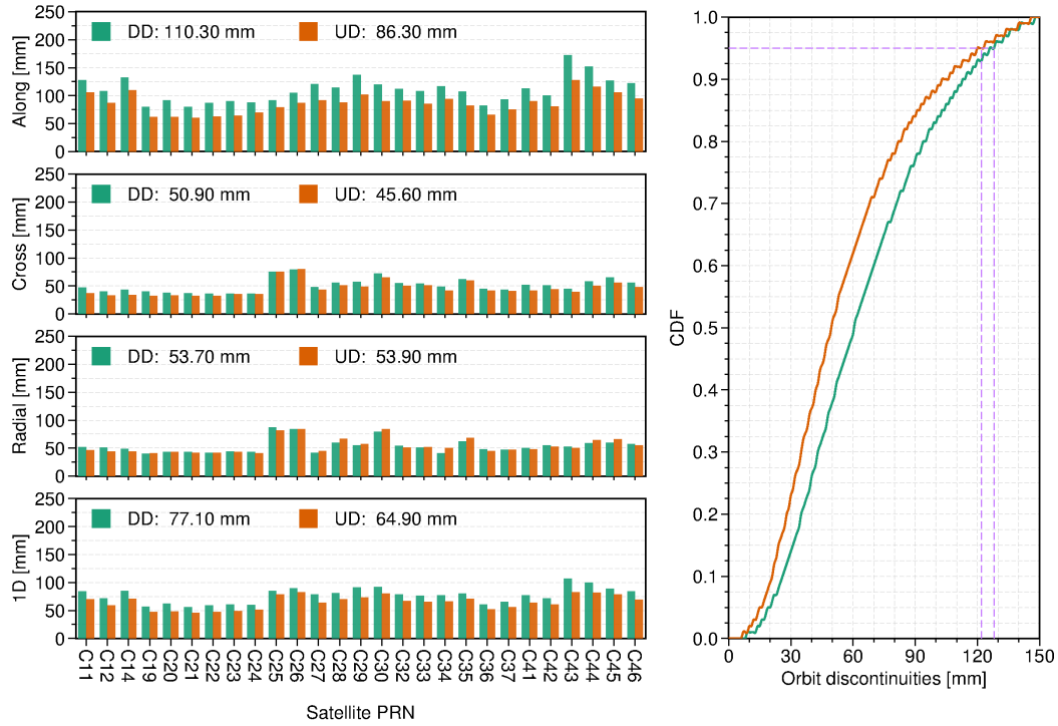

Figure 4.11 Day boundary discontinuities for BDS MEO orbits. Left panel is the average RMS values while right panel is the cumulative distribution function (CDF) of 1D RMS values for all BDS satellites. The pink dash-lines stand for 95th percentile.

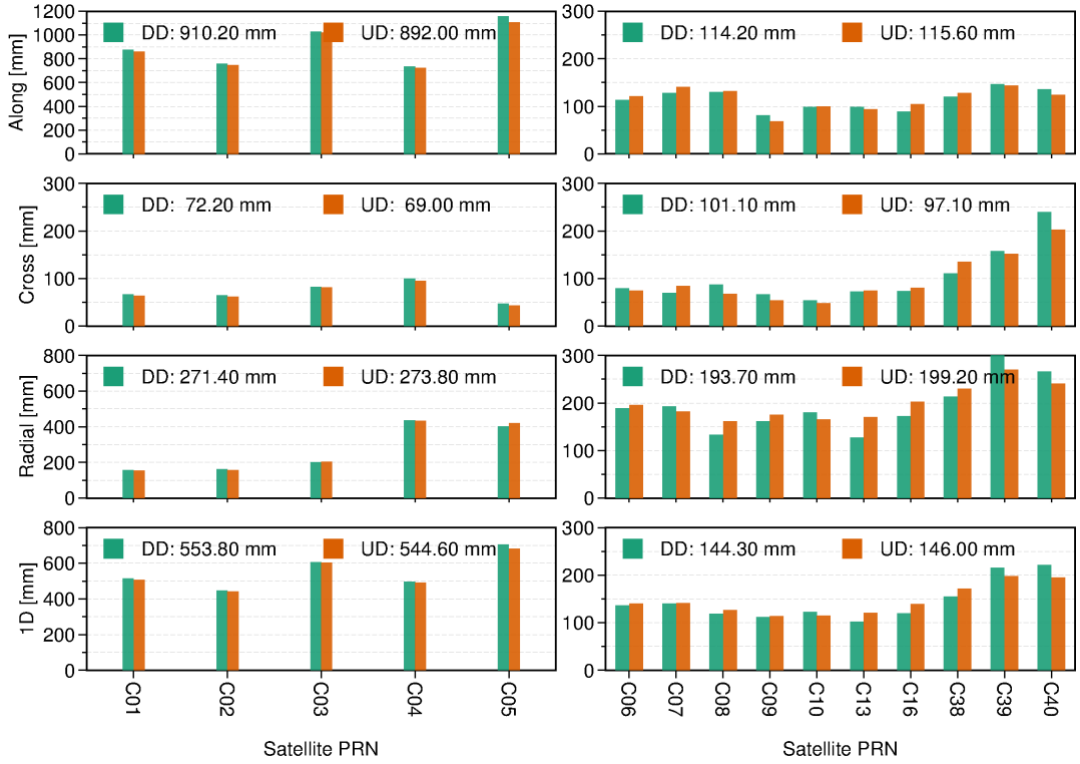

Figure 4.12 Day boundary discontinuities for BDS GEO and IGSO orbits. Left panel is the average RMS values of GEO orbits while the right panel is the average RMS values of IGSO orbits. Note that BDS GEO are excluded in IAR.

We expect that UD IAR ambiguity fixing can also improve the orbits of those satellites which are excluded in the ambiguity fixing like BDS GEO satellites and GLONASS satellites. The results of BDS GEO shown in Figure 4.12 preliminarily demonstrate that ambiguity fixing brings almost no improvements on their orbits. Further analysis of the accuracy of GLONASS satellite orbits in Figure 4.13 illustrates the differences in DD and UD IAR is negligible with a maximum value of 2.1% in the cross component.

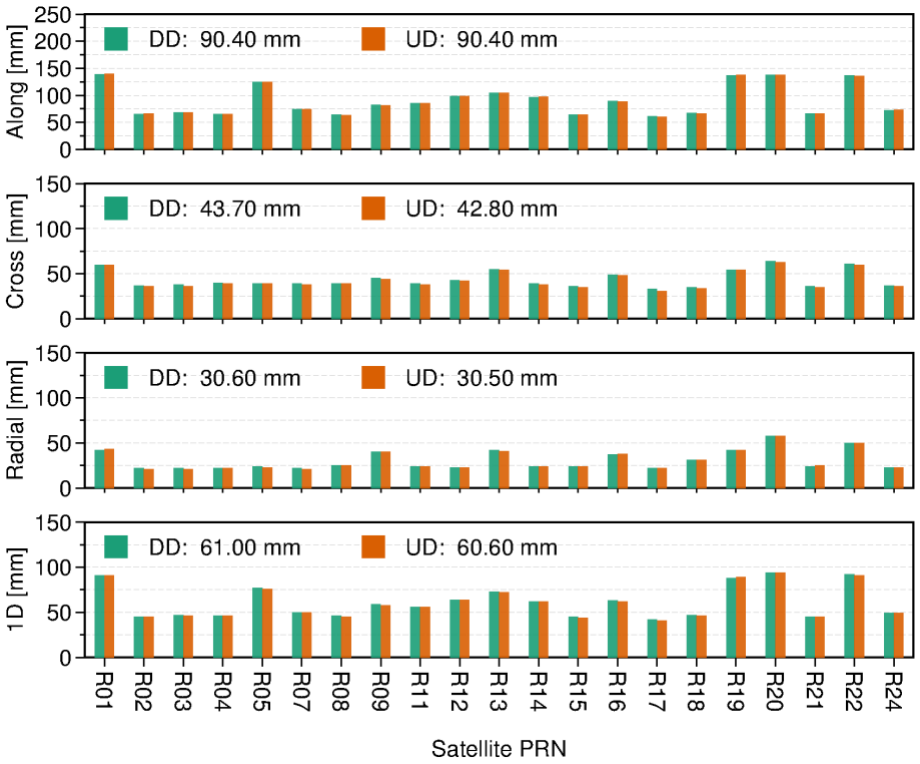

Figure 4.13 Day boundary discontinuities for GLOANSS orbits.

4.4 Impacts of UD IAR on global geodetic parameters

The impact of UD IAR on the parameters of ERPs, station coordinates, and GCC besides satellite orbits is further investigated in this section. For station coordinates and GCC, the weekly coordinate repeatability is used as an indicator of the quality of the station coordinates and GCC, respectively. A seven-day moving STD, taking the STD of last seven days, is performed. With a seven-day sliding window, most of the long-term signals are got rid of.

4.4.1 ERP

The statistics of the ERP parameters with respect to the IGS Final ERP products are shown in Figure 4.14 for the solutions of UD and DD IAR for comparison. From the aspects of MEAN and STD values, UD-IAR lowers both the system bias and noise in terms of the PM offsets and PM rates at the same time, except for the MEAN values of y-pole offset which is already very close to zero. Compared to DD-IAR, the STD values of x-pole, y-pole, x-pole

rate y-pole rate, and LOD is reduced by 21.6%, 18.5%, 19.0%, 8.7%, and 12.2%, respectively. The RMS values for x- and y-pole offset are decreased to 20.2 μas and 16.7 μas respectively, for x- and y-pole rates are decreased to 87.0 $\mu as/day$ and 111.0 $\mu as/day$ respectively, for LOD are decreased to 13.3 $\mu s/day$.

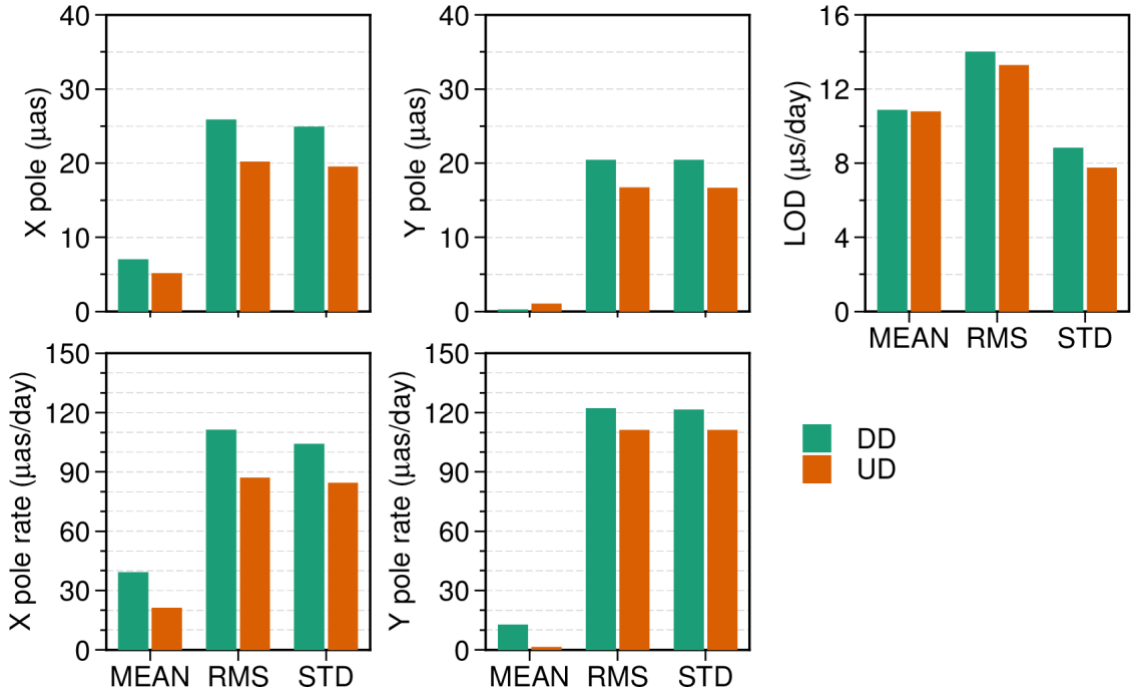

Figure 4.14 Statistics of earth rotation parameters of the UD and DD IAR with IGS final products. Note that the absolute mean values are presented.

Figure 4.15 shows the statistics of the ERP parameters concerning IERS-14-C04. Apparently, no matter system bias or noise, UD-IAR shows better consistency. Regarding the average RMS value, the PM offsets are improved by 11.1% (reduced from 89.5 μas to 79.5 μas) on the x-pole and 9.5% (reduced from 79.3 μas to 71.8 μas) on the y-pole. The PM rates are also improved by 8.0% (reduced from 187.9 $\mu as/day$ to 172.8 $\mu as/day$) and 9.2% (reduced from 164.6 $\mu as/day$ to 149.4 $\mu as/day$). Although the LOD component does not show significant improvements, as the RMS value reduction is only 2.1%, its formal error shows about 10% improvement, which is not shown here.

In addition to the comparison with the IGS final product and IERS-14-C04, the DBD of PM shown in Figure 4.16 can be further investigated to indicate the internal precision. Similar to the previous results, UD IAR outperforms DD IAR. On average, the RMS value is reduced by 16% for the x-pole (from 162.7 μas to 136.4 μas) and 6.8% for the y-pole (from 131.1 μas to 122.2 μas).

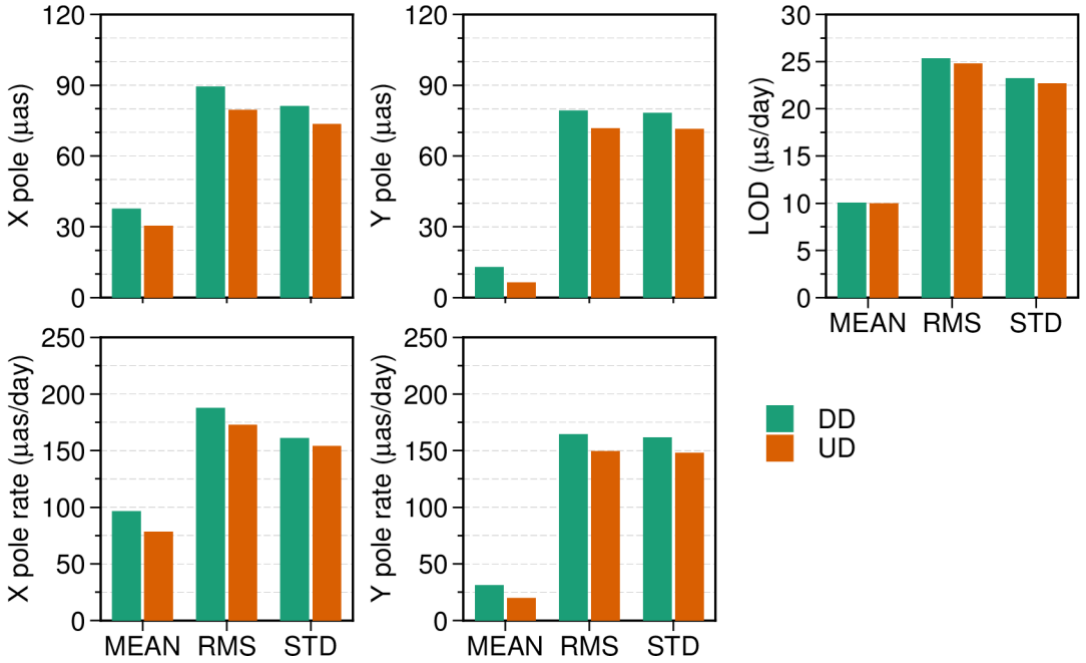

Figure 4.15 Statistics of earth rotation parameters compared with IERS 14 C04. Note that the absolute mean values are presented.

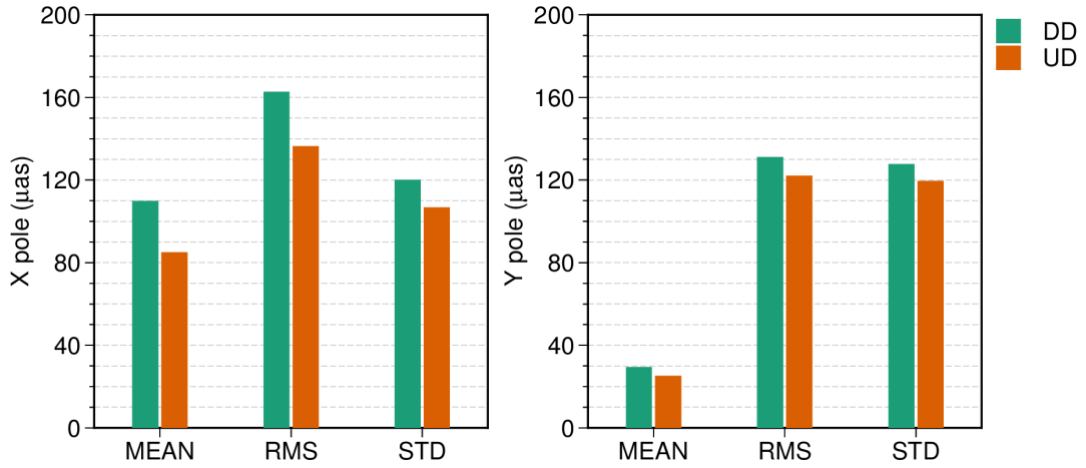

Figure 4.16 Statistics of day boundary discontinuities for polar motion. Note that the absolute mean values are presented.

4.4.2 Station coordinates

Figure 4.17 illustrates the distribution of station coordinate repeatability. The differences between DD IAR and UD IAR are minor from the average RMS values which are reduced by UD IAR by 3.6%, 1.5%, and 1.2% for the east, north, and up components, respectively. Figure 4.18 shows the geographical distribution of the east repeatability differences between UD IAR and DD IAR. It can be found that most stations with larger repeatability improvement (solid dots in blue and cyan) which can reach up to 0.4 mm are located in oceanic or remote areas with a sparse station distribution. By checking daily station coordinates and ambiguity-fixing results, it is found that, for a selected station, a large position difference will occur if the number of

fixable DD ambiguities is too low. In a sparse network, it is usually more difficult to resolve DD ambiguities, which is probably because the fractional parts over long baselines are not consistent. In contrast, the repeatability differences for regions with dense stations, for example in Europe, are normally well below 0.2 mm.

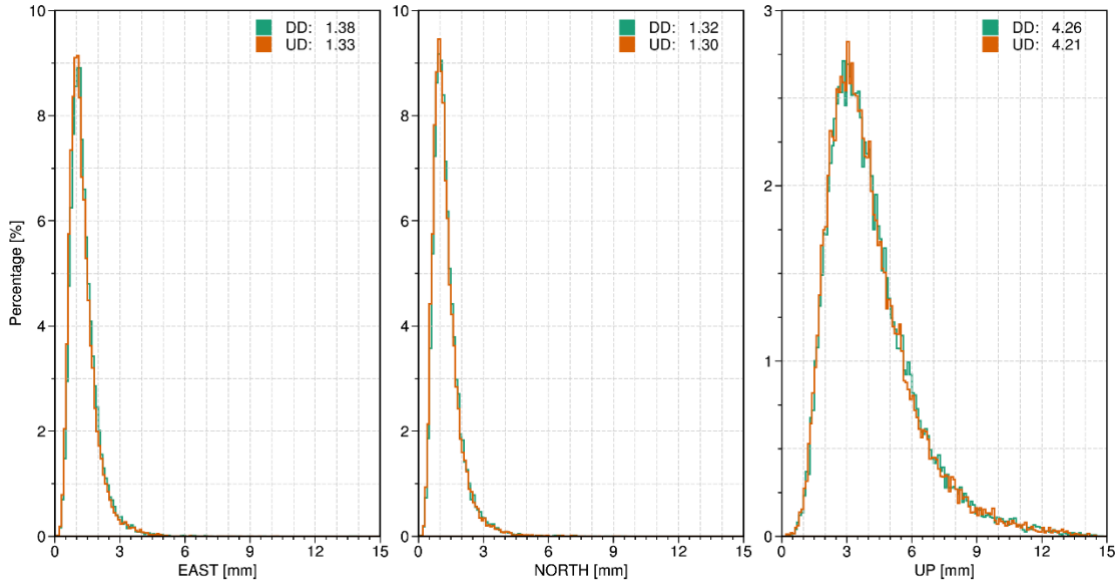

Figure 4.17 Distribution of station coordinate repeatability in the east, north and up component.

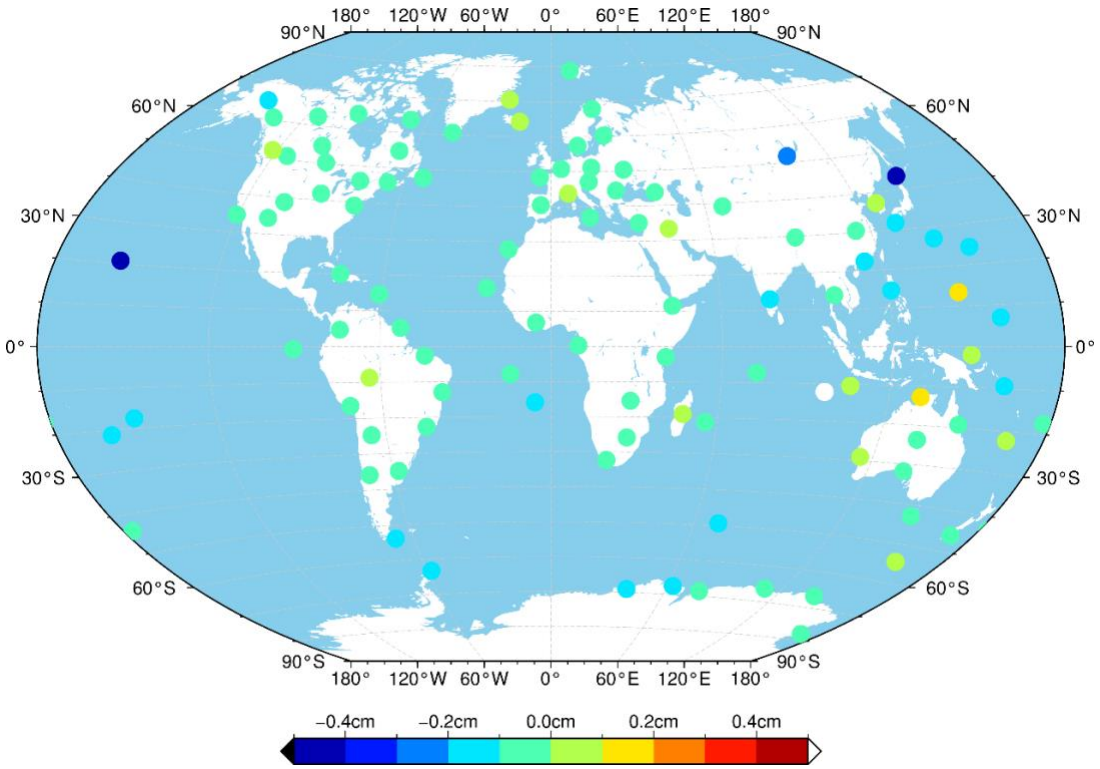

Figure 4.18 Geographical distribution of the repeatability differences of the east station component between UD and DD IAR. A negative difference means the UD IAR solution is better than the DD one.

4.4.3 Geocenter coordinates

As the ambiguity fixing rate also has a significant impact on the observability for GCC (Kuang et al., 2015), the weekly GCC repeatability is also checked in the same way as done for station coordinates. Figure 4.19 shows the mean repeatability for each GCC component. The GCC results derived from UD-IAR suffer from noise, the reduction of the average RMS values is hardly visible with 3.1%, 1.7%, and 1.0% for the X, Y, and Z components, respectively.

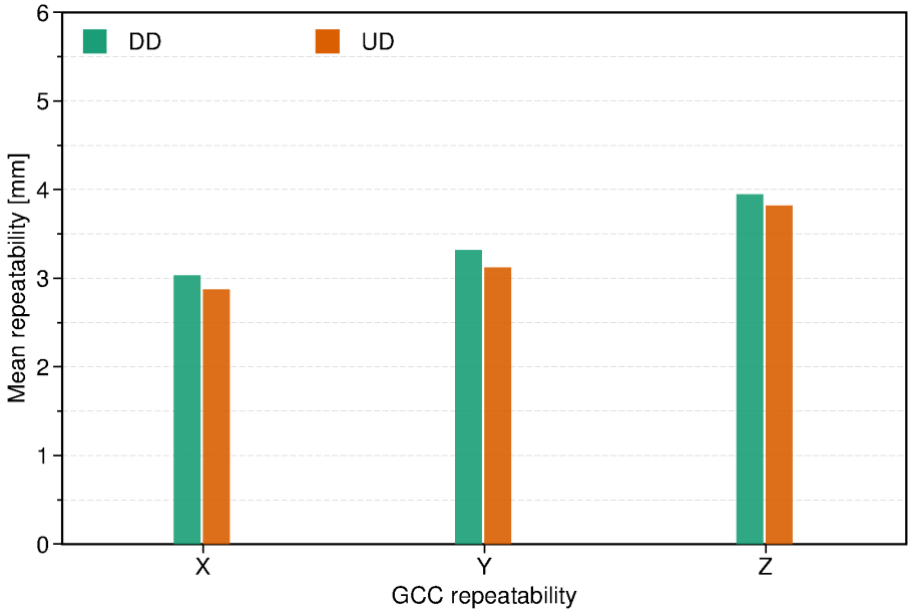

Figure 4.19 Mean repeatability of geocenter coordinates of the UD and DD IAR solutions.

4.5 Investigation on the difference of DD and UD IAR

In Sections 4.3 and 4.4, It is found that the results derived from UD IAR perform better than those of the DD IAR, especially for satellite orbits. As is mentioned in Section 4.1.1, a comparable result should be observed with two IAR strategies theoretically. To investigate the possible reasons, a comprehensive data analysis with ten different solutions which are described in Section 4.5.1 is carried out for GPS observations. Two possible factors causing orbit disparities between DD IAR and UD IAR are identified in this study, i.e. inappropriate selection of fixed DD ambiguities and possible wrong fixings. This section is arranged as follows. The overview of orbit results based on commonly used IAR strategies is then given in Section 4.5.2. Subsequently, the impact of incorrect DD ambiguities and insufficient independent DD ambiguities are discussed in Sections 4.5.3 and 4.5.4, respectively. Similar to Section 4.4, the impacts of the two factors on global geodetic parameters are also discussed in Section 4.5.5. However, in Section 4.5.3 and 4.5.4, orbits derived from the UD IAR solution serve as a reference to investigate orbit differences under various DD IAR strategies. In this investigation external orbit products, for example, the IGS combined orbits are not employed, because they are mainly based on solutions by IGS ACs generated using DD IAR strategy.

4.5.1 Data processing scenarios

Based on the processing strategies described in Section 4.1.2, ten different IAR strategies are chosen, as shown in Figure 4.20. The outlier DD ambiguities can be figured out according to list of unfixable UD ambiguities in the UD IAR solution (UD_std). After removing outlier DD ambiguities, different DD IAR strategies can be performed again. More details of different IAR strategies are listed in Table 2.3.

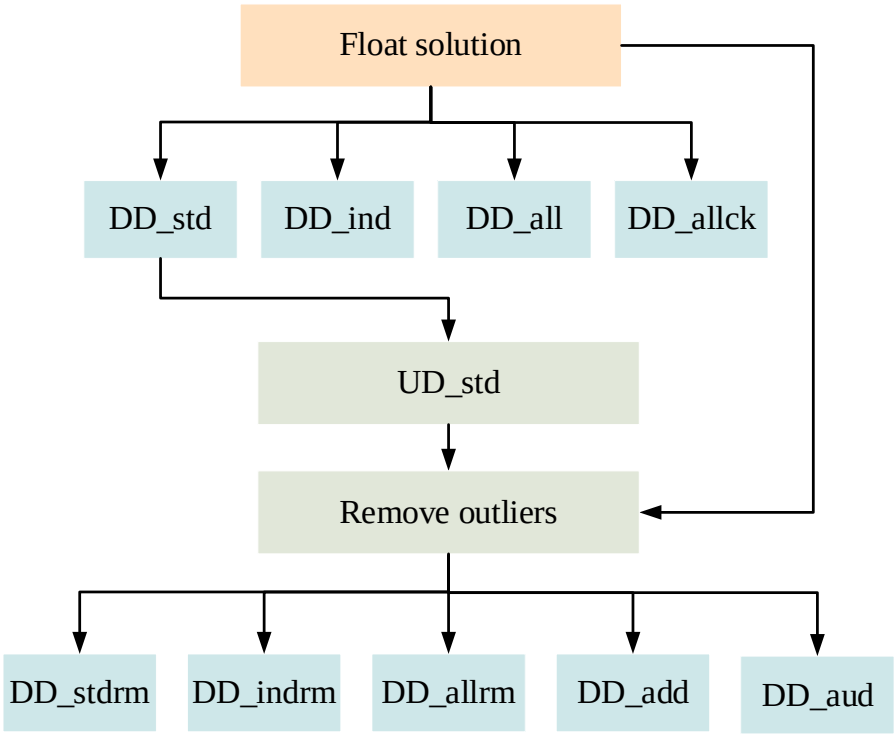

Figure 4.20 Flowchart for different processing strategies, including four DD IAR (i.e., DD_std, DD_ind, DD_all, and DD_allck), one UD IAR (i.e., UD_std) and five DD IAR based on UD IAR (i.e., DD_stdrm, DD_indrm, DD_allrm, DD_add, and DD_aud).

Two groups of DD IAR strategies are designed mainly for investigating the impact of wrong fixing and missing enough independent DD ambiguity constraints. The first group as listed in Table 4.1 includes four different strategies, i.e., DD_std, DD_ind, and DD_all which are utilized by IGS ACs in their operational data processing. The second group of DD IAR consists of DD_stdrm, DD_indrm, DD_allrm, DD_add, and DD_aud, in which all unfixable UD ambiguities have already been removed based on the result of UD-IAR. In this way, any possible wrong fixing can be avoided, so the impact of different strategies for selecting fixable DD ambiguities can be quantified. The UD IAR group comprises only one strategy namely UD_std.

Among the first DD-IAR group, the difference between DD_std and DD_ind lies in the way of picking independent DD ambiguities, namely, to select the independent ones from a pre-defined maximum independent baseline set and from all baselines, respectively, while DD_all selects all fixable DD ambiguities no matter they are independent or not. In the DD_allck

solution, a quality control strategy based on phase residuals is performed. Specifically, if the RMS of phase residuals corresponding to one pair of fixed ambiguities increases significantly after applying the fixing constraints, the constraint is considered as inappropriate, i.e., wrong-fixing, and removed. If the same quality control strategy on DD_std and DD_ind are applied, the excluded independent DD ambiguities need to be compensated with new independent DD ambiguities; otherwise, the two strategies will face the situation of lacking independent DD ambiguities. Therefore, this quality control strategy is only applied on DD_all to check whether all the outliers can be sifted.

Table 4.1 Description of 10 different IAR strategies.

Group	Strategy	Description
DD IAR	DD_std	Pick independent DD ambiguities from an subset consisting of the maximum number of independent baselines (Blewitt, 2008)
	DD_ind	Pick independent DD ambiguities for each baseline and then across the entire network. Independent DD ambiguities are then picked across the entire network by Gram–Schmidt (Cohen, 1993; M. Ge et al., 2005b)
	DD_all	Pick all DD ambiguities across the entire network
	DD_allck	The same as DD_all, but unfixable DD ambiguities are excluded by checking observation residuals
UD IAR	UD_std	Pick all fixable UD ambiguities
DD IAR based on UD IAR	DD_stdrm	The same as DD_std, but incorrect UD ambiguities are identified via UD-IAR and excluded before forming DD ambiguities.
	DD_indrm	The same as DD_ind, but incorrect UD ambiguities are identified via UD-IAR and excluded before forming DD ambiguities
	DD_allrm	The same as DD_all, but incorrect UD ambiguities are identified via UD-IAR and excluded before forming DD ambiguities
	DD_add	The same as DD_stdrm, but independent fixed DD ambiguities from the whole network are added
	DD_aud	The same as DD_stdrm, but independent fixed UD ambiguities derived from the UD_std solution are added

The last group, consists of DD_stdrm, DD_indrm, DD_allrm, DD_add, and DD_aud. In all the five strategies unfixable UD ambiguities have already been removed with the assistance of UD-IAR. In the above, the DD ambiguities containing unfixable ambiguities will be omitted while selecting independent DD ambiguities. This strategy can avoid the side effects of any possible wrong-fixing. The first three are the same as the corresponding ones in the first group except excluding the unfixable UD ambiguities. The comparison of the corresponding strategies of the two groups will reveal the impact of wrong fixings. The last two strategies in this group, i.e., DD_add and DD_aud, are designed for assessment of the impact of missing fixable independent DD ambiguities. The DD_add strategy is based on the DD_stdrm and supplements all independent fixable DD ambiguities until no further could be introduced or the maximum number of independent DD ambiguities is reached. Similarly, the DD-aud is based on DD-indrm but fixable UD ambiguities for UD_std are further selected to form the maximum independent fixable ambiguities (including both UD and DD ambiguities).

4.5.2 Orbit accuracy of DD and UD IAR

The orbit accuracy of the three representative DD IAR strategies (DD_std, DD_ind and DD_all) and one UD IAR strategy (UD_std) are firstly compared to take an overview of the

differences among DD IAR and UD IAR. Moreover, The DD IAR solution with quality control (DD_allck) is also considered for comparison. Table 4.2 presents DBDs of DD_std, DD_ind, DD_all, DD_allck and UD_std solution. From the table, the UD-std solution outperforms the other four DD IAR solutions. Among four DD IAR strategies, the DD_std solutions show the maximum differences with respect to that of the UD_std, reaching 7.2, 3.4, and 3.5 mm for the along, cross, and radial components, respectively. Conversely, the differences between the DD_ind, DD_all and DD_allck solutions are marginal, with a difference in the average 1D root mean square (RMS) of orbit less than 0.4 mm. In comparison to the DD-std solution, the DD_ind solution shows about 12% improvement in DBD for the average 1D RMS, indicating the importance of proper implementation of DD ambiguity fixing.

Table 4.2 Day boundary discontinuities of GPS satellite orbits for five different IAR strategies. Unit is mm.

Direction	UD_std	DD_std	DD_ind	DD_all	DD_allck
Along	24.8	32.0	26.5	26.5	26.3
Cross	22.1	25.5	22.9	22.8	22.8
Radial	22.5	26.0	23.0	24.7	24.5
1D	23.3	28.1	24.3	24.9	24.7

4.5.3 Impacts of wrong fixings

Figure 4.21 shows orbit DBDs for the DD_stdrm, DD_indrm and DD_allrm solutions, in which all incorrect UD ambiguities are excluded before forming DD ambiguities to avoid possible incorrectly fixed DD ambiguities. Note that this approach based on UD IAR result is usually not feasible in operational DD IAR processing. Excluding unfixable UD ambiguities improves the orbit accuracy of all three DD IAR strategies, especially for the along and radial components and the average 1D RMS value decreases by 1.1, 1.6 and 0.7 mm in the DD_stdrm, DD_indrm and DD_allrm solutions, respectively. Among the three DD IAR strategies, the DD_indrm and DD_allrm solutions are comparable to each other and both are close to the UD_std solution. The DBD differences between the DD_indrm and UD_std solutions are insignificant, i.e., 0.8, 0.3, and 0.1 mm for the along, cross, and radial components, respectively. In contrast, the differences between DD_stdrm and UD_std are still noticeable, about 4.0 mm for the mean average 1D RMS value. This discrepancy confirms that wrong-fixing of DD ambiguities is not the only factor.

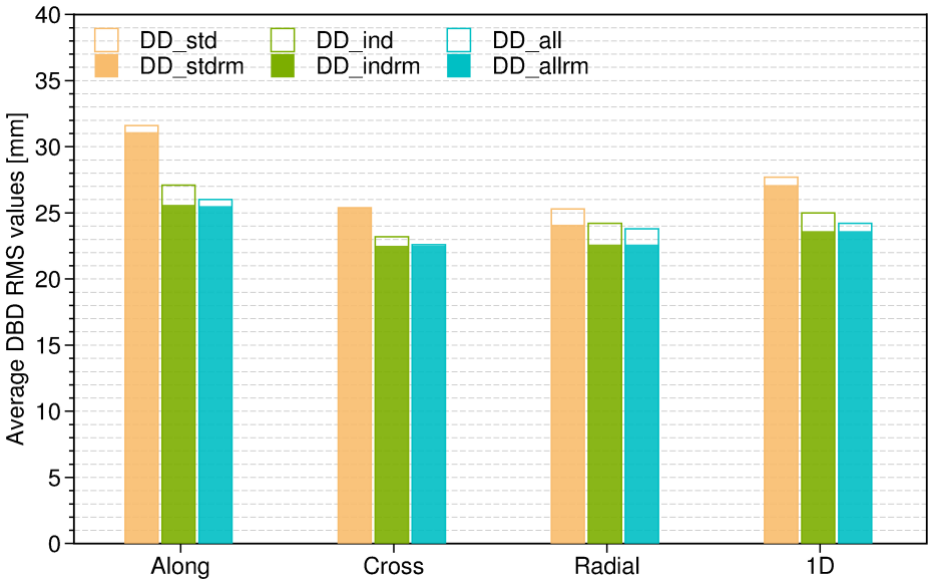

Figure 4.21 Day boundary discontinuities of satellite orbits for the DD_std, DD_ind, and DD_all solutions (all in hollow bars) without wrong-fixing detection; DD_stdrm, DD_indrm and DD_allrm solutions (all in solid bars) excluding wrong-fixing based on UD IAR solution. Note that the DBD in cross component of DD_std is same as that of DD_stdrm, and thus the two bars are overlapped.

Since the DD_all solution includes all fixable DD ambiguities, this solution is selected for a comprehensive assessment in terms of the impact of wrong-fixings on DD IAR solutions without having to worry about the possibility of lacking enough independent DD ambiguities. Figure 4.22 presents orbit differences of the DD_all, DD_allck and DD_allrm solutions with respect to the UD_std solution in three directions. The DD_all solution has the largest STD of orbit differences, which are 4.9, 3.3 and 2.4 mm for the along, cross, and radial components, respectively. Compared to the DD_all solution, the improvement of the DD_allck solution is around 1.0 mm in three components. Among the three solutions, the DD_allrm solution performs the best. Specifically, the percentage of orbit differences within ± 1 mm are increased from 54.8% to 85.2% for the along component, from 57.1% to 87.3% for the cross component and from 76.0% to 93.4% for the radial component. The difference beyond ± 10 mm for the along component is also decreased from 3.1% to 1.0%. The clock result (not shown here) is consistent with that of orbits, showing the most significant advantages of DD_allrm over DD-all and DD_allck.

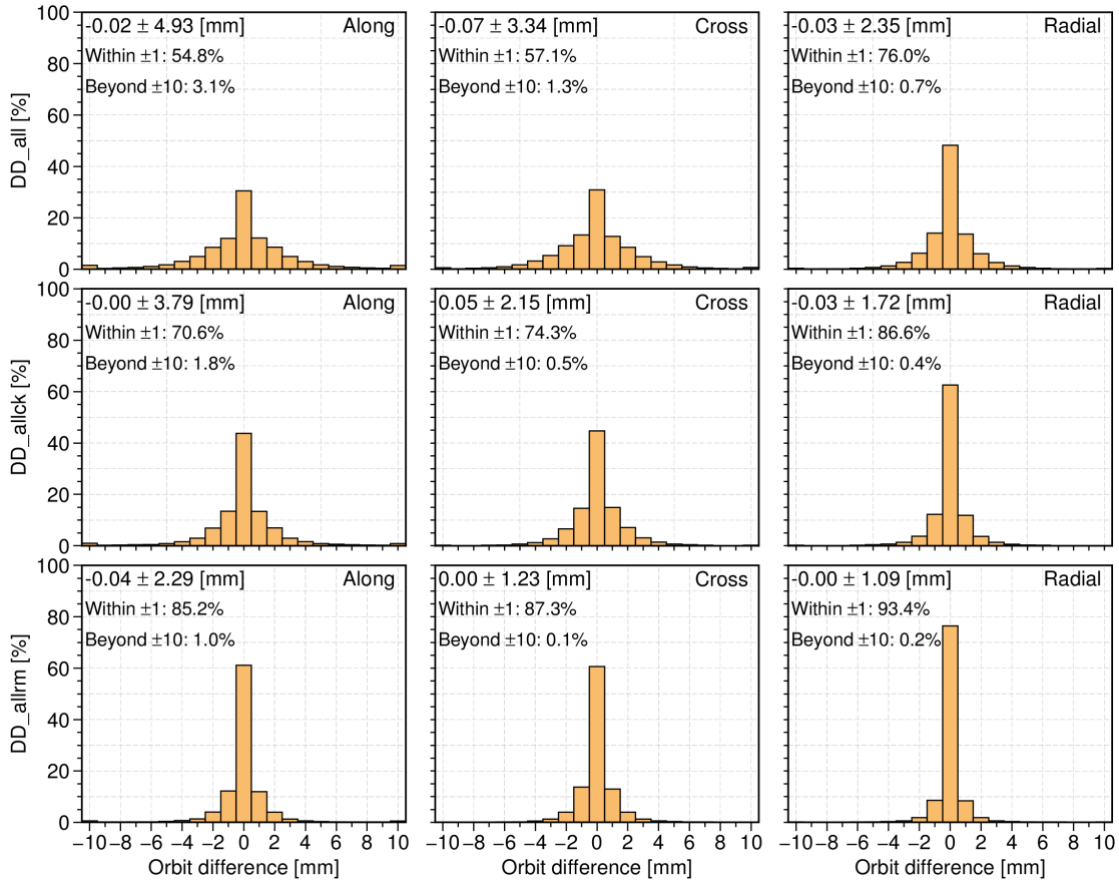

Figure 4.22 Distribution of the orbit differences of all satellites of the DD_all (upper), DD_allck (middle), and DD-allrm (lower) solutions with respect to the UD_std solution, in the along (left), cross (middle), and radial (right) components, respectively. In each panel, the mean, STD, and distribution statistics are given.

The results in Figure 4.22 suggest that wrong-fixings of DD ambiguities contribute to the relatively bad orbit accuracy compared to the UD IAR solution. Taking DD ambiguities at DOY 330 as an example, the distributions of WL and NL fractional parts of the DD ambiguities are further presented in Figure 4.23. The WL fractional part of an outlier DD ambiguity can be achieved by DD of WL fractional parts of corresponding four UD ambiguities. The WL fractional parts of four UD ambiguities are achieved in the UD_std solution. NL fractional parts of each outlier DD ambiguity can be done in the same way with WL fractional parts. In total, 2641 of 40265 DD ambiguities are identified as outlier DD ambiguities. All the fractional parts of WL DD ambiguities are within the threshold value (0.3 cycles), while fractional parts of NL DD ambiguities within the threshold value (0.15 cycles) are about 64.0%. These incorrectly fixed DD ambiguities cannot be easily figured out since most of them meet the fixing threshold values.

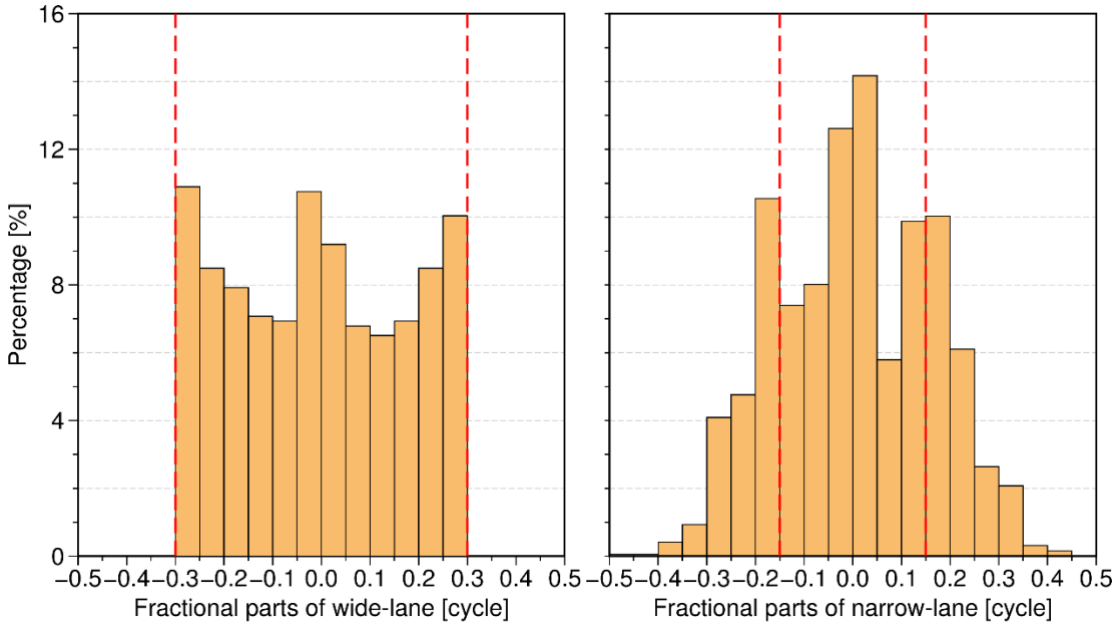

Figure 4.23 Distribution of fractional parts of DD ambiguities containing at least one unfixable UD ambiguity for DOY 330. The left panel shows the fractional parts of wide-lane ambiguities and the right panel shows the fractional parts of narrow-lane ambiguities. The red dash line represents the wide-lane and narrow-lane threshold, respectively.

4.5.4 Impacts of selecting independent DD ambiguities

As shown in Figure 4.21, the satellite orbits between DD-stdrm and DD-indrm show large difference, even though the incorrect DD ambiguity constraints are avoided in both cases. Therefore, the DD_stdrm, DD_indrm, DD_add, and DD_aud solutions are further compared with the UD_std solution to investigate the influence of the different selections of independent fixable DD ambiguities on satellite orbits, given in Figure 4.24. Among the four solutions, the DD_stdrm solution exhibits the largest differences compared to the UD_std solution, reaching 10.0, 6.0, and 3.9 mm for the along, cross, and radial components, respectively. Notably, the distribution of the orbit differences within ± 1 mm in the DD_stdrm solution is also significantly lower than the other solutions, especially for the along and cross component. On the contrary, the DD_indrm, DD_add, and DD_aud solutions exhibit comparable results with the UD_std solution. In contrast to the DD_stdrm solution, the percentage of orbit differences within ± 1 mm for the DD_aud solution is improved by 71.5%, 65.8% and 54.7% for the along, cross, and radial components, respectively. The comparable performance between the DD_indrm and DD_add solution conveys that lack of sufficient independent fixed DD ambiguities is a key factor that causes large orbit differences between DD IAR and UD IAR.

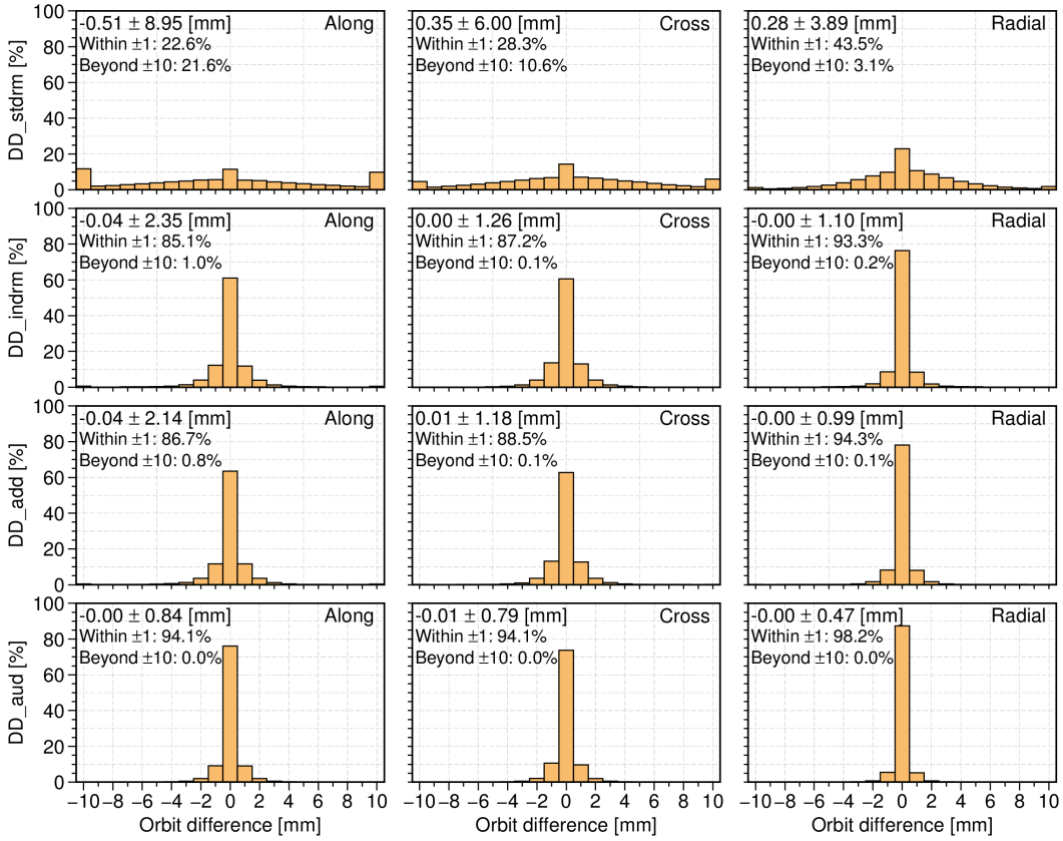

Figure 4.24 Distribution of the orbit differences of all satellites of the DD_stdrm (upper), DD_indrm (second row), DD_add (third row), and DD-allrm(lower) solutions with respect to the UD_std solution, in the along (left), cross (middle), and radial (right) components, respectively. In each panel, the mean, STD, and distribution statistics are given.

These results illustrate that the primary difference between DD_stdrm and DD_indrm arises from the absence of sufficient independent fixed DD ambiguities. After adding missing independent DD ambiguities (DD_add solution), the number of independent DD ambiguities will reach that of all inpdendent fixable DD-ambiguties and the corresponding orbit accuracy is, therefore, improved to the comparable level of the UD_std solution. Adding independent UD ambiguities (DD_aud solution) shows similar behavior. Concerning the DD_indrm solution, Figure 4.25 presents the differences in the number of newly added independent DD ambiguities between DD_stdrm and DD_indrm solution. The average daily number of missing independent DD ambiguities is around 269 over the whole year, which is around 4% of all independent DD ambiguity constraints, occasionally reaching 10.0% of all independent DD ambiguities.

To give an example of the missing DD ambiguities, the spatial distribution of independent baselines in the DD_stdrm solution and the supplemented independent baselines are given in Figure 4.26. Compared to the network established in the DD_stdrm solution, the new network, featuring additional 232 DD ambiguities. As mentioned before, picking independent DD ambiguities from those over a maximum independent baseline set has the risk of missing independent DD ambiguities and results in temporal and spatial discontinuities. Excessive

discontinuities have the potential to degrade orbit and clock accuracy. That is why fixable DD ambiguities over all baselines should be considered while selecting the independent fixable DD ambiguities.

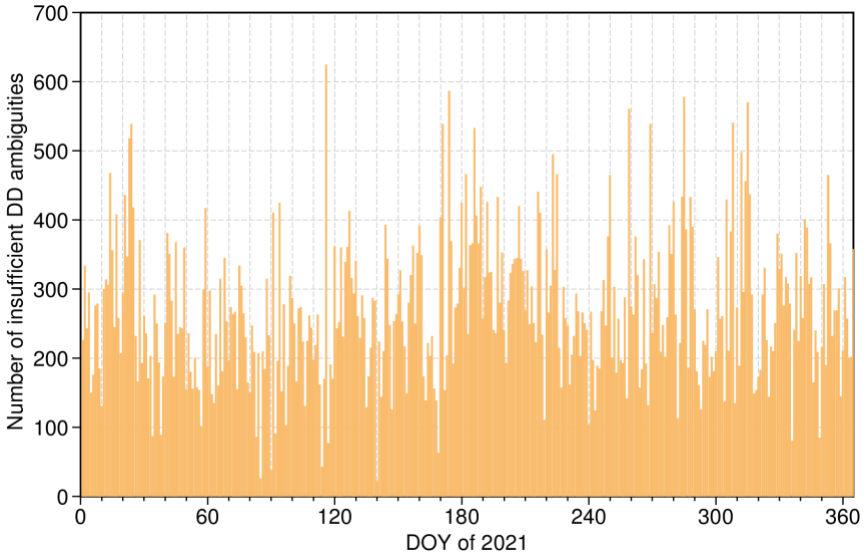

Figure 4.25 The daily number of insufficient independent DD ambiguities in the DD_stdrm solution.

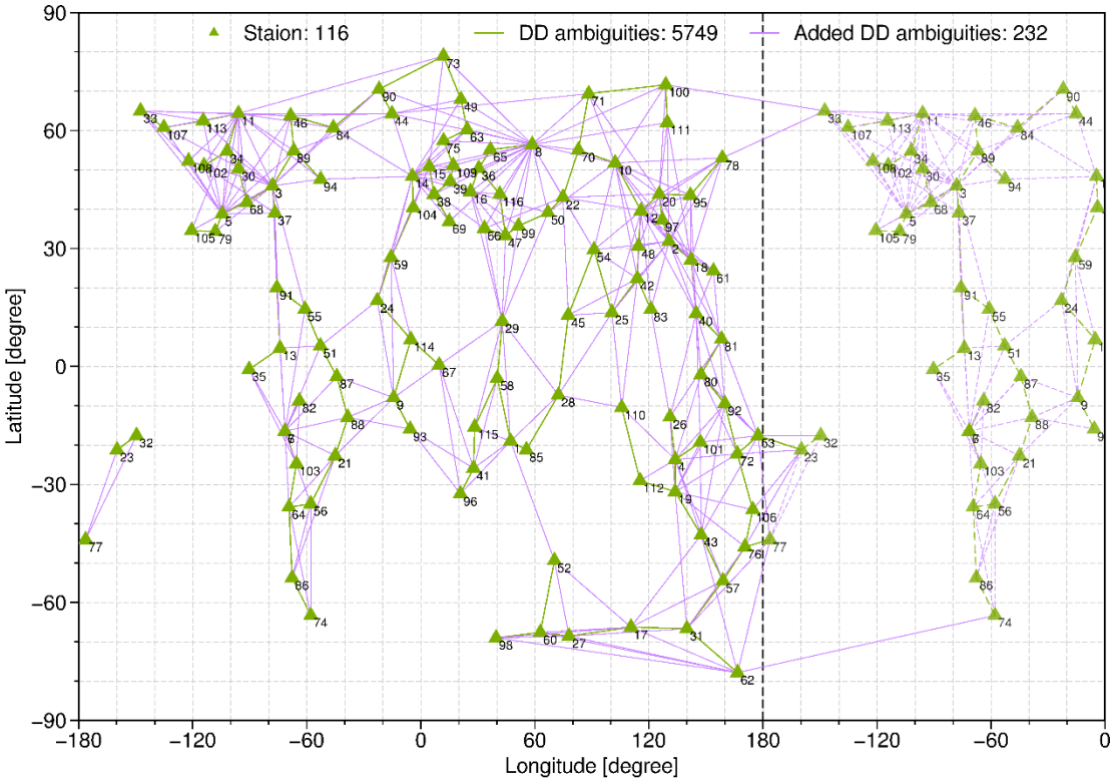

Figure 4.26 The spatial distribution of independent DD ambiguities in the DD_stdrm solution, along with supplemental independent DD ambiguities from the DD_add solution in DOY 233, 2021. Each triangle stands for a station and each baseline has at least one selected fixable DD ambiguity. In order to have a clear display of all independent baselines, the stations and baselines on the right side of the dashed line are identical to the left part of the map, with longitude ranging from -180 to 0 degrees.

4.5.5 Impacts of inappropriate IAR on geodetic parameters

The findings presented in Section 4.5.3 and 4.5.4 illustrate that the difference between the DD_std and UD_std solution arises from both incorrect ambiguity constraints and insufficient independent DD ambiguities. Upon removing incorrectly fixed UD ambiguities, the DD IAR strategy with maximum independent DD ambiguities set shows a comparable result to that of the UD IAR strategy. Besides removing unfixable UD ambiguities detected in UD IAR before constructing DD ambiguities, the alternative approaches are explored, including checking observation residuals (DD_allck solution), and avoid super long baselines while selecting independent baselines, which is not shown here. However, these refinements yield only marginal improvements in satellite orbits. Furthermore, the absence of independent DD ambiguities remains a fundamental issue when the set of the maximum independent baselines is selected firstly.

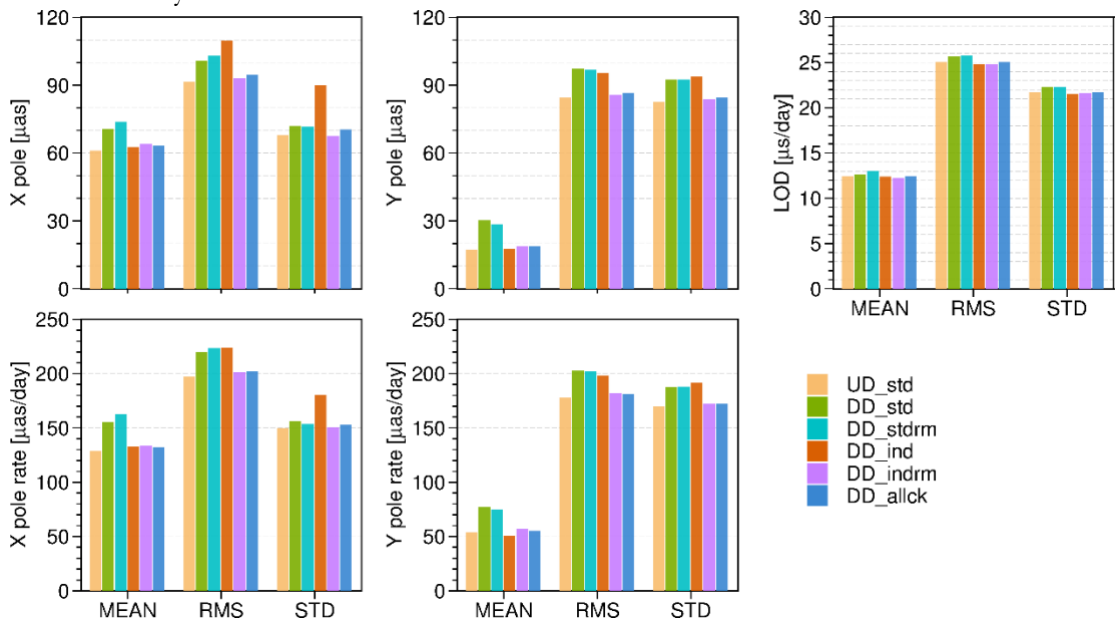

Figure 4.27 Statistics of ERP accuracy compared with IERS EOP 14 C04.

The above conclusions are summarized mainly based on the satellite orbits. The impact of different DD IAR and UD IAR strategies on other parameters, including ERPs, station coordinates and GCC are also investigated in this section. Figure 4.27 shows the statistics of ERPs for each DD IAR and UD IAR solution. Compared with IERS 14-C04, the UD_std solution is consistent with the DD_indrm and DD_allck solutions, but outperforms the other solutions, particularly regarding the polar motion and polar motion rate. The differences in mean values between the DD_std and UD_std solutions are substantial, reaching 9.5 and 12.9 μas for the x-pole and y-pole offsets, and 26.4 and 22.8 $\mu as/day$ for the x-pole and y-pole rates, respectively. As for the DD_ind solution, the mean values are comparable with those of the UD_std solution, but its STD values are notably higher, with the polar motion rate differences exceeding 20 $\mu as/day$. Following the elimination of incorrect UD ambiguities, the STD values in the DD_indrm solution return to the same level as the UD_std solution. Among the six solutions, the DD_indrm and DD_allck solutions exhibit greater alignment

with the UD_std solution and show about 4.0% RMS values for the polar offsets and rates in comparison to the DD_std, DD_stdrm and DD_ind solutions.

Table 4.3 shows the mean station position repeatability of the six IAR strategies in Table 4.1 with a seven-day sliding window. As expected, the outcomes for the DD_std, DD_stdrm and DD_ind solutions are on par with each other and inferior to the remaining three solutions. The maximum position repeatability differences between the UD and DD solutions are 0.16, 0.09, and 0.19 mm for the east, north, and up components, respectively. In solutions where an adequate number of independent DD ambiguities are available, the removal of incorrect UD ambiguities makes the DD_ind solution close to the UD_std solution, consistent with the section by Geng and Mao (2021).

Table 4.3 Mean repeatability of all stations for the six solutions and the percentage of each DD IAR solution w.r.t. UD-STD. Units are mm.

Direction	UD_std	DD_std	DD_stdrm	DD_ind	DD_indrm	DD_allck
East	1.36	1.44 (5%)	1.47 (7%)	1.52 (10%)	1.36 (0%)	1.37 (1%)
North	1.36	1.39 (2%)	1.41 (3%)	1.45 (6%)	1.36 (0%)	1.35 (-1%)
Up	4.67	4.71 (1%)	4.75 (2%)	4.85 (4%)	4.66 (0%)	4.65 (0%)

In addition, the weekly repeatability of GCC of different solutions are presented, shown in Table 4.4. The most significant differences in GCC repeatability lie between the UD_std solution and the DD_ind solution, reaching 0.56, 0.55, and 0.52 mm for the X, Y, and Z components, respectively. Particularly, the DD_ind solution is inferior to the DD_stdrm solution in terms of position and GCC repeatability. Therefore, both incorrect DD ambiguities and the absence of enough independent DD ambiguities are critical for DD solutions.

Table 4.4 Mean repeatability of geocenter coordinates for six types of solutions and the percentage of each DD IAR solution w.r.t. UD-STD. Units are mm.

Component	UD_std	DD_std	DD_stdrm	DD_ind	DD_indrm	DD_allck
X	2.54	2.68 (5%)	2.61 (3%)	3.10 (18%)	2.53 (-1%)	2.63 (3%)
Y	2.66	2.87 (7%)	2.86 (7%)	3.21 (17%)	2.65 (0%)	2.68 (1%)
Z	3.99	4.17 (4%)	4.06 (2%)	4.51 (11%)	4.05 (2%)	4.06 (2%)

4.6 Chapter summary

The main findings in this chapter are summarized as follows.

Section 4.1 introduces the relationship between DD IAR and UD IAR and the flowchart of UD IAR on GNSS data processing. DD IAR and UD IAR are considered equivalent theoretically when both independent DD ambiguities and remaining independent reference ambiguities are imposed as integers. However, there are some different characteristics between DD IAR and UD IAR. (1) UD IAR is more sensitive to the accuracy of float ambiguities compared with DD IAR. This is because the temporal variation of those UD ambiguities with lower accuracy in UD IAR, which is not a problem in DD IAR. That's why the UD IAR cannot be conducted directly based on float solutions. (2) The performance of DD IAR relies on the strategy of selecting independent DD ambiguities, as the number of selected independent DD

ambiguities could vary significantly. (3) UD IAR is more robust DD IAR. The unfixable ambiguities can be easily detected because the fractional parts of unfixable ambiguities deviate notably from the mean value of the majority. (4) UD IAR outperforms DD IAR in terms of processing efficiency as the fixable UD ambiguities can be removed before parameter estimation. Based on the characteristics of UD IAR, an efficient processing procedure of UD IAR for large network data processing is proposed.

Section 4.2 presents the performance of estimated UPDs and corresponding ambiguity fixing of GPS, Galileo, and BDS. The STD values of NL UPDs are 0.03 cycles, 0.03 cycles, 0.11 cycles, and 0.13 cycles for GPS, Galileo, BDS-2, and BDS-3, respectively. The ambiguity residuals of the three constellations obey the normal distribution in which BDS satellites behave a little bit worse than the other two constellations. The lower ambiguity fixing rate of BDS satellites is mainly attributed to the smaller number of available observations.

Section 4.3 presents the impact of UD IAR on satellite orbits. The orbits derived from UD IAR are better than those derived from DD IAR, except for BDS IGSO satellites with lower orbit accuracy. For GPS satellites, the average RMS values are 28.2 mm, 22.2 mm, and 23.8 mm in the along, cross, and radial components respectively. For Galileo satellites, the average RMS values decrease to 33.5 mm, 22.6 mm, and 37.7 mm in the along, cross, and radial components respectively. Similarly, the orbit accuracy of BDS MEO satellites is also improved by 21.7% and 10.4% in the along and cross component, respectively.

Section 4.4 presents the impact of UD IAR on ERPs and other global geodetic parameters. Adopting UD IAR exhibits a better performance for ERPs, station coordinates, and GCC, especially for ERPs. Compared with IERS 14 C04, the PM offsets are reduced from 89.5 μas to 79.5 μas on the x-pole and from 79.3 μas to 71.8 μas on the y-pole. The PM rates also show an improvement of 8.0% and 9.2% for the x-pole rate and the y-pole rate, respectively. The improvements of station coordinates and GCC in three components are less than 5%.

Section 4.5 interprets the reasons causing performance differences between DD IAR and UD IAR. Although DD IAR and UD IAR are considered as equivalent theoretically, the practical investigations show that UD IAR could achieve a better performance. The performances of different DD IAR and UD IAR solutions are investigated with one year of GPS POD processing. Depending on how it is implemented, DD IAR is usually worse than UD IAR, especially for the case that independent DD ambiguities are picked from the maximum independent baseline set determined in advance. The largest orbit differences are up to 7.2, 3.4, and 3.5 mm for the along, cross, and radial components, respectively. Compared with the UD IAR solution convey that incorrectly fixed DD ambiguity and the absence of independent DD ambiguities are two factors that degrade satellite orbits, in which the latter one takes the priority. The two reasons are also confirmed in the investigation of other parameters, including ERPs, station coordinates, and GCC. Compared with satellite orbits, station coordinate, and GCC are more sensitivs to incorrect DD ambiguity constraints. If all incorrect DD ambiguities are accurately identified and sufficient independent DD ambiguities are picked, DD IAR can achieve comparable results as those of UD IAR. However, it can be challenging to achieve

these two conditions, particularly when dealing with a massive network. First, incorrect DD ambiguities are hardly to be identified. Second, selecting independent DD ambiguities from pre-defined maximum independent baseline set carries the risk of missing a part of independent DD ambiguities. Moreover, picking independent DD ambiguities is computationly expensive for large networks. Compared with DD IAR, UD IAR is much more robust and efficient to automatically rejected ambiguities with inconsistent fractional part of the majority, which is highly recommended in daily GNSS data processing.

5 Improving processing efficiency of multi-GNSS data

To speed up the provision of Ultra-rapid orbits, a strategy by using epoch-parallel processing and historical information is proposed. The epoch-parallel processing strategy can achieve multi-GNSS batch POD solutions within 30 minutes and keep their consistency with sequential batch solutions. Considering the historic information, the processing of Ultra-rapid orbit can be finished in 10 min. Section 5.1 describes the consistency between legacy batch and proposed epoch-parallel processing strategies. Based on the epoch-parallel strategy, Section 5.2 investigates multi-GNSS data processing efficiency with multi-nodes. Based on the strategy proposed in Section 5.2, the historical information is further considered in Section 5.3. The performance of the predicted orbits of the user-available part is evaluated in Section 5.4. Owing to the rapid orbit update interval (e.g., 30 min), the accuracy of one-hour high-stability hydrogen clocks is better than 0.1 ns. Hence, an example of RT PPP with both predicted orbits and clocks is discussed in Section 5.5.

Note: This chapter has been published in Tang, Wang, Zhu, et al. (2023) and Tang, Wang, Cui, et al. (2023). The italicized text represents the content from the published paper.

5.1 Epoch-parallel processing strategies

Currently, the ultra-rapid POD solution is usually performed with 24-hour observations, which ensures a precise and reliable solution. The latency is 3-hour and later reduced to 1-hour by utilizing the SSDs (Li et al., 2018), but any further reduction of the processing time is difficult due to the large number of parameters to be processed. Instead of sequential processing from the first to last epoch, the epoch-parallel processing divides the 24-hour session into a set of sub-sessions processed parallelly. Each sub-session is processed using the sequential LSQ. Only the active parameters are kept in NEQ, and deactivated parameters are eliminated immediately. Within a sub-session processing, parameters which are not active in the priori or subsequent sub-session can be eliminated before connecting sub-sessions, and the eliminating equation can be used to recover the eliminated parameters to obtain the same result as for sequential processing. Different from the method introduced by Jiang et al. (2021), the proposed strategy considers parameter elimination as soon as they are deactivated, significantly decreasing memory requirement and computation burden.

To demonstrate this, all the deactivated parameters are assumed to eliminate at once and the NEQs of the i^{th} and $(i+1)^{th}$ sub-session are expressed as

$$\begin{bmatrix} \mathbf{N}_{11,i} & \mathbf{N}_{12} \\ \mathbf{N}_{21} & \mathbf{N}_{22} \end{bmatrix} \begin{bmatrix} \boldsymbol{x}_1 \\ \boldsymbol{x}_2 \end{bmatrix} = \begin{bmatrix} \boldsymbol{w}_{1,i} \\ \boldsymbol{w}_2 \end{bmatrix}, \tag{5.1}$$

and

$$\begin{bmatrix} \mathbf{N}_{11,i+1} & \mathbf{N}_{13} \\ \mathbf{N}_{31} & \mathbf{N}_{33} \end{bmatrix} \begin{bmatrix} \boldsymbol{x}_1 \\ \boldsymbol{x}_3 \end{bmatrix} = \begin{bmatrix} \boldsymbol{w}_{1,i+1} \\ \boldsymbol{w}_3 \end{bmatrix}. \tag{5.2}$$

Here $\boldsymbol{x}_1$ are the active parameters which cover at least the i^{th} and $(i+1)^{th}$ session, for example, satellite state parameters. $\boldsymbol{x}_2$ and $\boldsymbol{x}_3$ are the inactivated parameters in $(i+1)^{th}$ and i^{th} session, respectively, for example ambiguities and epoch-wise clocks.

For sequential processing, $\boldsymbol{x}_2$ are eliminated from Equation (5.1) and can be represented as

$$\boldsymbol{x}_2 = \mathbf{N}_{22}^{-1}(\boldsymbol{w}_2 - \mathbf{N}_{21}\boldsymbol{x}_1), \tag{5.3}$$

and

$$\left(\mathbf{N}_{11,i} - \mathbf{N}_{12}\mathbf{N}_{22}^{-1}\mathbf{N}_{21}\right)\boldsymbol{x}_1 = \boldsymbol{w}_{1,i} - \mathbf{N}_{12,i}\mathbf{N}_{22}^{-1}\boldsymbol{w}_2. \tag{5.4}$$

Contributing the next sub-session (Equation (5.2)) into the NEQ (Equation (5.4))

$$\begin{bmatrix} \overline{\mathbf{N}}_{11} & \mathbf{N}_{13} \\ \mathbf{N}_{31} & \mathbf{N}_{33} \end{bmatrix} \begin{bmatrix} \boldsymbol{x}_1 \\ \boldsymbol{x}_3 \end{bmatrix} = \begin{bmatrix} \overline{\boldsymbol{w}}_{11} \\ \boldsymbol{w}_3 \end{bmatrix} \tag{5.5}$$

with

$$\overline{\mathbf{N}}_{11} = \mathbf{N}_{11,i} + \mathbf{N}_{11,i+1} - \mathbf{N}_{12}\mathbf{N}_{22}^{-1}\mathbf{N}_{21}, \tag{5.6}$$

and

$$\overline{\boldsymbol{w}}_{11} = \boldsymbol{w}_{1,i} + \boldsymbol{w}_{1,i+1} - \mathbf{N}_{12}\mathbf{N}_{22}^{-1}\boldsymbol{w}_2. \tag{5.7}$$

Then $\boldsymbol{x}_3$ is eliminated from Equation (5.5)

$$\boldsymbol{x}_3 = \mathbf{N}_{33}^{-1}(\boldsymbol{w}_3 - \mathbf{N}_{31})\boldsymbol{x}_1 \tag{5.8}$$

$$\left(\overline{\mathbf{N}}_{11} - \mathbf{N}_{13}\mathbf{N}_{33}^{-1}\mathbf{N}_{31}\right)\boldsymbol{x}_1 = \overline{\boldsymbol{w}}_{11} - \mathbf{N}_{13}\mathbf{N}_{33}^{-1}\boldsymbol{w}_3. \tag{5.9}$$

After solving Equation (5.9), the eliminated parameters can be recovered with Equation (5.3) and Equation (5.8).

For the parallel processing, $\boldsymbol{x}_2$ and $\boldsymbol{x}_3$ are eliminated in parallel. The elimination of $\boldsymbol{x}_2$ is expressed by Equation (5.3) and Equation (5.4), while that for $\boldsymbol{x}_3$ is similar as

$$\boldsymbol{x}_3 = \mathbf{N}_{33}^{-1}(\boldsymbol{w}_3 - \mathbf{N}_{31})\boldsymbol{x}_1 \tag{5.10}$$

$$(\mathbf{N}_{11,i+1} - \mathbf{N}_{13}\mathbf{N}_{33}^{-1}\mathbf{N}_{31})\boldsymbol{x}_1 = \boldsymbol{w}_{1,i+1} - \mathbf{N}_{13,i}\mathbf{N}_{33}^{-1}\boldsymbol{w}_3. \tag{5.11}$$

Combining the NEQs of the sub-sessions, i.e., Equation (5.4) and Equation (5.11) results in the same NEQ of the sequential processing, i.e., Equation (5.9). Therefore, both eliminating equations and the final NEQ are the same.

Parameter elimination must be carried out carefully to guarantee the equivalence of epoch-parallel and sequential batch processing, especially when there are temporal constraints. First, in each sub-session processing, only parameters not used in the previous and subsequent sub-sessions can be eliminated, such as ambiguities and epoch-

wise clocks. However, temporal constraints between adjacent parameters should be imposed for the parameterization of the stochastic process, such as the random-walk process (RW). These parameters, for example, tropospheric delay parameters, can only be removed after all related observations and the corresponding temporal constraints are added.

It should also be pointed out that to keep the consistency of active ambiguities in the adjacent NEQs, phase windup corrections should be prepared before NEQ generation so that possible integer jumps could be corrected. The phase windup correction is accumulated along with time, starting from a fractional cycle at the beginning. Therefore, there could be integer cycle differences from one sub-session to another sub-session, that prevent the connection of ambiguities of continuous data arc.

From the above discussion, epoch-parallel processing strategy divides the long session into short sub-sessions and each sub-session can be processed parallelly using sequential processing software and all the sub-session results can be combined into the final solution. It is obvious that it can take full advantage of multi-cores and multiple computers with only a minor modification of GNSS sequential processing strategies. Hence, it can be easily implemented.

5.2 Improving data processing efficiency with multiple nodes

With the proposed epoch-parallel processing strategy, a 24-hour session can be divided into several sessions and distributed to several nodes. In this section, the processing efficiency of epoch-parallel processing strategy on multi nodes are explored.

5.2.1 Realization of epoch-parallel processing

The flowchart of the optimized POD strategy is shown in Figure 5.1*, including data preparation, data preprocessing, parameter estimation and update, ambiguity resolution, and product generation. In the data preparation, hourly observation and navigation files for specified stations are downloaded from the IGS data centers and recorded from IGS real-time streams; they are merged after preliminary quality control to session-files. The main function of data preprocessing is initializing satellite orbits, generating phase windup correction files, and initial quality control using the single station editing method referred to as TurboEdit (Blewitt, 1990), all in a parallel way. Different from the parameter estimation part in sequential batch processing, it is optimized by assigning and coordinating sub-session generation, sub-session stacking and solving, orbit update and post-fit residual-based quality control. To continue shortening the computation time, the OpenMP multithreading model is adopted as well for parameter elimination during sub-session generation and sub-session stacking.*

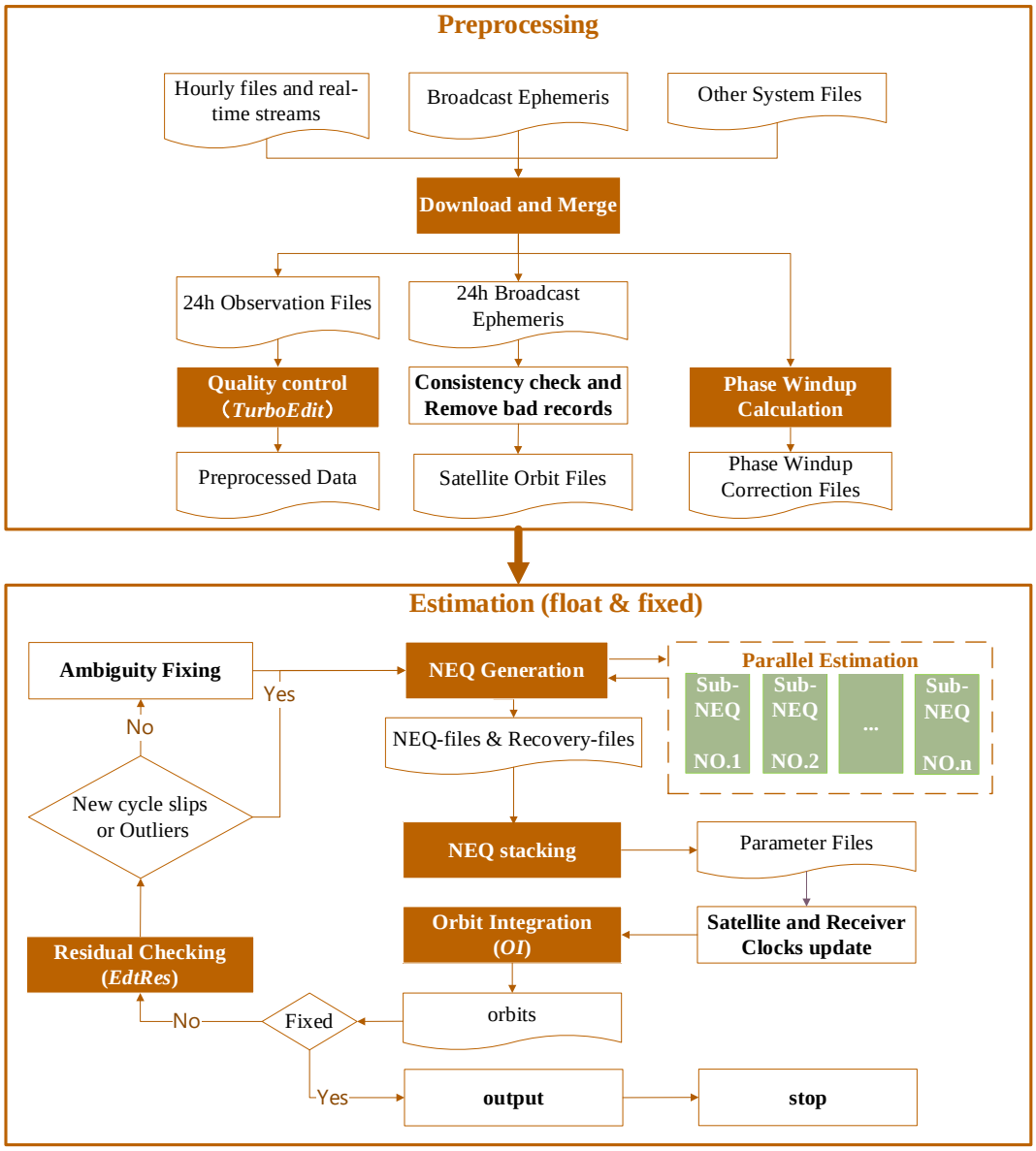

Figure 5.1 The optimized processing strategy for POD. The rectangle filled with dark orange colour means the processes are implemented in a parallel way. Note that the module name in the PANDA software is in italic here and in the following sections, e.g., *TurboEdit*, *EdtRes* and *OI*.

In the stacking of sub-session NEQs, it is also very important to eliminate deactivated parameters in a timely manner for computation efficiency. Consequently, after any two sub-session NEQs are stacked, the parameters which become deactivated in the subsequent combination should be eliminated immediately. Abide by this rule, there are usually two available approaches, adjacent stacking and sequential stacking. The adjacent stacking approach stacks two adjacent sub-session NEQs whenever available, until all sub-session NEQs are combined. In contrast, the sequential stacking approach stacks the sub-session NEQs one by one and it can be optimized by two parallel stacking processing starting from both ends towards the middle. Taking the stacking of 24 1-hour NEQs generated by each sub-session as an example, Figure 5.2 *illustrates the two*

different stacking approaches. Besides the 1-hour NEQ generation step (step 1), the adjacent stacking approach requires another five steps to obtain the final 24-hour NEQ, while the sequential stacking approach needs 12 steps. For the adjacent stacking approach, there are 12 2-hour NEQs needed to be generated in step 2, then six 4-hour NEQs in step 3, three 8-hour NEQs in step 4, one 16-hour NEQ and 8-hour NEQ in step 5 and a 24-hour NEQ in the last step. Assuming that there are sufficient threads available and the parallel combinations take the same time of a single combination, the adjacent stacking should take less time than the sequential stacking at the first glance. However, it is in the fact opposite due to too many active parameters kept in the NEQs generated in adjacent stacking The details will be given in Section 5.2.3.

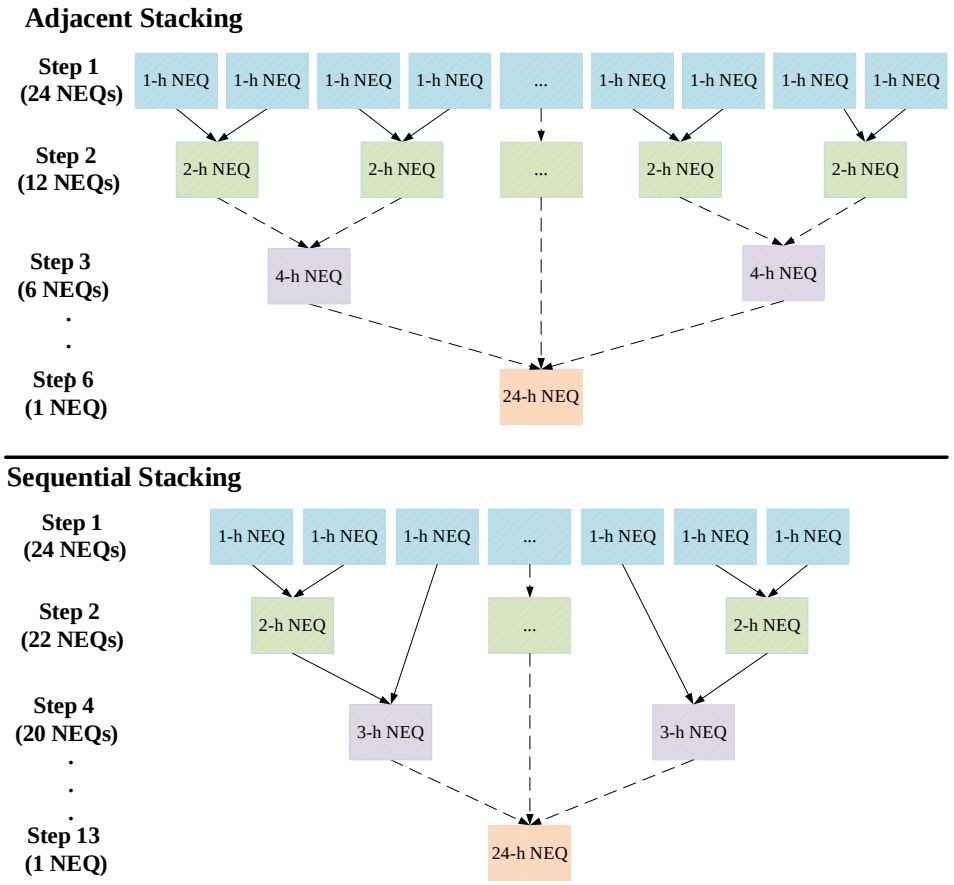

Figure 5.2 Illustration of the adjacent and sequential stacking of NEQs stacking. h stands for hour. 1-h NEQ is generated by sequential POD of a sub-session.

For this processing, multiple computer nodes should be included, among them one serves as the master or coordinator to distribute tasks, monitor processing status (start and complete, or any disrupt) and check results, as shown in Figure 5.3. The parallel tasks are distributed to the available nodes along with all necessary files for computation. The number of involved nodes is determined by how many sub -session NEQs are divided, for example, 12 nodes are required for epoch-parallel processing of 12 sub-session NEQs. On each node, the proposed strategy can also take advantage of multi-threads, for example, accelerating parameter elimination by OpenMP.

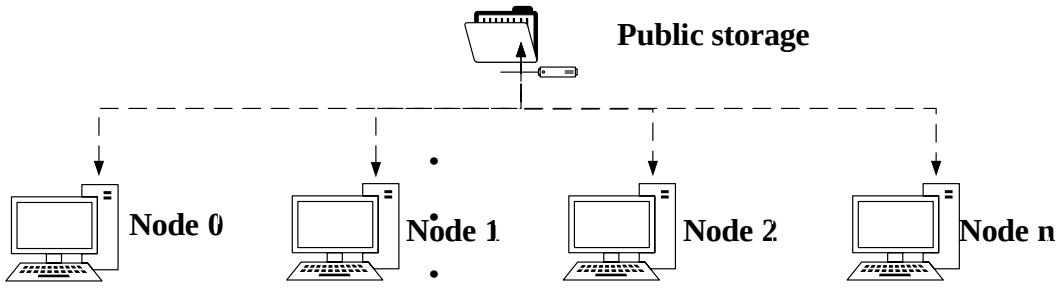

Figure 5.3 Architecture of the cluster in this study.

5.2.2 Data processing

Table 5.1 shows the CPU types equipped in computer nodes used in this study. The CPU frequency of each node ranges from 3.20 to 4.10 GHz. For a convenient and clear statement, one node here means a single server or computer. All nodes are equipped with SSDs for high-speed data input-output (IO).

Table 5.1 CPU architecture information.

Node name	3.20 GHz	3.60 GHz	3.80 GHz	4.10 GHz
CPU type	Intel(R) Xeon(R) CPU E3-1271 v3 @ 3.20GHz	Intel(R) Xeon(R) CPU E3-1271 v3 @ 3.60GHz	Intel(R) Xeon(R) CPU E3-1275 v6 @ 3.80GHz	Intel(R) Xeon(R) CPU E3-1285 v6 @ 4.10GHz

A network of 120 multi-GNSS ground stations are selected for multi-GNSS POD solutions. In addition, a subnet using 90, 100, or 110 stations within the 120 stations are selected, to further evaluate the POD efficiency and accuracy of different networks. Note that the MGEX tracking stations take the priority while choosing stations globally. The time span of our experiments ranges from Day of Year (DOY) 335 to 365, 2021.

Considering the CPU information, the number of threads for parallel parameter elimination in a node is set to four. In the following experiments, the session length is 24 hours, similar to IGS ACs, even though a longer session might bring marginal improvement. The entire session is divided into at most 24 sub-sessions, as the processing of 1-hour observations only takes a few seconds. Unless otherwise noted, the experiments in this section are carried out using 100 tracking stations and 120 satellites on the 4.1 GHz node.

5.2.3 The timeliness of multi-GNSS POD

As the length of a sub-session becomes shorter, more NEQs are generated and the NEQ stacking tends to be more time-consuming. But if a sub-session is too long, the benefit of epoch-parallel is less significant. Therefore, the balance between generating and

stacking of sub-sessions needs to be further investigated. Note that the number of nodes mentioned in the following equals to the number of sub-sessions as there is only one process of sub-session NEQ generation running on a node, e.g., the number of four nodes means that a 24-hour session is split into four 6-hour sub-sessions.

Taking into consideration all the optimized strategies mentioned in Section 5.2.1, along with parallel parameter elimination utilizing OpenMP, the computation efficiency on different numbers of sub-sessions is shown in Figure 5.4 *(a). With the assistance of parallel processing of TurboEdit, OI and EdtRes, the sequential batch POD strategy with and without parallel parameter elimination costs 54 minutes and 73 min, respectively. Compared with sequential batch solutions, all epoch-parallel cases have the priority in computation efficiency. When there are more than six nodes (six sub-sessions) available, the computation time of the new POD processing strategy is less than 30 min, while the improvement of using 12 nodes reaches up to 49% compared to using one node. The increased time using 24 nodes is caused by the stacking of too many sub-sessions coupled with many active ambiguities. Even for the two nodes case, the computation efficiency is improved by 25%. Obviously, the most time-consuming part in a POD is the process of parameter estimation.*

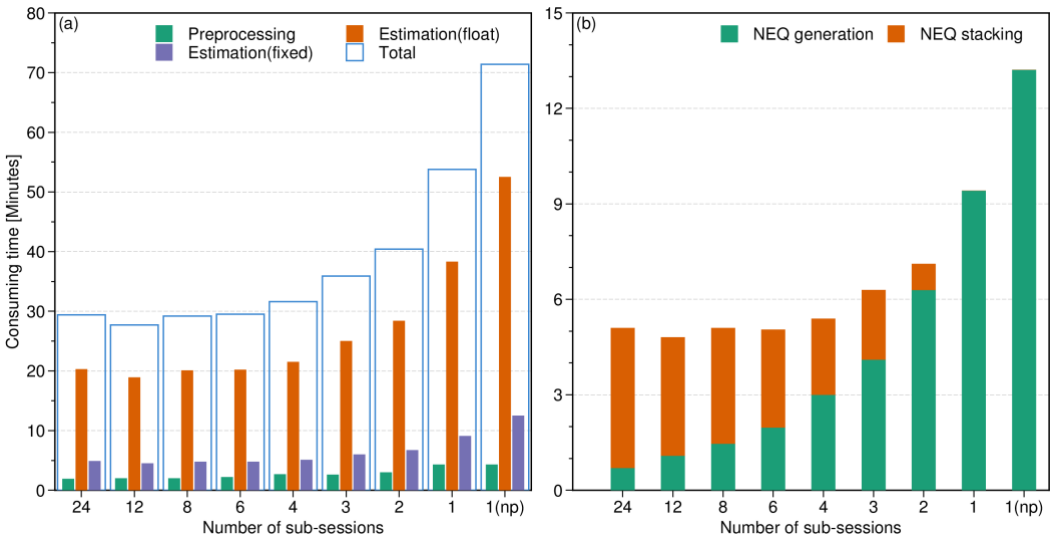

Figure 5.4 Computation efficiency of POD with various numbers of nodes over the period from December 1 to 7, 2021, using 100 stations on a 4.1 GHz node. (a) The running time of an entire POD (total), where "Preprocessing" stands for processing steps before parameter estimation, "Estimation(float)" for four iterations of parameter estimation without ambiguity resolution; "Estimation(fixed)" for one time of parameter estimation with ambiguity resolution. (b) The running time of one iteration of parameter estimation including the generation of NEQs (green) and NEQ stacking (orange). Sequential stacking method is selected here. The number of the sub-sessions is identical with the number of nodes, so that each node processes only one session for NEQ generation. Note that "1(np)" stands for using one node but non-parallel parameter elimination.

Figure 5.4 *(b) illustrates the computation time of one iteration of parameter estimation, including NEQ generation and NEQ stacking, using different numbers of nodes. If four or*

more nodes are used, then one iteration of parameter estimation takes only around 5 minutes and the difference caused by more nodes is less than 1 min. The computation efficiency on two nodes is reduced by more than 2 minutes compared with the sequential POD method.

When the number of sub-sessions increases, the time-consumption of sub-session stacking becomes more prominent. As aforesaid, there are mainly two ways of stacking NEQs: sequential stacking and adjacent stacking. Their consuming-time are presented in Figure 5.5*. The step of stacking two sub-sessions only costs around 17 s. When there are more than two sub-sessions, the stacking time increases sharply. In case of six or more sub-sessions, sequential stacking is more efficient, e.g., 67 s is saved in the situation of stacking 24 sub-sessions, even though the sequential stacking requires more stacking steps. The reason is that in the sequential stacking only the active ambiguities of one side (either starting or ending part of the sub-session) are kept in NEQ, while in adjacent stacking, many parameters which are also active in the adjacent two sub-session NEQs must be kept for further stacking, leading to a larger dimension of the NEQ and more time consuming in parameter elimination. When the number of sub-sessions is no more than four, the time-consuming of two methods are the same as they perform identically. Although both three sub- sessions and four sub-sessions need two times stacking, the latter costs much more time, as the additional 3rd and 4th NEQ stacking spends more time than the 1st and 2nd NEQ stacking. Therefore, sequential stacking is adopted in the following POD results. It is worth mentioning that the sequential stacking can be easily performed on a single node while the benefit of using two nodes is marginal.*

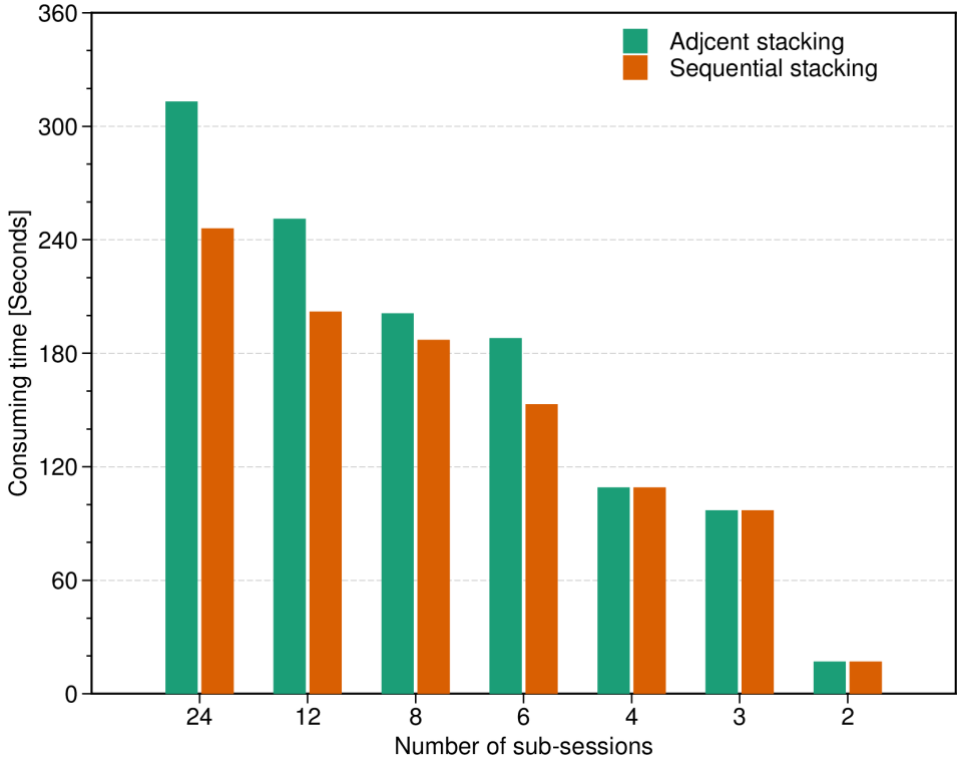

Figure 5.5 Computation efficiency for different stacking methods.

Apart from the NEQ generation and stacking, multi-nodes are profitable for the other steps, e.g., preprocessing of GNSS observations (TurboEdit), orbit integration (OI), and posterior residual-based quality control (EdtRes), which can be easily realized station-wise and/or satellite-wise. As shown in Figure 5.6*, the computation time of TurboEdit, OI, and EdtRes decreases gradually along with the increasing of the node number. When three or more nodes are involved, TurboEdit of 100 stations requires less than 1 min. However, with more nodes involved, the improvement of computation efficiency for OI and EdtRes decreases progressively as each program needs a little time to process single station or satellite, e.g., files reading which cannot be omitted. Provided that there are 100 stations and 120 satellites, four nodes equipped with eight threads processing at most four times of OI and EdtRes, costs around merely 10 s. The improvement of the available nodes more than four is less than 5 s.*

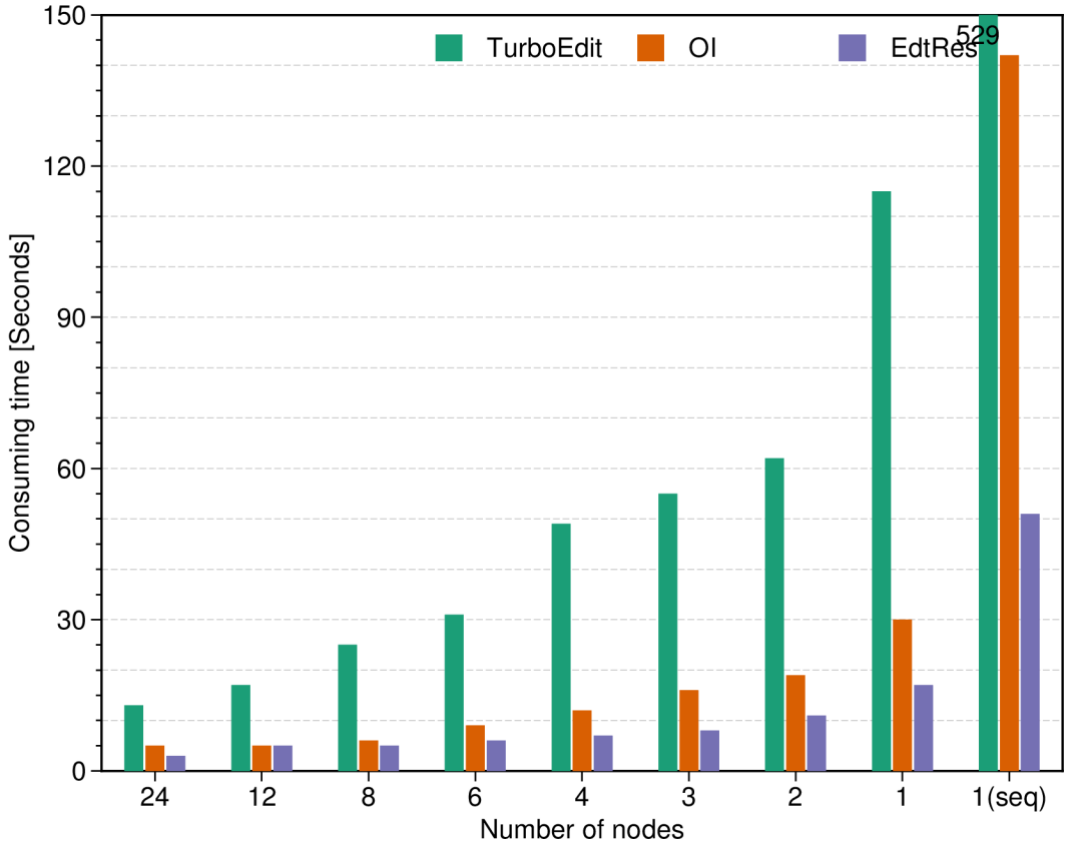

Figure 5.6 Computation efficiency of TurboEdit, OI, and EdtRes with various nodes. "1(seq)" in the horizontal axis stands for sequential processing without station or satellite parallel.

The above comparison and analysis are derived from processing 100 tracking stations based on the 4.1 GHZ CPU nodes. The computation efficiency of the new strategy using different types of CPU is further shown in Figure 5.7*. The process of POD is usually faster with higher CPU performance. Compared with the results based on nodes equipped with 3.2 GHZ CPU, the time consuming on the 4.1 GHz CPU of three solutions, including four, two, and one sub-sessions is down by 37%, 33%, and 29%, respectively. Consistent with the above conclusion, using four nodes is always faster than using two, especially for*

larger number of stations. In general, the new strategy can secure a processing time within one hour except for few special cases with too many stations and/or outdated CPU such as the case of processing 120 stations on 3.2 GHz node, whereas the sequential strategy has to reduce the number of stations and on a high-performance node to satisfy the 1-hour requirement, such as the case using 90 stations, and that using 100 stations on 4.1 GHz node. More important is that the half-hourly update can be achieved using the new strategy, for instance, using 90 stations on a 3.8 GHz or 4.1 GHz node.

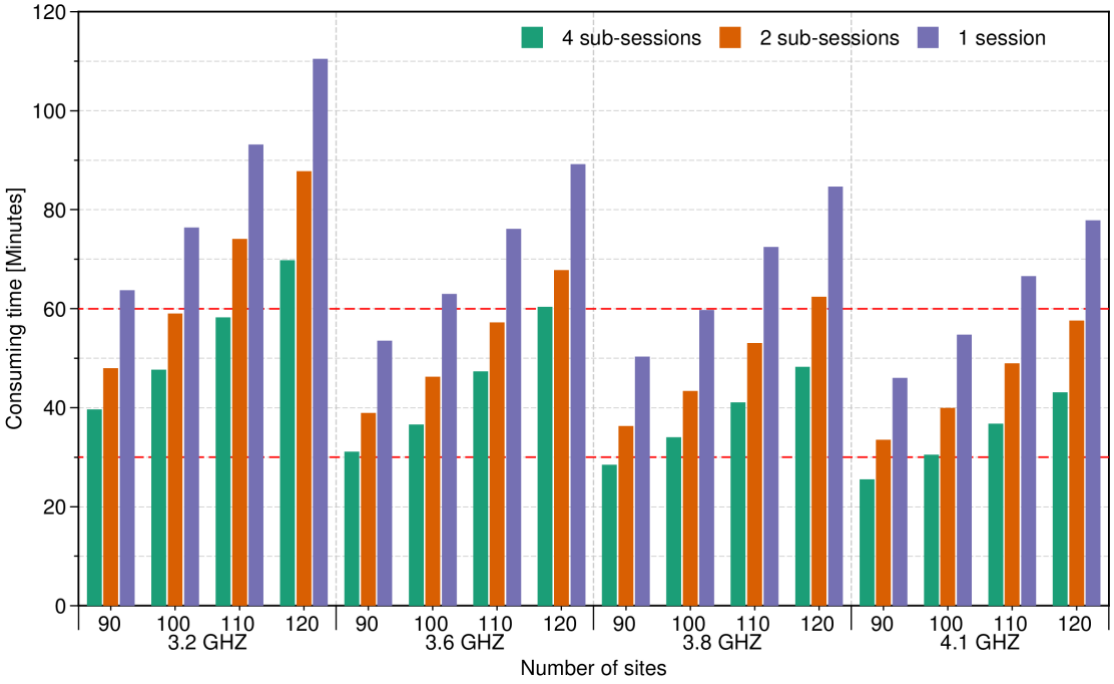

Figure 5.7 Computation efficiency with different number of nodes and stations over the period from December 1 to 7, 2021. More information of the different types of nodes is provided in Table 1. 1 session means a sequential batch POD solution.

5.3 Improving data processing efficiency with historic information

For the process of generating hourly orbits, the first 23-hours of a 24-hour session have been processed in the previous job, leaving only one hour of new observations to be processed. As mentioned in Section 5.2, the most time-consuming part of orbit generation is the iteration of parameter estimation for data cleaning, which usually consists of five times of iterations i.e., four-time parameter estimation for data cleaning and one-time parameter estimation for ambiguity fixing, to get high-precision products. If the historical information in the previous session can be utilized in the current session, the iterations of data cleaning can therefore be reduced because new observations need to be cleaned. Moreover, the fixed UD ambiguities can also be removed to reduce the number of estimated parameters (H. Chen et al., 2014).

5.3.1 Realization of epoch-parallel processing with historic information

Based on Figure 5.1, an optimized flowchart of the POD strategy is shown in Figure 5.8. According to our experience, the latest 3-hour observations will be processed in the preprocessing step. Specifically, 3-hour observations will contain 1-hour new observations if the orbit update interval is one hour. Therefore, the latest 3-hour observations contain at least 2-hour historic observations, which serves for the data connection in the next step. After preprocessing, 24-hour initialized satellite orbits, as well as 3-hour phase windup and initial quality control files (log-file) are generated. In the process of data connection, newly generated phase windup, log-file and fixed UD ambiguities are connected with corresponding files in the previous session to generate 24-hour files. For the parameter estimation and data cleaning (float) step, one iteration is enough since most outliers and cycle slips have been removed and labeled in the previous session. After removing fixed UD ambiguities, the parameter estimation step shall be faster. Owing to that most UD ambiguities are already fixed in the parameter estimation step, the accuracy of float ambiguities in float solution is good enough to realize UD IAR directly, which is different from the ambiguity fixing step mentioned in Chapter 4. After ambiguity fixing, all the estimated parameters are updated, including fixed UD ambiguities, and related information are prepared for the next session.

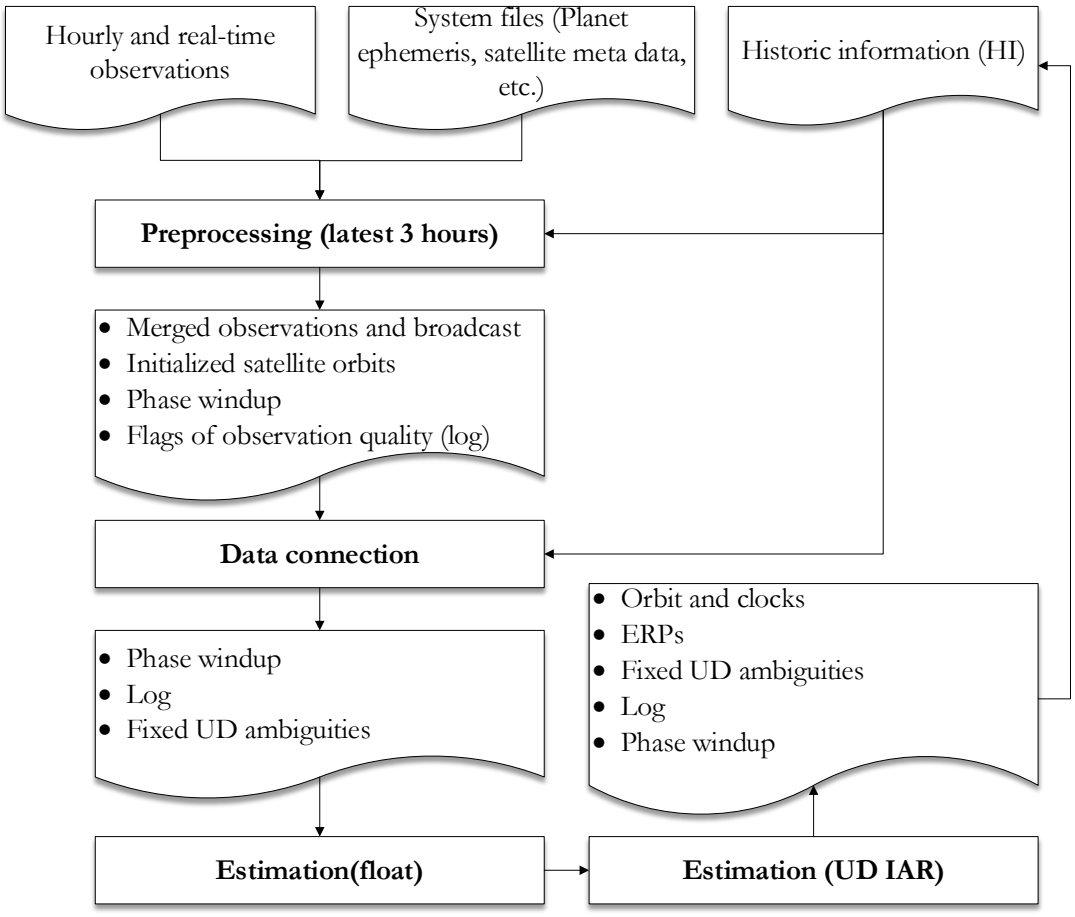

Figure 5.8 The optimized processing strategy for POD.

5.3.2 The timeliness of multi-GNSS POD

The following comparison and analysis are derived from processing 100 tracking stations and 120 satellites. Taking historic information mentioned in Section 5.3.1 into consideration, along with epoch-parallel processing strategy proposed in Section 5.2.1, the computation time of one iteration of parameter estimation, including NEQ generation and NEQ stacking, using different numbers of nodes is illustrated in Figure 5.9. With the assistance of historic information, one parameter estimation only costs 3 min. Otherwise, 100 stations and 120 satellites will cost more than 9 min. Compared with low-frequency CPU, the contribution of higher-frequency CPU is less than 0.2 min. This is because most ambiguity parameters have been fixed and removed during parameter estimation, with only around 2000 unknown parameters left in NEQ which do not cost too much time. When there are two nodes available, then one iteration of parameter estimation takes only around 2.4 min, in which the NEQ stacking step costs around 0.4 min. The computation efficiency on four nodes is reduced by more than 1 minutes compared with the sequential POD method.

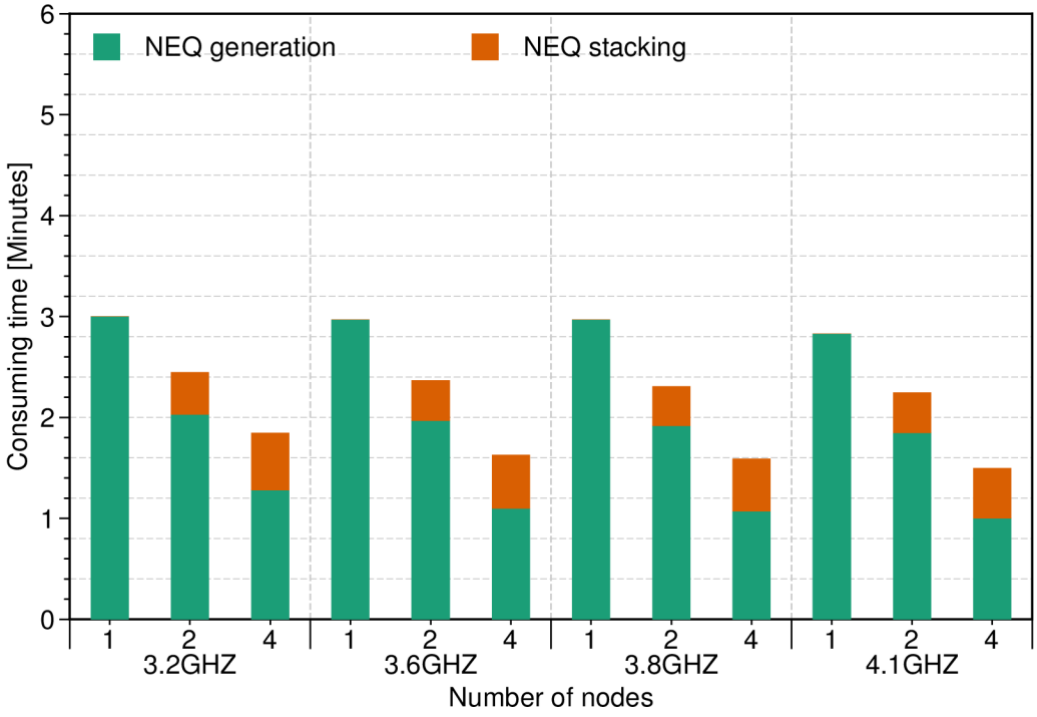

Figure 5.9 The computation time of one iteration of parameter estimation including the generation of NEQs (green) and NEQ stacking (orange) from December 1 to 7, 2021, using 100 stations. The number of the sub-sessions is identical with the number of nodes.

The computation efficiency of the proposed strategy using different types of CPU is further shown in Figure 5.10. The process of POD is usually faster with higher CPU performance. Compared with the results based on nodes equipped with 3.2 GHz CPU, the time consuming on the 4.1 GHz CPU of the three solutions, including one, two, and four sub-sessions is down by 10%, 10%, and 18%, respectively. Consistent with the above conclusion, using four nodes is always faster than using two. In general, the proposed strategy can secure a processing time

within half hour or even 10 minutes with the case including four nodes. More important is that the half-hourly update can be easily achieved using the new strategy without special consideration of CPU types. In practical processing, the half-hourly orbits can be provided in time even if a job is processed again due to errors.

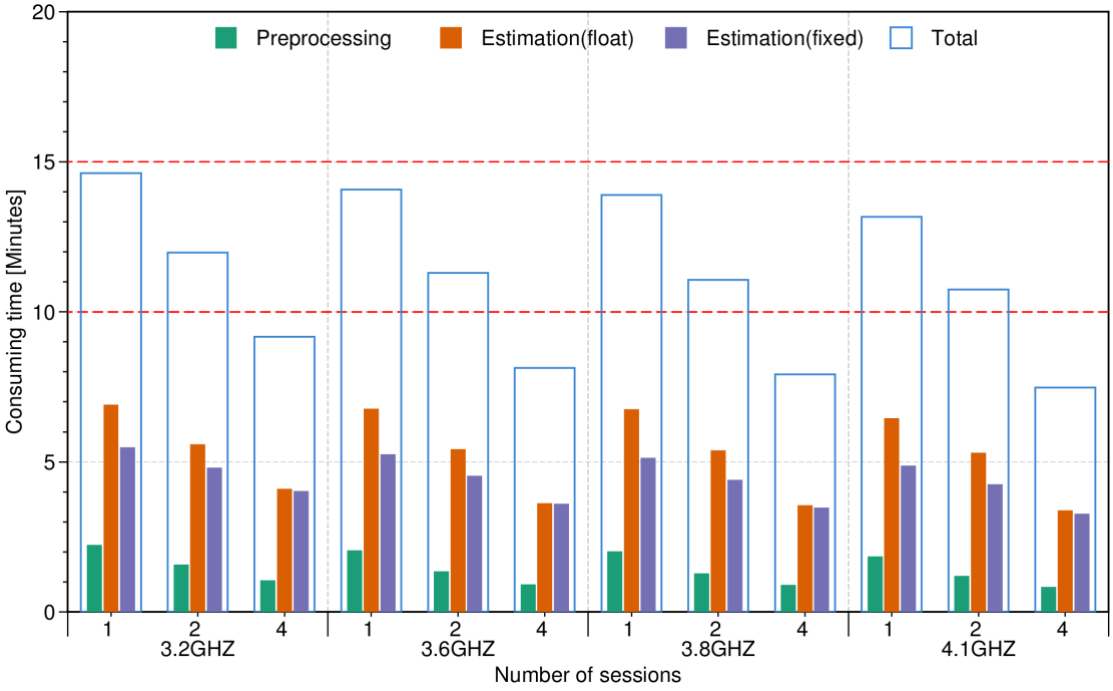

Figure 5.10 The running time of an entire POD (total) from December 1 to 7, 2021, using 100 stations.

5.4 Assessment of multi-GNSS real-time orbits

Currently, most IGS ACs select around 100 stations to realize the routine ultra-rapid orbit solution with latency between one to three hours, whereas the proposed strategy in Section 5.2 and Section 5.3 can realize half-hourly or even shorter orbit update. Therefore, five solutions over one month in January 2021 are designed to evaluate the performance of the epoch-parallel processing strategy. The 120min, 60min, 30min, 20min, and 10min solutions in Section 5.4.3 indicate that orbits are updated per 120, 60, 30, 20 and 10 min, respectively. Note that the sequential batch and epoch-parallel strategy are strictly equivalent, which are shown in Section 5.4.2. The performance of the user-available part is then investigated in Section 5.4.3.

5.4.1 Orbit validation strategy

For real-time positioning purpose, only the predicted orbits are available for users, therefore it is of great importance. However, here both estimated and predicted orbits are evaluated. Figure 5.11 *shows the processing and update scenarios of ultra-rapid orbits.*

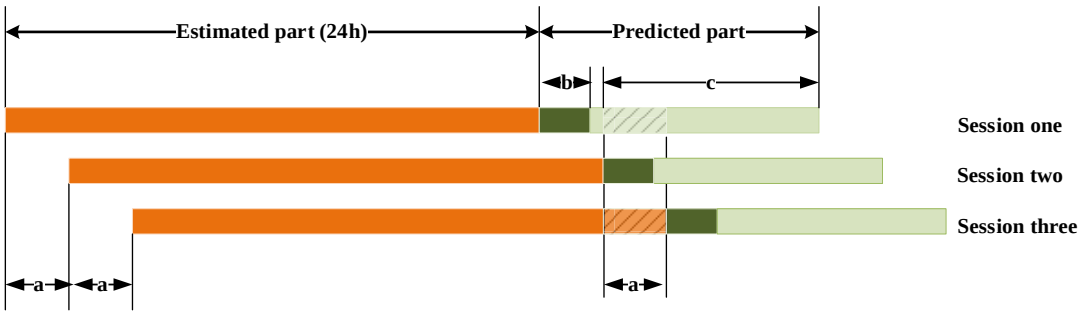

a: Update interval **b:** Processing period **c:** User-available part

Figure 5.11 Update latency for ultra-rapid orbits.

Let the processing of session one start at t_1, the session time of estimated part is $(t_1 - 24^h, t_1)$, the processing period is Δt_c, then the orbits are available from $t_1 + \Delta t_u$. Δt_u could be different from Δt_c as it is determined by product provider. Afterward, the session two starts at $t_1 + \Delta t_u$, in which Δt_u is the orbit update interval, the orbits are available from $t_1 + 2\Delta t_u$. From this epoch, the predicted orbits from session one will be replaced by that of session two. The inconsistency at switch epoch of the two consecutive predicted orbits are the boundary discontinuities, that are investigated. The current used predicted orbits can also be compared with the later available estimated orbits for quality validation, i.e., the predicted part of session one with the estimated part of session three, termed as orbit overlap. Compared with session three, orbit overlap in session one starts from $t_1 + \Delta t_u$ to $t_1 + 2\Delta t_u$, which is represented as shade part in Figure 5.11.

5.4.2 Consistency of batch and epoch-parallel solution

The estimated orbits are first evaluated and compared with the IGS Final products and Rapid products provided by GFZ, known as GBM, is shown in Figure 5.12. *The orbit accuracy for GPS, GLONASS, Galileo, and BDS MEO satellites in terms of averaged 1D RMS is 1.4, 4.7, 2.2, and 3.7 cm, respectively, while for BDS GEO and IGSO satellites the value is 117.0 cm and 11.6 cm, respectively. Due to the uneven tracking stations and insufficient force models, e.g., solar radiation pressure, the performance of BDS is inferior to that of GPS and Galileo, especially for BDS GEO and IGSO satellites (Zhao et al., 2022). As expected, there is almost no difference between the epoch-parallel and traditional batch solutions.*

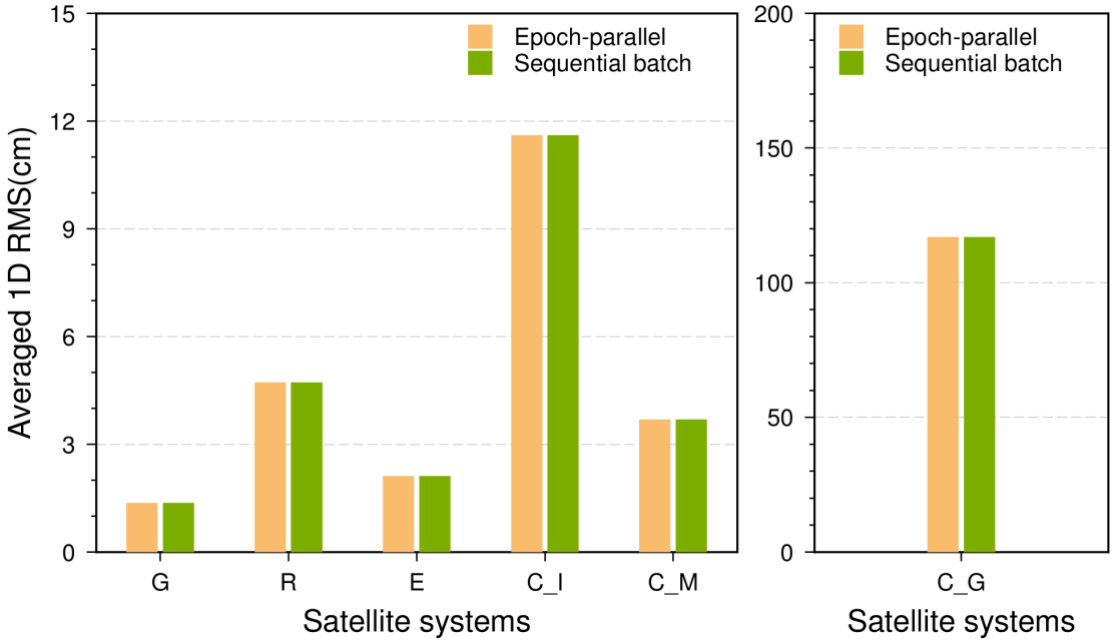

Figure 5.12 RMS values of estimated part for different solutions. GPS orbits are compared with the IGS Final products, while the other constellations are compared with the GBM Rapid products. Note the different y-axis scales between different panels.

5.4.3 Accuracy of real-time orbits

Taking the IGS Final products and GBM products as references, the averaged RMS values of user-available orbits are provided in Figure 5.13. The 120min solution shows the worst results, with an average 1D RMS value of 4.7, 7.3, 6.4, 164.7, 29.3, and 9.2 cm for the GPS, GLONASS, Galileo, BDS GEO, BDS IGSO, and BDS MEO satellites, respectively. With the decrease of the orbit update interval, the orbit accuracy in three directions is improved gradually, especially for the along direction. Compared with the 120min solution as a reference, the average 1D RMS values in the 60min solution are improved by 34%, 20%, 47%, 16%, 38%, and 26% for the GPS, GLONASS, Galileo, BDS GEO, BDS IGSO, and BDS MEO satellites, respectively. When the orbit update interval is reduced to 30 minutes (i.e., 30min solution), the average 1D RMS values is further reduced to 3.4, 6.0, 3.9, 141.1 19.8, and 7.3 cm for the GPS, GLONASS, Galileo, BDS GEO, BDS IGSO, and BDS MEO satellites, respectively. The differences of MEO satellites between 30min, 20min, and 10min solutions are less than 1.0 cm, in which the 10min solution shows the best performance. Specifically, the orbit differences between the 30min and 10min solution in the along direction are 0.5 cm, 0.6 cm, 0.9 cm, 2.2 cm, 1.9 cm, and 0.9 cm for the GPS, GLONASS, Galileo, BDS GEO, BDS IGSO, and BDS MEO satellites, respectively. In addition, a notable improvement is also found in the radial direction for BDS GEO and IGSO satellites. Compared with the 120min solution, the accuracy in the along direction is improved by 55% and 27%. The obvious improvements in radial direction are attributed to the imperfect satellite force models (Guo et al., 2023).

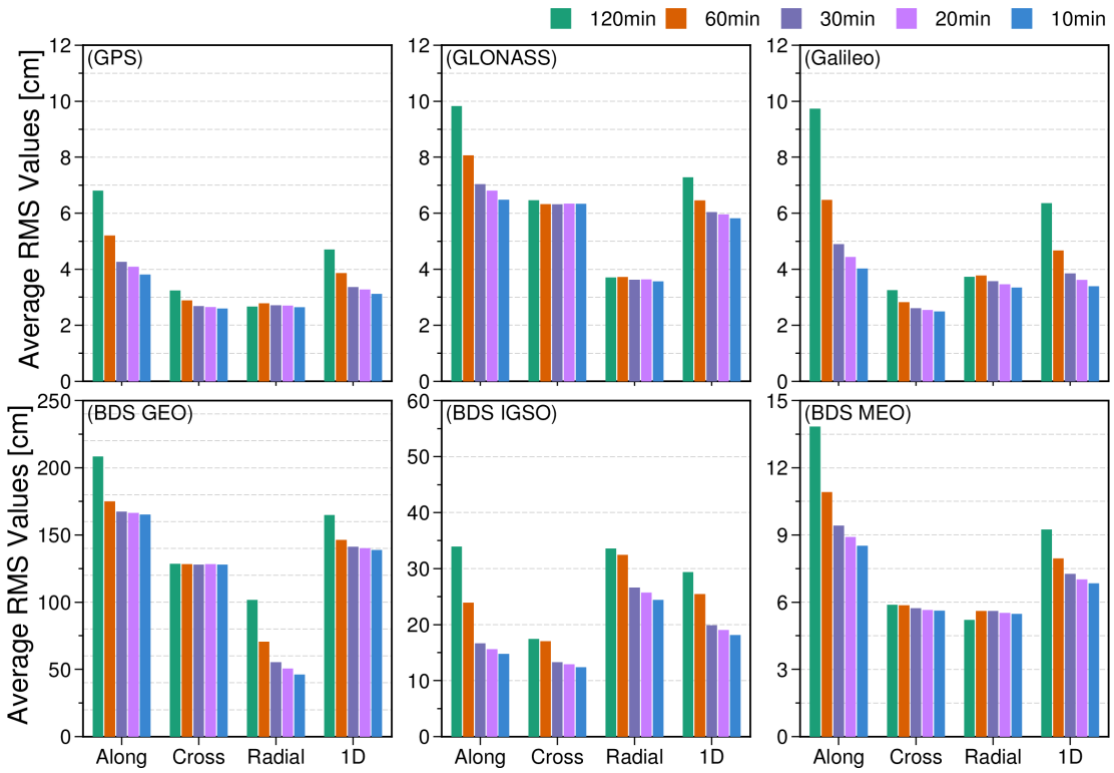

Figure 5.13 RMS values of user-available part for different solutions. GPS orbits are compared with the IGS Final products, while the other constellations are compared with the GBM Rapid products. Note the different y-axis scales between different panels.

The positioning performance could be affected by the update of the GNSS ultra-rapid orbits, i.e., switching from one to the next orbits inevitably leads to residual fluctuations in positioning solutions due to the discontinuities of two consecutive sessions. Hence, orbit discontinuity is a key indicator for evaluating orbit quality. Figure 5.14 shows the statistics of the orbit discontinuities for different solutions and constellations. The orbit discontinuities decrease gradually with the reduction of orbit update interval. For the satellite orbits updated per 120 min, the averaged 1D RMS values for GPS, GLONASS, Galileo, BDS GEO, BDS IGSO, and BDS MEO satellites are 3.5, 4.4, 4.5, 62.8, 15.6, and 6.0 cm. When the satellite orbit update interval is reduced to 60 min, the average 1D RMS value is improved by 30%, 29%, 28%, 40%, 13%, and 24% for the GPS, GLONASS, Galileo, BDS GEO, BDS IGSO, and BDS MEO satellites, respectively. Similar to the improvements observed in the 60min, the 30min solution also shows notable improvements with respect to the 60min solution, reaching 36%, 33%, 35%, 39%, 26%, and 29% for the GPS, GLONASS, Galileo, BDS GEO, BDS IGSO, and BDS MEO satellites, respectively. The best performance is observed in the 10min solution, with an average 1D RMS value around 1.0 cm for MEO satellites.

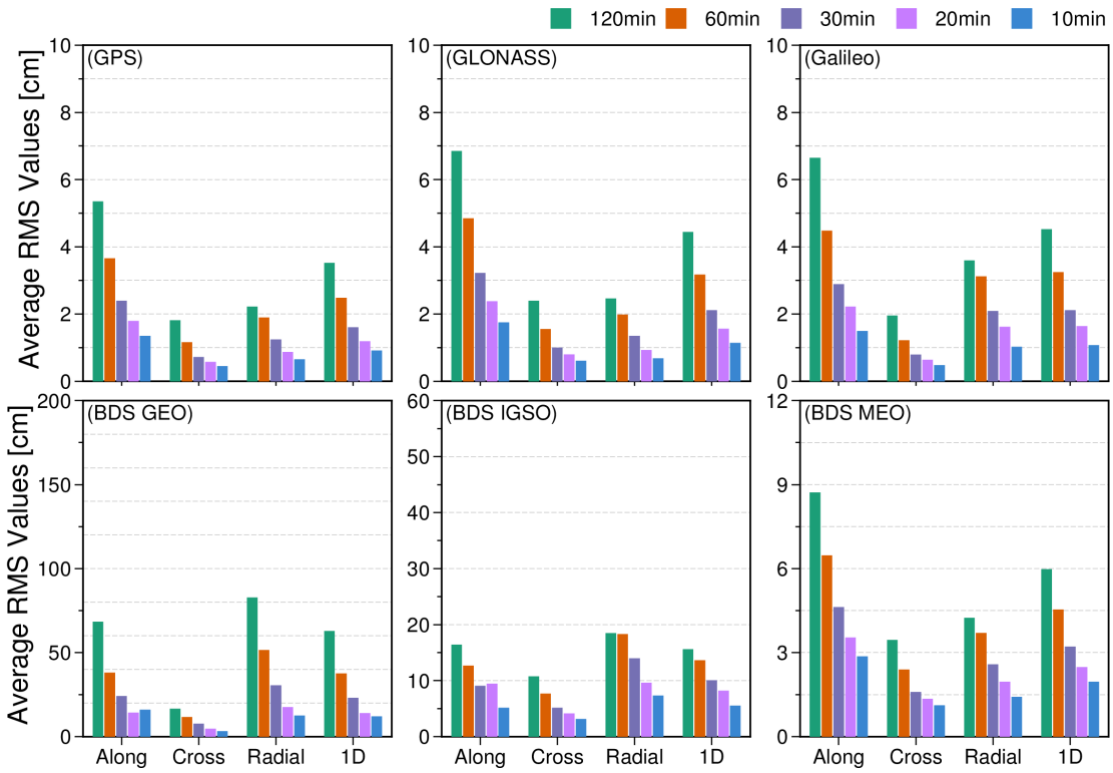

Figure 5.14 RMS values of orbit discontinuities for different solutions. Note the different y-axis scales between different panels.

In terms of the 95th percentile, as shown in Figure 5.15, the orbit discontinuity values are decreased by a factor of three to four. The orbit discontinuities in the 10min solution for GPS, GLONASS, Galileo, BDS GEO, BDS IGSO, and BDS MEO satellites are 1.6, 2.1, 2.0, 17.8, 11.0, and 3.9 cm, respectively, which show an obvious drop if the update latency is lengthened, from 10-min to 20-min, 20-min to 30-min, 30-min to 60-min and 60-min to 120-min. Both Figure 5.14 and Figure 5.15 show that satellite orbits with 10-minute update perform best among the four solutions.

The differences between the observed ranges (via SLR observations) and the computed spatial distances (via GNSS orbits and coordinates of SLR stations) form the so-called "SLR residuals". The analysis of these SLR residuals offers the opportunity to investigate the quality of the GNSS orbits. Figure 5.16 shows the statistics of SLR residuals for different solutions. The orbit differences between different solutions are minor, less than 0.5 cm, except for BDS IGSO and BDS MEO satellites in the 120min solutions. The differences between BDS MEO satellites in the 120min solution and the other solutions are attributed to the low orbit accuracy of PRN C10 (BDS-2 MEO). Reducing orbit update interval can improve orbit accuracy with poor orbit accuracy, e.g., BDS IGSO satellites.

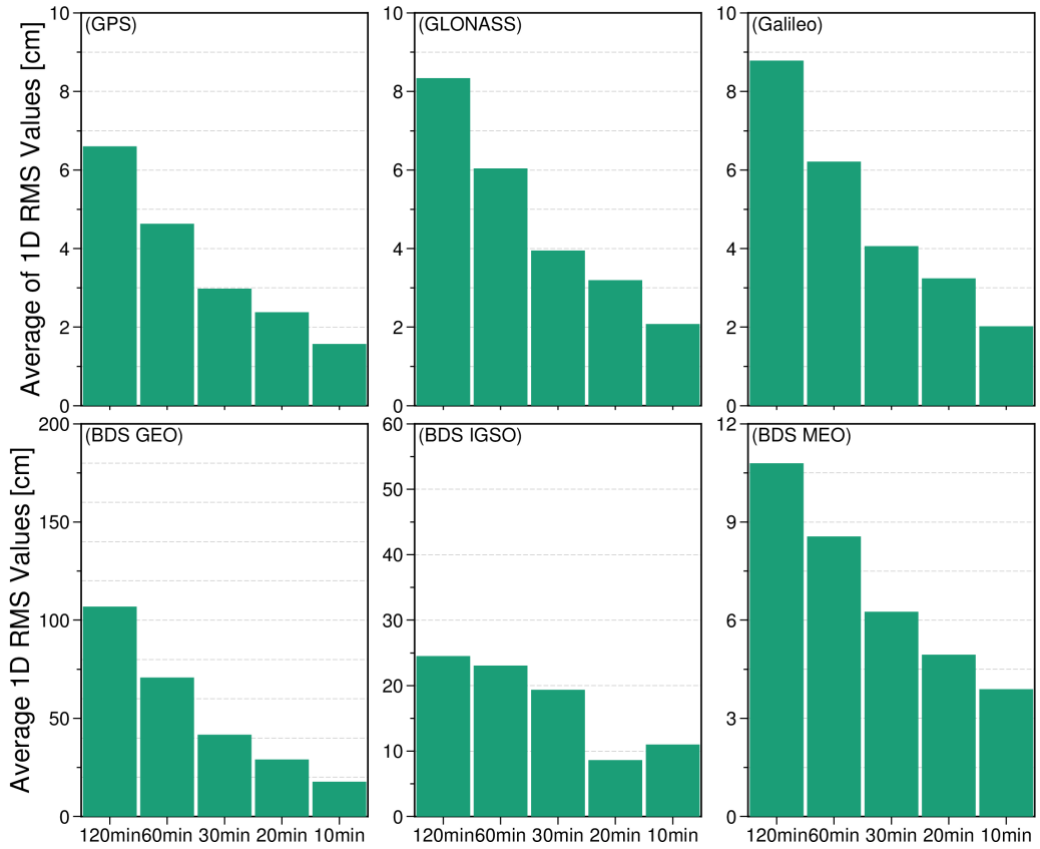

Figure 5.15 Averaged 1D RMS (solid bar) values of orbit discontinuities for different solutions. Note the different y-axis scales in different panels.

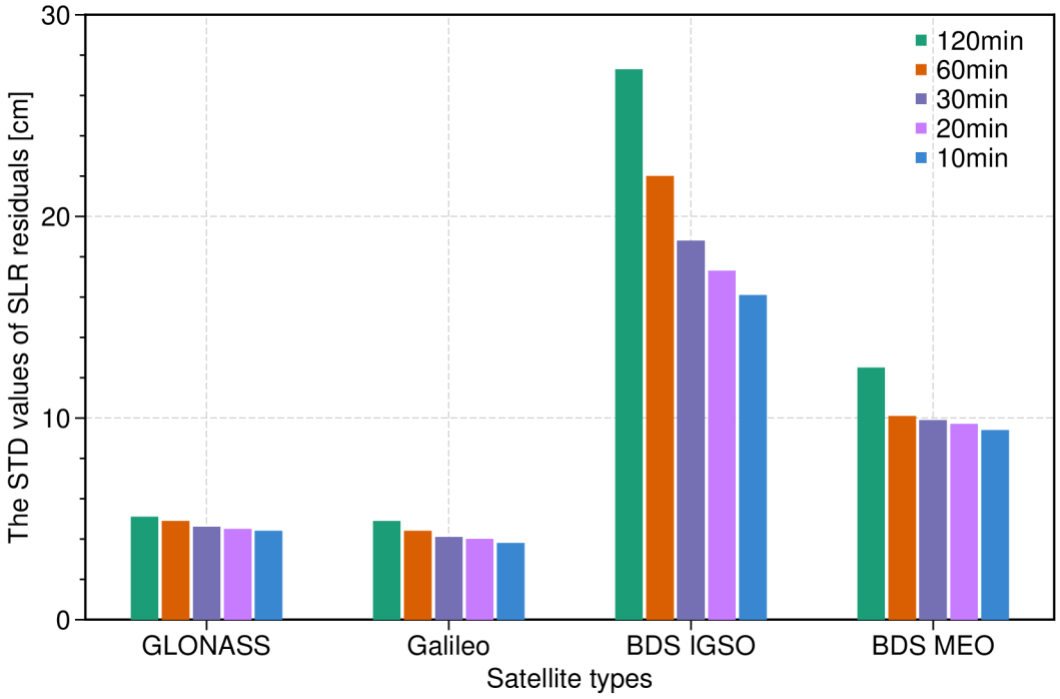

Figure 5.16 The statistics of SLR residuals for different solutions. Note that outliers have been removed before statistics. The BDS GEO satellites are excluded since there are no SLR observations available during January of 2021. Note that only the predicted part is used in the SLR validation.

5.5 Application of multi-GNSS orbits in positioning

GNSS RT-PPP strongly relies on precise satellite orbits and clocks, especially the latter requires a high update rate, e.g., five seconds, due to its limited prediction accuracy. Such a high-rate update frequency is a burden to both data analysis and communication. Moreover, interruption in data communication is almost unavoidable. For the new constellations such as Galileo and BDS-3 with high-stability hydrogen clocks onboard, it is possible to predict satellite clocks to a longer arc. The strategies proposed in Section 5.2 and Section 5.3 enable the half-hourly or even rapid orbit update. Section 5.4 further demonstrates that most satellite orbits with orbit update interval of less than 30 minutes show similar performance. Therefore, the feasibility of RT-PPP with predicted orbits and clocks updated per 30 minutes is investigated in this section. The solution with orbits and clocks updated per 60 minutes is taken as a reference.

5.5.1 Clock prediction strategy

Most GNSS satellites are equipped with highly-stable clocks, such as hydrogen maser clocks, especially the newly-launched Galileo, BDS-3, and GPS BLOCK III satellites. Various clock prediction models have been proposed for the prediction of short-term and long-term periods (Senior et al., 2008; Zheng et al., 2008; G. W. Huang et al., 2013; El-Mowafy et al., 2016; Nie et al., 2017). Despite several studies with sophisticated clock prediction methods, the polynomial model plus periodic terms is widely used and has been demonstrated with good performance (Nie et al., 2017; H. Ge et al., 2021). Therefore, the following function is adopted to describe the clock at epoch i (time t_i)

$$\tau^{sat}(t_i) = a_0 + a_1 t_i + a_s \sin\left(\frac{2\pi}{T} t_i\right) + a_c \cos\left(\frac{2\pi}{T} t_i\right), \tag{5.12}$$

where a_0 denotes clock offset at the reference time; a_1 is frequency, a_s and a_c are the coefficients of periodic terms. To avoid the impact of potential jumps, the initial value can be eliminated by differencing between two adjacent epochs, for example, t_i and t_{i+1}. The above function is rewritten as follows

$$\begin{aligned}\tau^{sat}(t_{i+1}) - \tau^{sat}(t_i) = a_1(t_{i+1} - t_i) + a_s\left[\sin\left(\frac{2\pi}{T} t_{i+1}\right) - \sin\left(\frac{2\pi}{T} t_i\right)\right] \\ + a_c\left[\cos\left(\frac{2\pi}{T} t_{i+1}\right) - \cos\left(\frac{2\pi}{T} t_i\right)\right]\end{aligned}. \tag{5.13}$$

Given a series of clocks with n epochs, the n-1 epoch-differenced clocks are fitted via the least-square adjustment to estimate the unknown parameters in Equation (5.13). Then, the predicted clock at a given time t after epoch n is represented as follows

$$\begin{aligned}\tau^{sat}(t) = \tau^{sat}(t_n) + a_1(t - t_n) + a_s\left[\sin\left(\frac{2\pi}{T} t\right) - \sin\left(\frac{2\pi}{T} t_n\right)\right] \\ + a_c\left[\cos\left(\frac{2\pi}{T} t\right) - \cos\left(\frac{2\pi}{T} t_n\right)\right]\end{aligned}, \tag{5.14}$$

where t_n is the last epoch of the fitting arc, $\tau^{sat}(t_n)$ is the clock offset at epoch n. According to Equation (5.14), the corresponding formal error of predicted clocks is represented as

$$\sigma^2_{\tau^{sat}(t)} = \sigma^2_{\tau^{sat}(t_n)} + \sigma^2_{a_1}(t-t_n)^2 + \sigma^2_{a_{s_1}}\left[sin\left(\frac{2\pi}{T}t\right) - sin\left(\frac{2\pi}{T}t_n\right)\right]^2 + \sigma^2_{a_{c_1}}\left[cos\left(\frac{2\pi}{T}t\right) - cos\left(\frac{2\pi}{T}t_n\right)\right]^2, \quad (5.15)$$

where σ_{a1}, σ_{a_s} and σ_{a_c} are the formal errors of a_1, a_s and a_c respectively, $\sigma^2_{\tau^{sat}(t_n)}$ is the precision of the clock offset at epoch n. Following H. Ge et al. (2021), the optimal length of fitting arc for the polynomial model is 24 hours. To avoid the impact of large clock discontinuities and outliers in the clock time series, quality control must be carried out before calculating clock coefficients and obtaining predicted clocks using Equation (5.13) - (5.15). The clock time series are converted to the frequency, which is defined as

$$d\tau_i = \frac{\tau_i - \tau_{i-1}}{t_i - t_{i-1}}. \quad (5.16)$$

In addition, anomalies in frequency data are detected based on five times of the Median Absolute Deviation. As satellite clocks are estimated simultaneously with orbits, the update rate is the same as orbits.

5.5.2 Observation weighting strategies

After considering all errors related to the satellite, propagation path, and ground station, the following stochastic model is applied (Takasu, 2013)

$$\sigma^2 = \frac{\sigma^2_{obs}}{\sin^2(elev)} + \sigma^2_{orb} + \sigma^2_{clk}, \quad (5.17)$$

where σ_{obs} denotes the constant observation noise, 1 m for pseudorange and 1 cm for phase observations, respectively. $elev$ is the elevation angle and the term $sin^2(elev)$ considers the mismodeling effects and multi-path for observation at low elevation angle. To further consider the impact of satellite orbits and clocks, the terms of σ_{orb} and σ_{clk} are included. Note that the last two terms can be ignored in most post- or real-time processing where the precise satellite orbits and clocks are available. It would not cause any problem as long as the quality of orbits and clocks of each satellite is comparable. However, if the performance of different satellites differs with each other significantly, for example, in a multi-GNSS solution where a certain type of satellite yields poorer quality, it is necessary to properly downweight them to avoid any degradation to the solution (Kazmierski et al., 2018; Kiliszek et al., 2022).

In this section, optimized weighting strategies of the observations are introduced to account for the orbit and clock prediction error. For a comprehensive assessment of orbit and clock errors, SISRE is the first choice (Kazmierski et al., 2018). By considering the

contribution of orbit and clock errors to observation equation, Equation (5.17) is represented as

$$\sigma^2 = \frac{\sigma_{obs}^2}{\sin^2(elev)} + \sigma_{sis}^2, \tag{5.18}$$

where σ_{sis} is SISRE. The typical SISRE, which is calculated by comparing the real-time orbits and clocks to a reference product, cannot be achieved due to the lack of reliable reference products in real-time. However, the accuracy of estimated and predicted orbits and clocks of consecutive sessions is comparable in most cases, and thus the SISRE is also expected to show a similar pattern. Therefore, the real-time SISRE of the epoch (epoch $iepo$) at the current session (session $ises$) can be predicted by previous sessions and an approximation of S_{sis} is proposed

$$\sigma_{sis}^2(ises, iepo) = \left(\frac{S_{sis}(ises-n,iepo)+\cdots+S_{sis}(ises-1,iepo)}{n}\right)^2, \tag{5.19}$$

where $ises$ is the session number, $iepo$ is the epoch number of a session, $nses$ is the number of sessions. $S_{sis}(\cdot)$ is the function of SISRE calculation, detailed description of SISRE is made by Oliver Montenbruck, Steigenberger, and Hauschild (2014). Different from the statistic description of SISRE, the SISRE value $\sigma_{sis}(ises, iepo)$ is derived from the several epochs of previous sessions, one epoch per session. According to my experience, three sessions, that is, $nses$ is set to 3 are taken.

The SISRE is mainly dependent on the error of the radial component of orbits and clocks, especially the latter one (Cheng et al., 2018). Consequently, the time variation of the clocks differs not only between constellations but also between satellites (Kazmierski et al., 2020; Carlin et al., 2021). Therefore, the precision of predicted clocks is assessed in Figure 5.17*. Similarly, the Galileo, GPS, BLOCK IIIA, and BDS-3 MEO satellites have better performance than other satellites, in which Galileo performs the best, with an average RMS of less than 0.1 ns (30-min updated clocks). For GLONASS, BDS GEO and IGSO satellites, the clock accuracy is as large as 0.5 ns. The performance of different types of satellites is similar for the 60-min updated clocks, and the magnitude is much larger than the 30-min updated clocks. Compared with the clock precision presented in Figure* 5.17*, the clock error still dominates the SISRE value for most satellites. Therefore, Equation (5.17) can be simplified as*

$$\sigma^2 = \frac{\sigma_{obs}^2}{\sin^2(elev)} + \sigma_{clk}^2. \tag{5.20}$$

In this case, only the clock accuracy information is required for PPP users.

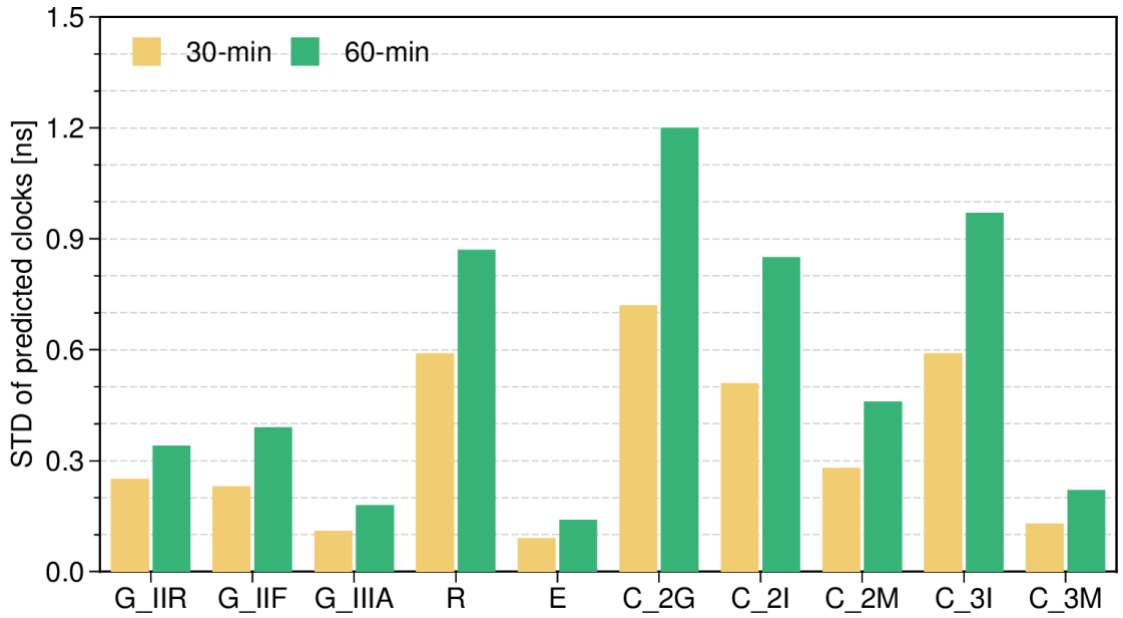

Figure 5.17 Satellite clock prediction precisions for different types of satellites with 30-min and 60-min update rate.

Although the clock formal error in Equation (5.15) *can serve as an indicator to reflect the performance of predicted product, it can be over-optimistic. Therefore, the above formal error should be scaled to represent the real precision with*

$$\sigma_{clk} = f * \sigma_{clk\_formal}, \tag{5.21}$$

where σ_{clk_formal} *is the formal error. The factor is calculated based on the satellite-specific empirical value from several previous sessions*

$$f = \frac{MEAN_{std}}{MEAN_{clk\_formal}}, \tag{5.22}$$

where $MEAN_{std}$ *is the mean STD of clock precision for a certain satellite group,* $MEAN_{clk\_formal}$ *is the corresponding mean formal error. Through Equation (5.22), the rough scaling law between the precision of the satellite clock and its formal error is established. Table* 5.2 *lists the scaling factors for satellites used in this study. These values are determined empirically using one month of data, but could be updated using different periods in real-time applications.*

Table 5.2 Scaling factors between the accuracy and formal errors of predicted clocks for different types of satellites.

Type	**G_IIR**	**G_IIF**	**G_III**	**R**	**E**
Scaling factor	13	49	49	28	56
Type	**C_2G**	**C_2I**	**C_2M**	**C_3I**	**C_3M**
Scaling factor	171	75	46	319	74

5.5.3 Data processing

According to the proposed orbit and clock prediction strategy, one month of 100 multi-GNSS stations is processed to generate predicted orbits and clocks with 30- and 60-min update rate. The 30-s sampling observations from additional 62 stations (Figure 5.18*) are then processed in static and kinematic PPP mode to validate our method. In total, five cases are designed to evaluate our proposed methods, as shown in Table* 5.3*.*

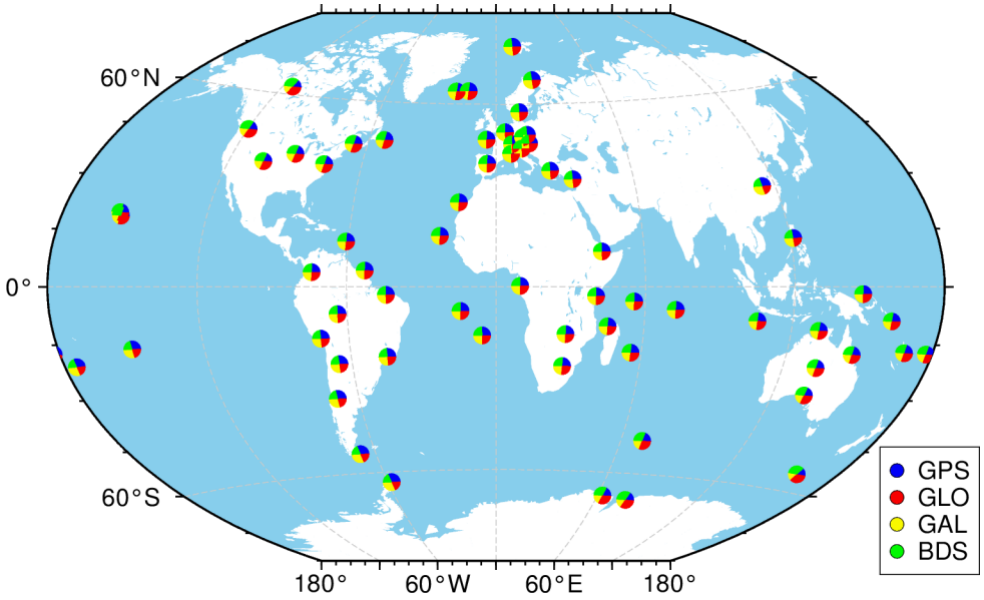

Figure 5.18 IGS stations for PPP validation.

Table 5.3 Cases of weighting the observations and handling the SISRE in PPP solutions.

Case	Observation weighting	Estimating SISRE
ORIG	$\sigma^2 = \frac{\sigma_{obs}^2}{\sin^2(elev)}$	No
CLK	$\sigma^2 = \frac{\sigma_{obs}^2}{\sin^2(elev)} + \sigma_{clk}^2$	No
CLK_F	$\sigma^2 = \frac{\sigma_{obs}^2}{\sin^2(elev)} + f^2 \cdot \sigma_{clk}^2$	No
SISPRE	$\sigma^2 = \frac{\sigma_{obs}^2}{\sin^2(elev)} + \sigma_{sisre}^2$	No
SISEST	$\sigma^2 = \frac{\sigma_{obs}^2}{\sin^2(elev)}$	Yes

Three single-constellation solutions, including GPS, Galileo, and BDS are investigated. GLONASS-only solution is not included due to the poor clock prediction accuracy (around 0.6 ns for 30-min update interval) and thus the expected poor positioning performance. Multi-GNSS solutions, including Galileo+BDS (GE), Galileo+GPS+BDS (GEC) are investigated and the quad-constellation solution where the contribution of GLONASS is considered (GREC). Apart from the different weighting methods, the same processing strategies are adopted by the five cases. To evaluate the accuracy, the coordinates from the IGS weekly combined solution are taken as a reference, and calculate the 3-

dimensional (3D) error, that is, $3D = \sqrt{N^2 + E^2 + U^2}$ *where* (N, E, U) *are the coordinate bias in the north, east, and up components, respectively*.

5.5.4 PPP Validation

Static positioning

Figure 5.19 *presents the statistics of positioning accuracy for different cases. When no special consideration of the orbit and clock errors is applied, that is, solution ORIG, the positioning accuracy using the 30-min updated products is within 5 cm for the Galileo-only and multi-GNSS solutions, meanwhile for the GPS-only and BDS-only solutions, the accuracy is around 7 to 11 cm. A significant improvement is introduced in all solutions if the predicted clock accuracy is considered, especially in the CLK_F case where the clock formal error is scaled properly (see Table* 5.2*). The proposed strategy (SISPRE) achieves a comparable accuracy with solution CLK_F for both single-GNSS and multi-GNSS solutions, which is slightly better than the solution where the SISRE is estimated as unknown parameters in the GPS-only and multi-GNSS solutions. It is also obvious that the accuracy of predicted clocks instead of orbits has a larger impact on positioning, as expected. Regarding the contribution of different constellations, the Galileo-only solutions are much better than the GPS-only and BDS-only solutions, and both have comparable accuracy with respect to its combination with other constellations, mainly thanks to the highly stable clocks onboard the Galileo satellites. Note that in ORIG where no special handling of the observation weighting is applied, the Galileo-only solutions are better than the multi-GNSS solutions. The reason is that the clock prediction accuracy of BDS and GPS is much worse (see Figure* 5.17*), and without downweighing these satellites properly they will degrade the accuracy in multi-GNSS solutions.*

For the 60-min predicted solutions, the positioning accuracy is worse than the 30-min solutions by a factor of up to two (the BDS-only case), due to the poorer clock prediction accuracy in the 60-120 minutes arc than in the 30-60 minutes arc (see Figure 5.17*). The quad-constellation solution achieves an accuracy of 9 cm in the ORIG case, and is improved to 5 cm if the proper weighing is adopted (CLK_F and SISPRE) or additional parameter is estimated (SISES). It is also confirmed that the Galileo constellation contributes larger than GPS and BDS constellations in the multi-GNSS solutions, and proper weighting of different systems is necessary, otherwise the positioning accuracy would be deteriorated.*

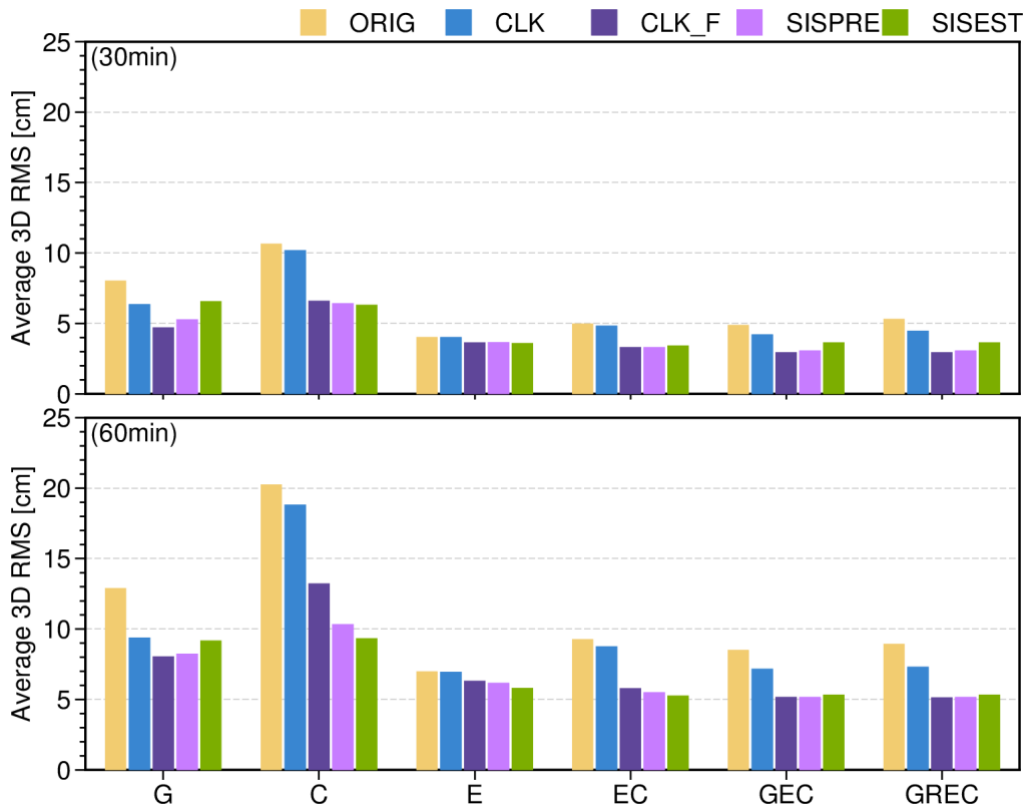

Figure 5.19 Accuracy of different cases in static PPP in terms of 3D RMS position error. The upper and lower panel is the positioning results based on 30-min and 60-min predicted orbits and clocks, respectively.

To investigate the difference between CLK_F and SISEST cases, a further comparison of each station is shown in Figure 5.20 *and Figure* 5.21*. For the Galileo-only solution, the SISEST case performs better than the CLK_F on most stations, except for the horizontal component of a few stations. In contrast, the horizontal components for the SISEST case with quad-constellation are worse than those for the CLK_F case. By comparing the Galileo-only solution and quad-constellation solution, the results show that the contribution of multi-GNSS in the CLK_F case is larger than that in the SISEST case in the horizontal components. The possible reason for the different behaviors is that CLK_F approach gives a deterministic relationship between different satellite types, which needs to be estimated in the SISEST approach.*

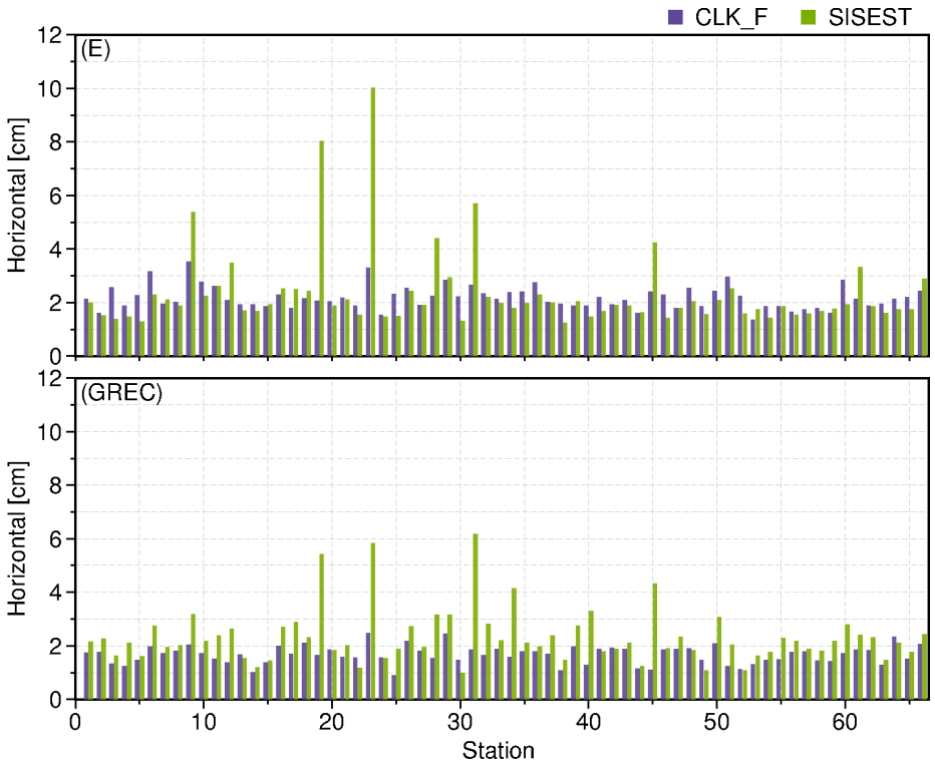

Figure 5.20 Horizontal position accuracy of each station with 30-min updated orbits and clocks for Galileo-only (upper) and GREC (lower) solutions.

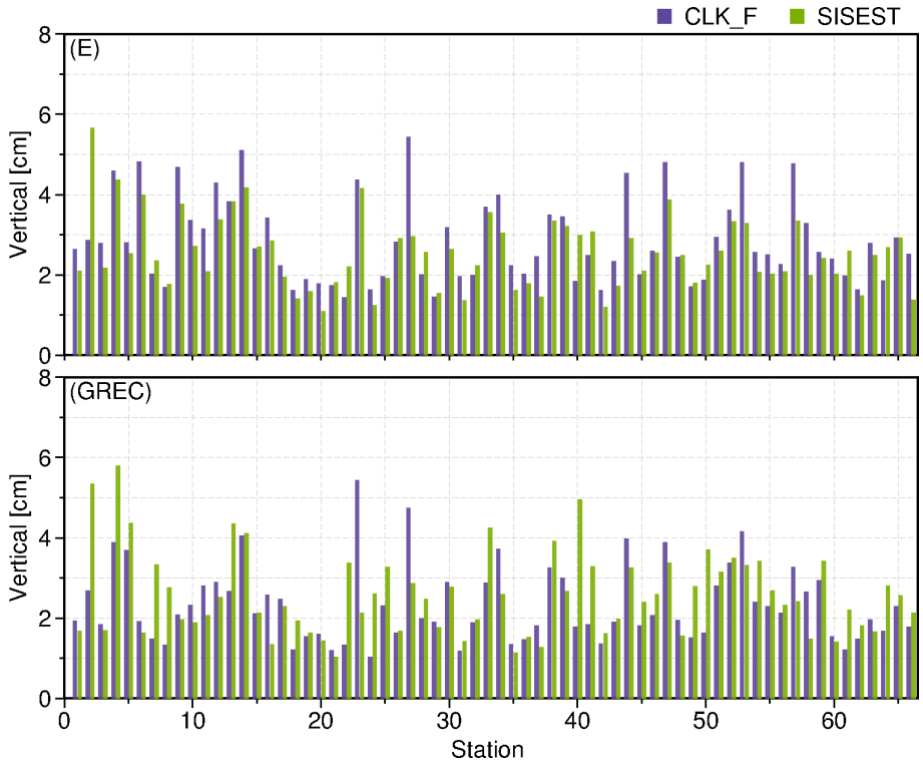

Figure 5.21 Vertical position accuracy for each station with 30-min updated orbits and clocks for Galileo-only (upper) and GREC (lower) solutions.

In addition to the average 3D RMS results, the horizontal and vertical RMS for Galileo-only and quad-constellation solution are also given in Table 5.4*. The Galileo-only and GREC solutions are presented as they have optimal performances compared to other solutions. For the 30-min solutions, the horizontal accuracy of Galileo-only solutions is 2.2 cm, and the vertical one varies between 2.5 and 3.2 cm. The quad-system GREC solutions on the other hand, are more sensitive to handling weights. In the ORIG case, the accuracy is worse than the Galileo-only solutions in horizontal and vertical components, whereas in the CLK_F and SISPRE cases, the accuracy is much better. The 60-min solutions are worse than the 30-min ones, indicating the necessity to further reduce the update rate when using predicted products in real-time PPP. In any case, horizontal and vertical accuracy within 5 cm and 7 cm can be achieved for the 30-min and 60-min solutions, respectively.*

Table 5.4 Average static position error for Galileo-only and GREC solutions using 30- and 60-min updated orbits and clocks. The unit is cm.

Solution	**30-min**						**60-min**					
	E			GREC			E			GREC		
	Up	2D	3D	Up	2D	3D	Up	2D	3D	Up	2D	3D
ORIG	3.2	2.3	4.0	4.4	2.9	5.3	5.6	4.0	7.0	6.8	5.2	8.9
CLK	3.2	2.3	4.0	3.6	2.5	4.5	5.6	3.9	7.0	5.4	4.7	7.3
CLK_F	2.8	2.2	3.6	2.3	1.7	2.9	5.0	3.7	6.3	4.0	3.1	5.1
SISPRE	2.9	2.2	3.7	2.4	1.8	3.1	4.9	3.6	6.2	3.8	3.3	5.2
SISEST	2.5	2.3	3.6	2.6	2.3	3.6	4.3	3.6	5.8	3.9	3.5	5.3

Kinematic positioning

Kinematic PPP results of five cases with different constellation combinations are also performed using the same set of observations. Figure 5.22 *depicts the positioning accuracy of kinematic PPP results based on 30-min orbits and clocks. For the first 30-min, the cases of CLK-F and SISPRE both have better performance than the SISEST, especially for the GEC and GREC solution, even though a jump is observed at the 30-min epochs in some solutions, for example, the Galileo-only and EC solutions in the CLK and CLK_F case. This could be attributed to the orbit quality change when switching the different products. In general, our proposed solution (CLK_F and SISPRE) can reach a higher accuracy quickly than the SISEST case, and after 30-min the performances are similar. After 1-h convergence, single constellation can converge to 40.0 cm, while GEC and GREC converge to 30 cm. All the kinematic solutions with Galileo included can converge to 30.0 cm at the end of a 300 minutes session.*

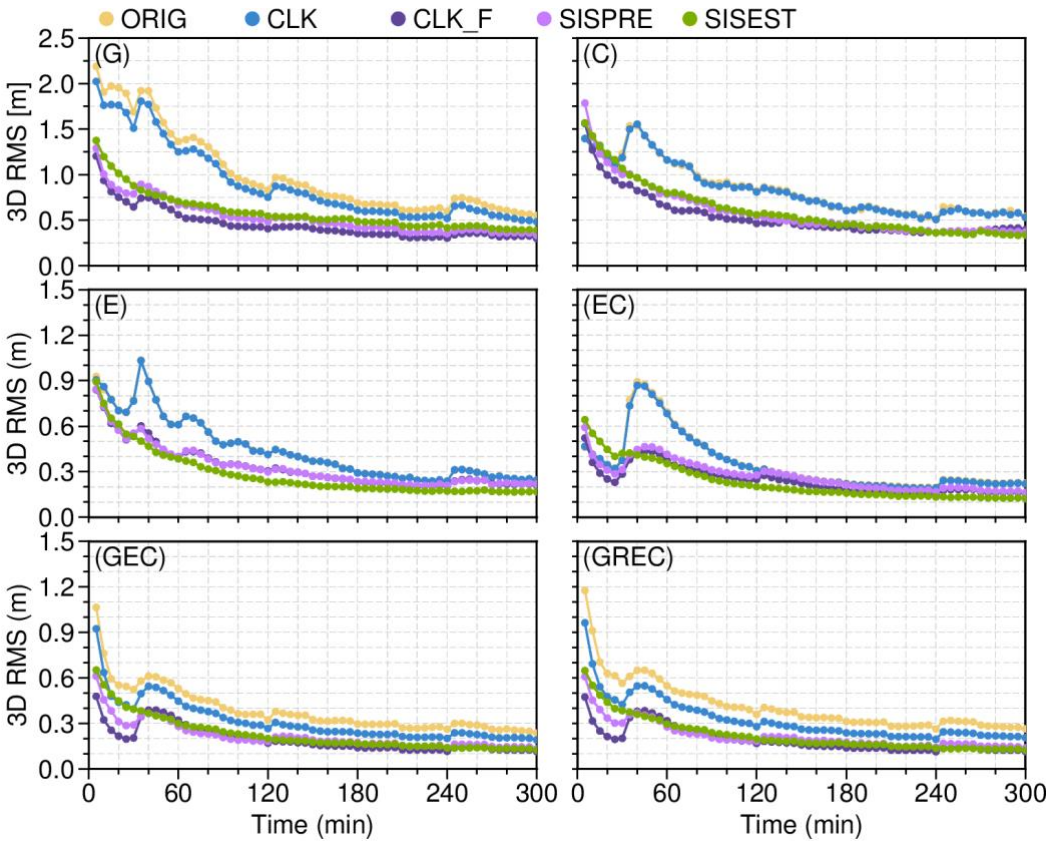

Figure 5.22 3D positioning accuracy using 30-min updated orbits and clocks. The average RMS of 62 stations over one month is presented. Note that each dot denotes the RMS of all epochs within 5-min and the observation sampling rate is 30-sec.

As an example, Figure 5.23 *shows the 24-h coordinates time series with the quad-constellation observations at station XMIS on DOY 340, 2021. One hour after the first epoch, the north and east components reach within 10 cm, whereas the up one fluctuates within 20 cm. The CLK_F and SISEST cases are more stable than other solutions, even though the SISEST case converges faster than the SISPRE one.*

The kinematic PPP accuracy based on 30-min updated orbits and clocks over all stations in one month is summarized in Figure 5.24*, where both the single-system and multi-GNSS solutions are included. Similar to the static PPP results, Galileo-only solution performs the best because of the superior quality of satellite clocks, while BDS-only still performs the worst. The horizontal accuracy of multi-GNSS solutions is around 5 cm, and the vertical one is within 10 cm, as long as the proper weighing strategy is adopted (CLK_F) or the SISRE is estimated (SISEST), which is much better than the ORIG and CLK cases. It is also interesting to observe that the SISEST case has the best accuracy for the Galileo-only solution compared to the other cases in both horizontal and vertical components.*

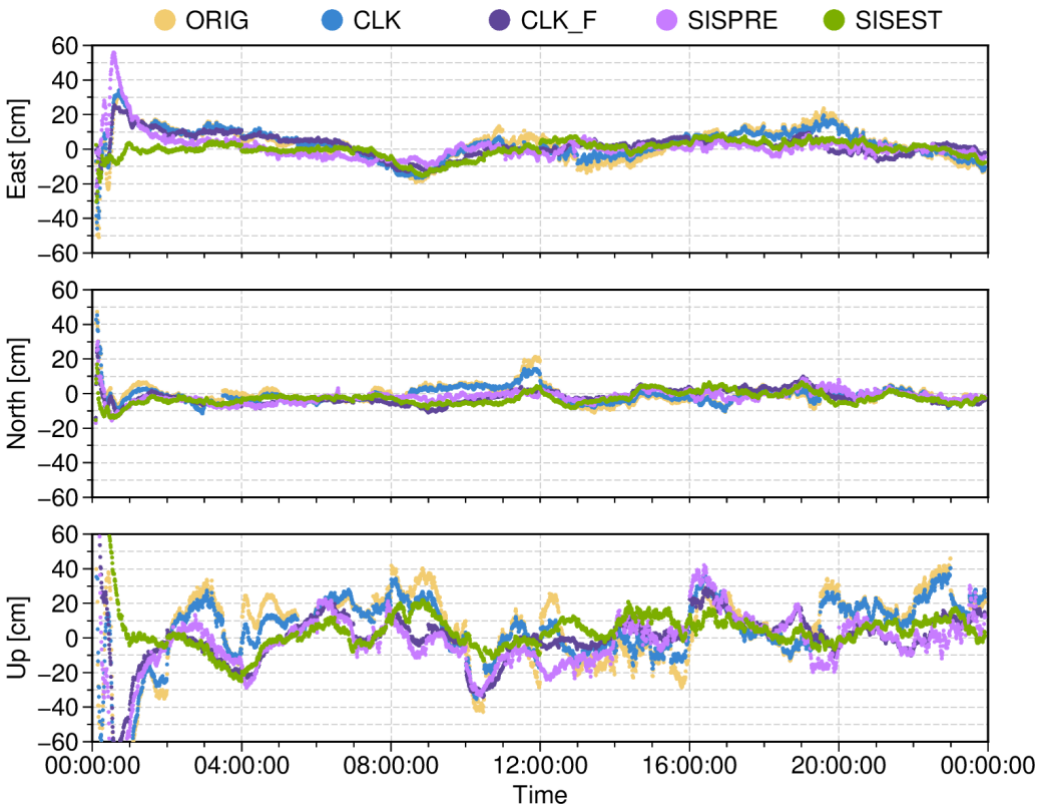

Figure 5.23 Positioning errors in the East, North, and Up components on DOY 340 of 2021 for station XMIS in kinematic mode.

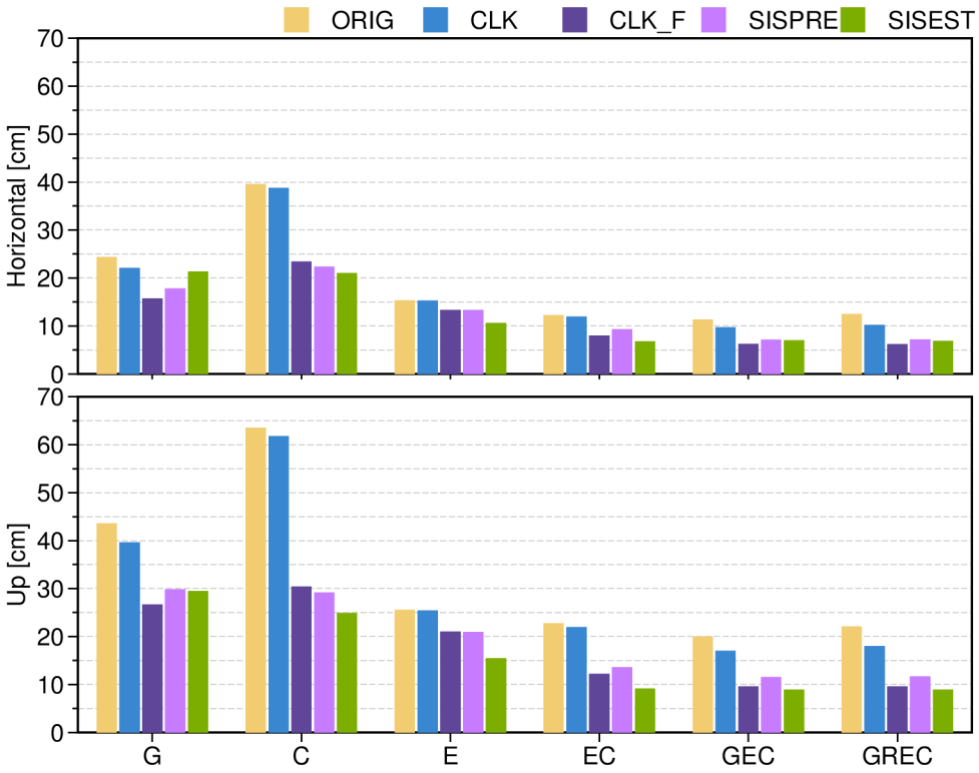

Figure 5.24 Average 3D positioning error with 30-min updated orbits and clocks for horizontal (upper) and vertical (lower) components.

The statistics of using both 30-min and 60-min updated products are given in Table 5.5*, including both Galileo-only and GREC solutions. For 30-min solutions, the GREC solution shows a position accuracy of 6.9 cm and 8.9 cm for the horizontal and vertical component, respectively. The CLK_F in the GREC solution is better than the ORIG case by a factor of two, reaching 6.2 cm horizontally and 9.6 cm vertically. The 60-min solutions have less optimal performance, as expected, and the best accuracy is achieved by the GREC solution in the SISEST case, with a horizontal and vertical RMS of 9.8 and 12.5 cm, respectively. For the Galileo-only solution, the SISPRE case is worse than the CLK_F results in both horizontal and vertical components, which is also observed in all single-constellation solutions (not shown here). Compared with the SISPRE case, the CLK_F considers not only empirical behaviors for each satellite type by the scaling factor in Equation (5.21), but also the real clock performance of the current session by the formal error in Equation (5.21). When there are more observations involved (the GREC situation) or the prediction time becomes shorter (30 min), the discrepancy between the two cases becomes smaller.*

Table 5.5 Averaged position error for the Galileo-only and GREC solutions with 30- and 60-min updated orbits and clocks. The unit is cm.

Solution	**30-min**						**60-min**					
	E			GREC			E			GREC		
	Up	2D	3D	Up	2D	3D	Up	2D	3D	Up	2D	3D
ORIG	25.5	15.3	29.9	22.0	12.4	25.4	38.8	22.4	44.9	33.4	20.1	39.1
CLK	25.4	15.3	29.8	18.0	10.2	20.8	38.7	22.5	44.9	26.6	15.9	31.2
CLK_F	21.0	13.3	24.9	9.6	6.2	11.4	27.7	17.8	33.0	14.8	10.0	17.9
SISPRE	21.0	13.3	24.9	11.7	7.2	13.8	35.8	23.0	42.7	23.2	14.5	27.4
SISEST	15.4	10.6	18.8	8.9	6.9	11.3	20.5	14.0	25.0	12.5	9.8	16.0

5.6 Chapter summary

The main findings in this chapter are summarized as follows.

Section 5.1 demonstrates the consistency between batch and epoch-parallel processing strategies. The proposed method is rigorously equivalent to the sequential batch processing strategy. Moreover, it can take full advantage of multi-cores and multiple computers by dividing the long session into short sub-sessions and each sub-session can be processed parallelly.

Section 5.2 presents the flowchart of epoch-parallel processing strategy and computation efficiency for multi-GNSS observations. Together with parallel processing of data downloading, quality control, phase windup calculation, residual checking and orbit integration, the main contribution of this strategy is the realization of parallel parameter estimation, including parameter recovery. The time required for one parameter estimation of around 100 stations and 120 satellites can be reduced from 13 minutes to 6 min. Compared with sequential

batch processing, the overall computation time is reduced by 25% to 49%, with more than two nodes utilized. However, the benefits of using more than four nodes are less significant. With an optimized epoch-parallel POD strategy, the ultra-rapid orbits can be updated within 30 minutes for a global network of 90 tracking stations and one hour for a global network of 120 tracking stations.

Section 5.3 presents the orbit computation efficiency of the epoch-parallel processing strategy with historical information. Based on the UD-IAR strategy mentioned in Chapter 4, most fixed UD ambiguities will be removed. Since only a short arc of new observations is introduced, only one or two iterations of parameter estimation and observation cleaning is required. With the aid of historical information, the data processing with 100 stations and 120 satellites can be finished within 15 min, in which one iteration of parameter estimation only costs 3 min. To provide half-hourly orbits, the strategy proposed in Section 5.2 requires a high-frequency CPU (3.8 GHZ or 4.1 GHZ) and a smaller number of stations (e.g., 90), whereas the strategy proposed in this section does not require such strict hardware setup.

Section 5.4 presents the real-time orbit accuracy. The shorter the orbit update interval, the higher the orbit accuracy. Compared with IGS and GBM products, the average 1D RMS values of orbit updated per 10 minutes reach 3.1, 5.8, 3.4, 138.8, 18.1, and 6.8 cm for GPS, GLONASS, Galileo, BDS GEO, BDS IGSO, and BDS MEO satellites, respectively. The corresponding orbit DBDs is around 1.0 cm for MEO satellites. Except for BDS GEO and IGSO satellites, the orbits updated per 10-, 20-, and 30-minutes show similar performance, with a difference of less than 10%.

Section 5.5 investigates the performance of RT PPP with predicted orbits and clocks. Thanks to the high stability of onboard satellite clocks, the SISRE of newly launched satellites with predicted orbits and clocks, for example, Galileo, BDS-3, and GPS BLOCK IIIA satellites, is less than 8 cm within orbits updated per 30 to 60 min. Static and simulated kinematic PPP experiments show that applying predicted orbits and clocks to a PPP model is achievable, and 3D positioning accuracy is within 4.0 cm and 25.0 cm, respectively.

6 Conclusions and outlook

6.1 Conclusions and recommendations

With the increasing number of available satellites, the multiple GNSS constellations bring more opportunities and challenges for more reliable GNSS applications, in which the precise orbit and clock products are the key elements, especially for real-time GNSS applications. Currently, the available real-time orbits provided by IGS ACs are mainly predicted from the batch least-squares solution owing to its feasibility of routine processing. In order to provide high-precision satellite orbits, not only accurate force and signal-delay models are necessary, but also data processing efficiency should be improved. Parameter estimation takes the majority of the consuming time of a GNSS data processing task. Therefore, this thesis aims to provide high-precision real-time orbits from the following three aspects: (1) refining SRP modeling during eclipse seasons; (2) investigating the necessity of choosing UD IAR instead of DD IAR; and (3) improving data processing efficiency without destroying the consistency of estimated parameters.

Through three years of GPS observations, the performance of different SRP models, including the box-wing and adjustable box-wing as the a priori model and the ECOM1 and ECOM2 as the parameterization mode are investigated, especially for eclipsing satellites. Moreover, the two methods of handling the shadow factor, applying it to either the D (pointing toward to the Sun) or all directions, are also discussed. According to the theoretical analysis of acceleration expressions in D and B directions in DYB frame, where Y points along the satellite's solar panel axis and B completes the right-handed frame, it is confirmed that the number of significant periodic terms depends on the shape of a satellite and optical properties. The number of unknown parameters in the ECOM model can be reduced if there is a precise a priori box-wing model. The large coefficient values in the Y direction for some satellites convey that they possibly stem from non-gravitational forces in $\pm Y$ surfaces. Therefore, the parameter in Y direction should remain active during eclipse seasons. The high correlation between coefficients in the B direction and β angle is also possibly caused by unmodeled non-SRP forces. Therefore, keeping parameters in Y and B directions during eclipse seasons, that is, applying the shadow factor only in the D direction, is helpful to absorb some unmodeled forces. The statistics of estimated ECOM coefficients show that the best performance is achieved when applying the a priori adjustable box-wing model and applying the shadow factor to the D direction. This conclusion is also confirmed by orbit and ERP results. Compared with the solution using ECOM1 as the parameterization model without the a priori box-wing model and the shadow factor applied in three directions as reference, the RMS values of orbit DBD in the solution using a priori adjustable box-wing model with shadow factor applied in the D

direction are improved by 17.8%, 22.7%, and 26.1% for the BLOCK IIR satellites in eclipsing seasons in the along, cross, and radial direction, respectively.

Besides the investigation of SRP models, the superiorities of UD IAR are exploited in GNSS POD solutions. Although DD IAR and UD IAR are considered equivalent theoretically, there are still some differences between DD IAR and UD IAR: (1) UD IAR is based on the similarity of the fractional parts of float ambiguities and so is more sensitive to the accuracy of float ambiguities compared with DD IAR due to the temporal variation of UD ambiguities; (2) UD IAR is more robust than DD IAR since UD IAR has the ability to exclude outliers automatically; (3) UD IAR outperforms DD IAR in terms of processing efficiency, as the fixable UD ambiguities can be removed before parameter estimation. Owing to the dependence of UD IAR on the accuracy of float ambiguities in POD solution, UD IAR cannot be performed directly based on a float solution. Therefore, DD IAR should be performed in advance to achieve UD IAR solution. In the UD IAR solution, the STD values of NL UPDs are 0.03, 0.03, 0.11, and 0.13 cycles for GPS, Galileo, BDS-2, and BDS-3, respectively. Compared with the DD IAR solution, a better performance of orbits is observed in the UD IAR solution. For example, the orbit accuracy of BDS MEO satellites is also improved by 21.7% and 10.4% in the along and cross component, respectively. A similar conclusion can be derived for ERPs and other global geodetic parameters. Compared with IERS 14 C04, the PM offsets are reduced from 89.5 μas to 79.5 μas on the x-pole and from 79.3 μas to 71.8 μas on the y-pole. The PM rates also show an improvement of 8.0% and 9.2% for the x-pole rate and the y-pole rate, respectively. The improvements of station coordinates and GCC in three components are less than 5%.

Addressing the differences that occurred between UD IAR and DD IAR solutions, the performances of different realization of DD IAR and UD IAR are investigated with one year of GPS POD processing. DD IAR is usually worse than UD IAR, depending on how it is implemented. The largest orbit differences reach 7.2, 3.4, and 3.5 mm for the along, cross, and radial components, respectively. Compared with the UD IAR solution, orbit results show that the absence of independent DD ambiguities is the main factor causing significant orbit differences. Incorrectly fixed DD ambiguity is the other factor that degrades orbit accuracy. The two reasons are also confirmed in the investigation of other parameters, including ERPs, station coordinates, and GCC. In practice, achieving the two conditions is challenging, particularly when dealing with a massive network. One reason is that incorrect DD ambiguities can be hardly identified. The other reason is selecting independent DD ambiguities just from a pre-defined maximum independent baseline set carries the risk of missing a part of independent DD ambiguities. In general, UD IAR is highly recommended for daily GNSS data processing.

Based on the refined SRP model and UD IAR strategies, an epoch-parallel processing strategy, which is rigorously equivalent to the sequential batch processing strategy, is proposed to improve data processing efficiency. For the proposed epoch-parallel processing strategy, almost all the processes (e.g., orbit integration) can run in a parallel way. The time required for one parameter estimation of 100 stations and 120 satellites is reduced from around 13 minutes to

6 minuets. When there are two or more nodes, the whole processing time of achieving a POD solution is reduced from 25% to 49%. The improvement of overall computation efficiency is minor when the number of nodes is larger than four. With an optimized epoch-parallel POD strategy, the ultra-rapid orbits can be updated within 30 minutes for a global network of 90 tracking stations and one hour for a global network of 120 tracking stations. Taking advantages of UD IAR, the fixed UD ambiguities can be removed from normal equation. Moreover, we can reduce the number of data-cleaning steps from four to two as only a short arc containing new observations need data cleaning. With the aid of historical information, the data processing with 100 stations and 120 satellites can be finished in 15 minutes, in which one iteration of parameter estimation only costs 3 minutes. Thanks to the 30 minutes or even less orbit update interval and high stability of onboard satellite clocks, 3D positioning accuracy in static and simulated kinematic PPP with GPS, Galileo and BDS observations and predicted orbits and clocks is within 4.0 cm and 25.0 cm, respectively.

In conclusion, the real-time orbits with refined SRP model and UD IAR strategies show the best performance. Compared with IGS and GBM products, the average 1D RMS values of orbit updated per 10 minutes are 3.1, 5.8, 3.4, 138.8, 18.1, and 6.8 cm for GPS, GLONASS, Galileo, BDS GEO, BDS IGSO, and BDS MEO satellites, respectively. The corresponding orbit DBDs is around 1.0 cm for MEO satellites. Except for BDS GEO and IGSO satellites, the orbits updated per 10-, 20-, and 30-minutes show similar performance and the orbit difference of them is less than 10%. The superiority of shortening orbit update interval also is demonstrated from PPP results.

6.2 Future work

Inspired by the work already done in this study, the following studies will be performed in future.

It is well known that the modeling of solar radiation pressure is the main limiting factor in terms of orbit quality. SRP modeling still needs further investigation, especially for unmodeled forces during eclipse seasons. As shown in Figure 3.7, a visible linear trend of the coefficient Y_0 is observed for BLOCK IIF during eclipse seasons and then reduced after the β angle switches the sign. A similar phenomenon is found in Figure 4 of Duan and Hugentobler (2021). This phenomenon cannot be explained solely by thermal radiation, as the variation is asymmetrical. According to the results of this thesis, the SRP performances of different satellites in the same group are also different. Therefore, the classification of box-wing models should be divided according to satellite types.

A better understanding of the signal biases occurring in satellite and receiver hardware could lead to improved parametrizations. Currently, receiver-end deviations are not considered in the UD IAR solution. In practice, the receivers distributed worldwide are from multiple manufacturers of different types and/or versions. Different manufacturers or brands of receivers could cause deviations in the pseudo-range observations. The significant biases of

up to 0.4 cycles found in WL UPDs among different receiver types will impact the UPD estimation and hinder ambiguity resolution (B. Cui, Li, et al., 2021). Achieving accurate ambiguity resolution across all receiver types necessitates consistent pseudo-range and precise UPD products. Therefore, these deviations should be carefully estimated and compensated in the future.

Investigating the feasibility of UD IAR based on the ambiguity directly derived from float solution. Although in POD, the fractional parts of estimated UD ambiguities vary significantly along with time, some of satellites still have stable time series of NL UPD as shown in Figure 4.3. Hence, it is worthwhile to investigate the ambiguities of certain satellites with stable time series of NL UPDs to find out why these satellites performs better. After solving this problem, the realization of direct UD IAR based on the ambiguity derived from the float solution is possible.

Last but not least, data processing efficiency still needs to be improved. Including as many signals and stations as possible could make GNSS data processing time-consuming, For example, daily number of stations contributing to the IGS combination is up to 800 (Rebischung, 2021), which will increase sharply once Galileo, GLONASS and BDS enter the processing. For a network with 800, estimating millions of parameters many need more than 20 hours on a cluster of servers. Moreover, when we choose an undifferenced and uncombined processing strategy, unknown parameters could be much larger, for example, ionosphere parameters. Therefore, efficiency improvement of GNSS data processing is an ongoing topic.

Bibliography

Altamimi Z, Boucher C, Sillard P. (2002). New trends for the realization of the international terrestrial reference system. Advances in Space Research, 30, 175-184.

Altamimi Z, Collilieux X. (2009). IGS contribution to the ITRF. Journal of Geodesy, 83, 375-383.

Altamimi Z, Rebischung P, Collilieux X, Metivier L, Chanard K. (2018). Roadmap toward ITRF2020. In: AGU Fall Meeting Abstracts, pp. G42A-08.

Arnold D, Meindl M, Beutler G, Dach R, Schaer S, Lutz S, Prange L, Sosnica K, Mervart L, Jaggi A. (2015). CODE's new solar radiation pressure model for GNSS orbit determination. Journal of Geodesy, 89, 775-791. doi: 10.1007/s00190-015-0814-4.

Ashby N. (2003). Relativity in the global positioning system. Living Reviews in relativity, 6, 1-42.

Ashkenazi V, Hill C, Moore T, Whalley S. (1990). Orbit determination for GPS Satellites. In: Global Positioning System: An Overview: Symposium No. 102 Edinburgh, Scotland, August 7–8, 1989. Springer, pp. 187-194.

Bar-Sever Y, Kuang D. (2005). New empirically derived solar radiation pressure model for global positioning system satellites during eclipse seasons. IPN Progress Report, 42-160.

Bar-Sever YE. (1996). A new model for GPS yaw attitude. Journal of Geodesy, 70, 714-723.

Bertiger W, Bar-Sever Y, Dorsey A, Haines B, Harvey N, Hemberger D, Heflin M, Lu W, Miller M, Moore AW. (2020). GipsyX/RTGx, A New Tool Set for Space Geodetic Operations and Research. Advances in Space Research, 66, 469-489. doi: j.asr.2020.04.015.

Bertiger W, Bar-Sever Y, Dorsey A, Haines B, Harvey N, Hemberger D, Heflin M, Lu W, Miller M, Moore AW, Murphy D, Ries P, Romans L, Sibois A, Sibthorpe A, Szilagyi B, Vallisneri M, Willis P. (2020). GipsyX/RTGx, a new tool set for space geodetic operations and research. Advances in Space Research, 66, 469-489. doi: 10.1016/j.asr.2020.04.015.

Beutler G, Brockmann E, Gurtner W, Hugentobler U, Mervart L, Rothacher M, Verdun A. (1994). Extended orbit modeling techniques at the CODE processing center of the international GPS service for geodynamics (IGS): theory and initial results. Manuscripta Geodaetica, 19, 367-386.

Beutler G, Brockmann E, Hugentobler U, Mervart L, Rothacher M, Weber R. (1996). Combining consecutive short arcs into long arcs for precise and efficient GPS orbit determination. Journal of Geodesy, 70, 287-299.

Bizouard C, Lambert S, Gattano C, Becker O, Richard J-Y. (2018). The IERS EOP 14C04 solution for Earth orientation parameters consistent with ITRF 2014. Journal of Geodesy, 93, 621-633. doi: 10.1007/s00190-018-1186-3.

Blewitt G. (1989). Carrier phase ambiguity resolution for the Global Positioning System applied to geodetic baselines up to 2000 km. Journal of Geophysical Research: Solid Earth, 94, 10187-10203.

Blewitt G. (1990). An automatic editing algorithm for GPS data. Geophysical research

letters, 17, 199-202.
Blewitt G. (2008). Fixed point theorems of GPS carrier phase ambiguity resolution and their application to massive network processing: Ambizap. Journal of Geophysical Research, 113. doi: 10.1029/2008jb005736.
Blewitt; G, Bertiger; W, Weiss J-P. (2010). Ambizap3 and GPS carrierrange: a new data type with IGS applications. In. Proceedings of IGS workshop and vertical rates, Newcastle.
Boehm J, Niell A, Tregoning P, Schuh H. (2006). Global Mapping Function (GMF): A new empirical mapping function based on numerical weather model data. Geophysical Research Letters, 33. doi: 10.1029/2005gl025546.
Boehm J, Werl B, Schuh H. (2006). Troposphere mapping functions for GPS and very long baseline interferometry from European Centre for Medium‐Range Weather Forecasts operational analysis data. Journal of Geophysical Research: Solid Earth, 111.
Böhm J, Möller G, Schindelegger M, Pain G, Weber R. (2014). Development of an improved empirical model for slant delays in the troposphere (GPT2w). GPS Solutions, 19, 433-441. doi: 10.1007/s10291-014-0403-7.
Böhm J, Schuh H. (2013). Atmospheric Effects in Space Geodesy. Springer-Verlag Berlin Heidelberg.
Brockmann E. (1997). Combination of Solutions for Geodetic and Geodynamic Applications of the Global Positioning System (GPS), Astronomical Institute University of Berne. Ph. D. thesis.
Bruni S, Rebischung P, Zerbini S, Altamimi Z, Errico M, Santi E. (2018). Assessment of the possible contribution of space ties on-board GNSS satellites to the terrestrial reference frame. Journal of Geodesy, 92, 383-399.
Bury G, Sosnica K, Zajdel R, Strugarek D. (2020). Toward the 1-cm Galileo orbits: challenges in modeling of perturbing forces. Journal of Geodesy, 94. doi: ARTN 16 10.1007/s00190-020-01342-2.
Calero-Rodríguez EJ, Villiger A, Schaer S, Dach R, Jäggi A. (2023). Between-satellite ambiguity resolution based on preliminary GNSS orbit and clock information using a globally applied ambiguity clustering strategy. GPS Solutions, 27. doi: 10.1007/s10291-023-01435-3.
Carlin L, Hauschild A, Montenbruck O. (2021). Precise point positioning with GPS and Galileo broadcast ephemerides. GPS Solutions, 25. doi: 10.1007/s10291-021-01111-4.
Chandra R, Dagum L, Kohr D, Menon R, Maydan D, McDonald J. (2001). Parallel programming in OpenMP. Morgan kaufmann.
Chang X, Männel B, Schuh H. (2021). An analysis of a priori and empirical solar radiation pressure models for GPS satellites. Advances in Geosciences, 55, 33-45.
Chen G, Herring T. (1997). Effects of atmospheric azimuthal asymmetry on the analysis of space geodetic data. Journal of Geophysical Research-Solid Earth, 102, 20489-20502. doi: Doi 10.1029/97jb01739.
Chen H, Jiang W, Ge M, Wickert J, Schuh H. (2014). An enhanced strategy for GNSS data processing of massive networks. Journal of Geodesy, 88, 857-867. doi: 10.1007/s00190-014-0727-7.

Chen K, Ge M, Babeyko A, Li X, Diao F, Tu R. (2016). Retrieving real-time co-seismic displacements using GPS/GLONASS: a preliminary report from the September 2015 M w 8.3 Illapel earthquake in Chile. Geophysical Journal International, 206, 941-953.
Chen Q, Song S, Zhou W. (2021). Accuracy Analysis of GNSS Hourly Ultra-Rapid Orbit and Clock Products from SHAO AC of iGMAS. Remote Sensing, 13. doi: 10.3390/rs13051022.
Chen X, Ge M, Hugentobler U, Schuh H. (2022). A new parallel algorithm for improving the computational efficiency of multi-GNSS precise orbit determination. GPS Solutions, 26. doi: 10.1007/s10291-022-01266-8.
Chen X, Ge M, Liu Y, He L, Schuh H. (2023). Adapting empirical solar radiation pressure model for BDS-3 medium Earth orbit satellites. GPS Solutions, 27. doi: 10.1007/s10291-023-01524-3.
Cheng C, Zhao Y, Li L, Cheng J, Sun X. (2018). Preliminary analysis of URA characterization for GPS real-time precise orbit and clock products. In: 2018 IEEE/ION Position, Location and Navigation Symposium (PLANS). IEEE, pp. 615-621.
Cohen H. (1993). A course in computational algebraic number theory. Springer Berlin, Heidelberg.
Collins P, Bisnath S, Lahaye F, HÉRoux P. (2010). Undifferenced GPS Ambiguity Resolution Using the Decoupled Clock Model and Ambiguity Datum Fixing. Navigation, 57, 123-135. doi: 10.1002/j.2161-4296.2010.tb01772.x.
CSNO. (2019a). Announcement on the release of BeiDou satellite related parameters. http://www.beidou.gov.cn/yw/gfgg/201912/t20191209_19613.html. Accessed 1 Feb. 2024.
CSNO. (2019b). Release of the BDS-2 satellite related parameters. http://en.beidou.gov.cn/WHATSNEWS/201912/t20191209_19641.html. Accessed 1 Feb. 2024.
Cui B, Li P, Wang J, Ge M, Schuh H. (2021). Calibrating receiver-type-dependent wide-lane uncalibrated phase delay biases for PPP integer ambiguity resolution. Journal of Geodesy, 95. doi: 10.1007/s00190-021-01524-6.
Cui Y, Chen Z, Li L, Zhang Q, Luo S, Lu Z. (2021). An efficient parallel computing strategy for the processing of large GNSS network datasets. GPS Solutions, 25. doi: 10.1007/s10291-020-01069-9.
Dai X, Ge M, Lou Y, Shi C, Wickert J, Schuh H. (2015). Estimating the yaw-attitude of BDS IGSO and MEO satellites. Journal of Geodesy, 89, 1005-1018. doi: 10.1007/s00190-015-0829-x.
Deng Z, Nischan T, Bradke M. (2017). Multi-GNSS rapid orbit-, clock-& EOP-product series.
Deng Z, Wang J, Ge M. (2022). The GBM Rapid Product and the Improvement from Undifferenced Ambiguity Resolution. In: EGU General Assembly 2022, Vienna, Austria.
Dilssner F. (2010). GPS IIF-1 satellite antenna phase center and attitude modeling. Inside GNSS, 5, 59-64.
Dilssner F. (2017). A note on the yaw attitude modeling of BeiDou IGSO-6.pdf.
Dilssner F, Springer T, Enderle W. (2011). GPS IIF yaw attitude control during eclipse

season. In: AGU Fall Meeting Abstracts.
Dilssner F, Springer T, Gienger G, Dow J. (2011). The GLONASS-M satellite yaw-attitude model. Advances in Space Research, 47, 160-171.
Dong DN, Bock Y. (1989). Global positioning system network analysis with phase ambiguity resolution applied to crustal deformation studies in California. Journal of Geophysical Research: Solid Earth, 94, 3949-3966.
Duan B, Hugentobler U. (2021). Enhanced solar radiation pressure model for GPS satellites considering various physical effects. GPS Solutions, 25. doi: 10.1007/s10291-020-01073-z.
Duan B, Hugentobler U. (2022). Estimating surface optical properties and thermal thrust for Galileo satellite body and solar panels. GPS Solutions, 26. doi: 10.1007/s10291-022-01324-1.
Duan B, Hugentobler U, Hofacker M, Selmke I. (2020). Improving solar radiation pressure modeling for GLONASS satellites. Journal of Geodesy, 94. doi: 10.1007/s00190-020-01400-9.
Duan B, Hugentobler U, Selmke I. (2019). The adjusted optical properties for Galileo/BeiDou-2/QZS-1 satellites and initial results on BeiDou-3e and QZS-2 satellites. Advances in Space Research, 63, 1803-1812.
Duan B, Hugentobler U, Selmke I, Marz S, Killian M, Rott M. (2022). BeiDou Satellite Radiation Force Models for Precise Orbit Determination and Geodetic Applications. IEEE Transactions on Aerospace and Electronic Systems, 58, 2823-2836. doi: 10.1109/taes.2021.3140018.
El-Mowafy A, Bilbas E. (2016). Quality control in using GNSS CORS network for monitoring plate tectonics: a Western Australia case study. Journal of surveying engineering, 142, 05015003.
El-Mowafy A, Deo M, Kubo N. (2016). Maintaining real-time precise point positioning during outages of orbit and clock corrections. GPS Solutions, 21, 937-947. doi: 10.1007/s10291-016-0583-4.
Elsheikh M, Abdelfatah W, Noureldin A, Iqbal U, Korenberg M. (2019). Low-cost real-time PPP/INS integration for automated land vehicles. Sensors, 19, 4896.
Ferland R, Piraszewski M. (2009). The IGS-combined station coordinates, earth rotation parameters and apparent geocenter. Journal of Geodesy, 83, 385-392. doi: 10.1007/s00190-008-0295-9.
Fliegel H. (1989). Radiation pressure models for Block II GPS satellites. In: Proceedings of the Fifth International Geodetic Symposium on Satellite Positioning. National Geodetic Survey, pp. 789-798.
Fliegel H, Feess W, Layton W, Rhodus N. (1985). The GPS radiation Force Model In: Proceedings 1st international Symposium on Precise Positioning with the Global Positioning System.
Fliegel HF, Gallini TE. (1996). Solar force modeling of block IIR global positioning system satellites. Journal of Spacecraft and Rockets, 33, 863-866. doi: Doi 10.2514/3.26851.
Fliegel HF, Gallini TE, Swift ER. (1992). Global Positioning System Radiation Force

Model for Geodetic Applications. Journal of Geophysical Research-Solid Earth, 97, 559-568. doi: Doi 10.1029/91jb02564.
Formichella V, Galleani L, Signorile G, Sesia I. (2021). Time–frequency analysis of the Galileo satellite clocks: looking for the J2 relativistic effect and other periodic variations. GPS Solutions, 25, 1-14.
Ge H, Li B, Jia S, Nie L, Wu T, Yang Z, Shang J, Zheng Y, Ge M. (2022). LEO enhanced global navigation satellite system (LeGNSS): Progress, opportunities, and challenges. Geo-spatial Information Science, 25, 1-13.
Ge H, Li B, Wu T, Jiang S. (2021). Prediction models of GNSS satellite clock errors: Evaluation and application in PPP. Advances in Space Research, 68, 2470-2487. doi: 10.1016/j.asr.2021.05.025.
Ge M, Gendt G, Dick G, Zhang F. (2005a). Impact of GPS satellite antenna offsets on scale changes in global network solutions. Geophysical research letters, 32.
Ge M, Gendt G, Dick G, Zhang F, Rothacher M. (2006). A new data processing strategy for huge GNSS global networks. Journal of Geodesy, 80, 199-203. doi: 10.1007/s00190-006-0044-x.
Ge M, Gendt G, Dick G, Zhang FP. (2005b). Improving carrier-phase ambiguity resolution in global GPS network solutions. Journal of Geodesy, 79, 103-110. doi: 10.1007/s00190-005-0447-0.
Ge M, Gendt G, Rothacher M, Shi C, Liu J. (2007). Resolution of GPS carrier-phase ambiguities in Precise Point Positioning (PPP) with daily observations. Journal of Geodesy, 82, 389-399. doi: 10.1007/s00190-007-0187-4.
Geng J, Mao S. (2021). Massive GNSS Network Analysis Without Baselines: Undifferenced Ambiguity Resolution. Journal of Geophysical Research: Solid Earth, 126. doi: 10.1029/2020jb021558.
Geoffrey B, Yehuda B, Jan K. (1994). Constraining the IGS polyhedron by distributed processing. In: IGS workshop proceedings "Densification of the ITRF through regional GPS networks", JPL, pp. 21-37.
Gong X, Gu S, Lou Y, Zheng F, Ge M, Liu J. (2017). An efficient solution of real-time data processing for multi-GNSS network. Journal of Geodesy, 92, 797-809. doi: 10.1007/s00190-017-1095-x.
Griffiths J, Ray JR. (2009). On the precision and accuracy of IGS orbits. Journal of Geodesy, 83, 277-287.
GSA. (2017). Galileo Satellite Metadata. https://www.gsc-europa.eu/support-to-developers/galileo-satellite-metadata, Last access: 31 Oct. 2019.
GSA. (2019). Galileo IOV and FOC satellite metadata. https://www.gsc-europa.eu/support-to-developers/galileo-satellite-metadata, Accessed 2020-02-21.
Guo J, Chen G, Zhao Q, Liu J, Liu X. (2017). Comparison of solar radiation pressure models for BDS IGSO and MEO satellites with emphasis on improving orbit quality. GPS Solutions, 21, 511-522. doi: 10.1007/s10291-016-0540-2.
Guo J, Wang C, Chen G, Xu X, Zhao Q. (2023). BDS-3 precise orbit and clock solution at Wuhan University: status and improvement. Journal of Geodesy, 97. doi: 10.1007/s00190-

023-01705-5.
Guo J, Xu X, Zhao Q, Liu J. (2016). Precise orbit determination for quad-constellation satellites at Wuhan University: strategy, result validation, and comparison. Journal of Geodesy, 90, 143-159. doi: 10.1007/s00190-015-0862-9.
Heki K, Jin S. (2023). Geodetic study on earth surface loading with GNSS and GRACE. Satellite Navigation, 4. doi: 10.1186/s43020-023-00113-6.
Huang GW, Zhang Q, Xu GC. (2013). Real-time clock offset prediction with an improved model. GPS Solutions, 18, 95-104. doi: 10.1007/s10291-013-0313-0.
Huang W, Männel B, Brack A, Schuh H. (2020). Two methods to determine scale-independent GPS PCOs and GNSS-based terrestrial scale: comparison and cross-check. GPS Solutions, 25. doi: 10.1007/s10291-020-01035-5.
Huang W, Männel B, Sakic P, Ge M, Schuh H. (2020). Integrated processing of ground- and space-based GPS observations: improving GPS satellite orbits observed with sparse ground networks. Journal of Geodesy, 94, 96.
Jäggi A, Hugentobler U, Beutler G. (2006). Pseudo-Stochastic Orbit Modeling Techniques for Low-Earth Orbiters. Journal of Geodesy, 80, 47-60. doi: 10.1007/s00190-006-0029-9.
Jefferson DC, Heflin MB, Muellerschoen RJ. (2001). Examining the C1-P1 pseudorange bias. GPS Solutions, 4, 25-30.
Jiang C, Xu T, Nie W, Fang Z, Wang S, Xu A. (2021). A Parallel Approach for Multi-GNSS Ultra-Rapid Orbit Determination. Remote Sensing, 13. doi: 10.3390/rs13173464.
Katsigianni G, Loyer S, Perosanz F, Mercier F, Zajdel R, Sośnica K. (2019). Improving Galileo orbit determination using zero-difference ambiguity fixing in a Multi-GNSS processing. Advances in Space Research, 63, 2952-2963. doi: 10.1016/j.asr.2018.08.035.
Kazmierski K, Hadas T, Sośnica K. (2018). Weighting of Multi-GNSS Observations in Real-Time Precise Point Positioning. Remote Sensing, 10. doi: 10.3390/rs10010084.
Kazmierski K, Zajdel R, Sośnica K. (2020). Evolution of orbit and clock quality for real-time multi-GNSS solutions. GPS Solutions, 24. doi: 10.1007/s10291-020-01026-6.
Kiliszek D, Kroszczyński K, Araszkiewicz A. (2022). Analysis of Different Weighting Functions of Observations for GPS and Galileo Precise Point Positioning Performance. Remote Sensing, 14. doi: 10.3390/rs14092223.
Klos A, Dobslaw H, Dill R, Bogusz J. (2021). Identifying the sensitivity of GPS to non-tidal loadings at various time resolutions: examining vertical displacements from continental Eurasia. GPS Solutions, 25. doi: 10.1007/s10291-021-01135-w.
Knocke P, Ries J, Tapley B. (1988). Earth radiation pressure effects on satellites. In: Astrodynamics conference, pp. 4292.
Knoop VL, De Bakker PF, Tiberius CC, Van Arem B. (2017). Lane determination with GPS precise point positioning. IEEE Transactions on Intelligent Transportation Systems, 18, 2503-2513.
Kobayashi A, Tsuyuki T. (2019). Long-term slow slip event detected beneath the Shima Peninsula, central Japan, from GNSS data. Earth, Planets and Space, 71. doi: 10.1186/s40623-019-1037-3.
Koch K-R. (2013). Parameter estimation and hypothesis testing in linear models. Springer

Science & Business Media.
Kouba J. (2004). Improved relativistic transformations in GPS. GPS Solutions, 8, 170-180. doi: 10.1007/s10291-004-0102-x.
Kouba J. (2009a). A guide to using International GNSS Service (IGS) products.
Kouba J. (2009b). A simplified yaw-attitude model for eclipsing GPS satellites. GPS Solutions, 13, 1-12. doi: 10.1007/s10291-008-0092-1.
Kuang D, Desai S, Sibois A. (2017). Observed features of GPS Block IIF satellite yaw maneuvers and corresponding modeling. GPS Solutions, 21, 739-745. doi: 10.1007/s10291-016-0562-9.
Landskron D, Böhm J. (2018). VMF3/GPT3: refined discrete and empirical troposphere mapping functions. Journal of Geodesy, 92, 349-360.
Laurichesse D, Cerri L, Berthias J, Mercier F. (2013). Real time precise GPS constellation and clocks estimation by means of a Kalman filter. In: Proceedings of the 26th international technical meeting of the satellite division of the institute of navigation (ION GNSS+ 2013), pp. 1155-1163.
Laurichesse D, Mercier F, Berthias J-P, Broca P, Cerri L. (2009). Integer Ambiguity Resolution on Undifferenced GPS Phase Measurements and Its Application to PPP and Satellite Precise Orbit Determination. Navigation, 56, 135-149. doi: 10.1002/j.2161-4296.2009.tb01750.x.
Li X, Chen X, Ge M, Schuh H. (2018). Improving multi-GNSS ultra-rapid orbit determination for real-time precise point positioning. Journal of Geodesy, 93, 45-64. doi: 10.1007/s00190-018-1138-y.
Li X, Dick G, Lu C, Ge M, Nilsson T, Ning T, Wickert J, Schuh H. (2015). Multi-GNSS meteorology: real-time retrieving of atmospheric water vapor from BeiDou, Galileo, GLONASS, and GPS observations. IEEE Transactions on Geoscience Remote Sensing, 53, 6385-6393.
Li X, Li X, Yuan Y, Zhang K, Zhang X, Wickert J. (2017). Multi-GNSS phase delay estimation and PPP ambiguity resolution: GPS, BDS, GLONASS, Galileo. Journal of Geodesy, 92, 579-608. doi: 10.1007/s00190-017-1081-3.
Li X, Yuan Y, Huang J, Zhu Y, Wu J, Xiong Y, Li X, Zhang K. (2019). Galileo and QZSS precise orbit and clock determination using new satellite metadata. Journal of Geodesy, 93, 1123-1136. doi: 10.1007/s00190-019-01230-4.
Liu J, Ge M. (2003). PANDA software and its preliminary result of positioning and orbit determination. Wuhan University Journal of Natural Sciences, 8, 603.
Liu Y, Liu YX, Tian ZW, Dai XL, Qing Y, Li MH. (2019). Impact of ECOM Solar Radiation Pressure Models on Multi-GNSS Ultra-Rapid Orbit Determination. Remote Sensing, 11, 3024. doi: ARTN 302410.3390/rs11243024.
Lutz S, Beutler G, Schaer S, Dach R, Jäggi A. (2014). CODE's new ultra-rapid orbit and ERP products for the IGS. GPS Solutions, 20, 239-250. doi: 10.1007/s10291-014-0432-2.
Lyard FH, Allain DJ, Cancet M, Carrère L, Picot N. (2021). FES2014 global ocean tide atlas: design and performance. Ocean Science, 17, 615-649.
Meindl M, Beutler G, Thaller D, Dach R, Jaggi A. (2013). Geocenter coordinates estimated

from GNSS data as viewed by perturbation theory. Advances in Space Research, 51, 1047-1064. doi: 10.1016/j.asr.2012.10.026.
Melbourne WG. (1985). The case for ranging in GPS-based geodetic systems. In: Proceedings of the first international symposium on precise positioning with the Global Positioning System. US Department of Commerce Rockville, Maryland, pp. 373-386.
Milani A, Nobili AM, Farinella P. (1987). Non-gravitational perturbations and satellite geodesy.
Milbert D, Jekeli C. (2023). On the initialization of the sensitivity matrix in variational equations. Journal of Geodesy, 97. doi: 10.1007/s00190-023-01776-4.
Montenbruck O, Gill E, Lutze F. (2002). Satellite orbits: models, methods, and applications. Appl. Mech. Rev., 55, B27-B28.
Montenbruck O, Hauschild A, Steigenberger P. (2014). Differential code bias estimation using multi‐GNSS observations and global ionosphere maps. Navigation: Journal of the Institute of Navigation, 61, 191-201.
Montenbruck O, Schmid R, Mercier F, Steigenberger P, Noll C, Fatkulin R, Kogure S, Ganeshan AS. (2015). GNSS satellite geometry and attitude models. Advances in Space Research, 56, 1015-1029. doi: 10.1016/j.asr.2015.06.019.
Montenbruck O, Steigenberger P, Hauschild A. (2014). Broadcast versus precise ephemerides: a multi-GNSS perspective. GPS Solutions, 19, 321-333. doi: 10.1007/s10291-014-0390-8.
Montenbruck O, Steigenberger P, Hugentobler U. (2014). Enhanced solar radiation pressure modeling for Galileo satellites. Journal of Geodesy, 89, 283-297. doi: 10.1007/s00190-014-0774-0.
Navarro-Reyes D, Castro R, Bosch PR. (2015). Galileo first FOC launch: Recovery mission design. In: Proceedings of the 25th International Symposium on Space Flight Dynamics ISSFD, Munich, Germany, pp. 19-23.
Nie Z, Gao Y, Wang Z, Ji S, Yang H. (2017). An approach to GPS clock prediction for real-time PPP during outages of RTS stream. GPS Solutions, 22. doi: 10.1007/s10291-017-0681-y.
Peng Y, Lou Y, Gong X, Wang Y, Dai X. (2019). Real-time clock prediction of multi-GNSS satellites and its application in precise point positioning. Advances in Space Research, 64, 1445-1454. doi: 10.1016/j.asr.2019.06.040.
Penna NT, Morales Maqueda MA, Martin I, Guo J, Foden PR. (2018). Sea surface height measurement using a GNSS wave glider. Geophysical research letters, 45, 5609-5616.
Petit G, Luzum B. (2010). IERS conventions (2010). In. Bureau International des Poids et Mesures Sevres (France).
Pintori F, Serpelloni E, Gualandi A. (2021). Common mode signals and vertical velocities in the great Alpine area from GNSS data. Solid Earth Discussions, 1-37.
Prange L, Beutler G, Dach R, Arnold D, Schaer S, Jäggi A. (2020). An empirical solar radiation pressure model for satellites moving in the orbit-normal mode. Advances in Space Research, 65, 235-250. doi: 10.1016/j.asr.2019.07.031.
Prange L, Villiger A, Sidorov D, Schaer S, Beutler G, Dach R, Jaggi A. (2020). Overview

of CODE's MGEX solution with the focus on Galileo. Advances in Space Research, 66, 2786-2798. doi: 10.1016/j.asr.2020.04.038.
Qin Z, Zhang Q, Huang G, Tang L, Wang J, Wang X. (2023). BDS Orbit Maneuver Detection Based on Epoch-Updated Orbits Estimated by SRIF. Remote Sensing, 15. doi: 10.3390/rs15102558.
Quintana-Orti G, Quintana-Orti ES, Chan E, Van de Geijn RA, Van Zee FG. (2008). Scheduling of QR factorization algorithms on SMP and multi-core architectures. In: 16th Euromicro Conference on Parallel, Distributed and Network-Based Processing (PDP 2008). IEEE, pp. 301-310.
Ragauskas U, Bručas D, Sužiedelytė Visockienė J. (2017). Research on presice point positioning and Real-Time Kinematics corrections for unmanned aerial vehicle global positioning systems. Aviation, 21, 17-22.
Rebischung P. (2021). Terrestrial frame solutions from the IGS third reprocessing. In: EGU General Assembly Conference Abstracts, pp. EGU21-2144.
Rebischung P, Altamimi Z, Ray J, Garayt B. (2016). The IGS contribution to ITRF2014. Journal of Geodesy, 90, 611-630. doi: 10.1007/s00190-016-0897-6.
Reckeweg F. (2020). Integer Ambiguity Resolution for Multi-GNSS and Multi-Signal Raw Phase Observations. Technische Universität Darmstadt.
Reigber C, Schmidt R, Flechtner F, König R, Meyer U, Neumayer K-H, Schwintzer P, Zhu SY. (2005). An Earth gravity field model complete to degree and order 150 from GRACE: EIGEN-GRACE02S. Journal of Geodynamics, 39, 1-10.
Rodriguez-Solano CJ, Hugentobler U, Steigenberger P. (2012). Adjustable box-wing model for solar radiation pressure impacting GPS satellites. Advances in Space Research, 49, 1113-1128. doi: 10.1016/j.asr.2012.01.016.
Rodriguez-Solano CJ, Hugentobler U, Steigenberger P, Allende-Alba G. (2013). Improving the orbits of GPS block IIA satellites during eclipse seasons. Advances in Space Research, 52, 1511-1529. doi: 10.1016/j.asr.2013.07.013.
Rodriguez-Solano CJ, Hugentobler U, Steigenberger P, Blossfeld M, Fritsche M. (2014). Reducing the draconitic errors in GNSS geodetic products. Journal of Geodesy, 88, 559-574. doi: 10.1007/s00190-014-0704-1.
Rodriguez-Solano CJ, Hugentobler U, Steigenberger P, Lutz S. (2011). Impact of Earth radiation pressure on GPS position estimates. Journal of Geodesy, 86, 309-317. doi: 10.1007/s00190-011-0517-4.
Rothacher M, Beutler G, Herring TA, Weber R. (1999). Estimation of nutation using the Global Positioning System. Journal of Geophysical Research-Solid Earth, 104, 4835-4859. doi: Doi 10.1029/1998jb900078.
Rothacher M, Schmid R. (2010). ANTEX: The antenna exchange format, version 1.4. Document available at igscb. jpl. nasa. gov/igscb/station/general/antex14. txt. Search in.
Ruan R, Wei Z. (2019). Between-satellite single-difference integer ambiguity resolution in GPS/GNSS network solutions. Journal of Geodesy, 93, 1367-1379. doi: 10.1007/s00190-019-01251-z.
Schmid R, Steigenberger P, Gendt G, Ge M, Rothacher M. (2007). Generation of a

consistent absolute phase-center correction model for GPS receiver and satellite antennas. Journal of Geodesy, 81, 781-798. doi: 10.1007/s00190-007-0148-y.
Senior KL, Ray JR, Beard RL. (2008). Characterization of periodic variations in the GPS satellite clocks. GPS Solutions, 12, 211-225. doi: 10.1007/s10291-008-0089-9.
Shi C, Zhao Q, Geng J, Lou Y, Ge M, Liu J. (2008). Recent development of PANDA software in GNSS data processing. In: International Conference on Earth Observation Data Processing and Analysis (ICEODPA). SPIE, pp. 558-566.
Sibthorpe A, Bertiger W, Desai SD, Haines B, Harvey N, Weiss JP. (2011). An evaluation of solar radiation pressure strategies for the GPS constellation. Journal of Geodesy, 85, 505-517. doi: 10.1007/s00190-011-0450-6.
Sidorov D, Dach R, Polle B, Prange L, Jaggi A. (2020). Adopting the empirical CODE orbit model to Galileo satellites. Advances in Space Research, 66, 2799-2811. doi: 10.1016/j.asr.2020.05.028.
Sośnica K, Thaller D, Dach R, Steigenberger P, Beutler G, Arnold D, Jäggi A. (2015). Satellite laser ranging to GPS and GLONASS. Journal of Geodesy, 89, 725-743. doi: 10.1007/s00190-015-0810-8.
Springer T. (2009). NAPEOS mathematical models and algorithms. Technical note, DOPS-SYS-TN-0100-OPS-GN 1.0. Accessed.
Springer T, Hugentobler U. (2001). IGS ultra rapid products for (near-) real-time applications. Physics and Chemistry of the Earth, Part A: Solid Earth and Geodesy, 26, 623-628.
Springer TA, Beutler G, Rothacher M. (1999). A New Solar Radiation Pressure Model for GPS Satellites. GPS Solutions, 2, 50-62. doi: 10.1007/Pl00012757.
Standish EMJ. (1996). JPL Planetary and Lunar Ephemerides, DE405/LE405. JPL Interoffice Memorandum, 312.F-98-048.
Steigenberger P, Montenbruck O, Hugentobler U. (2015). GIOVE-B solar radiation pressure modeling for precise orbit determination. Advances in Space Research, 55, 1422-1431. doi: 10.1016/j.asr.2014.12.009.
Steigenberger P, Thoelert S, Montenbruck O. (2017). GNSS satellite transmit power and its impact on orbit determination. Journal of Geodesy, 92, 609-624. doi: 10.1007/s00190-017-1082-2.
Steigenberger P, Thoelert S, Montenbruck O. (2020). GPS III Vespucci: results of half a year in orbit. Advances in Space Research.
Strasser S, Mayer-Gürr T, Zehentner N. (2018). Processing of GNSS constellations and ground station networks using the raw observation approach. Journal of Geodesy, 93, 1045-1057. doi: 10.1007/s00190-018-1223-2.
Takasu T. (2013). Rtklib. Available: https://www.rtklib.com/.
Tang L, Wang J, Cui B, Zhu H, Ge M, Schuh H. (2023). Multi-GNSS precise point positioning with predicted orbits and clocks. GPS Solutions, 27. doi: 10.1007/s10291-023-01499-1.
Tang L, Wang J, Zhu H, Ge M, Xu A, Schuh H. (2021). A Comparative Study on the Solar Radiation Pressure Modeling in GPS Precise Orbit Determination. Remote Sensing, 13. doi:

10.3390/rs13173388.
Tang L, Wang J, Zhu H, Ge M, Xu A, Schuh H. (2023). Multi-GNSS ultra-rapid orbit determination through epoch-parallel processing. Journal of Geodesy, 97. doi: 10.1007/s00190-023-01787-1.
Teunissen PJG, Montenbruck O. (2017). Springer Handbook of Global Navigation Satellite Systems, Cham, Switzerland.
Thaller D. (2008). Inter-technique combination based on homogeneous normal equation systems including station coordinates, Earth orientation and troposphere parameters. Technische Universität München.
Villiger A, Schaer S, Dach R, Prange L, Sušnik A, Jäggi A. (2019). Determination of GNSS pseudo-absolute code biases and their long-term combination. Journal of Geodesy, 93, 1487-1500. doi: 10.1007/s00190-019-01262-w.
Wang C, Guo J, Zhao Q, Liu J. (2018a). Empirically derived model of solar radiation pressure for BeiDou GEO satellites. Journal of Geodesy, 93, 791-807. doi: 10.1007/s00190-018-1199-y.
Wang C, Guo J, Zhao Q, Liu J. (2018b). Yaw attitude modeling for BeiDou I06 and BeiDou-3 satellites. GPS Solutions, 22. doi: 10.1007/s10291-018-0783-1.
Wang J, Ge M, Glaser S, Balidakis K, Heinkelmann R, Schuh H. (2022). Improving VLBI analysis by tropospheric ties in GNSS and VLBI integrated processing. Journal of Geodesy, 96. doi: ARTN 32
10.1007/s00190-022-01615-y.
Wang J, Wu Z, Semmling M, Zus F, Gerland S, Ramatschi M, Ge M, Wickert J, Schuh H. (2019). Retrieving Precipitable Water Vapor From Shipborne Multi-GNSS Observations. Geophysical research letters, 46, 5000-5008. doi: 10.1029/2019gl082136.
Wang N, Li Z, Duan B, Hugentobler U, Wang L. (2020). GPS and GLONASS observable-specific code bias estimation: comparison of solutions from the IGS and MGEX networks. Journal of Geodesy, 94. doi: 10.1007/s00190-020-01404-5.
Wang N, Yuan Y, Li Z, Montenbruck O, Tan B. (2015). Determination of differential code biases with multi-GNSS observations. Journal of Geodesy, 90, 209-228. doi: 10.1007/s00190-015-0867-4.
Wang X, Chai H, Wang C. (2020). A high-precision short-term prediction method with stable performance for satellite clock bias. GPS Solutions, 24. doi: 10.1007/s10291-020-01019-5.
White AM, Gardner WP, Borsa AA, Argus DF, Martens HR. (2022). A Review of GNSS/GPS in Hydrogeodesy: Hydrologic Loading Applications and Their Implications for Water Resource Research. Water Resour Res, 58, e2022WR032078. doi: 10.1029/2022WR032078.
Wu J-T, Wu SC, Hajj GA, Bertiger WI, Lichten SM. (1992). Effects of antenna orientation on GPS carrier phase. asdy, 1647-1660.
Wu Z, Liu Y, Liu Y, Wang J, He X, Xu W, Ge M, Schuh H. (2020). Validating HY-2A CMR precipitable water vapor using ground-based and shipborne GNSS observations. Atmospheric Measurement Techniques, 13, 4963-4972. doi: 10.5194/amt-13-4963-2020.

Wübbena G. (1985). Software developments for geodetic positioning with GPS using TI-4100 code and carrier measurements. In: Proceedings of the first international symposium on precise positioning with the global positioning system. US Department of Commerce Rockville, Maryland, pp. 403-412.

Xie W, Huang G, Fu W, Li M, Du S, Tan Y. (2023). Realizing rapid re-convergence in multi-GNSS real-time satellite clock offset estimation with dual-thread integer ambiguity resolution. GPS Solutions, 27. doi: 10.1007/s10291-022-01393-2.

Yang H, Xu C, Gao Y. (2017). Analysis of GPS satellite clock prediction performance with different update intervals and application to real-time PPP. Survey Review, 51, 43-52. doi: 10.1080/00396265.2017.1359473.

Zajdel R, Sośnica K, Dach R, Bury G, Prange L, Jäggi A. (2019). Network Effects and Handling of the Geocenter Motion in Multi‐GNSS Processing. Journal of Geophysical Research: Solid Earth, 124, 5970-5989. doi: 10.1029/2019jb017443.

Zhang L, Tang H, Sun W. (2021). Comparison of GRACE and GNSS Seasonal Load Displacements Considering Regional Averages and Discrete Points. Journal of Geophysical Research: Solid Earth, 126. doi: 10.1029/2021jb021775.

Zhao Q, Guo J, Wang C, Lyu Y, Xu X, Yang C, Li J. (2022). Precise orbit determination for BDS satellites. Satellite Navigation, 3. doi: 10.1186/s43020-021-00062-y.

Zhao Q, Ma H, Xu X, Guo J, Li M. (2017). Hourly Updated Precise Orbit Products of Quad-constellation Satellites in IGS Analysis Center at Wuhan University. In: IGS workshop, France.

Zheng Z, Chen Y, Lu X. (2008). An improved grey model for the prediction of real-time GPS satellite clock bias. Acta Astronomica Sinica, 49, 306-320.

Ziebart M. (2004). Generalized analytical solar radiation pressure modeling algorithm for spacecraft of complex shape. Journal of spacecraft and rockets, 41, 840-848.

Zuo X, Jiang X, Li P, Wang J, Ge M, Schuh H. (2021). A square root information filter for multi-GNSS real-time precise clock estimation. Satellite Navigation, 2. doi: 10.1186/s43020-021-00060-0.

Zuo X, Li P, Cui B, Ge M, Schuh H. (2024). A computational efficient approach for multi-GNSS real-time precise clock estimation with undifferenced ambiguity resolution. Journal of Geodesy.

Zurutuza J, Caporali A, Bertocco M, Ishchenko M, Khoda O, Steffen H, Figurski M, Parseliunas E, Berk S, Nykiel G. (2019). The Central European GNSS Research Network (CEGRN) dataset. Data in brief, 27, 104762.